

SOME NUMERICAL STUDIES ON TISSUE PARAMETER QUANTITATION AND CONTRAST ENHANCEMENT IN MRI

A Thesis Submitted
in Partial Fulfillment of the Requirements
for the Degree of

DOCTOR OF PHILOSOPHY

by

SAJJA BALASRINIVASA RAO

to the

DEPARTMENT OF MATHEMATICS

INDIAN INSTITUTE OF TECHNOLOGY KANPUR

January, 2002

*Dedicated
To
My Parents and Teachers*

TH
MAH/2002/D
R18 &

26 OCT 2004

पुस्तोत्तम
भारतीय प्रौद्योगिकी संस्थान ज्ञानपुर
अवधि क्र० A. 149323



A149323

CERTIFICATE

It is certified that the work contained in the thesis entitled, "**SOME NUMERICAL STUDIES ON TISSUE PARAMETER QUANTITATION AND CONTRAST ENHANCEMENT IN MRI**", by Sajja Balasrinivasa Rao, has been carried out under my supervision and that this work has not been submitted elsewhere for a degree.

R.K.S. Rathore
Professor
Department of Mathematics
I.I.T. Kanpur

January, 2002

ACKNOWLEDGEMENTS

I express my sincere gratitude to Professor R.K.S. Rathore for introducing me to the field of Magnetic Resonance Imaging. I am thankful to his invaluable guidance, help and support. I take this opportunity to acknowledge the affection, homely treatment of Dr. (Mrs) Rathore, and cheerful love of Divya and Satya.

I owe a special debt of gratitude to Professor R.K. Gupta, Department of Radiology, SGPGIMS, Lucknow for his stimulating discussions, encouragement and providing us very useful MRI data to carry out this research.

My heartiest thanks to Prof. P.C. Das, Prof. M.K. Kadalbajoo, Prof. Peeyush Chandra, and Prof. P. Sharma for their advice, help and encouragement.

I'm thankful to my friends Mahesh, Kali, Kalyan, Sushmita, Bishwa, Parasar, Manish, Muthu, Mini, Swagata, Alok, Rajan, and Balaji for making my stay at I.I.T. Kanpur a memorable one. I am also thankful to my friends Rajesh, Sanjeev, and Monika who made my visits to SGPGI, Lucknow comfortable and memorable.

I can't find words to express the intensity of my feeling for the love and affection I got from my parents. My special thanks are to my brother, for his affection, encouragement, and good suggestions right from my childhood. My sincere thanks are to my sisters: Hyma, Suja, and Vijayalaksmi and brothers-in-law: Murali, Vijayababu, Rudra and sister-in-law: Rajyalakshmi for their love and affection.

Finally, I acknowledge the financial support provided by C.S.I.R., India to carrying out this research.

-sb rao

CONTENTS

	Page No.
List of Figures	vi
List of Tables	ix
List of Graphs	xiii
Chapter 1	Introduction
1.1	Basics of Magnetic Resonance Imaging
1.1.1	Precession
1.1.2	Radiofrequency Field
1.1.3	Free-Induction Decay
1.1.4	Proton Density
1.1.5	Spin-Lattice Relaxation Time
1.1.6	Spin-Spin Relaxation Time
1.1.7	Bloch Equations
1.1.8	Selective Excitation
1.1.9	Imaging Techniques
1.1.10	Fourier Zeugmatography
1.1.11	Spin-warp
1.1.12	Spin-echo
1.2	Pulse Sequences
1.2.1	Pulse Sequence Timing Diagram
1.2.2	Saturation Recovery Spin Echo Sequence
1.2.3	Inversion Recovery Spin Echo Sequence
1.2.4	Magnetization Transfer Pulse
1.3	Literature Review
1.4	Contents of the Thesis
Chapter 2	Numerical Methods for Tissue Parameter Quantitation and Sensitivity Analysis
2.1	Two Point Calculations
2.2	Iterative Methods

2.2.2	A Least Squares Method for T_2 Calculation	52
2.2.3	A Linearized Least Squares Method for T_1 , T_2 , and ρ Calculation	56
2.2.4	Reduction to a Single Variable Case	58
2.2.5	Least Squares Method for T_1 , T_2 , and ρ	63
2.2.6	Computables of Tissue Parameters and Field Susceptibility Maps	64
2.3	Error Propagation in Tissue Parameters Estimation	73
2.3.1	Errors due to Bit Reduction	74
2.3.2	Effect of Filtering	86
Chapter 3	Generation of High Contrast Images for Diagnosis	98
3.1	Entropy-Like Maximization	99
3.2	Orthonormal Images	102
3.3	Functional Maps	104
3.4	Generation of Parameter Map Like Contrast Images	106
3.5	Synthetic MRI	110
3.6	Partial Volume Correction for Synthesis	112
3.7	Tissue Parameter Maps for Segmentation	114
Chapter 4	Quantitation of Cystic Cavity, Perilesional Gliosis, and Edema	119
4.1	Statistical Tools	120
4.1.1	F-test for Significantly Different Variances	120
4.1.2	Student's t-Test for Significantly Different Means	121
4.1.3	Linear Correlation Coefficients	122
4.2	Quantitation of Cystic Cavity	122
4.3	Quantitation of Perilesional Gliosis	131
4.4	Quantitation of Edema	140
References		149

LIST OF FIGURES

Figure No.	Figure Description	Page No.
1.1	Simplified block diagram of a representative MR system	3
1.2	Tipping of longitudinal magnetization into transverse magnetization by a magnetic field H_1 , associated with an RF pulse. (a) For appreciable tipping to occur, the H_1 field must rotate synchronously with the precessing transverse magnetization. This condition is met by a circularly polarized RF pulse at the Larmor frequency. (b) All of the longitudinal magnetization is tipped into the transverse plane by an RF pulse that is strong enough and applied long enough to tip the magnetization 90° (90-degree RF pulse)	5
1.3	Timing diagram of spin echo sequence	17
1.4	Images of human head with different forms of contrast. (a) a spin density weighted image, (b) a T_2 weighted image and (c) a T_1 weighted image. These different acquisitions can be seen to create different contrasts between white matter, gray matter and cerebrospinal fluid. They all reveal excellent anatomic details.	20
1.5	Inversion recovery pulse sequence timing diagram	21
1.6	Images of a 12 year old with HIV and associated CNS lesions. (a) T_1 weighted image with TE/TR: 14 ms/ 640 ms using a conventional spin echo. (b) Proton Density weighting with a TE/TR: 22 ms / 3800 ms using a Turbo-Spin Echo. (c) A FLAIR image with a Turbo-IR, with TE/TR/TI : 105 ms/ 7000 ms/2500 ms, and (d) A T_2 weighted image obtained as the second image in a double echo sequence with proton density image in (b), but with TE = 90 ms. Note how the lesion becomes more conspicuous in the FLAIR compared to the T_2 , and how the CSF is rendered entirely dark.	24
1.7	Magnetization transfer effects. The first image (a) was obtained without MT, the second (b) with MT and the third (c) is calculated magnetization transfer ratio, as per equation given in the text	26
2.1	(a) and (b) are two spin echo images with TE/TR = 20/ 2200, 1100 ms. Image (c) is the computed T_1 map	38
2.2	(a) and (b) are two spin echo images with TR/TE = 2200/20, 80 ms. Image (c) is the computed T_2 map	44
2.3	First four are spin echo images with TR/TE = 850, 1100, 1650, 2200/20 ms. The last image is the computed T_1 map	51

2.4	The first four are multi spin echo images with TE/TR = 20, 46, 80, 144/2200 ms. The last image is the computed T ₂ map	55
2.5	Images in the first column are T ₁ T ₂ , and PD weighted spin echo images with TR/TE = 1012/14, 2200/80, 2200/20 ms of a patient with perilesional gliosis around the cystic cavity. Second column images are the T ₁ , T ₂ , PD map computed using the method described in subsection 2.2.4	61
2.6	Divergent map	62
2.7	Maps of T _{1x} , T _{2x} /T ₂ ² , ρ_x/ρ and their histogram equalizations	70
2.8	1 st column: Computed parameters from three weighted images. 2 nd column: Computed parameters from the same images except for one image is multiplied with 1.1	71
2.9	Different factors and their histogram equalized maps used as simulated varying field maps	72
2.10	T ₁ weighted image with different number of bits removed	76
2.11	T ₂ weighted image with different number of bits removed	77
2.12	PD weighted image with different number of bits removed	78
2.13	T ₁ map computed from different number of bits removed weighted images	79
2.14	T ₂ map computed from different number of bits removed weighted images	80
2.15	PD map computed from different number of bits removed weighted images	81
2.16	Blurred and iteratively de-blurred by Poisson filter (T ₁ weighted image)	88
2.17	Blurred and iteratively de-blurred by Poisson filter (T ₂ weighted image)	89
2.18	Blurred and iteratively de-blurred by Poisson filter (PD weighted image)	90
2.19	T ₁ map calculated from weighted images blurred and de-blurred by Poisson filter	91
2.20	T ₂ map calculated from weighted images blurred and de-blurred by Poisson filter	92
2.21	PD map calculated from weighted images blurred and de-blurred by Poisson filter	93
3.1	Generation of entropy like contrast images using weighted linear combination of acquired images	101
3.2	Generation of orthonormal images using Gram-Schmidt orthogonalization process	103
3.3	Generation of T ₁ and T ₂ functional maps	105

3.4(a)	Generation of tissue parameter contrast images by a linear weighted combination of images	107
3.4(b)	Generation of tissue parameter contrast images by a linear weighted combination of images	108
3.5	1 st row: T ₁ , T ₂ , PD weighted images. 2 nd row: T ₁ , T ₂ , PD maps computed weighted images. 3 rd row: 1 st image: MT SE T ₁ weighted image, 2 nd and 3 rd images: Synthesized IRSE images at TR/TE/TI = 2200/80/1500, 6000/40/2500 ms	111
3.6	Demonstration of partial volume correction for image synthesis	113
3.7	Histogram plots of white matter values in weighted images and in computed parameter maps	116
3.8(a)	1 st column: weighted spin echo images, 2 nd column: corresponding computed parameter maps	117
3.8(b)	1 st column: weighted combination images, 2 nd column: segmented with different images.	118

LIST OF TABLES

Table No.	Table Description	Page No.
1.1	Magnetic resonance properties of some diagnostically relevant nuclei	4
1.2	Brain tissue parameters measured in selected sections at 1.5 Tesla	7
1.3	Longitude and transverse magnetic moment values at each step of the first spin-echo of SRSE	18
1.4	Longitude and transverse magnetic moment values at each step of the second spin-echo of SRSE	18
1.5	Effect of TE and TR on image contrast in spin-echo imaging	19
1.6	Longitude and transverse magnetic moment values at each step of the first spin-echo of IRSE	22
1.7	Longitude and transverse magnetic moment values at each step of the second spin-echo of IRSE	22
1.8	Common clinical variants of the inversion recovery sequence	23
2.1	% Errors in T_1 computation of different brain tissues using equation (2.1.2) with $TR_1 = 1200$ ms and $TR_2 = 600$ ms at different noise levels	39
2.2	% Errors in T_1 computation of different brain tissues using equation (2.1.2) with $TR_1 = 1500$ ms and $TR_2 = 750$ ms at different noise levels	39
2.3	% Errors in T_1 computation of different brain tissues using equation (2.1.2) with $TR_1 = 2000$ ms and $TR_2 = 1000$ ms at different noise levels	40
2.4	% Errors in T_1 computation of different brain tissues using equation (2.1.2) with $TR_1 = 3000$ ms and $TR_2 = 1500$ ms at different noise levels	40
2.5	% Errors in T_2 computation of different brain tissues using equation (2.1.4) with $TE_1 = 20$ ms and $TE_2 = 60$ ms at different noise levels	45
2.6	% Errors in T_2 computation of different brain tissues using equation (2.1.4) with $TE_1 = 20$ ms and $TE_2 = 80$ ms at different noise levels	45
2.7	% Errors in T_2 computation of different brain tissues using equation (2.1.4) with $TE_1 = 20$ ms and $TE_2 = 140$ ms at different noise levels	45
2.8	% Errors in T_2 computation of different brain tissues using equation (2.1.4) with $TE_1 = 20$ ms and $TE_2 = 200$ ms at different noise levels	46

2.9	Parameters computed with single variable and two point methods	62
2.10	% Errors in computed T_1 , T_2 , and PD values when derivatives are evaluated by divided differences	68
2.11	% Errors in computed T_1 , T_2 , and PD values with one of the images multiplied with a constant 1.1	68
2.12	% Errors in computed T_1 , T_2 , and PD values using images multiplied with factor for different k values	69
2.13	% Errors in estimation of multiplication factors	69
2.14	Average & average relative errors due to bit reduction in T_1 weighted image	82
2.15	Average & average relative errors due to bit reduction in T_2 weighted image	82
2.16	Average & average relative errors due to bit reduction in PD weighted image	82
2.17	Average & average relative errors due to bit reduction in T_1 map	83
2.18	Average & average relative errors due to bit reduction in T_2 map	83
2.19	Average & average relative errors due to bit reduction in PD map	83
2.20	% Error in deblurring by Poisson filter ($r = 0.99$) (T_1 weighted)	94
2.21	% Error in deblurring by Poisson filter ($r = 0.99$) (T_2 weighted)	94
2.22	% Error in deblurring by Poisson filter ($r = 0.99$) (PD weighted)	94
2.23	% Error in deblurring by Poisson filter ($r = 0.99$) (T_1 map)	95
2.24	% Error in deblurring by Poisson filter ($r = 0.99$) (T_2 map)	95
2.25	% Error in deblurring by Poisson filter ($r = 0.99$) (PD map)	95
3.1	L_2 average percentage errors in weighted combinations with respect to T_1 map and corresponding weights	109
3.2	L_2 average percentage errors in weighted combinations with respect to T_2 map and corresponding weights	109
3.3	L_2 average percentage errors in weighted combinations with respect to PD map and corresponding weights	109
3.4	L_2 average percentage errors in weighted combinations with respect to MTR map and corresponding weights	109
3.5	Contrast measurements in tissue parameter maps and weighted images between different brain tissues	115
4.1	Mean and standard deviation of normal and cystic cavity regions and Student's t , F statistics and their probabilities on MT SE T_1 weighted images	132
4.2	Mean and standard deviation of normal and cystic cavity regions and Student's t , F statistics and their probabilities on MTR maps	123

4.3	Mean and standard deviation of normal and cystic cavity regions and Student's t, F statistics and their probabilities on T ₁ weighted images	124
4.4	Mean and standard deviation of normal and cystic cavity regions and Student's t, F statistics and their probabilities on T ₁ maps	124
4.5	Mean and standard deviation of normal and cystic cavity regions and Student's t, F statistics and their probabilities on T ₂ weighted images	124
4.6	Mean and standard deviation of normal and cystic cavity regions and Student's t, F statistics and their probabilities on T ₂ maps	125
4.7	Mean and standard deviation of normal and cystic cavity regions and Student's t, F statistics and their probabilities on PD weighted images	125
4.8	Mean and standard deviation of normal and cystic cavity regions and Student's t, F statistics and their probabilities on PD maps	125
4.9	Linear correlation coefficients between different weighted images in normal regions	127
4.10	Linear correlation coefficients between different weighted images in cystic cavity regions	127
4.11	Linear correlation coefficients between different parameter maps in normal regions	128
4.12	Linear correlation coefficients between different parameter maps in cystic cavity regions	128
4.13	Mean and standard deviation of normal and gliosis regions and Student's t, F statistics and their probabilities on MT SE T ₁ weighted images	131
4.14	Mean and standard deviation of normal and gliosis regions and Student's t, F statistics and their probabilities on MTR maps	132
4.15	Mean and standard deviation of normal and gliosis regions and Student's t, F statistics and their probabilities on T ₁ weighted images	132
4.16	Mean and standard deviation of normal and gliosis regions and Student's t, F statistics and their probabilities on T ₁ maps	133
4.17	Mean and standard deviation of normal and gliosis regions and Student's t, F statistics and their probabilities on T ₂ weighted images	133
4.18	Mean and standard deviation of normal and gliosis regions and Student's t, F statistics and their probabilities on T ₂ maps	133
4.19	Mean and standard deviation of normal and gliosis regions and Student's t, F statistics and their probabilities on PD weighted images	134
4.20	Mean and standard deviation of normal and gliosis regions and Student's t, F statistics and their probabilities on PD maps	134
4.21	Linear correlation coefficients between different weighted images in normal regions	136
4.22	Linear correlation coefficients between different weighted images in gliosis regions	136
4.23	Linear correlation coefficients between different parameter maps in	137

	normal regions	
4.24	Linear correlation coefficients between different parameter maps in gliosis regions	137
4.25	Mean and standard deviation of normal and edema regions and Student's t, F statistics and their probabilities on MT SE T ₁ weighted images	140
4.26	Mean and standard deviation of normal and edema regions and Student's t, F statistics and their probabilities on MTR maps	141
4.27	Mean and standard deviation of normal and edema regions and Student's t, F statistics and their probabilities on T ₁ weighted images	141
4.28	Mean and standard deviation of normal and edema regions and Student's t, F statistics and their probabilities on T ₁ maps	142
4.29	Mean and standard deviation of normal and edema regions and Student's t, F statistics and their probabilities on T ₂ weighted images	142
4.30	Mean and standard deviation of normal and edema regions and Student's t, F statistics and their probabilities on T ₂ maps	142
4.31	Mean and standard deviation of normal and edema regions and Student's t, F statistics and their probabilities on PD weighted images	143
4.32	Mean and standard deviation of normal and edema regions and Student's t, F statistics and their probabilities on PD maps	143
4.33	Linear correlation coefficients between different weighted images in normal regions	145
4.34	Linear correlation coefficients between different weighted images in edema regions	145
4.35	Linear correlation coefficients between different parameter maps in normal regions	146
4.36	Linear correlation coefficients between different parameter maps in edema regions	146

LIST OF GRAPHS

Graph No.	Graph Description	Page No.
2.1(a)	% Errors in T_1 computation of white matter with different TR_2 values at different noise levels	41
2.1(b)	% Errors in T_1 computation of gray matter with different TR_2 values at different noise levels	41
2.1(c)	% Errors in T_1 computation of edema with different TR_2 values at different noise levels	41
2.1(d)	% Errors in T_1 computation of CSF with different TR_2 values at different noise levels	42
2.1(e)	% Errors in T_1 computation of upper cystic fluid with different TR_2 values at different noise levels	42
2.1(f)	% Errors in T_1 computation of lower cystic fluid with different TR_2 values at different noise levels	42
2.1(g)	% Errors in T_1 computation of methemoglobin with different TR_2 values at different noise levels	43
2.2(a)	% Errors in T_2 computation of white matter with different TE_2 values at different noise levels	46
2.2(b)	% Errors in T_2 computation of gray matter with different TE_2 values at different noise levels	47
2.2(c)	% Errors in T_2 computation of edema with different TE_2 values at different noise levels	47
2.2(d)	% Errors in T_1 computation of CSF with different TE_2 values at different noise levels	47
2.2(e)	% Errors in T_2 computation of upper cystic fluid with different TE_2 values at different noise levels	48
2.2(f)	% Errors in T_2 computation of lower cystic fluid with different TE_2 values at different noise levels	48
2.2(g)	% Errors in T_2 computation of methemoglobin with different TE_2 values at different noise levels	48
2.3	Plot of $F(T_1)$ vs T_1 values with $TR/TE = 2200/20, 1024/14, 2200/80$ ms	59
2.4(a)	Average L_1 errors in T_1 , T_2 , and PD weighted images due to bit reduction	84
2.4(b)	Average L_2 errors in T_1 , T_2 , and PD weighted images due to bit reduction	84

2.4(c)	Average L_{∞} errors in T_1 , T_2 , and PD weighted images due to bit reduction	84
2.5(a)	Average L_1 errors in T_1 , T_2 , and PD maps computed from bit reduced images	85
2.5(b)	Average L_2 errors in T_1 , T_2 , and PD maps computed from bit reduced images	85
2.5(c)	Average L_{∞} errors in T_1 , T_2 , and PD maps computed from bit reduced images	85
2.6(a)	Average L_1 errors in T_1 , T_2 and PD weighted images blurred and iteratively deblurred by Poisson filter ($r = 0.99$)	96
2.6(b)	Average L_2 errors in T_1 , T_2 and PD weighted images blurred and iteratively deblurred by Poisson filter ($r = 0.99$)	96
2.6(c)	Average L_{∞} errors in T_1 , T_2 and PD weighted images blurred and iteratively deblurred by Poisson filter ($r = 0.99$)	96
2.7(a)	Average L_1 errors in T_1 , T_2 and PD maps computed from blurred and iteratively deblurred images	97
2.7(b)	Average L_2 errors in T_1 , T_2 and PD maps computed from blurred and iteratively deblurred images	97
2.7(c)	Average L_{∞} errors in T_1 , T_2 and PD maps computed from blurred and iteratively deblurred images	97
4.1	Mean values in cystic cavity and contra-lateral normal regions on MT SE T_1 weighted images	129
4.2	Mean values in cystic cavity and contra-lateral normal regions on T_1 weighted images	129
4.3	Mean values in cystic cavity and contra-lateral normal regions on T_2 weighted images	129
4.4	Mean values in cystic cavity and contra-lateral normal regions on PD weighted images	129
4.5	Mean values in cystic cavity and contra-lateral normal regions on MTR maps	130
4.6	Mean values in cystic cavity and contra-lateral normal regions on T_1 maps	130
4.7	Mean values in cystic cavity and contra-lateral normal regions on T_2 maps	130
4.8	Mean values in cystic cavity and contra-lateral normal regions on PD maps	130
4.9	Mean values in perilesional gliosis and contra-lateral normal regions on MT SE T_1 weighted images	138
4.10	Mean values in perilesional gliosis and contra-lateral normal regions on T_1 weighted images	138

4.11	Mean values in perilesional gliosis and contra-lateral normal regions on T ₂ weighted images	138
4.12	Mean values in perilesional gliosis and contra-lateral normal regions on PD weighted images	138
4.13	Mean values in perilesional gliosis and contra-lateral normal regions on MTR maps	139
4.14	Mean values in perilesional gliosis and contra-lateral normal regions on T ₁ maps	139
4.15	Mean values in perilesional gliosis and contra-lateral normal regions on T ₂ maps	139
4.16	Mean values in perilesional gliosis and contra-lateral normal regions on PD maps	139
4.17	Mean values in edema and contra-lateral normal regions on MT SE T ₁ weighted images	147
4.18	Mean values in edema and contra-lateral normal regions on T ₁ weighted images	147
4.19	Mean values in edema and contra-lateral normal regions on T ₂ weighted images	147
4.20	Mean values in edema and contra-lateral normal regions on PD weighted images	147
4.21	Mean values in edema and contra-lateral normal regions on MTR maps	148
4.22	Mean values in edema and contra-lateral normal regions on T ₁ maps	148
4.23	Mean values in edema and contra-lateral normal regions on T ₂ maps	148
4.24	Mean values in edema and contra-lateral normal regions on PD maps	148

Chapter 1

Introduction

Magnetic resonance imaging (MRI) is a powerful non-invasive diagnostic tool in medicine because of its non-radioactive nature and high tissue contrast compared to other medical imaging modalities like X-ray CT. Magnetic resonance (MR) is based on the interaction between a system of atomic nuclei and an external magnetic field. A typical MR experiment consists of perturbing this system from its equilibrium configuration, and observing how it relaxes back to the equilibrium. During this relaxation process an induced electric signal is measured. This signal depends on three quantities proton spin density (PD or ρ), the interactions of the nuclei with their surrounding molecular environment (T_1 relaxation time), and those between close nuclei (T_2 relaxation time). Based on a suitable set of measured electric signals, a function of ρ , T_1 , and T_2 is computed which is called MR image. In this thesis, the word 'tissue parameters' is used to represent all proton density, T_1 and T_2 relaxation times.

In nuclear magnetic resonance (NMR), the estimation of relaxation times dates back to shortly after discovery of the NMR phenomenon itself. These relaxation times estimation has been used extensively in NMR spectroscopy largely for the determination of the longitudinal relaxation time, T_1 . Since the advent of magnetic resonance imaging in the early 1980s, parameters estimation has been extended to in vivo applications. NMR parameters have been proven useful in a variety of applications, including optimization of NMR pulse sequences, understanding of the contrast mechanisms in MRI, and identification of normal and disease processes.

In biology, much of the interest in tissue relaxation times has started from the observation by R. Damadian (1971) that spin-lattice relaxation times are elevated in tumorous tissues (see P.G. Morris (1986)). This was demonstrated using two malignant rat tumors, Novikoff hepatoma and Walker sarcoma, which had T_1 values at 24 MHz of 736 and 826 ms respectively, compared with values in normal tissues extending over the range of 257 to 595 ms. Confirmation that this was a general effect followed rapidly with measurements of T_1 values in animal and human tissues. Soon after Damadian's initial discovery, C.F. Hazlewood, D.C. Chang, D. Medina, G. Cleveland and B.L.

Nichols (1972) showed that it was possible to detect cancer at early stage of development. They were able to distinguish normal, preneoplastic and tumourous murine glands not only on the basis of elevated T_1 values but also by way of their increased T_2 values and diffusion constants.

The specific goal of tissue characterization using an imaging technique is the possibility of discrimination between a lesion and adjacent normal tissues, between benign and malignant neoplasias, and between primary tumors and metastases using special analysis procedures. The objective is to improve diagnosis and prognosis and optimize therapy planning. Intrinsic multi parameter dependence is a peculiarity of MRI, which provides both high tissue contrast flexibility and a possible special source of in vivo tissue characterization. A primary role in the expression of these features is played by MR spin-lattice and spin-spin relaxation times of tissues in the body (see, F. Podo (1990)). An objective evaluation of the clinical significance of tissue characterization by MRI can, however, only derive from quantitative measurement of the physical parameters involved, together with their correlations with relevant clinical, biochemical, and histopathological data.

This introductory chapter describes some basic concepts of MRI, two important pulse sequences viz., saturation recovery spin echo (SRSE), and inversion recovery spin echo (IRSE) and is followed by a summary of contents of the rest of the chapters of the thesis.

1.1. Basics of Magnetic Resonance Imaging

For the basics of Nuclear Magnetic Resonance (NMR) imaging, a number of excellent texts, e.g., T. Farrar and E. Becker (1971), P. T. Callaghan (1991), P. Mansfield and P. Morris (1982), C.L. Partain, R.R. Price, J.A. Patton, M.V. Kulkarni and E.V. James Jr. (1988), and D.D. Stark and W.G. Bradley Jr. (1999) are available.

A simplified block diagram of a computer-controlled MR system is shown in the Figure 1.1. The computer and accessories constitute the command and control center of the MR system, performing shaping and timing the radiofrequency pulses, turning the gradients on and off, selecting region of interest (ROI) of the scanning object, instructing the receiver to collect data, manipulation, storage, retrieval, multi-format processing and providing the data for diagnosis.

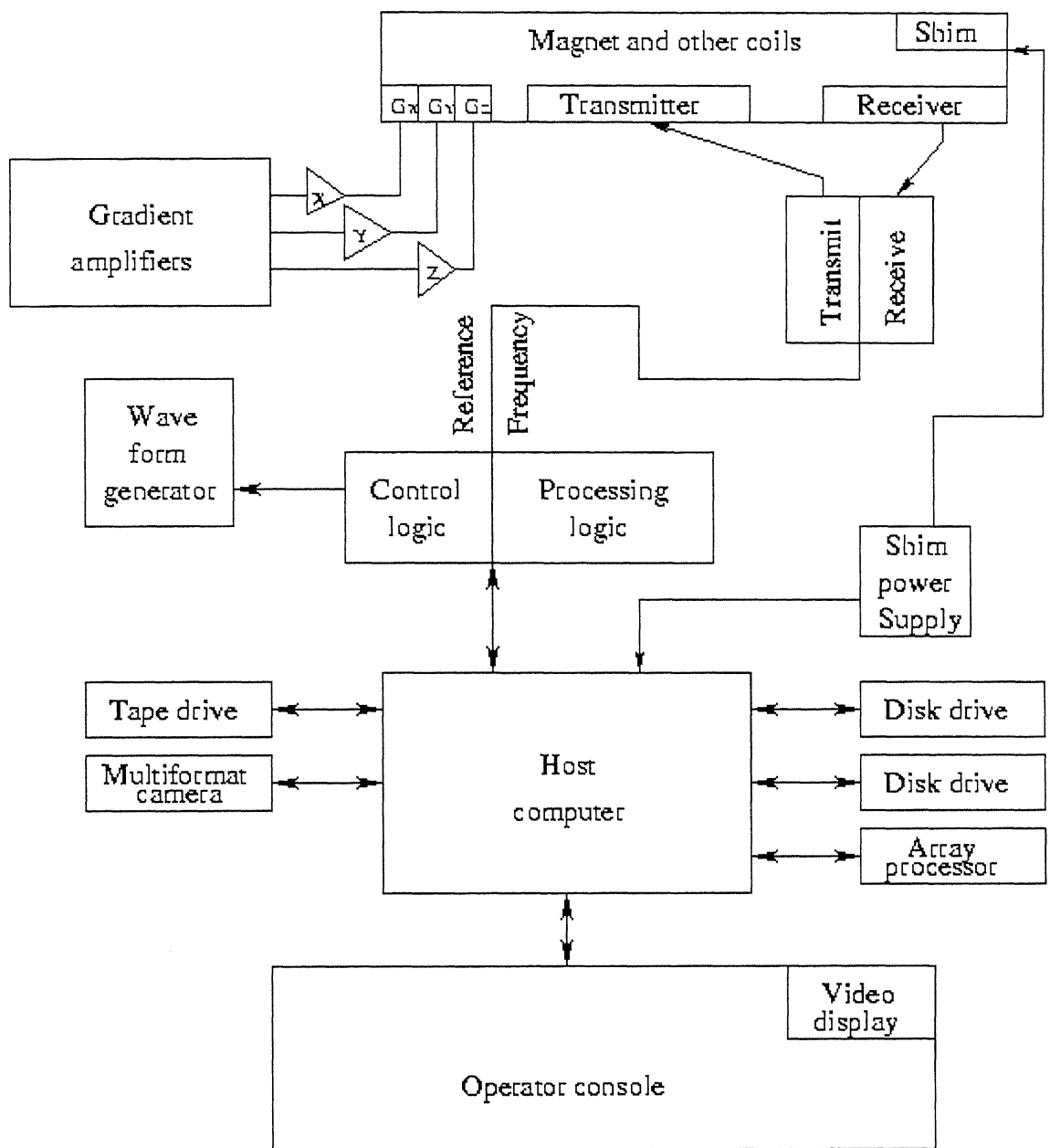


Figure 1.1: Simplified block diagram of a representative MR system

1.1.1. Precession

In presence of an applied magnetic field \mathbf{H}_0 , the magnetic momentum vectors experience a torque and precess about the axis of the magnetic field with a rate given by the Larmor's relationship

$$f_L = (\omega / 2\pi) = (\gamma / 2\pi) \mathbf{H}_0, \quad (1.1.1)$$

where f_L is the resonance frequency, ω is the angular frequency and γ is the gyromagnetic ratio. The gyromagnetic ratio is equal to the ratio of the magnitude of the magnetic moment of the nucleus to the magnitude of its spin angular momentum.

Gyromagnetic ratios, relative detection sensitivities, and isotopic abundances for a few diagnostically relevant nuclei are listed in Table 1.1 (M.L. Wood and F.W. Wehrli (1999)). The proton, which is the major isotope of hydrogen, is favored for MRI because of its abundance and sensitivity.

Nucleus	Relevant Abundance (%)	Relative Sensitivity	Gyromagnetic Ratio (MHz/T)
^1H	99.98	1	42.58
^2H	0.015	9.65×0.00965	6.53
^{13}C	1.11	0.016	10.71
^{19}F	100	0.830	40.05
^{23}Na	100	0.093	11.26
^{31}P	100	6.6×0.066	17.23
^{39}K	93.1	5.08×0.000508	1.99

Table 1.1: Magnetic resonance properties of some diagnostically relevant nuclei

1.1.2. Radiofrequency (RF) Field

MR can be detected only if transverse magnetization (magnetization perpendicular to \mathbf{H}_0) is created because this transverse magnetization is time dependent and thus, according to Faraday's law of induction, can induce a voltage in a receiver coil. The longitudinal magnetization in thermal equilibrium is static and therefore does not meet the criteria for magnetic induction. Transverse magnetization is created when an RF field of amplitude H_1 , rotating synchronously with the precessing spins, is applied (Figure 1.2(a)). When this RF field is directed perpendicular to the main field, the net magnetization rotates away from its equilibrium orientation. If H_1 field rotates the net magnetization by 90° , all of the longitudinal magnetization is converted to transverse magnetization, as in Figure 1.2(b) (M.L. Wood and F.W. Wehrli (1999)).

1.1.3. Free-Induction Decay (FID)

Once the RF pulse is removed, the magnetization precesses about the static magnetic field at the Larmor frequency. The precessing magnetization can be detected as a time-varying electrical voltage across the ends of coil of wire placed around the object. The

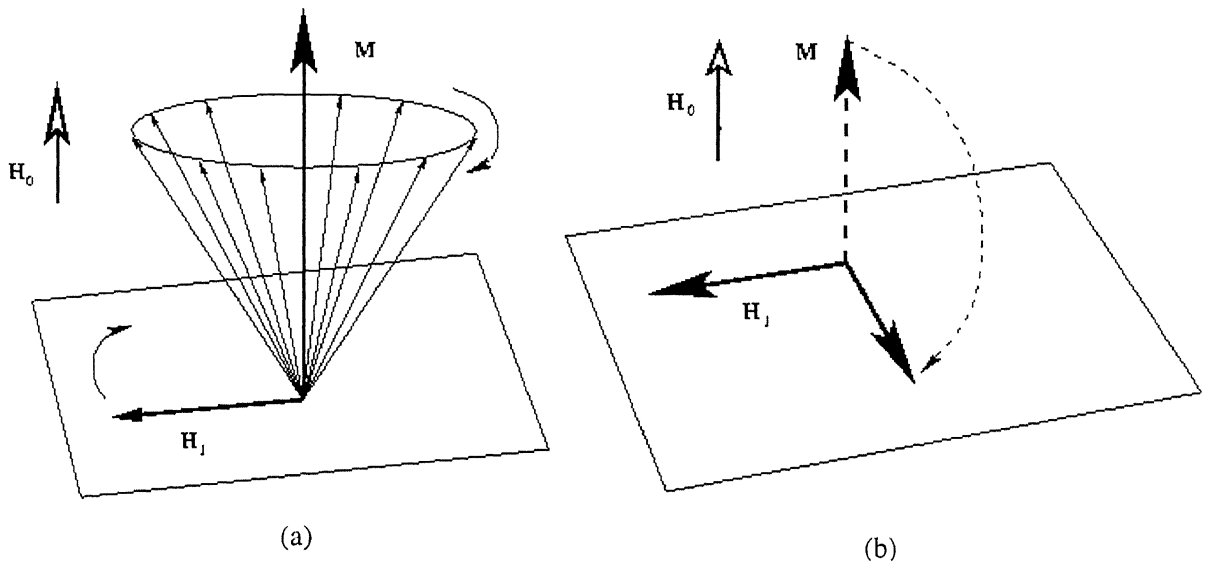


Figure 1.2: Tipping of longitudinal magnetization into transverse magnetization by a magnetic field H_1 , associated with an RF pulse. (a) For appreciable tipping to occur, the H_1 field must rotate synchronously with the precessing transverse magnetization. This condition is met by circularly polarized RF pulse at the Larmor frequency. (b) All of the longitudinal magnetization is tipped into the transverse plane by an RF pulse that is strong enough and applied long enough to tip the magnetization 90° (90-degree RF pulse)

magnetization also decays exponentially with a time constant T_2 . A simple model for this induced voltage is (M.L. Wood and F.W. Wherli (1999))

$$V = \kappa M_0 \exp(i2\pi f_L t) \exp(-t/T_2),$$

where κ is a constant, $i = (-1)^{1/2}$, and M_0 is magnetic momentum at thermal equilibrium. The induced voltage has the characteristics of a damped cosine and hence is also called free-induction decay (FID).

1.1.4. Proton Density (PD or ρ)

The overall strength of the signal is decided by the proton density (PD or ρ) that makes up the macroscopic magnetization. The proton density relevant in MRI is the number of mobile protons per unit volume in contrast to the total number of protons (that include stationary protons). Typically, for example, protons that belong to the organic matter in dense bone do not contribute to the signal that comprises the MR imaging experiment. They produce an MR signal, except that its characteristics are such that it is not relevant to the MR imaging process – more specifically, the signal from protons belonging to solids decays at too fast a rate (\sim tens of microseconds) compared to mobile protons

(hundreds of milliseconds) for any meaningful data to be collected. For this reason, solids, with an absence of mobile protons appear dark in an MR image. However, the lack of signal does not render such information useless - a lot can be surmised from the appearance of the anatomy surrounding the solid structure. Typical structures that appear dark due to a lack of protons are cortical bone, sinus passages, lung parenchyma and calcium deposits. Changes in proton density occur from changes in the cellular composition in tissues that accompanies disease and will be reflected in the signal intensity (S. Sinha M.A. Thomas, A.S. Huda, and R.B. Lufkin (2001)).

1.1.5. Spin-Lattice Relaxation Time (T_1)

RF stimulation causes nuclei to absorb energy, lifting them to the excited state. The nuclei can return to the ground state only by dissipating their excess energy to their surroundings, which is called the lattice. The process, which is known as the spin-lattice relaxation or T_1 relaxation describes the recovery of the longitudinal magnetization toward its equilibrium value. The relaxation of the excited spin requires an interaction with a time-dependent perturbation, typically a dipole-dipole interaction with a fluctuating electromagnetic field at the Larmor frequency. Such perturbations or fluctuating fields are produced by rotation and translation of the nuclei in the molecules of the lattice undergoing Brownian motion. The average frequency of this Brownian motion depends on the size of the molecules in the lattice. Small molecules re-orient more rapidly than larger molecules. The frequency of rotation in medium size molecules, such as lipids, is closest to typical Larmor frequencies. Therefore the magnetization associated with lipids relaxes faster than that associated with pure water or much larger molecules, such as proteins. Moreover, T_1 relaxation times depend on the magnetic field strength because the latter affects the Larmor frequency.

1.1.6. Spin-Spin Relaxation Time (T_2)

Before the RF pulse is switched on, the individual magnetic spins (protons) are on the average aligned with the main magnetic field \mathbf{H}_0 , and in random distribution of phase with respect to each other. The RF pulse not only tips the magnetization away from the z-axis but also puts them in phase coherence with each other. This coherent magnetization tipped into the transverse or xy plane, precesses about the \mathbf{H}_0 (z-axis), inducing the MR signal at the Larmor precessional frequency. The transverse

magnetization decays because its component magnetic moments get out of phase as a result of their mutual interaction and thereby are exposed to static as well as slowly varying local magnetic field fluctuations. These fluctuations cause a spread of the magnetic field around the central value of \mathbf{H}_0 , causing each to be exposed to a slightly different magnetic field, which in turn causes them to precess at slightly different angular frequencies, some faster than f_L , others slower. The net effect is that the ordered phase coherent state slowly disappears, with the spins fanning out in the xy plane. This causes the induced MR signal to decay at a rate governed by a factor called T_2 or, the spin-spin relaxation time since it is caused primarily by intrinsic fluctuations in magnetic field arising from interactions between adjacent spins, or alternatively, the transverse relaxation rate, since it takes place in the transverse plane.

Unlike T_1 relaxation, no energy is transferred from nuclei to the lattice in T_2 relaxation. Nuclei in the excited and ground state may exchange energy with each other. However, in biological tissues the main contribution to T_2 relaxation is from the relatively static magnetic field from neighboring protons. Large molecules such as those of protein, which tend to reorient more slowly than small molecules, promote T_2 relaxation and have shorter T_2 times. In contrast, smaller molecules such as water, at least at body temperature, have very rapid Brownian motion that average out any field fluctuations, or produce high frequency components. The result is that water has very large T_2 values, which implies that once a transverse spin-spin coherence is built up in an ensemble of spins, this coherence takes a long time to dephase – water and fluids such as cerebrospinal fluid (CSF) and edema have long T_2 's. The magnetic field strength influences T_2 much less than T_1 , at least under the conditions encountered in MRI.

Table 1.2 shows the T_1 and T_2 relaxation times and proton spin density values of some brain tissues measured at 1.5 Tesla (R.E. Hendrick (1999)). Here, the proton spin density values are normalized with respect to the CSF proton density value.

Tissue	T_1 (ms)	T_2 (ms)	ρ
White matter	510	67	0.61
Gray matter	760	77	0.69
Edema	900	126	0.86
Cerebrospinal fluid	2650	280	1.00
Upper cystic fluid (extracellular methomoglobin)	1080	215	1.12
Lower cystic fluid (intracellular deoxyhemoglobin)	720	43	1.02
Methomoglobin	460	106	0.96

Table 1.2: Brain tissue parameters measured in selected section at 1.5 T

1.1.7. Bloch Equations

F. Bloch (1946) found that the motion of the macroscopic magnetization in the presence of an applied magnetic field could be explained in terms of phenomenological differential equations. The classical equation of motion of a magnetic moment in a magnetic field \mathbf{H} states that the rate of change of angular momentum of the spinning nucleus, \mathbf{p} , depends upon the torque, $\mu \times \mathbf{H}$, exerted on the magnetic moment by the applied field and can be represented as:

$$\frac{d\mathbf{p}}{dt} = \mu \times \mathbf{H}.$$

Multiplying both sides of this equation by γ and using $\mu = \gamma \mathbf{p}$, we obtain

$$\frac{d\mu}{dt} = \gamma \frac{d\mathbf{p}}{dt} = \gamma \mu \times \mathbf{H}.$$

If \mathbf{M} is the vector sum of the μ 's, then by summing equation vectorially over all μ we obtain the following relation for macroscopic magnetization:

$$\frac{d\mathbf{M}}{dt} = \gamma \mathbf{M} \times \mathbf{H}. \quad (1.1.2)$$

During the RF pulse, the magnetic field is

$$\mathbf{H}(t) = H_1(t) \cos \omega t \vec{i} + H_1(t) \sin \omega t \vec{j} + H \vec{k}.$$

Here, $H = H_0 + h$, where h is the contribution from the gradients. Thus the equation (1.1.2) can be written component wise as:

$$\frac{dM_x}{dt} = \gamma M_y H - \gamma M_z H_1(t) \sin \omega t,$$

$$\frac{dM_y}{dt} = \gamma M_z H_1 \cos \omega t - \gamma M_x H,$$

$$\frac{dM_z}{dt} = \gamma M_x H_1 \sin \omega t - \gamma M_y H_1 \cos \omega t.$$

Let $M_x = u \cos \omega t - v \sin \omega t$ and $M_y = u \sin \omega t + v \cos \omega t$.

Then the differential equation satisfied by u and v is

$$\frac{d\mathbf{X}}{dt} = \mathbf{A}\mathbf{X},$$

$$\text{where } \mathbf{X} = \begin{pmatrix} u \\ v \\ M_z \end{pmatrix} \text{ and } \mathbf{A} = \begin{pmatrix} 0 & \gamma H + \omega & 0 \\ -(\gamma H + \omega) & 0 & \gamma H_1 \\ 0 & -\gamma H_1 & 0 \end{pmatrix}.$$

Therefore $\mathbf{X}(t) = \exp(\mathbf{A}t)\mathbf{X}(0)$.

Now,

$$|\mathbf{A} - \lambda \mathbf{I}| = 0 \Rightarrow \begin{vmatrix} -\lambda & \gamma H + \omega & 0 \\ -(\gamma H + \omega) & -\lambda & \gamma H_1 \\ 0 & -\gamma H_1 & -\lambda \end{vmatrix} = 0 \Rightarrow \lambda^3 + (\gamma^2 H^2 + (\gamma H + \omega)^2) \lambda = 0.$$

Therefore the three eigen values of the matrix \mathbf{A} are

$$\lambda_1 = 0; \lambda_{2,3} = \pm i \sqrt{\gamma^2 H_1^2 + (\gamma H + \omega)^2}.$$

If we write $\mathbf{A} = \begin{pmatrix} 0 & a & 0 \\ -a & 0 & b \\ 0 & -b & 0 \end{pmatrix}$ where $a = \gamma H + \omega$ and $b = \gamma H_1$, then

$$\mathbf{U}^* = \begin{pmatrix} \frac{b}{\sqrt{a^2 + b^2}} & -\frac{a}{\sqrt{a^2 + b^2}} & 0 \\ 0 & 0 & 1 \\ \frac{a}{\sqrt{a^2 + b^2}} & \frac{b}{\sqrt{a^2 + b^2}} & 0 \end{pmatrix} \text{ and } \mathbf{A}\mathbf{U}^* = \begin{pmatrix} 0 & 0 & a \\ 0 & \frac{a^2 + b^2}{\sqrt{a^2 + b^2}} & 0 \\ 0 & 0 & -b \end{pmatrix}.$$

Therefore the transformed matrix is $\begin{pmatrix} 0 & 0 & 0 \\ 0 & 0 & -\sqrt{a^2 + b^2} \\ 0 & \sqrt{a^2 + b^2} & 0 \end{pmatrix}$

Write $\mathbf{C} = \begin{pmatrix} 0 & -c \\ c & 0 \end{pmatrix}$; $\mathbf{C}^2 = -c^2 \begin{pmatrix} 1 & 0 \\ 0 & 1 \end{pmatrix}$; $\mathbf{C}^3 = -c^3 \begin{pmatrix} 0 & -1 \\ 1 & 0 \end{pmatrix}$; $\mathbf{C}^4 = c^4 \begin{pmatrix} 1 & 0 \\ 0 & 1 \end{pmatrix}$ and so on,

where $c = \sqrt{a^2 + b^2}$.

$$\begin{aligned} \text{Therefore } \exp(\mathbf{C}t) &= \sum_{n=0}^{\infty} \left[\frac{(\mathbf{C}t)^{2n}}{2n!} + \frac{(\mathbf{C}t)^{2n+1}}{(2n+1)!} \right] \\ &= \sum_{n=0}^{\infty} \left[\frac{t^{2n}}{2n!} (-1)^n c^{2n} \begin{pmatrix} 1 & 0 \\ 0 & 1 \end{pmatrix} + \frac{(-1)^n}{(2n+1)!} t^{2n+1} c^{2n+1} \begin{pmatrix} 0 & -1 \\ 1 & 0 \end{pmatrix} \right] \\ &= \cos ct \begin{pmatrix} 1 & 0 \\ 0 & 1 \end{pmatrix} + \sin ct \begin{pmatrix} 0 & -1 \\ 1 & 0 \end{pmatrix} \\ &= \begin{pmatrix} \cos ct & -\sin ct \\ \sin ct & \cos ct \end{pmatrix}. \end{aligned}$$

Therefore $\mathbf{X}(t) = \exp(\mathbf{A}t) \mathbf{X}(0)$

$$= \exp(\mathbf{U}\mathbf{D}\mathbf{U}^*) \mathbf{X}(0)$$

$$= \mathbf{U} \begin{pmatrix} 1 & 0 & 0 \\ 0 & \cos ct & -\sin ct \\ 0 & \sin ct & \cos ct \end{pmatrix} \mathbf{U}^* \mathbf{X}(0).$$

Case (I): If the initial condition is $\mathbf{X}(0) = (0 \quad 0 \quad M_0)^T$, then the solution will be

$$\begin{pmatrix} u \\ v \\ M_z \end{pmatrix} = \begin{pmatrix} \frac{abM_0}{a^2+b^2}(1-\cos ct) \\ \frac{bM_0}{\sqrt{a^2+b^2}}\sin ct \\ \frac{M_0}{a^2+b^2}(a^2+b^2\cos ct) \end{pmatrix}.$$

Therefore

$$M_x(t) = \frac{ab}{a^2+b^2}M_0(1-\cos ct)\cos\omega t - \frac{b}{\sqrt{a^2+b^2}}M_0\sin ct\sin\omega t,$$

$$M_y(t) = \frac{ab}{a^2+b^2}M_0(1-\cos ct)\sin\omega t + \frac{b}{\sqrt{a^2+b^2}}M_0\sin ct\sin\omega t,$$

$$M_z(t) = \frac{M_0}{\sqrt{a^2+b^2}}(a^2+b^2\cos ct).$$

Case (II): If the initial condition is $\mathbf{X}(0) = (M_x(0) \quad M_y(0) \quad M_z(0))^T$, then

$$\begin{pmatrix} u \\ v \\ M_z \end{pmatrix} = \begin{pmatrix} \frac{1}{a^2+b^2}(b^2+a^2\cos ct)M_x(0) + \frac{a}{\sqrt{a^2+b^2}}\sin ct M_y(0) + \frac{a}{a^2+b^2}(1-\cos ct)M_z(0) \\ \frac{-a}{\sqrt{a^2+b^2}}\sin ct M_x(0) + \cos ct M_y(0) + \frac{b}{\sqrt{a^2+b^2}}\sin ct M_z(0) \\ \frac{ab}{a^2+b^2}(1-\cos ct)M_x(0) - \frac{b}{\sqrt{a^2+b^2}}\sin ct M_y(0) + \frac{1}{a^2+b^2}(a^2+b^2\cos ct)M_z(0) \end{pmatrix}$$

Therefore

$$\begin{aligned} M_x(t) &= M_x(0) \left\{ \frac{b^2}{a^2+b^2}\cos\omega t + \frac{a^2}{a^2+b^2}\cos ct\cos\omega t + \frac{a}{\sqrt{a^2+b^2}}\sin ct\sin\omega t \right\} \\ &\quad + M_y(0) \left\{ \frac{a^2}{\sqrt{a^2+b^2}}\sin\omega t\cos\omega t - \cos ct\sin\omega t \right\} \\ &\quad + M_z(0) \left\{ \frac{ab}{a^2+b^2}\cos\omega t - \frac{ab}{a^2+b^2}\cos ct\cos\omega t - \frac{b}{\sqrt{a^2+b^2}}\sin ct\sin\omega t \right\}, \\ M_y(t) &= M_x(0) \left\{ \frac{b^2}{a^2+b^2}\sin\omega t + \frac{a^2}{a^2+b^2}\cos ct\sin\omega t - \frac{a}{\sqrt{a^2+b^2}}\sin ct\cos\omega t \right\} \\ &\quad + M_y(0) \left\{ \frac{a^2}{\sqrt{a^2+b^2}}\sin ct\sin\omega t - \cos ct\cos\omega t \right\} \\ &\quad + M_z(0) \left\{ \frac{ab}{a^2+b^2}\sin\omega t - \frac{ab}{a^2+b^2}\cos ct\sin\omega t + \frac{b}{\sqrt{a^2+b^2}}\sin ct\cos\omega t \right\}, \end{aligned}$$

$$M_z(t) = M_x(0) \frac{ab}{a^2 + b^2} (1 - \cos ct) - M_y(0) \frac{b}{\sqrt{a^2 + b^2}} \sin ct + M_z(0) \frac{1}{a^2 + b^2} (a^2 + b^2 \cos ct).$$

Since the above equations do not account for relaxation, F. Bloch et al. (1946) assumed that spin-lattice and spin-spin relaxations could be treated as first order processes with characteristic times T_1 and T_2 respectively. M_x and M_y decay back to their equilibrium value of zero, while M_z returns to its equilibrium value of M_0 .

In the absence of RF and considering T_1 , T_2 relaxation, Bloch equations become

$$\begin{aligned} \frac{dM_x}{dt} &= \gamma M_y H - \frac{M_x}{T_2}, \\ \frac{dM_y}{dt} &= -\gamma M_x H - \frac{M_y}{T_2}, \\ \frac{dM_z}{dt} &= -\frac{M_z - M_0}{T_1}. \end{aligned}$$

The third equation of the above coupled system of equations can be solved independently and the solution with the initial condition $M_z(0)$ is

$$M_z(t) = M_0 + (M_z(0) - M_0) \exp(-t/T_1).$$

First and second equations of the above system can be written in the matrix form as

$$\frac{d}{dt} \mathbf{X}(t) = \mathbf{A} \mathbf{X},$$

where $\mathbf{X} = \begin{pmatrix} M_x \\ M_y \end{pmatrix}$ and $\mathbf{A} = \begin{pmatrix} -\frac{1}{T_2} & \gamma H \\ -\gamma H & -\frac{1}{T_2} \end{pmatrix}$.

Solution will be

$$\mathbf{X}(t) = \exp(\mathbf{A}t) \mathbf{X}(0)$$

$$= \exp(-t/T_2) \begin{pmatrix} \cos \gamma H t & \sin \gamma H t \\ -\sin \gamma H t & \cos \gamma H t \end{pmatrix} \begin{pmatrix} M_x(0) \\ M_y(0) \end{pmatrix}.$$

Therefore,

$$M_x(t) = \exp(-t/T_2) \{M_x(0) \cos \gamma H t + M_y(0) \sin \gamma H t\},$$

$$M_y(t) = \exp(-t/T_2) \{M_y(0) \cos \gamma H t - M_x(0) \sin \gamma H t\},$$

$$M_z(t) = M_0 + (M_z(0) - M_0) \exp(-t/T_1).$$

In actual MR experiment, due to local field inhomogeneities, the transverse magnetization relaxes at a faster rate T_2^* instead of T_2 . Considering spatial coordinate $\mathbf{x} = (x, y, z)$, and T_2^* , the above solutions can be written as

$$M_x(\mathbf{x}, t) = \exp(-t/T_2^*) \{M_x(\mathbf{x}, 0) \cos \gamma H t + M_y(\mathbf{x}, 0) \sin \gamma H t\}, \quad (1.1.3a)$$

$$M_y(\mathbf{x}, t) = \exp(-t/T_2^*) \{M_y(\mathbf{x}, 0) \cos \gamma H t - M_x(\mathbf{x}, 0) \sin \gamma H t\}, \quad (1.1.3b)$$

$$M_z(\mathbf{x}, t) = M_0(\mathbf{x}) + (M_z(\mathbf{x}, 0) - M_0(\mathbf{x})) \exp(-t/T_1). \quad (1.1.3c)$$

By placing a conductive coil around the sample, with axis lying on the xy -plane by Faraday-Neumann's law, it will induce, an electric signal $s(t)$ in the coil. This is the only measurable quantity in an MR experiment. The signal $s(t)$ is usually called free induction decay (FID) signal; it is a two-dimensional vector and thus it can be represented as a complex function

$$s(t) \propto s_x(t) + i s_y(t).$$

Due to hardware constraints the signal $s(t)$ is measured not in the laboratory frame, but in a frame, called signal detection frame, rotating around \mathbf{k} with frequency ω_r very near to the Larmor frequency $\omega_0 = \gamma H_0$. Following G. Sebastiani and P. Barone (1991),

$$\begin{aligned} s(t) &\propto \exp i(\omega_r - \omega_0)t \times \int_V (M'_x(\mathbf{x}, t) + i M'_y(\mathbf{x}, t)) d\mathbf{x} \\ &= \exp i(\omega_r - \omega_0)t \int_V \left[\mathbf{M}'_{xy}(\mathbf{x}, 0) \right] \times \exp((i\theta_1(\mathbf{x}, t) + \varphi'(\mathbf{x})) - t/T_2^*(\mathbf{x})) d\mathbf{x}, \end{aligned} \quad (1.1.4)$$

where $\theta_1(\mathbf{x}, t) = -\gamma \int_0^t H_1(\mathbf{x}, \tau) d\tau$, and the symbol ' refers to Zeeman's frame.

Subsections 1.1.8-1.1.12 are mainly followed from G. Sebastiani and P. Barone (1991).

1.1.8. Selective Excitation

To select a slice parallel to the xy -plane at height z_0 , a radio frequency pulse lying in xy -plane will be applied, but with a time varying H (sinc-shaped), together with a linear gradient along z -axis in the static field \mathbf{k} , which is known as a selective pulse. In case of resonance, we will have

$$\mathbf{H}(\mathbf{x}, t) = H \frac{\sin \Delta\omega \tilde{t}}{\Delta\omega \tilde{t}} \times ([\cos \omega_0 \tilde{t}] \mathbf{i} - [\sin \omega_0 \tilde{t}] \mathbf{j}) + [H_0 + g_z(z - z_0)] \mathbf{k},$$

where $\tilde{t} = t - \frac{1}{2}t_p$, $0 \leq t \leq t_p$ ($\Delta\omega$, H and g_z are constants); the $g_z(z - z_0)\mathbf{k}$ is called slice selection gradient. The application of a sinc shaped radio frequency pulse cannot

be implemented exactly because of its infinite time extension, but the truncated version of it ($0 \leq t \leq t_p$) will be used, including ripples in frequency spectrum and, as a consequence, in the slice profile. This effect can be reduced by using a sinc function multiplied by a damped function, for example $\exp(-b(t - \frac{1}{2} t_p)^2)$ (b is a positive constant), so that the slice profile is similar to a Gaussian density. After the application of a 90° selective pulse, FID signal can be approximated by

$$s(t) \propto \int_S M_0(x, y, z_0) \times \exp\left(i\theta_1(x, y, z_0) - \frac{t}{T_2^*(x, y, z_0)}\right) dx dy \quad (1.1.5)$$

where S is the xy -projection of the intersection between V and the plane $z = z_0$.

1.1.9. Imaging Techniques

The basic idea for the encoding process was introduced by P.C. Lauterbur (1973), to obtain the first MR images. After slice selection by a 90° selective pulse, the signal acquisition is performed in presence of linear gradient along x -axis in the field, i.e. $\mathbf{H}(\mathbf{x}, t) = (H_0 + g_x x)\mathbf{k}$ (g_x is a constant), so that the Larmor frequency is equal to $\gamma(H_0 + g_x x)$, which is constant on the straight lines $x = x_0$ and is a linear function of x . This technique is known as *frequency encoding*.

1.1.10. Fourier Zeugmatography

Zeugmatography is the name given by Lauterbur to what has now become MRI taken from the Greek *Zeugma* (to join together); referring to the combining of the static \mathbf{H}_0 field and its gradient with the NMR signal from tissue nuclei to produce a graphic image. A. Kumar et al. (1975) have introduced a process called phase encoding, which consists of the application, after the slice selection and before the frequency encoding, of a linear gradient y in the field, i.e. $\mathbf{H}(\mathbf{x}, t) = (H_0 + g_y y)\mathbf{k}$ for a time t_y . During the time t_y , the re-phasing field gradient $-g_z(z - z_0)\mathbf{k}$ is also applied, but we can assume that this happens before the encoding process. The gradients $g_x\mathbf{k}$ and $g_y\mathbf{k}$ are called readout frequency gradient and phase encoding gradient respectively.

$$s(t') \propto \int_S M_0(x, y, z_0) \times \exp\left(\frac{t' + t_y}{T_2^*(x, y, z_0)} + i\gamma(g_x x t' + g_y y t_y)\right) dx dy \quad (1.2.6)$$

or

$$s(t') \propto \int_S \rho(x, y, z_0) \times \exp \left(\frac{t' + t_y}{T_2^*(x, y, z_0)} + i\gamma(g_x x t' + g_y y t_y) \right) dx dy \quad (1.2.7)$$

Let us consider ensemble of signals $s'_{t_y}(t')$, obtained from the experiments with g_x , and g_y fixed and positive, and $0 \leq t_y \leq T_y$ (T_y is a positive constant). For each of them the acquisition is formed for $0 \leq t' \leq T$.

$$\begin{aligned} F(\omega, \xi) &= \int_{-\infty}^{\infty} \int s(t', t_y) \exp i(\omega t' + \xi t_y) dt' dt_y \\ &\propto \int_S \rho(x, y, z_0) \left(\frac{\sin(\omega - \gamma g_x x) T}{\omega - \gamma g_x x} \right) \left(\frac{\sin(\xi - \gamma g_y y) T_y}{\xi - \gamma g_y y} \right) dx dy \end{aligned} \quad (1.2.8)$$

As $T, T_y \rightarrow \infty$, the two sinc functions appearing in the Fourier transforms will tend, as distributions, to $\delta(\omega - \gamma g_x x)$ and $\delta(\xi - \gamma g_y y)$, respectively, so that $F(\omega, \xi)$ will approach to $\rho(\omega/\gamma g_x, \xi/\gamma g_y, z_0)$. It is clear that T_y can not increase indefinitely without becoming large with respect to the values of T_2^* . This is the limitation of Fourier zeugmatography. In order to overcome this problem W.A. Edelstein, J.M.S. Hutchison, G. Johnson, and T. Redpath (1980) proposed a technique called spin-warp.

1.1.11. Spin-warp

Let us consider the ensemble of signals $s_{g_y}(t')$, obtained by the experiments with $|g_y| \leq G_y$ (G_y is a constant), and all other parameters are fixed. For each g_y value, the acquisition is performed for $0 \leq t' \leq T$. As before, Fourier zeugmatography, for any values t' , g_y such that $|t'| \leq T$, $|g_y| \leq G_y$, we define the function $s(t', g_y)$ and apply the two dimensional inverse Fourier transform with respect to t' and g_y . If T and t_y are small with respect to $T_2^*(\mathbf{x})$ values, we have

$$\begin{aligned} F(\omega, \eta) &= \int_{-\infty}^{\infty} \int s(t', g_y) \exp i(\omega t' + \eta g_y) dt' dg_y \\ &\propto \int_S \rho(x, y, z_0) \left(\frac{\sin(\omega - \gamma g_x x) T}{\omega - \gamma g_x x} \right) \left(\frac{\sin(\eta - \gamma g_y y) G_y}{\eta - \gamma g_y y} \right) dx dy \end{aligned} \quad (1.2.9)$$

1.1.12. Spin-echo

Spin-echo is similar to spin-warp: at time $TE/2$ from the end of the 90° selective pulse, a 180° non-selective pulse is performed for a negligible time. Before this pulse, the field $(H_0 + g_y y + g_x x)\mathbf{k}$ is applied which is substituted, after the pulse, by the field $(H_0 + g_x x)\mathbf{k}$. Therefore, immediately before and after 180° pulse, the xy -projection of the magnetization density in Zeeman's frame has a phase equal to $-\gamma(g_y y + g_x x)TE/2$ and $\gamma(g_y y + g_x x)TE/2$ respectively, and its modulus is $M_0(\mathbf{x})\exp(-TE/2T_2^*(\mathbf{x}))$. In the following when the field $(H_0 + g_x x)\mathbf{k}$ is applied, a signal called spin-echo is produced at $t = TE$ is proportional to

$$\int_V \rho(\mathbf{x}) \exp\left(-\left(\frac{TE}{T_2(\mathbf{x})} + i\gamma g_y y \frac{TE}{2}\right)\right) d\mathbf{x}.$$

For $t \geq TE$, signal decays because of x -gradient, spin-spin interaction and field inhomogeneities. Shifting time origin at $t = TE$, we have

$$s(t) = \int_S \rho(\mathbf{x}) \exp(-TE/T_2) \exp\left(-\left(\frac{t}{T_2^*(\mathbf{x})} + i(\gamma g_y y \frac{TE}{2} + \gamma g_x xt)\right)\right) dx dy. \quad (1.2.10)$$

As for spin-warp, the inverse Fourier transform is performed to decode the signal.

1.2. Pulse Sequences

One of the strengths of MR imaging is the myriad of measurement techniques, known as pulse sequences and parameter modifications, available for use. Even though there are many pulse sequences available, every pulse sequence must accomplish two basic tasks. First, transverse magnetization must be created using one or more radio frequency pulses, and this magnetization must then be encoded using gradient pulses so that the spatial positions of the tissues can be determined from the image. Second, the desired contrast between tissues must be created based on the time of the application and duration of the various RF and gradient pulses.

1.2.1. Pulse-Sequence Timing Diagram

A useful method for conveying the important characteristics of a pulse sequence is a graphical representation called the pulse sequence timing diagram. In general, at

minimum five lines are needed to completely describe any pulse sequence (see M.A. Brown and R.C. Semelka (1999) and J.P. Mugler III (1999)). One for RF transmitter, one for each gradient and the last one for data acquisition. The first line, labeled RF, illustrates the time of application and waveforms for the RF pulses, in this case 90° (excitation) and 180° (refocusing) pulses. The next three lines depict the time of application and the waveforms for gradients applied along three mutually orthogonal axes. These are labeled GS, GP, and GF, for the section select, phase-encoding, and readout gradients, respectively, although other labels, for example G_x , G_y , G_z , can be used to indicate the assignment of the gradients for a particular section orientation. For the two dimensional (2D) acquisition depicted in the Figure 1.2, section-select gradients are applied in synchrony with the RF pulses, thus spatially localizing their effects, or in other words selecting the section of interest. The other gradient waveforms, applied along the phase-encoding and readout axes, spatially encode the magnetization within this section along the remaining two directions. The gradient waveform on the phase-encoding axis, containing a series of closely spaced horizontal lines, is the graphical representation of a gradient table: strength of the gradient is stepped through a series of values as the basic pulse sequence timing is repeated to collect the data required to form the image. With each repetition, another line of data is collected. The fifth line of the diagram, shows when the MR signal occurs. Although some pulse sequences generate a number of distinct signals, typically only the signals of interest are depicted.

1.2.2. Saturation Recovery Spin-Echo (SRSE) Sequence

Saturation recovery spin echo sequence is a routinely used sequence for medical diagnosis. It is also simply called as spin echo (SE) sequence. Depending upon the way it is implemented, some variants of this sequence are also available. For example, fast spin echo (FSE) sequence is a variant of SE. Pulse sequence timing diagram of SE is shown in Figure 1.3.

In saturation recovery spin echo sequence, the magnetization density at the beginning of the 90° pulse of the first unit is $M_0(\mathbf{x})\mathbf{k}$, and at the end of the pulse it lies on the xy -plane with the magnitude $M_0(\mathbf{x})$. At the beginning of the 180° pulse of the same unit the component along \mathbf{k} is equal to $M_0(\mathbf{x})[1-\exp(-TE/2T_1(\mathbf{x}))]$. At the end of this pulse the component along \mathbf{k} of the magnetization density will be $-M_0(\mathbf{x})[1-\exp(-TE/2T_1(\mathbf{x}))]$. At the beginning of the 90° pulse of the second unit, a time TR is elapsed,

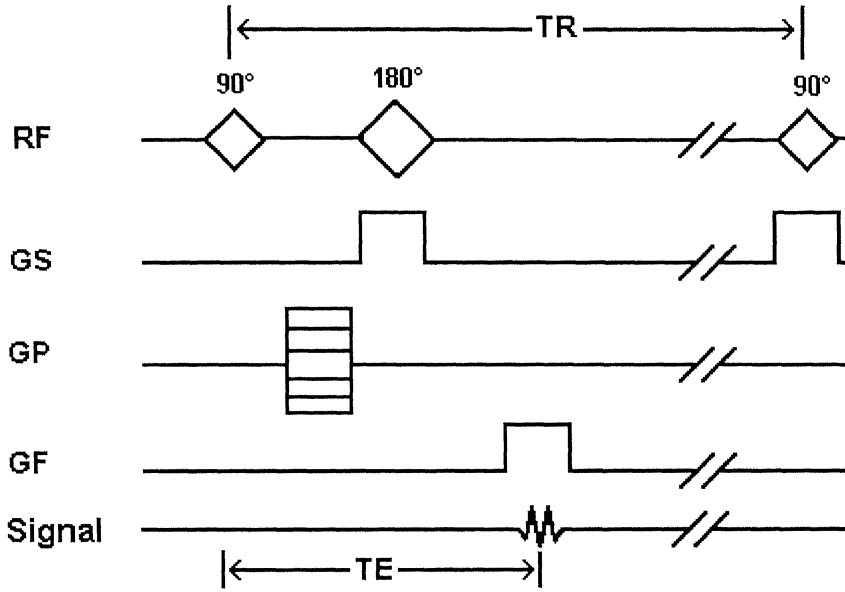


Figure 1.3: Timing diagram of spin echo sequence

and, since TR is long compared to $T_2(\mathbf{x})$, it follows from solutions of Bloch equation that the transversal components of the magnetization density will be zero, while M_z will be equal to

$$M_0(\mathbf{x})[1 + \exp(-TR/T_1(\mathbf{x})) - 2\exp(-(TR - TE/2)/T_1(\mathbf{x}))]$$

with $M_z(\mathbf{x}, 0) = -M_0(\mathbf{x})[1 - \exp(-TE/2T_1(\mathbf{x}))]$.

At the end of the pulse, the magnetization density lies on the xy -plane with magnitude equal to the above value M_z . This is true for all the other units too. The signal expression will be obtained from equation (1.2.10) replacing $\rho(x, y, z_0)$ by

$$\rho(x, y, z_0)[1 + \exp(-TR/T_1(x, y, z_0)) - 2\exp(-(TR - TE/2)/T_1(x, y, z_0))].$$

If $TR \gg TE$, then this last expression becomes $\rho[1 - \exp(-TR/T_1)]$; for two tissues A and B with the same spin density and different T_1 , the difference of their contribution to the signal for unit volume is proportional to $(\exp(-TR/T_{1A}) - \exp(-TR/T_{1B}))$. The suitable value of TR is the one that maximizes this function and, as a consequence, the contrast.

The transverse and longitudinal magnetic moment components M_T and M_L respectively which account for the relaxation process can be written as (J.P. Jones (1988a)):

$$M_L(t) = M(1 - \exp(-t/T_1)) + M_L(0)\exp(-t/T_1)$$

$$M_T(t) = M_T(0) \exp(-t/T_2) \quad (\text{true } T_2 \text{ decay})$$

$$M_T(t) = M_T(0) \exp(-t/T_2^*) \quad (\text{FID decay})$$

where $M_L(0)$ is the value of M_L immediately following an RF pulse, t is any time after the pulse, and similarly for M_T . Longitudinal and transverse components of magnetic moment vector at different stages of first cycle of pulse sequence timing diagram are shown in Table 1.3. Table 1.4 shows the values for second cycle and these values are same for all other cycles.

Event	M_L	M_T
Start	M	0
90°	0	M
TE/2	$M(1 - \exp(-TE/2T_1))$	$M \exp(-TE/2T_2^*)$
180°	$-M(1 - \exp(-TE/2T_1))$	$M \exp(-TE/2T_2^*)$
TE/2	$M(1 - 2\exp(-TE/2T_1) + \exp(-TE/T_1))$	$M \exp(-TE/T_2)$
		← measure
End	$M(1 - 2\exp(-(TR - TE/2)/T_1) + \exp(-TR/T_1))$	$M \exp(-TE/T_2) \exp(-TD/T_2^*)$

Table 1.3: Longitude and transverse magnetic moment values at each step of the first spin-echo of SRSE

Event	M_L	M_T
Start	$M(1 - 2\exp(-(TR - TE/2)/T_1) + \exp(-TR/T_1))$	≈ 0
90°	0	$M(1 - 2\exp(-(TR - TE/2)/T_1) + \exp(-TR/T_1))$
TE/2	$M(1 - \exp(-TE/2T_1))$	$M(1 - 2\exp(-(TR - TE/2)/T_1) + \exp(-TR/T_1)) \exp(-TE/2T_2^*)$
180°	$-M(1 - \exp(-TE/2T_1))$	$M(1 - 2\exp(-(TR - TE/2)/T_1) + \exp(-TR/T_1)) \exp(-TE/2T_2^*)$
TE/2	$M(1 - 2\exp(-TE/2T_1) + \exp(-TE/T_1))$	$M(1 - 2\exp(-(TR - TE/2)/T_1) + \exp(-TR/T_1)) \exp(-TE/T_2)$
		← measure
End	$M(1 - 2\exp(-(TR - TE/2)/T_1) + \exp(-TR/T_1))$	$M(1 - 2\exp(-(TR - TE/2)/T_1) + \exp(-TR/T_1)) \exp(-TE/T_2) \exp(-TD/T_2^*)$

Table 1.4: Longitude and transverse magnetic moment values at each step of the second spin-echo of SRSE

Combinations of long values of TR with respect to those of T_1 , and of the values of TE comparable with those of T_2 , are useful to weigh the image by T_2 , while combinations of short values of TE with respect to those of T_2 , and values of TR comparable with those of T_1 , give images weighted by T_1 . If long values of TR are associated to short values of TE produce images influenced essentially by spin density. These effects of TE and TR are shown in Table 1.5.

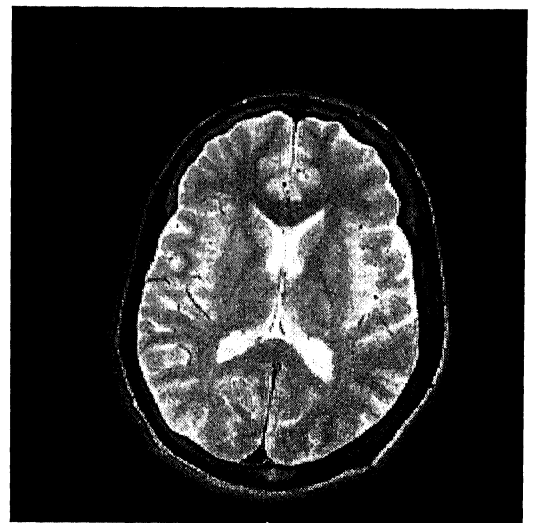
Contrast Source	TE Setting	TR Setting
T_1	As short as possible, limited by band width and noise (≤ 15 ms)	Comparable to T_1 s of the two tissues (better towards the shorter T_1)
T_2	Comparable to T_2 s of the two tissues (better towards the longer T_2)	Long compared with the T_1 s of the two tissues (≥ 2000 ms)
ρ	As short as possible (≤ 15 ms)	Long compared with the T_1 s of the two tissues (≥ 2000 ms)

Table 1.5: Effect of TE and TR on image contrast in spin-echo imaging

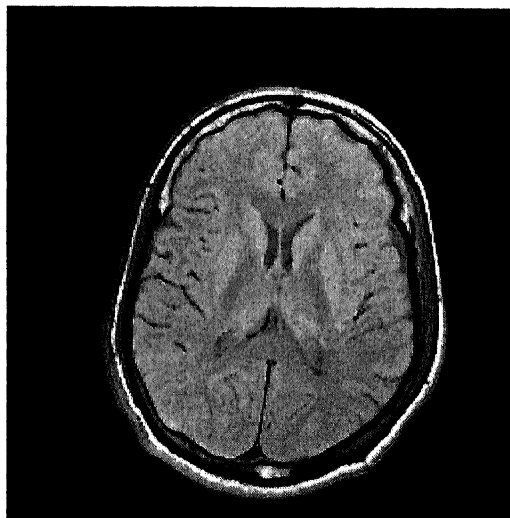
Figure 1.4 shows the images of brain with different forms of contrast produced by TE and TR values in spin echo sequence. Figure 1.4(a) is obtained with TE and TR as 20 ms and 2500 ms respectively to produce a proton density weighted image. Figure 1.4(b) is a T_2 weighted image with TE = 80 ms and TR = 2500 ms. On T_2 weighted image white matter appears as dark, gray matter as gray and CSF as very bright. In contrast to this, on the T_1 weighted image obtained with TE = 15 ms and TR = 650 ms (Figure 1.4(c)) whiter matter appears bright and CSF as dark. All these three weighted images produce different contrasts and reveal excellent anatomic details.



(a)



(b)



(c)

Figure 1.4: Images of the human head with different forms of contrast: (a) a spin density-weighted image, (b) a T_2 weighted image and (c) a T_1 weighted image. These different acquisitions can be seen to create different contrasts between white matter, gray matter and cerebrospinal fluid. They all reveal excellent anatomic detail.

1.2.3. Inversion Recovery Spin-Echo (IRSE) Sequence

Inversion recovery spin echo (IRSE) pulse sequence is used to weight the spin density by T_1 too. In the literature of MRI this sequence is simply known as inversion recovery (IR). It consists of performing the same sequence as above, with an additional 180° non-selective pulse at time TI before the 90° selective pulse (180° non-selective pulse - 90° selective pulse - phase and frequency encoding - 180° non-selective pulse - frequency encoding with acquisition). The pulse sequence timing diagram of IR sequence is shown in Figure 1.5.

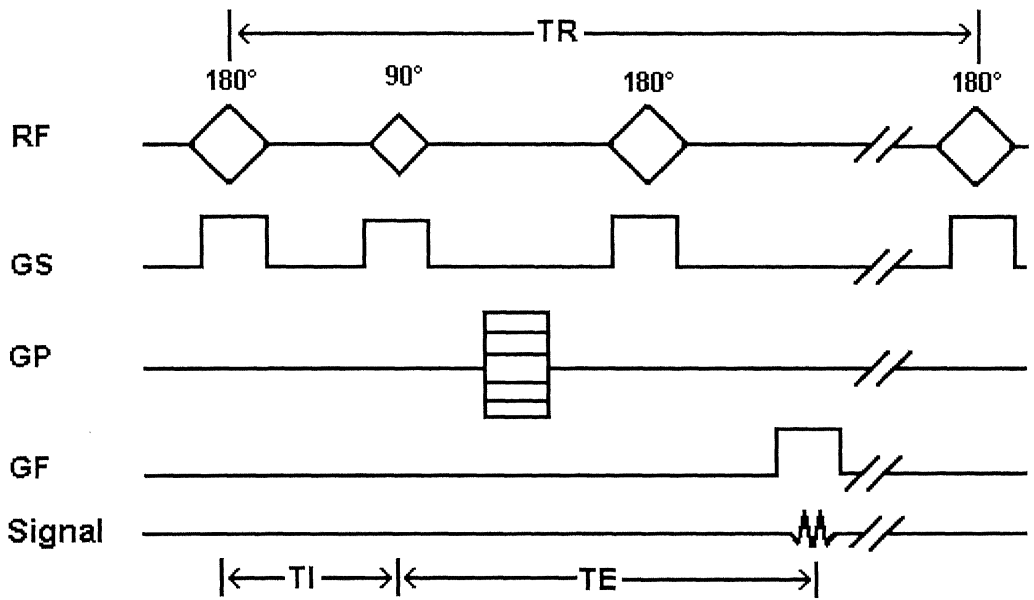


Figure 1.5: Inversion recovery pulse sequence timing diagram

At the beginning of the first 180° and of the 90° pulses of the first unit the magnetization density lies along \mathbf{k} , so that at the end of the 90° pulse it lies on the xy -plane. If $TR - TI$ is long with respect to the values of T_2 ; then, at the beginning (the end) of the first 180° pulse of the next unit, the transversal components of the magnetization density will be zero and M_z will be

$$-M_0(1 - \exp(-(TR - TI)/T_1)).$$

The value of M_z at the beginning of the 90° pulse of the same unit, will be obtained by (1.1.3c) with the conditions

$$M_z(\mathbf{x}, 0) = -M_0(\mathbf{x})[1 - \exp(-(TR - TI)/T_1)]$$

at $t = TI$. Therefore we have that the magnetization density at the end of the 90° of each unit following the first one, lies in the xy -plane, with magnitude

$$M_0[1 - 2\exp(-TI/T_1) + \exp(-TR/T_1)]$$

The expression of the signal is obtained from (1.2.10) by substituting $\rho(x, y, z_0)$ with

$$\rho[1 - 2\exp(-TI/T_1) + \exp(-TR/T_1)].$$

If TR is long compared to the values of T_1 , then this last expression becomes

$$\rho[1 - 2\exp(-TI/T_1)].$$

We note that, for two tissues with the same spin density but different T_1 the maximum difference of their contributions to the signal for unit volume is twice that obtained with SRSE.

Following the notation for M_L and M_T as given in the previous subsection, longitudinal and transverse components of magnetic moment vector at different stages of first cycle of pulse sequence timing diagram for IR sequence are shown in Table 1.5. Table 1.6 shows the values for second cycle and these values are same for all other cycles.

Event	M_L	M_T
Start	M	0
180°	-M	0
TI	$M(1-2\exp(-TI/T_1))$	0
90°	0	$M(1-2\exp(-TI/T_1))$
TE/2	$M(1-\exp(-TE/2T_1))$	$M(1-2\exp(-TI/T_1))\exp(-TE/2T_2^*)$
180°	$-M(1-\exp(-TE/2T_1))$	$M(1-2\exp(-TI/T_1))\exp(-TE/2T_2^*)$
TE/2	$M(1-2\exp(-TE/2T_1)+\exp(-TE/T_1))$	$M(1-2\exp(-TI/T_1))\exp(-TE/T_2)$
		← measure
End	$M(1-2\exp(-(TD+TE/2)/T_1)+\exp(-(TD+TE)/T_1))$	$M(1-2\exp(-TI/T_1))\exp(-TE/T_2) \times \exp(-TD/T_2^*)$

Table 1.6: Longitude and transverse magnetic moment values at each step of the first spin-echo of IRSE

Event	M_L	M_T
Start	$M(1-2\exp(-(TD+TE/2)/T_1)+\exp(-(TD+TE)/T_1))$	0
180°	$-M(1-2\exp(-(TD+TE/2)/T_1)+\exp(-(TD+TE)/T_1))$	0
TI	$M(1+2\exp(-(TR-TE/2)/T_1)-\exp(-TR/T_1)-2\exp(-TI/T_1))$	0
90°	0	$M(1+2\exp(-(TR-TE/2)/T_1)-\exp(-TR/T_1)-2\exp(-TI/T_1))$
TE/2	$M(1-\exp(-TE/2T_1))$	$M(1+2\exp(-(TR-TE/2)/T_1)-\exp(-TR/T_1)-2\exp(-TI/T_1))\exp(-TE/2T_2^*)$
180°	$-M(1-\exp(-TE/2T_1))$	$M(1+2\exp(-(TR-TE/2)/T_1)-\exp(-TR/T_1)-2\exp(-TI/T_1))\exp(-TE/2T_2^*)$
TE/2	$M(1-2\exp(-TE/2T_1)+\exp(-TE/T_1))$	$M(1+2\exp(-(TR-TE/2)/T_1)-\exp(-TR/T_1)-2\exp(-TI/T_1))\exp(-TE/T_2)$
		← measure
End	$M(1-2\exp(-(TD+TE/2)/T_1)+\exp(-(TD+TE)/T_1))$	$M(1+2\exp(-(TR-TE/2)/T_1)-\exp(-TR/T_1)-2\exp(-TI/T_1))\exp(-TE/T_2)\exp(-TD/T_2^*)$

Table 1.7: Longitude and transverse magnetic moment values at each step of the second spin-echo of IRSE

Inversion recovery accomplishes selective nulling of a specific tissue based on its T_1 relaxation time and the chosen inversion time TI. Depending upon the choice of TI and

the way the sequence is implemented, there are many variants of IR sequences routinely used in clinical diagnosis to achieve different contrast images . A few of them are short TI inversion recovery (STIR), fluid-attenuation inversion recovery (FLAIR), balanced inversion recovery (BIR), Fast inversion recovery (FIR), and magnetization prepared rapid acquisition gradient echo inversion (MP-RAGE). Following G.M. Bydder, J.V. Hajnal, and I.R. Young (1999), the effect of different ranges of TI values in diagnosis of different diseases may be summarized as follows:

Short TI: High contrast, fat nulled T_1 and T_2 weighted sequences for imaging the head and neck, abdomen, pelvis, and musculo skeletal systems (e.g., fast STIR or turbo STIR).

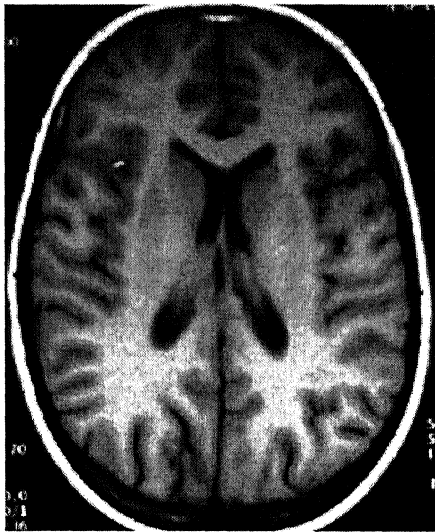
Medium TI: Highly T_1 weighted sequence with sensitivity to contrast enhancement (e.g., MP-RAGE).

Long TI: CSF-nulled sequence with high sensitivity to acute subarachnoid hemorrhage and parenchymal disease, especially disease at the brain-CSF interface, such as multiple sclerosis, cortical infarcts, infection, and tumors (e.g., fast FLAIR or turbo FLAIR)

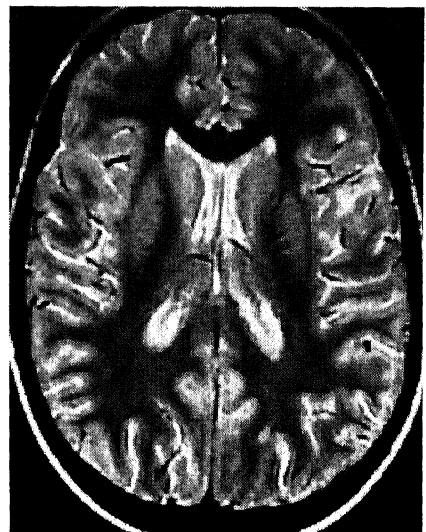
Description	Typical TI values	Sign of longitudinal magnetization	State of longitudinal magnetization	Usual contrast weighting for target tissue	Tissues and fluids with T_1 s suitable for nulling	Examples
Short TI	80-150	Negative	Beginning recovery	Combined T_1 & T_2	Fat, white matter, liver	STIR
Medium	200-800	Mixed negative & positive	Partially recovered	Heavy T_1	Blood (CSF)	BIR, FIR, MP-RAGE
Long TI	1500-2500	Positive	Almost fully recovered	Heavy T_2	CSF	FLAIR

Table 1.8: Common clinical variants of the inversion recovery sequence

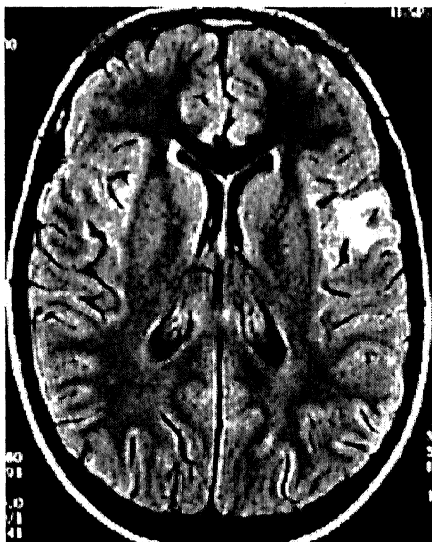
Figure 1.6 shows, as given in S. Sinha, M.A. Thomas, A.S. Huda, and R.B. Lufkin (2001), the contrast obtained from spin echo images. The images are of a 12 year old with HIV and associated CNS lesions. Figure 1.6(a) shows a T_1 weighted scan obtained using a TE of 14 ms and a TR of 640 ms. Note that T_1 contrast dictates that CSF is the darkest; white matter is white and gray matter gray. Quite good demarcation is observed between the white and gray matter. Figures 1.6(b) and 1.6(c) are obtained simultaneously as two images of a double echo sequence. Since a FSE sequence is utilized, the relatively short acquisition time permits an increase in the TR to 3800 ms.



(a)



(b)



(c)



(d)

Figure 1.6: Images of a 12 year old with HIV and associated CNS lesions. (a) T_1 -weighted image with TE/TR: 14 ms/ 640 ms using a conventional spin echo. (b) Proton density weighting with a TE/TR: 22ms/3800ms using a Turbo-Spin Echo. (c) A FLAIR image with a Turbo-IR, with TE/TR/TI: 105ms/7000ms/2500ms, and (d) A T_2 -weighted image obtained as the second image in a double echo sequence with the proton density image in (b), but with TE: 90ms. Note how the lesion becomes more conspicuous in the FLAIR compared to the T_2 , and how the CSF is rendered entirely dark.

The TE for the proton density image is 22 ms and for the T_2 image, 90 ms. Note the extremely good quality of the scan, with clear delineation of the different tissues of the brain. The contrast in the T_2 weighted scan is opposite compared to the T_1 scan, with

CSF bright, gray matter gray and white matter the darkest. The contrast between tissues is lower in the proton density image than in the T_2 image. Finally, in spite of the good quality of the T_2 scan, the lesion is almost not visualized. However, when one uses FLAIR, the lesion becomes quite distinct. The CSF signal is suppressed but the rest of the contrast is similar to T_2 . Very large values of TR and TI are used (7000 ms and 2500 ms). These would not have been clinically practical but for the use of the Fast Spin Echo technique which brings down the scan time to reasonable values with excellent image quality.

1.2.4. Magnetization Transfer Pulse

Besides the more familiar T_1 , T_2 and proton density (ρ) parameters, Magnetization Transfer Contrast (MTC) is one more MR contrast mechanism by means of which tissues can be differentiated based on the differences between their intensity values on an MR image. Magnetization transfer (MT) utilizes the fact that there is continuous magnetization exchange between two proton pools in the brain: the motionally restricted pool, which arise from nonaqueous tissue, and the mobile pool from water. MRI can only directly detect signal from the mobile pool. If the magnetization from the motionally restricted pool is distributed by an MT pulse, then the effect of exchange can be seen on the mobile pool as a decrease in signal. This effect is called magnetization transfer. This decrease is quantified by means of a magnetization transfer ratio (MTR) defined as:

$$MTR = \left(1 - \frac{M_s}{M_0} \right) \times 100\%,$$

where M_s and M_0 represent the signals measured with and without off resonance radiation respectively.

Figure 1.7(a) is an image acquired without any MT saturation with TE as 14 ms and TR as 1012 ms, and the Figure 1.7(b) is with MT saturation and other sequence parameters are same as in Figure 1.7(a). MTR image computed using the above equation, shown in Figure 1.7(c), has an excellent contrast between white matter, gray matter and CSF. MT effects have started finding increasing clinical usage. Interesting use is found in combining MT effect with Gadolinium (Gd) enhancement. MT effects do not suppress signal enhancement from T_1 shortening caused by Gd infusion in extracellular spaces. Consequently, the two effects, parenchymal intensity suppression

by MT and lesion enhancement by Gadolinium act synergistically to increase the lesion conspicuity (see J.I. Tantt, R.E. Sepponen, M.J. Lipton and T. Kuusela (1992)).

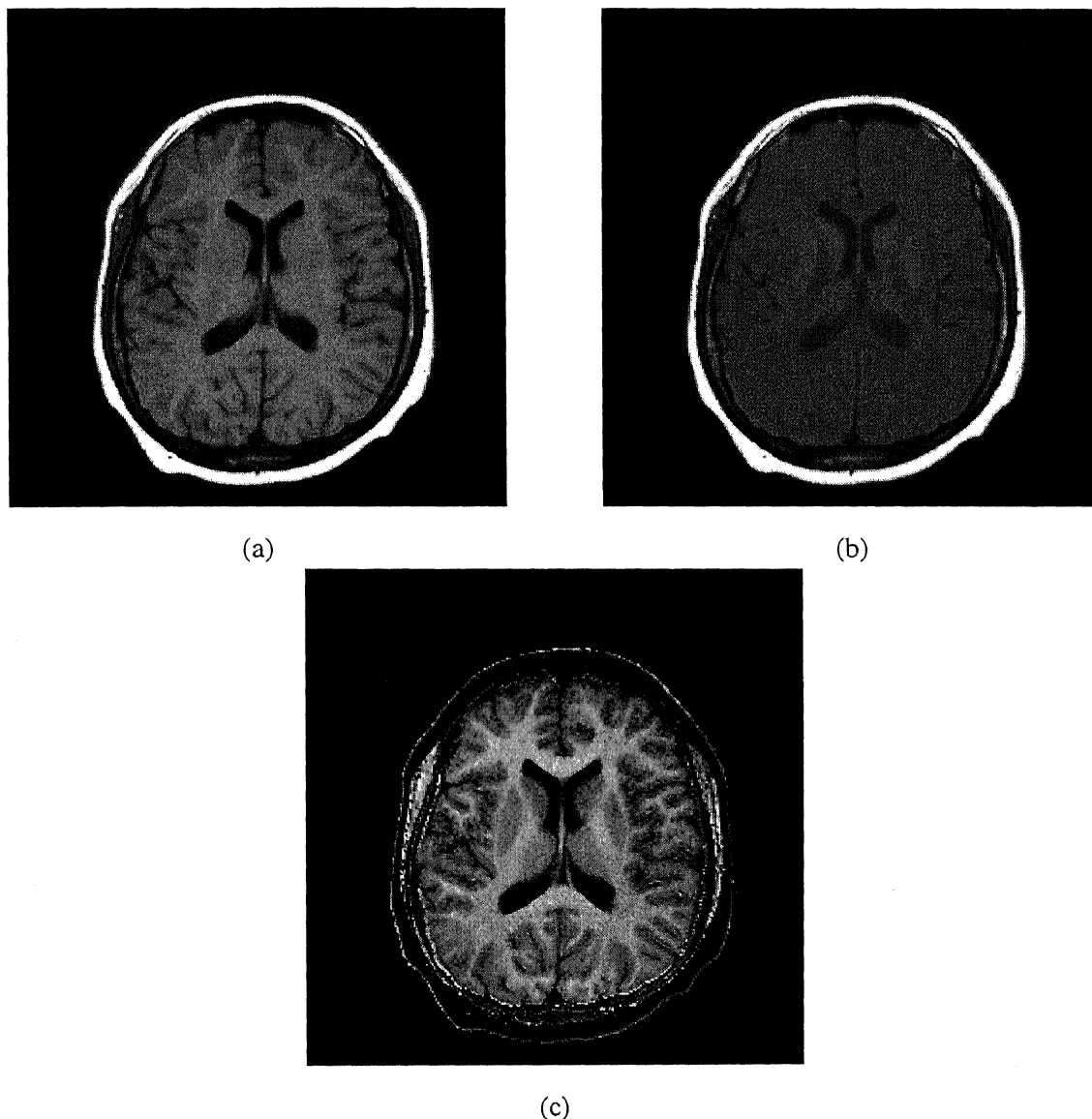


Figure 1.7: Magnetization transfer effects. The first image (a) was obtained without MT, the second (b) with MT and the third (c) is calculated magnetization transfer ratio, as per equation given in text

1.3. Literature Review

In chemistry, computation NMR relaxation times started immediately after the discovery of nuclear magnetic resonance phenomena. Many methods and sequences were used for computing relaxation times. For example, D.L. De Fontaine, D.K. Ross, and B. Ternai (1975) described a nonlinear least squares method for the calculation of spin-lattice relaxation times. This procedure offered considerable time savings

compared with other methods, as repetition times only up to the order of T_1 are required, and, in particular, this procedure obviated the necessity for the determination of S_∞ , the signal intensity at thermal equilibrium.

During the early 1980s, attention was given to parametric mapping since it was felt that, in addition to the clinical value of pathology demonstration in parameter-weighted images, fundamental information about disease processes and useful classification of diseases might be obtained by quantitation of the parameters that yield contrast in the weighted images. Attempts were made to obtain this information either by pixel-by-pixel calculated parameter maps or by calculations within regions of interest in images (M.A. Foster and A. Haase, 1996). Most of the early attempts at T_1 and T_2 mapping used adaptations of the pulse sequences normally employed for *in vitro* studies, e.g., IR for T_1 mapping and CPMG, or repeated single spin echo sequences for T_2 .

A detailed mathematical description of the basic physics and the image formation process in MRI could be found in W.S. Hinshaw and A.H. Lent (1983), and G. Sebastiani and P. Barone (1991).

P. A. Bottomley, C. J. Hardy, R. E. Argersinger, and G. Allen-Moore (1987) have archived, reviewed, and analyzed the proton NMR relaxation times of pathological human and animal tissues in the frequency range 1–100 MHz as a function of tissue of origin, NMR frequency, temperature, species, and *in vivo* versus *in vitro* status. T_1 data from specific disease states of the bone, brain, breast, kidney, liver, muscle, pancreas, and spleen was characterized by simple dispersions of the form $T_1 = Av^B$ in the range 1–100 MHz with A and B empirically determined pathology-dependent constants. Pathological tissue T_2 values are essentially independent of NMR frequency. Raw relaxation data, best-fit T_1 parameters A and B, and the mean T_2 values, were tabulated along with standard deviations and sample size to establish the normal range of pathological tissue relaxation times applicable to NMR imaging or *in vitro* NMR examination. They have observed from statistical analysis of relaxation data that most tumor and edematous tissue T_1 values and some breast, liver, and muscle tumor T_2 values were significantly elevated ($p \geq 0.95$) relative to normal, but did not differ significantly from other tumors and pathologies. Statistically significant abnormalities in the T_1 values of some brain, breast, and lung tumors, and most pathological tissue T_2 values could not, however, be demonstrated in the presence of large statistical errors. Both T_1 and T_2 in uninvolved tissue from tumor-bearing animals or organs did not demonstrate statistically significant differences from normal when considered as a

group, suggesting no appreciable systemic effects associated with the presence of tumors compared to the statistical uncertainty. Statistical prediction analysis for both T_1 and T_2 indicated that of all the tissues studied, only liver hepatoma could be reliably distinguished from normal liver based on a single T_1 measurement ($p \geq 0.95$) given the scatter in the published data. Indeed, data scatter, not easily attributable to temperature, species, in vivo versus in vitro status, the inclusion of implanted or chemical induced tumors, or the possible existence of multiple component relaxation, was recognized as the major factor inhibiting the diagnostic utility of quantitative NMR relaxation measurements.

L.R. Schad, G. Brix, I. Zuna, W. Härle, W.J. Lorenz, and W. Semmler (1989) have performed the *in vivo* measurements of proton relaxation processes in human brain tumors by MR imaging using a whole-body superconductive MR scanner, operating at 1.5 T. The T_1 and T_2 relaxation time measurements were based on a combined Carr-Purcell/Carr-Purcell-Meiboom-Gill sequence with two interleaved repetition times and 32 echoes. First, comparative measurements in the imager and with spectrometer of relaxation times were performed on a phantoms containing fluids of different T_1 and T_2 to evaluate accuracy. A maximum deviation of $\sim 10\%$ was found. Multislicing with a gap width of one slice thickness influenced the accuracy of T_1 relaxation measurement. A gap width of at least two times the slice thickness was necessary for reliable determination of T_1 . No influence on T_2 values was observed by multislicing. Second, in human head imaging the multiexponential behavior of the T_2 decay curves was analyzed in each pixel, where the mean square deviation were used as a criterion to discriminate between mono and biexponential behavior. Mean values of monoexponential T_1 and multiexponential T_2 relaxation data for white matter, gray matter, CSF, edema, and tumor were sampled in 12 patients with brain tumors. These authors observed that T_2 showed mono exponential behavior in white matter and gray matter, whereas CSF, edema, and tumor showed distinct biexponentiality. The biexponential analysis generally yields "fast" and "slow" components with $T_{2f} = 80 \pm 17$ ms and $T_{2s} = 2,030 \pm 210$ ms for CSF (partial volume effect), $T_{2f} = 104 \pm 25$ ms and $T_{2s} = 677 \pm 152$ ms for edematous tissues, $T_{2f} = 97 \pm 19$ ms and $T_{2s} = 756 \pm 99$ ms for tumor tissues, respectively. For the discrimination of edematous and tumor tissues a retrospective overall accuracy of 94% was found.

H. Iwaoka, T. Hirata and H. Mastuura (1987) have tested several scan sequences,

of T_1 , T_2 , and proton density values encountered in representative human tissues. They found that, for given scan time, the combination of inversion recovery 3 spin echo (IR3SE) and saturation recovery 4 spin echo (SR4SE) sequences gave more accurate computed images than other comparable methods tested.

J. Gong and J.P. Hornak (1992) have addressed an improvement in the post processing time required to generate T_1 images. They have described a nonlinear least-squares algorithm for rapidly generating spin-lattice relaxation time images from variable repetition time magnetic resonance images. The algorithm generates a 256x256 pixel T_1 image from nine variable repetition time images in approximately 60 sec. on a VAX-6510 computer.

Xing Li and J.P. Hornak (1994) have generated T_2 images are from a series of variable echo-time magnetic resonance images by either a linear or a nonlinear least-squares technique. The linear technique is contrasted with a rapid nonlinear technique developed by the authors. Compared with linear techniques, the nonlinear technique produced calculated T_2 images with less noise and less error in those tissues with low T_2 values, such as adipose and muscle.

Calculated T_1 images require that magnetic resonance signal be detected as several inversion or repetition times. Multiple spin-echo acquisitions provide several measurements of the magnetization at each TR, the signal size diminishing according to T_2 decay. S.J. Riederer, S.A. Bobman, J.N. Lee, F. Farzaneh, and H.Z. Wang (1986) have reviewed one method (case 1) for estimating T_1 from single echoes and presented four new methods (case 2-5) in which multiple acquired echoes were used. For case 2 a fit was performed using the first echo at each TR, repeated using second echo, etc., and the final T_1 estimate was the simple average of the individual fits at each echo time (TE). For case 3 the optimum weighted average was performed. For cases 4 and 5 synthetic SE images were generated at each TR prior to the T_1 fit, case 4 using a synthetic TE of zero, and case 5 using a TE providing maximum signal-to-noise ratio in the synthetic image. The relative precision in T_1 provided by each method was calculated. It was proven that case 3 and 5 are optimum and equivalent and could theoretically reduce the noise in T_1 images by as much as 40% over case 1 with no increase in scanning time. Approximations were proposed that enable the optimum methods to be implemented in a practical fashion.

Techniques used in NMR imaging, not routinely employed in conventional

For the saturation recovery approach of T_1 measurement, these include selective excitation to define the image plane and magnetization refocusing for NMR signal acquisition. B.R. Rosen, L.I. Pykett, and T.J. Brady (1984) showed by computer modeling of the Bloch equations that errors well over 50% could be made in image derived T_1 measurements if the conventional SR relations between signal intensity and the 90-90° inter pulse delay, TR , is used. They have derived corrected expressions for the actual pulse and gradient sequence used by their imaging system, and phantom data acquired in imaging experiments have verified the validity of these equations. This allowed for the correction of T_1 data to compensate for systematic bias introduced during imaging procedures and suggested a means whereby errors introduced by radio frequency inhomogeneities across the imaging volume could be reduced.

I. Harvey, P.S. Tofts, J.K. Moris, D.A.G. Wicks, and M.A. Ron (1991) have studied the major factors contributing to T_1 variance at 0.5 T in white matter in healthy people. Anatomical location of the white matter sampled and differences between individuals contributed 74% of the total variance in serial measurements of the same objects. There was also significant change over time within an individual subject that could not be attributed to machine drift. This information permitted estimates to be made concerning adequate sample size in studies that examine for pathological white matter T_1 change.

Some of the major problems encountered when measuring relaxation times *in vivo* are (M.A. Foster and A. Haase, 1996):

1. magnetic field inhomogeneity effects, including those due to the field gradients,
2. slice profile effects, related to pulse sequence timing etc.,
3. problems relating to rf pulses and signal phase,
4. errors when multislice collection procedures are used,
5. misregistration problems when T_1 and T_2 are calculated from several imaging data sets,
6. partial volume effects due to tissue inhomogeneity,
7. assumptions made in the T_1 and T_2 calculation, e.g., regarding relaxation monoexponentiality,
8. a wide variety of effects arising from the living tissue/body itself, such as flow, diffusion, magnetic susceptibility, etc. which can all either affect the relaxation time value directly or alter the apparent place from which the information is coming.

S.A. Bobman, S.J. Riederer, J.N. Lee, S.A. Suddarth, H.Z. Wang, J.R. MacFall (1985) have studied the comparison of synthesized MR images with acquired images. They have found that the synthetic images subjectively compared favorably in both accuracy and precision with acquired images when formed for the same values of echo and repetition times and for interpolated and extrapolated values of both TE and TR. Percent error was consistently less 5% for brain parenchyma, and synthetic signals were accurate to within four times the noise level at acquisition. The apparent signal-to-noise ratio of synthetic images was comparable, superior, or inferior to similar acquired images, depending on the values of TE and TR. S.A. Bobman, S.J. Riederer, J.N. Lee, T. Tasciyan, F. Farzaneh, H.Z. Wang (1986) have done the pulse sequence extrapolation with MR image synthesis. They have used the multiple spin-echo data acquired in a time equivalent to a TR of 2,000 ms and generated inversion-recovery images for arbitrarily chosen inversion times. Synthetic IR signals of the brain parenchyma consistently matched directly acquired signals to within 6%.

Any chemical exchange or magnetization transfer between the water and macromolecular protons will result in a decrease in the water proton signal or saturation transfer as originally described by S. Forsén and R.A. Hoffman (1966) for simple chemical and dipolar interactions. The demonstration of normally unobservable proton pools in exchange with the observable pools is an important finding which increases the potential image contrast parameters available in MR imaging. S.D. Wolff and R.S. Balaban (1989) first produced *in vivo* images with magnetization transfer weighted contrast. They have studied the exchange between ^1H magnetization in "free" water ($^1\text{H}_f$) and that in a pool with restricted motion ($^1\text{H}_r$) observed in tissues *in vivo* using NMR saturation transfer methods. Exchange between these two pools was demonstrated by a decrease in the steady-state magnetization and relaxation times of $^1\text{H}_f$ with radiofrequency irradiation of $^1\text{H}_r$. Proton NMR imaging demonstrated that this exchange was tissue specific and generated a novel form of NMR image contrast.

B.S. Hu, S.M. Conolly, G.A. Wright, D.G. Nishimura, and A. Macovski (1992) have examined the theoretical behavior of short T_2 species in the presence of RF irradiation with regard to pulse duration, amplitude, and total integrated RF power, as well as off-resonance effects. J.V. Hajnal, C.J. Baudouin, A. Oatridge, I.R. Young, and G.M. Bydder (1992) have discussed the design and implementation of magnetization transfer pulse sequences for clinical use.

A good amount of literature on the applicability of magnetization transfer effect and the quantitative magnetization transfer ratios for medical diagnosis of different diseases is available. R.C. Mehta, G.B. Pike, D. Enzmann (1996) have studied the measure magnetization transfer in multiple sclerosis demyelinating plaques, white matter ischemic lesions, and edema. J.R. Petrella, R.I. Grossman, J.C. McGowan, G. Campbell, J.A. Cohen (1996) have analyzed the relationship between MR enhancement pattern and magnetization transfer effect in multiple sclerosis lesions. There are a number of studies e.g., A. Gass, G.J. Barker, D. Kidd, et al. (1994), J.F. Hiehle, R.I. Grossman, K.N. Ramer, F. Gonzalez-Scarano, J.A. Cohen (1995), L.A. Loevner, R.I. Grossman, J.C. McGowan, K.N. Ramer, J.A. Cohen (1995), M. Fillippi, M.D. Campi, V. Dousset, et al. (1995) carried out on the magnetization transfer effect on normal appearing white matter in multiple sclerosis.

Measurement of magnetization transfer in different stages of neurocysticercosis was carried out by M.K. Kathuria, R.K. Gupta, R.Roy, V. Gour, N. Hussain, and S. Pradhan (1998). R.K. Gupta, M.K. Kathuria and S. Pradhan (1999) have found that an MT effect increases the detectability of CNS tuberculosis and helps in better assessment of the disease load.

1.4. Contents of the Thesis

A study of the computational methods for tissue parameters estimation and the effect of perturbations in signals on parameter estimation is discussed in chapter 2.

In section 2.1, most commonly used two point methods for estimating T_1 and T_2 are presented. Errors due to the choices of TR's for T_1 estimation and TE's for T_2 estimation in the presence of noise for some brain tissues are presented.

In section 2.2, some iterative methods for tissue parameter estimation are described. Subsection 2.2.1 describes a least squares method given by J. Gong and J.P. Hornak (1992) for computation of T_1 . This method requires the data acquired at different TR's keeping TE fixed. A look-up table approach is suggested for faster computation of T_1 values compared to the controlled iterative process suggested by the authors. The accuracy in the computed T_1 values is improved by Newton's method by using the look-up table values as initial approximations. In subsection 2.2.2, a nonlinear

constant. For this method also a look-up table approach is suggested to make this method faster than the controlled iterative process proposed by the authors. The accuracy in the computed T_2 values is improved by Newton's method by using the look-up table values as initial approximations. Subsection 2.2.3 describes a least squares method given by H. Iwaoka, T. Hirata and H. Matsuura (1987) for the computation of T_1 , T_2 , and PD values simultaneously. Given three or more independent images corresponding to a cross-section, this method computes T_1 , T_2 , and PD values iteratively. The convergence of this method depends on the initial approximations for T_1 , T_2 and PD values. In practice, these initial approximations are not known before hand. Any look-up table kind of approaches would take a lot of time in searching for these initial values due to the high degree of freedom available in this method and the memory space required. In subsection 2.2.4, we have presented a new method which reduces the system of equations to one involving a single function of single variable case. Given independent data set of three images, it is shown by proper re-arrangement of the signal expressions that one could reduce them in to a function of T_1 . Then T_1 values are obtained from a generated look-up table. Using these as initial approximations, the accuracy in the computed values could be improved iteratively by Newton's method. By substituting these T_1 values into any two image intensities, T_2 could be computed. This T_2 computation does not require any specific data, unlike in the method described in subsection 2.1.2. Now, PD values are obtained by directly substituting the computed T_1 and T_2 values in to any one of the image intensity equations. If more than three images are available, by considering suitable data triples, a least-squares method is suggested to compute more accurate T_1 values and consequently T_2 and PD values. Subsection 2.2.5 presents a least squares method for computing T_1 , T_2 and PD values simultaneously. Initial approximations for this iterative method are obtained from the computed values using the method described in subsection 2.2.4.

In all the methods described above, the signal amplification proportionality constant is assumed to be constant. But in practice, this constant may vary over the regions or images due to gradient and signal receiver coil imperfections. In subsection 2.2.6 a method is presented for the estimation of tissue parameter computables like T_1 , T_{1x} , T_2 , T_{2x} , ρ , and ρ_x in the presence of amplification factors where the suffix x denotes the variation in x -direction. Computation of the field susceptibility maps is presented. Simulation results are given to demonstrate this method.

A numerical study of the sensitivity of the tissue parameters computation due to perturbations in the input images is presented in section 2.3. In subsection 2.3.1, errors in the computed parameters due to bit reduction in the images are presented. Subsection 2.3.1. deals with the errors in parameters estimation due to blurring in the input images.

Chapter 3 mainly deals with the generation of high contrast images. In section 3.1, an entropy-like maximization procedure which computes the weights is presented. Using these weights, a linear combination of the T_1 , T_2 , and PD weighted acquired images is produced. The resultant image is similar to PD weighted image, but has shown a good contrast between perilesional gliosis region and brain parenchyma than in any individual image. Given a set of linearly independent images, Gram-Schmidt orthogonalization process is discussed in section 3.2 to generate a set of orthonormal images. Results of orthonormalizing T_1 weighted image with respect to T_2 weighted image and T_2 weighted image with respect to T_1 weighted image are presented. In section 3.3, generation of contrast images through functional maps is discussed. By substituting the computed tissue parameter values into the functions of T_1 and T_2 (e.g., for saturation recovery spin echo, $f(T_1) = 1 - 2\exp(-(TR - TE/2)/T_1) + \exp(-TR/T_1)$, and, $g(T_2) = \exp(-TE/T_2)$) at desired TE and TR values, an excellent contrast in the images is produced. In section 3.4, a least squares method is presented to produce tissue parameter maps contrast through a weighted combination of the images. The weights computed at one slice did not vary much from the weights associated with adjacent slices. So, weights computed at one slice could be used to produce tissue parameter maps contrast like images without computing these maps. In section 3.5, generation of good contrast in perilesional gliosis region on synthesized IR images is demonstrated. Synthesis of image values at divergent point, where tissue parameter values could not be computed due to partial volume effect, is discussed in section 3.6. It is observed that the tissue parameter values in different segments (regions) of brain are normally distributed. Utility of tissue parameter maps for segmentation using a variant of MLE algorithm (R.K.S. Rathore, S. Datta, R.K. Gupta, S.B. Rao and R. Verma (2001)) is shown in section 3.7.

Chapter 4 is dedicated to the quantitative analysis of the regions of three pathologies: cystic cavity, perilesional gliosis and edema. In section 4.1, the statistical tools used for the analysis are discussed. The means and variances in pathological regions and contra-lateral normal regions on MT SE T_1 , T_1 , T_2 and PD weighted images as well as on MTR, T_1 , T_2 and PD computed maps have been analyzed. In all these

the significance of the changes in the means and variances. The linear correlation coefficients between different weighted images and between computed maps in normal and pathological regions are presented. Section 4.2 is devoted to a quantitative analysis of cystic cavity region. On MT SE T_1 , T_1 and PD weighted images the means in the cystic cavity regions are less compared with contra-lateral normal regions. But T_2 weighted images have shown high values in the lesion region in comparison with normal region. T_1 , T_2 and PD maps have shown high mean values, while MTR map has less values in the lesion regions compared with normal regions. In section 4.3, perilesional gliosis around the cystic cavity has been studied. Analysis suggests the usefulness of magnetization transfer for gliosis. On T_1 maps, the mean values in the lesion are significantly high compared with normal region even though it is not observed on T_1 weighted images. Analysis of edema regions is discussed in section 4.4.

Chapter 2

Numerical Methods for Tissue Parameter Quantitation and Sensitivity Analysis

Knowledge of T_1 and T_2 is not simply an academic curiosity. Many diseases are apparent with certain pulse sequences but not visible with others (e.g., multiple sclerosis plaques). The fact that these lesions can be seen at all shows that they have different ρ , T_1 , and/or T_2 values from normal tissues, but the fact that they are not seen on some sequences means that an optimization scheme is needed to assure that the proper sequence is used without spending excessive time to find it. In one such scheme, M.R. Mitchell, T.E. Conturo, T.J. Gruber, and J.P. Jones (1984) are able to optimize the contrast based upon a knowledge of T_1 and T_2 . Further, there is a possibility that ρ , T_1 , and T_2 may aid in the differential diagnosis of disease. Without knowledge of T_1 and T_2 , MR imaging will remain a trail and error technique with good sensitivity but low specificity. In other words, some of its potential may be wasted (J.P. Jones (1988b)).

A study of the computational methods for tissue parameters estimation and the effect of perturbations in signals on parameters is discussed in this chapter.

In section 2.1, most commonly used two point methods for estimating T_1 and T_2 are presented. Errors due to the choices of TR's for T_1 estimation and TE's for T_2 estimation in the presence of noise for some brain tissues are presented.

In section 2.2, some iterative methods for tissue parameter estimation are described. Subsection 2.2.1 describes a least squares method given by J. Gong and J.P. Hornak (1992) for computation of T_1 . In subsection 2.2.2, a nonlinear least squares method for computation of T_2 values given by Xing Li and J.P. Hornak (1994) is described. Subsection 2.2.3 describes a least squares method given by H. Iwaoka, T. Hirata and H. Matsuura (1987) for the computation of T_1 , T_2 and PD values simultaneously. In subsection 2.2.4, we have presented a new method which reduces the system of equations to one involving a single function of single variable case. A new

where suffix x denotes the variation in x -direction, in the presence of amplification factors is presented in subsection 2.2.6.

A numerical study of the sensitivity of the tissue parameters computation due to perturbations in the input images is presented in section 2.3. In subsection 2.3.1, errors in the computed parameters due to bit reduction in the images are presented. Subsection 2.3.1 deals with the errors in parameters estimation due to blurring in the input images.

2.1. Two Point Calculations

Both the magnetic resonance signal intensity and contrast between tissues depend upon the local values of spin density (ρ), and the relationships between T_1 , T_2 , and the interpulse time intervals. Neglecting flow, signal expression can be written as

$$S = k \rho f(T_1) g(T_2),$$

where S is the signal intensity, k is a proportionality constant, and f & g are functions of the type of pulse sequence (J.P. Jones (1988)). In the case of spin echo sequence, f and g are given by:

$$f = 1 + \exp(-TR/T_1) - 2\exp(-(TR - TE/2)/T_1),$$

$$g = \exp(-TE/T_2),$$

where TR and TE are the repetition and echo times respectively.

Calculating T_1 : Keeping TE fixed while collecting images with different TR values, the ratio of signal intensities is

$$\frac{S_1}{S_2} = \frac{(1 + \exp(-TR_1/T_1) - 2\exp(-(TR_1 - TE/2)/T_1))}{(1 + \exp(-TR_2/T_1) - 2\exp(-(TR_2 - TE/2)/T_1))}.$$

This can be solved for T_1 . In practice, $TR \gg TE/2$, so this ratio can be written as

$$\frac{S_1}{S_2} = \frac{(1 - \exp(-TR_1/T_1))}{(1 - \exp(-TR_2/T_1))}, \quad (2.1.1)$$

and the value of T_1 can be deduced by an iterative scheme. Initial guesses could be obtained from a lookup table. In addition, if $TR_1 = 2TR_2$, from the above equation it can be written as

$$T_1 = -TR_2 / \ln((S_1/S_2) - 1). \quad (2.1.2)$$

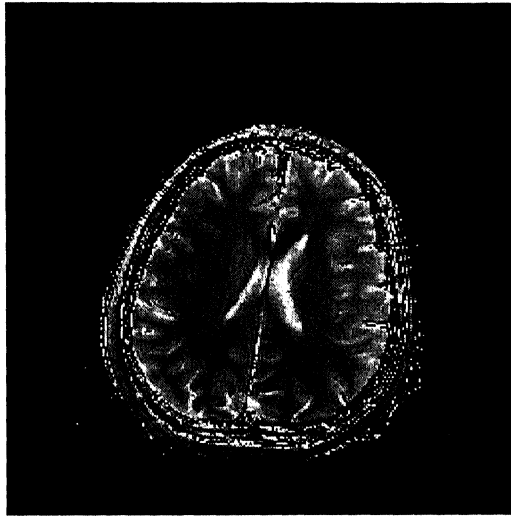
Figure 2.1(a) and Figure 2.1(b) are the two single spin echo images with same $TE = 14$ ms and with different TR 's, 1000 ms and 2000 ms respectively. Figure 2.1(c) is the corresponding T_1 map computed using the equation (2.1.2).



(a) $TE/TR = 20/2200$ ms



(b) $TE/TR = 20/1100$ ms



(c) T_1 map

Figure 2.1: (a) and (b) are two spin echo images with $TE/TR = 20/2200, 1100$ ms. Image (c) is the computed T_1 map

Percentage errors are computed in T_1 estimations of some common brain tissues using equation (2.1.2) with different TR 's at different noise levels. First, at each brain tissue T_1 value, for given two TR values the true signal ratio S_1/S_2 as in equation (2.1.1) is computed. Different percentages of these ratios are added as noise and resulted signal ratios are used in equation (2.1.2) to compute T_1 values (J.P. Jones (1988b)). Tables 2.1-2.4 show the percentage errors in computed T_1 values of different brain tissues in the

presence of different noise levels in the signal ratios using the equation (2.1.2) with $(TR_1, TR_2) = (1200, 600), (1500, 750), (2000, 1000)$ and $(3000, 1500)$ ms respectively. Table 2.1 shows at $(TR_1, TR_2) = (1200, 600)$ ms the estimation of T_1 's of brain tissues with high T_1 values are more sensitive to the presence of noise compared to the tissues with low T_1 's. For example, at 1% noise methemoglobin and CSF have shown errors 3.64 and 10.92 respectively, and at 10% noise while methemoglobin has error 41.76, CSF increased up to 878.46. From Tables 2.1-2.4, it is observed that at high range of (TR_1, TR_2) values, errors in computation of T_1 values of tissue with high T_1 values like CSF, upper cystic fluid, edema, gray matter and lower cystic fluid are less compared to the errors in estimation at lower (TR_1, TR_2) values. But tissues with low T_1 values like methemoglobin and white matter have shown increased errors at higher range of (TR_1, TR_2) values.

Tissue Type	T_1	At 1% Noise		At 5% Noise		At 10% Noise	
		T_1	%Error	T_1	%Error	T_1	%Error
White matter	510	528.67	3.66	609.71	19.55	729.22	42.98
Gray matter	760	791.60	4.16	936.10	23.17	1172.62	54.29
Edema	900	941.01	4.56	1133.83	25.98	1469.40	63.27
CSF	2650	2939.38	10.92	5015.83	89.28	25929.21	878.46
Upper Cystic Fluid	1080	1135.30	5.12	1405.04	30.10	1915.92	77.40
Lower Cystic Fluid	720	749.20	4.05	881.61	22.45	1094.73	52.05
Methomoglobin	460	476.73	3.64	548.51	19.24	652.11	41.76

Table 2.1: % Errors in T_1 computation of different brain tissues using equation (2.1.2) with $TR_1 = 1200$ ms and $TR_2 = 600$ ms at different noise levels

Tissue Type	T_1	At 1% Noise		At 5% Noise		At 10% Noise	
		T_1	%Error	T_1	%Error	T_1	%Error
White matter	510	528.74	3.67	608.04	19.22	719.81	41.14
Gray matter	760	788.91	3.80	917.06	20.67	1113.93	46.57
Edema	900	936.50	4.05	1102.02	22.45	1368.41	52.05
CSF	2650	2884.46	8.85	4336.55	63.64	10162.40	283.49
Upper Cystic Fluid	1080	1128.06	4.45	1352.40	25.22	1736.59	60.79
Lower Cystic Fluid	720	746.98	3.75	865.76	20.24	1045.84	45.25
Methomoglobin	460	477.35	3.77	549.85	19.53	650.01	41.31

Table 2.2: % Errors in T_1 computation of different brain tissues using equation (2.1.2) with $TR_1 = 1500$ ms and $TR_2 = 750$ ms at different noise levels

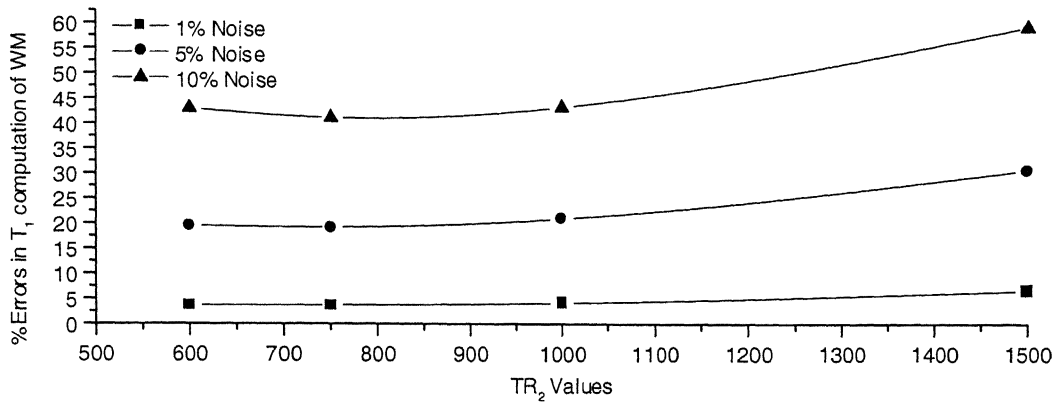
Tissue Type	T ₁	At 1% Noise		At 5% Noise		At 10% Noise	
		T ₁	%Error	T ₁	%Error	T ₁	%Error
White matter	510	531.11	4.14	617.07	20.99	731.43	43.42
Gray matter	760	787.65	3.64	906.13	19.23	1076.84	41.69
Edema	900	933.25	3.69	1078.49	19.83	1295.42	43.94
CSF	2650	2832.29	6.88	3825.19	44.35	6347.34	139.52
Upper Cystic Fluid	1080	1121.97	3.89	1309.54	21.25	1602.49	48.38
Lower Cystic Fluid	720	746.27	3.65	858.13	19.18	1017.57	41.33
Methomoglobin	460	480.66	4.49	563.26	22.45	670.61	45.78

Table 2.3: % Errors in T₁ computation of different brain tissues using equation (2.1.2) with TR₁ = 2000 ms and TR₂ = 1000 ms at different noise levels

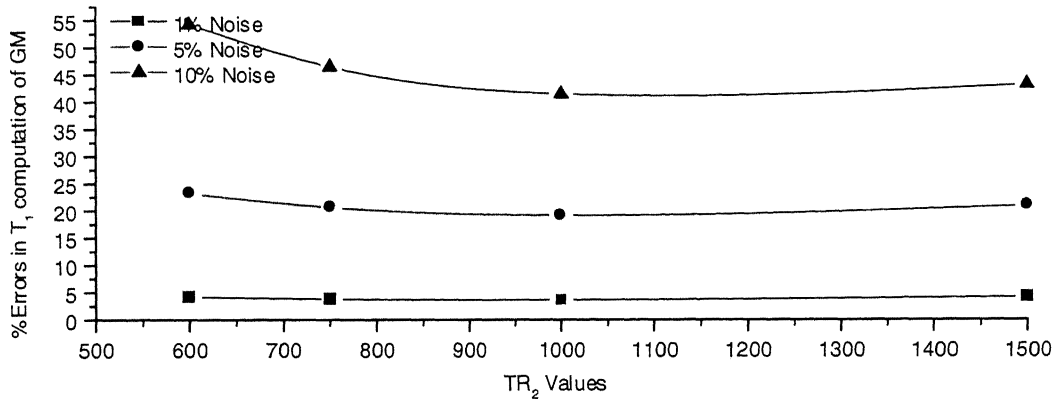
Tissue Type	T ₁	At 1% Noise		At 5% Noise		At 10% Noise	
		T ₁	%Error	T ₁	%Error	T ₁	%Error
White matter	510	543.60	6.59	666.79	30.74	813.17	59.44
Gray matter	760	791.60	4.16	920.13	21.07	1090.90	43.54
Edema	900	934.22	3.80	1076.78	19.64	1272.89	41.43
CSF	2650	2783.97	5.05	3434.78	29.61	4655.38	75.67
Upper Cystic Fluid	1080	1119.40	3.65	1287.19	19.18	1526.36	41.33
Lower Cystic Fluid	720	751.18	4.33	876.84	21.78	1041.78	44.69
Methomoglobin	460	496.48	7.93	623.72	35.59	769.00	67.17

Table 2.4: % Errors in T₁ computation of different brain tissues using equation (2.1.2) with TR₁ = 3000 ms and TR₂ = 1500 ms at different noise levels

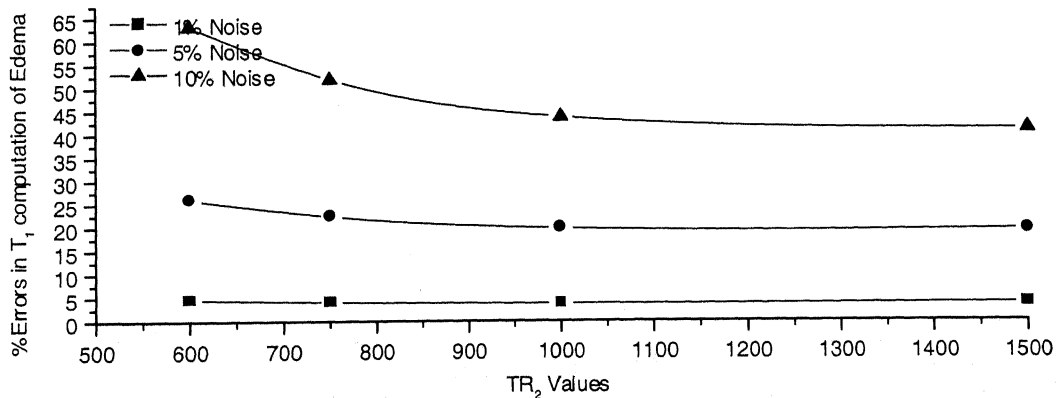
As TR₁ and TR₂ are related (TR₁=2TR₂), Graphs 2.1(a)-2.1(g) show the % errors in T₁ computation against different TR₂ (= 600, 750, 1000,1500 ms) values in white matter, gray matter, edema, CSF, upper cystic fluid, lower cystic fluid and methemoglobin respectively at 1%, 5% and 10% noise levels. Curves are plotted with spline interpolation. Graphs 2.1(a) and 2.1(f) show that gray matter and LCF have less errors at TR₂ =1000 ms compared to the other TR₂ values. Graph 2.1(c)-2.1(e) and 2.1(g) show the decrease in errors with increase in TR₂ values.



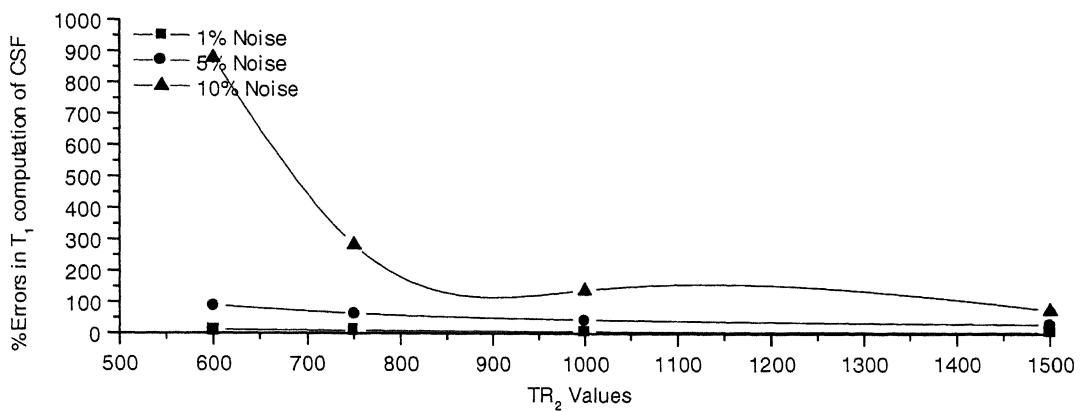
Graph 2.1 (a): % Errors in T_1 computation of white matter with different TR_2 values at different noise levels



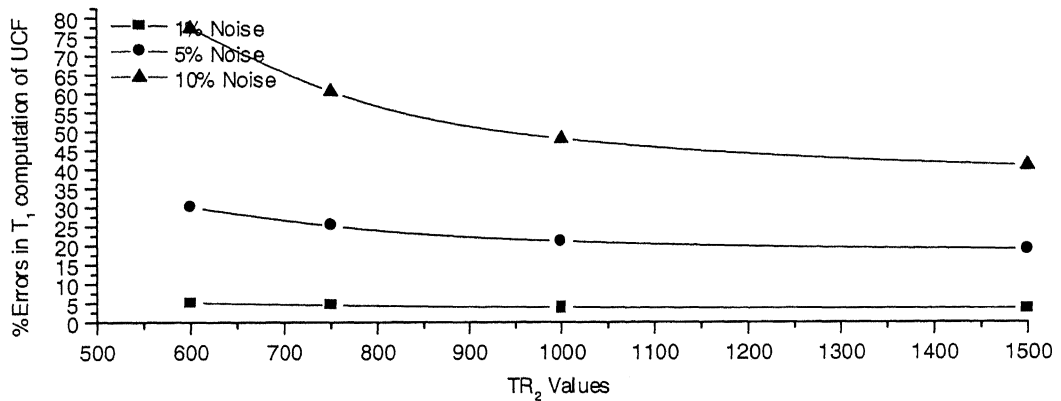
Graph 2.1 (b): % Errors in T_1 computation of gray matter with different TR_2 values at different noise levels



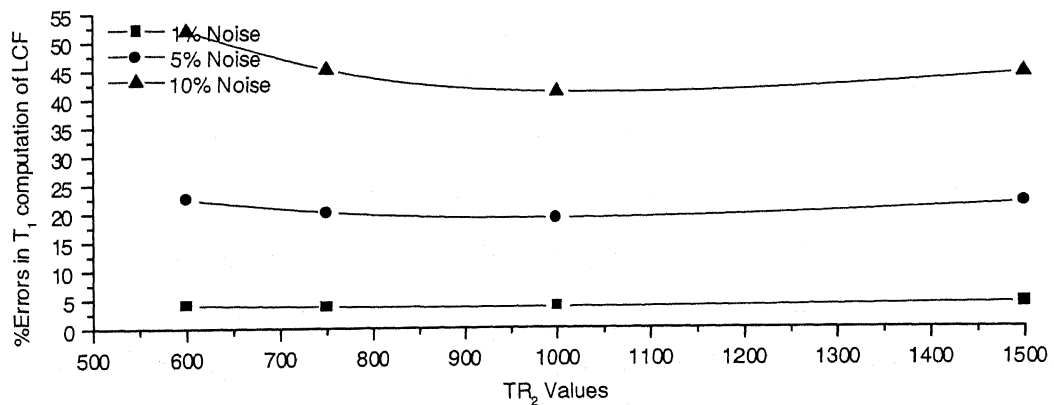
Graph 2.1 (c): % Errors in T_1 computation of edema with different TR_2 values at different noise levels



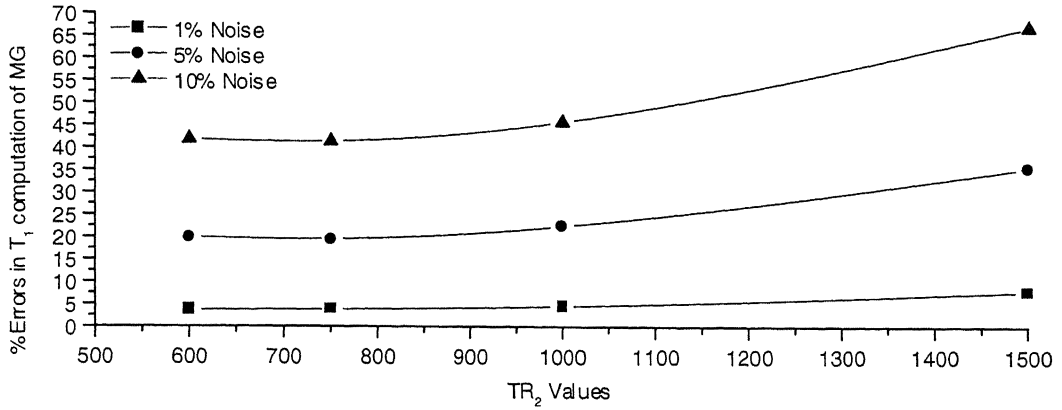
Graph 2.1 (d): % Errors in T_1 computation of CSF with different TR_2 values at different noise levels



Graph 2.1 (e): % Errors in T_1 computation of upper cystic fluid with different TR_2 values at different noise levels



Graph 2.1 (f): % Errors in T_1 computation of lower cystic fluid with different TR_2 values at different noise levels



Graph 2.1 (g): % Errors in T_1 computation of methemoglobin with different TR_2 values at different noise levels

Calculating T_2 : Using the approximation $TR \gg TE/2$, the value of T_2 can be deduced by holding TR constant while varying TE . The ratio is then

$$\frac{S_1}{S_3} = \frac{\exp(-TE_1/T_2)}{\exp(-TE_3/T_2)}, \quad (2.1.3)$$

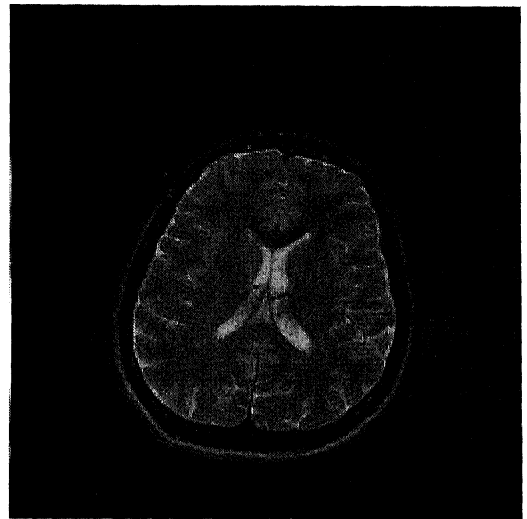
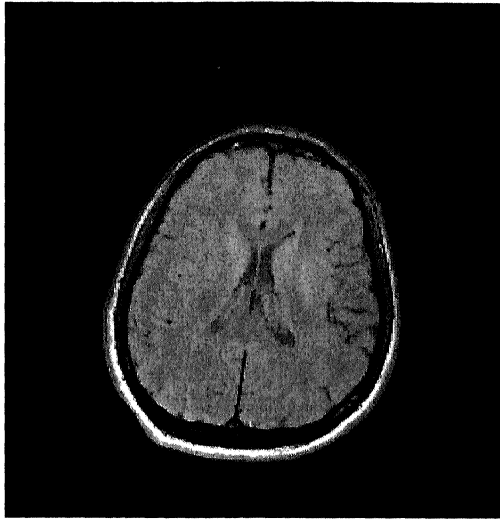
from which T_2 directly follows as:

$$T_2 = (TE_3 - TE_1) / \ln(S_1 / S_3). \quad (2.1.4)$$

Figure 2.2(a) and Figure 2.2(b) are, respectively, PD and T_2 weighted spin echo images obtained from a double echo sequence with TR as 2200 ms and TE_1 as 12 ms and TE_2 as 80 ms. Figure 2.2(c) shows the T_2 map computed as given in the equation (2.1.4).

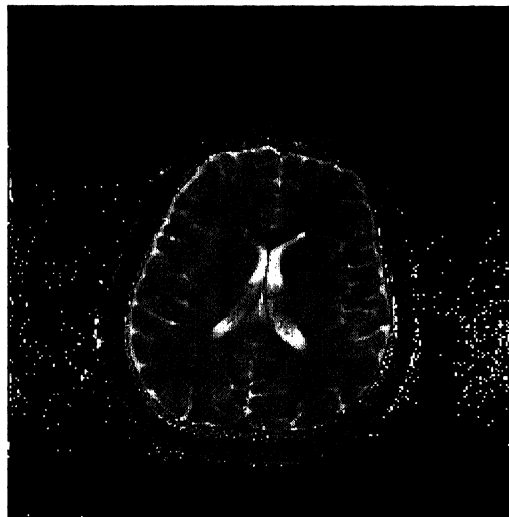
Percentage errors are computed in T_2 estimations of some common brain tissues using equation (2.1.4) with different TE 's at different noise levels. First, at each brain tissue T_2 value, for given two TE values the true signal ratio S_2/S_3 as in equation (2.1.3) is computed. Different percentages of these ratios are added as noise and resulted signal ratios are used in equation (2.1.4) to compute T_2 values (J.P. Jones (1988b)). Tables 2.5-2.8 show the percentage errors in computed T_2 values of different brain tissues in the presence of different noise levels in the signal ratios using the equation (2.1.2) with $(TE_1, TE_2) = (20, 60), (20, 80), (20, 140)$ and $(20, 200)$ ms respectively. From these tables it is observed that the errors in T_2 computation for all tissues at different noise levels decrease as the difference between TE_1 and TE_2 increases. In acquired MR

images the SNR will be low at higher TE values and consequently T_2 values computed with low TE_1 and high TE_2 correspond to the case of the presence of high noise level. For example, from Tables 2.7 and 2.8, the T_2 values computed for CSF with $(TE_1, TE_2) = (20, 200)$ at 10% noise level has an error 12.91 while with $(TE_1, TE_2) = (20, 140)$ at 5% noise level has an error 10.22 only.



(a) TR/TE = 2200/20 ms

(b) TR/TE = 2200/80 ms



(c) T_2 map

Figure 2.2: (a) and (b) are two spin echo images with TR/TE = 2200/20,80 ms. Image (c) is the computed T_2 map

Tissue Type	T_2	At 1% Noise		At 5% Noise		At 10% Noise	
		T_2	%Error	T_2	%Error	T_2	%Error
White matter	67	65.90	1.64	61.94	7.55	57.78	13.77
Gray matter	77	75.55	1.88	70.39	8.59	65.06	15.50
Edema	126	122.17	3.04	109.21	13.32	96.91	23.09
CSF	280	261.77	6.51	208.72	25.46	167.95	40.02
Upper Cystic Fluid	215	204.08	5.08	170.33	20.78	142.17	33.87
Lower Cystic Fluid	43	42.54	1.06	40.86	4.98	39.00	9.29
Methomoglobin	106	103.28	2.57	93.86	11.45	84.63	20.16

Table 2.5: % Errors in T_2 computation of different brain tissues using equation (2.1.4) with $TE_1 = 20$ ms and $TE_2 = 60$ ms at different noise levels

Tissue Type	T_2	At 1% Noise		At 5% Noise		At 10% Noise	
		T_2	%Error	T_2	%Error	T_2	%Error
White matter	67	66.26	1.10	63.54	5.12	60.55	9.62
Gray matter	77	76.03	1.26	72.46	5.89	68.61	10.90
Edema	126	123.42	2.05	114.29	9.29	104.99	16.68
CSF	280	267.57	4.44	228.07	18.55	193.80	30.78
Upper Cystic Fluid	215	207.60	3.44	183.00	14.88	160.26	25.46
Lower Cystic Fluid	43	42.69	0.71	41.55	3.38	40.25	6.39
Methomoglobin	106	104.17	1.73	97.59	7.94	90.72	14.41

Table 2.6: % Errors in T_2 computation of different brain tissues using equation (2.1.4) with $TE_1 = 20$ ms and $TE_2 = 80$ ms at different noise levels

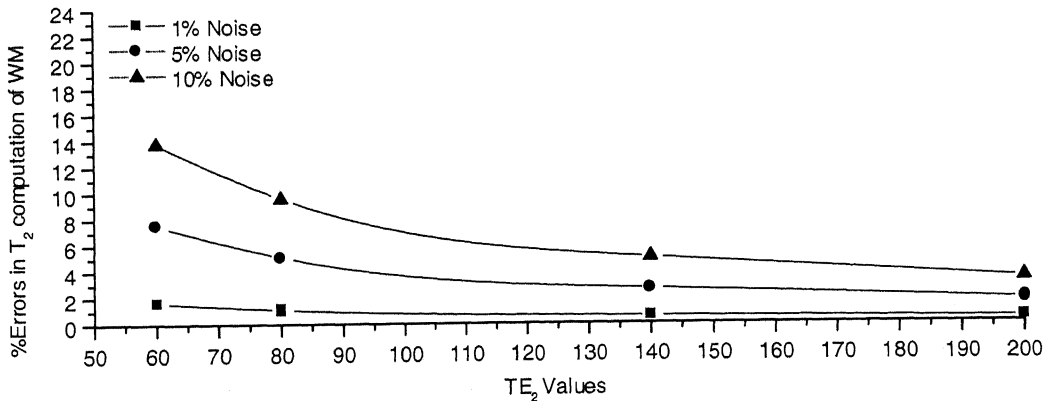
Tissue Type	T_2	At 1% Noise		At 5% Noise		At 10% Noise	
		T_2	%Error	T_2	%Error	T_2	%Error
White matter	67	66.63	0.55	65.22	2.65	63.61	5.05
Gray matter	77	76.51	0.63	74.66	3.04	72.56	5.76
Edema	126	124.70	1.03	119.86	4.87	114.54	9.10
CSF	280	273.65	2.27	251.38	10.22	229.06	18.19
Upper Cystic Fluid	215	211.23	1.75	197.72	8.04	183.64	14.59
Lower Cystic Fluid	43	42.85	0.35	42.26	1.72	41.58	3.30
Methomoglobin	106	105.08	0.87	101.62	4.13	97.77	7.76

Table 2.7: % Errors in T_2 computation of different brain tissues using equation (2.1.4) with $TE_1 = 20$ ms and $TE_2 = 140$ ms at different noise levels

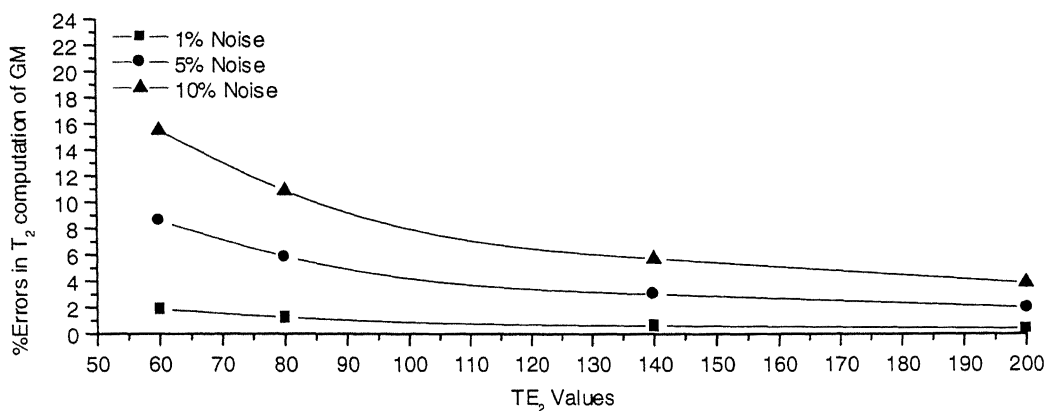
Tissue Type	T_2	At 1% Noise		At 5% Noise		At 10% Noise	
		T_2	%Error	T_2	%Error	T_2	%Error
White matter	67	66.75	0.37	65.80	1.78	64.70	3.43
Gray matter	77	76.67	0.42	75.43	2.04	73.98	3.92
Edema	126	125.13	0.69	121.84	3.30	118.12	6.25
CSF	280	275.73	1.52	260.25	7.05	243.85	12.91
Upper Cystic Fluid	215	212.47	1.17	203.16	5.51	193.02	10.22
Lower Cystic Fluid	43	42.90	0.24	42.50	1.15	42.04	2.23
Methomoglobin	106	105.38	0.58	103.04	2.79	100.37	5.31

Table 2.8: % Errors in T_2 computation of different brain tissues using equation (2.1.4) with $TE_1 = 20$ ms and $TE_2 = 200$ ms at different noise levels

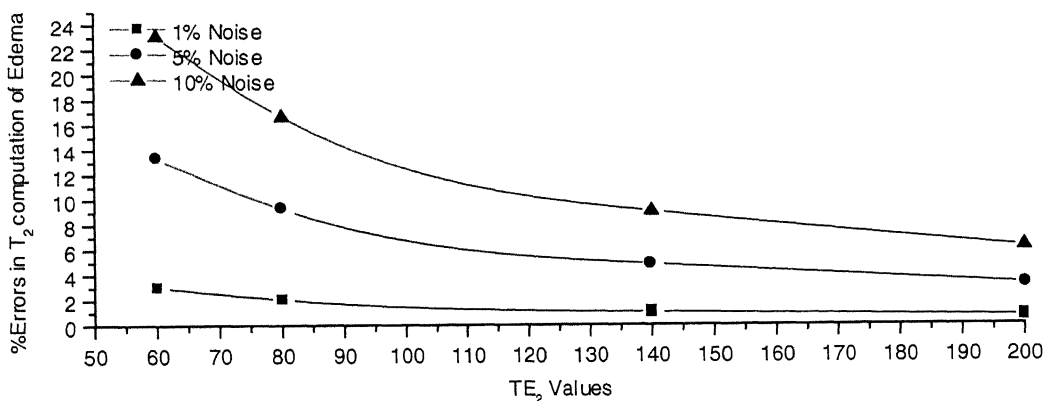
As TE_1 is 20 ms in all the (TE_1, TE_2) pairs, Graphs 2.2(a)-2.2(g) show the % errors in T_2 computation against different TE_2 (= 60, 80, 140, 200 ms) values in white matter, gray matter, edema, CSF, upper cystic fluid, lower cystic fluid and methemoglobin respectively at 1%, 5% and 10% noise levels. Curves are plotted with spline interpolation. All these graphs show that the errors in T_2 computation decreases with the increase in TE_2 values.



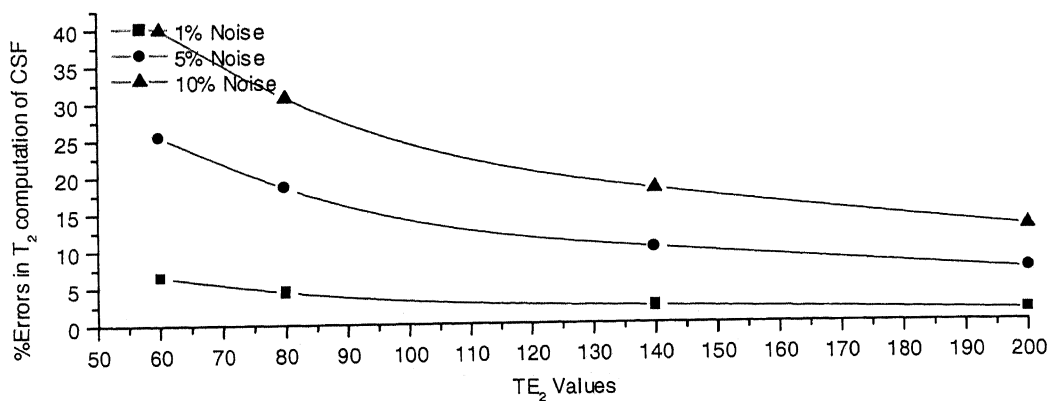
Graph 2.2 (a): % Errors in T_2 computation of white matter with different TE_2 values at different noise levels



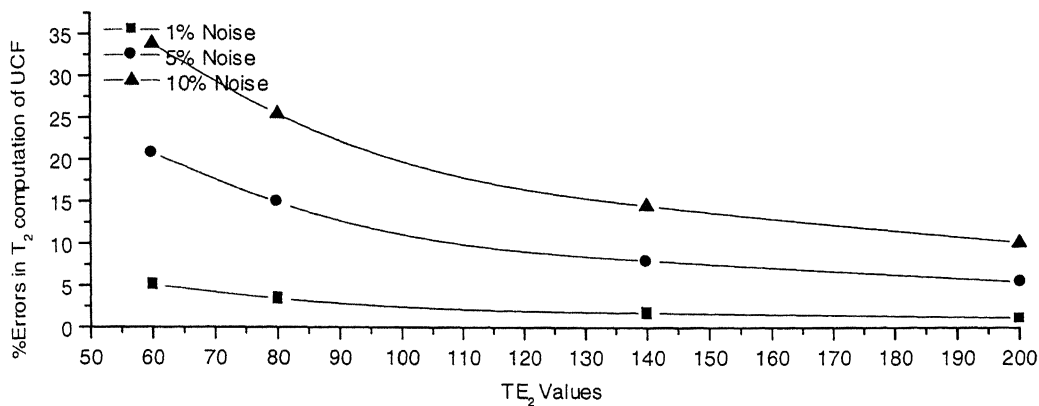
Graph 2.2 (b): % Errors in T₂ computation of gray matter with different TE₂ values at different noise levels



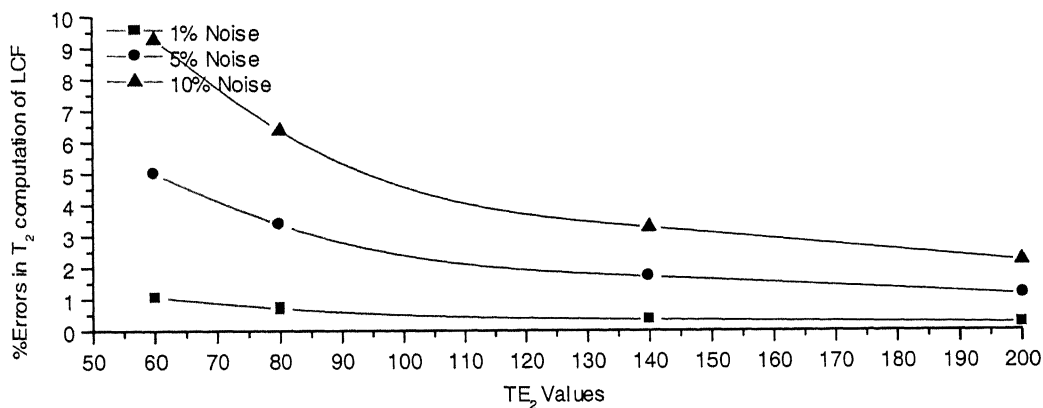
Graph 2.2 (c): % Errors in T₂ computation of edema with different TE₂ values at different noise levels



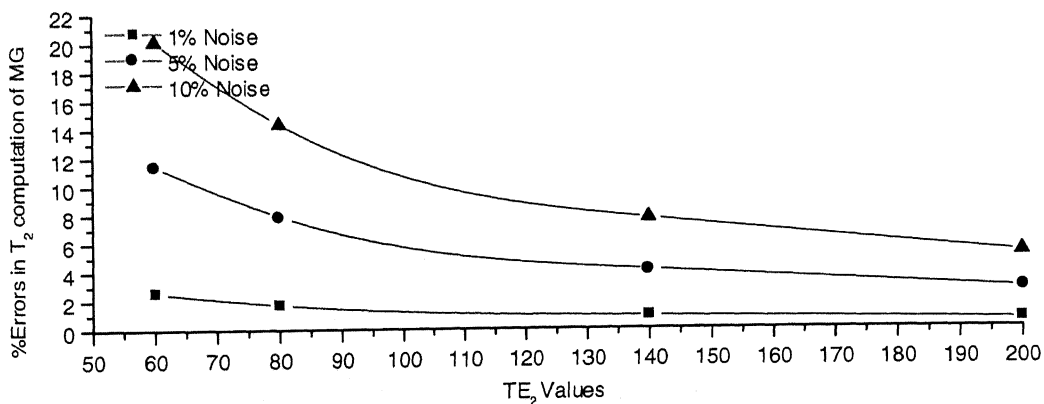
Graph 2.2 (d): % Errors in T₂ computation of CSF with different TE₂ values at different noise levels



Graph 2.2 (e): % Errors in T_2 computation of upper cystic fluid with different TE_2 values at different noise levels



Graph 2.2 (f): % Errors in T_2 computation of lower cystic fluid with different TE_2 values at different noise levels



Graph 2.2 (g): % Errors in T_2 computation of methemoglobin with different TE_2 values at different noise levels

2.2. Iterative Methods

Usually, nonlinear equations are solved numerically by iterative methods. Tissue parameter estimation in MRI is a nonlinear problem in nature. In this section we discuss some iterative methods for computation these parameters.

2.2.1. A Least Squares Method for T_1 Calculation

In this subsection we describe a least squares method proposed by J. Gong and J.P. Hornak (1992) for the computation of T_1 values. Under ideal conditions, that is, the absence of spin exchange, primarily one component filling an image voxel, and perfect radio-frequency pulses, the magnetic resonance signal from a saturation recovery type imaging experiment may be approximated as

$$S(TR_j) = k(1 - \exp(-TR_j / T_1)) \quad (2.2.1)$$

where TR is the repetition time of the experiment and k is a proportionality constant dependent on such factors as the spin density and amplifier gains. In the case of commonly used spin-echo sequence, k is also a function of the spin-spin relaxation time, TE. A T_1 value is typically calculated by fitting equation (2.2.1) to imaging data obtained at several values of TR. The imaging data is the actual MR signal S_i at TR_i . A least squares technique seeks to minimize $\phi(T_1, k)$ for the n data points, where

$$\phi(T_1, k) = \sum_i^n [S(TR_i) - S_i]^2.$$

Therefore

$$\delta\phi(T_1, k) = \frac{\partial\phi}{\partial k} \delta k + \frac{\partial\phi}{\partial T_1} \delta T_1 = 0.$$

Since neither δk nor δT_1 may be zero then

$$\frac{\partial\phi}{\partial k} = 0 \text{ and } \frac{\partial\phi}{\partial T_1} = 0.$$

From the above equation one has

$$\sum_{i=1}^n [k(1 - \exp(-TR_i / T_1)) - S_i](1 - \exp(-TR_i / T_1)) = 0$$

and
$$\sum_{i=1}^n [k(1 - \exp(-TR_i / T_1)) - S_i]TR_i \exp(-TR_i / T_1) = 0.$$

$$\frac{\sum_{i=1}^n S_i (1 - \exp(-TR_i / T_1))}{\sum_{i=1}^n (1 - \exp(-TR_i / T_1))^2} = \frac{\sum_{i=1}^n S_i TR_i \exp(-TR_i / T_1)}{\sum_{i=1}^n TR_i \exp(-TR_i / T_1) (1 - \exp(-TR_i / T_1))}.$$

Now the above equation is a function of T_1 only. After reordering the summations one obtains a function $Z(T_1)$ given as

$$Z(T_1) = \sum_{i=1}^n \sum_{j=1}^n \{ TR_j \exp(-TR_j / T_1) (1 - \exp(-TR_i / T_1)) \times [S_i (1 - \exp(-TR_j / T_1)) - S_j (1 - \exp(-TR_i / T_1))] \}.$$

The authors have used a controlled iterative method to computed T_1 values.

This least squares method requires the data acquired at different TR values but with same TE values. It is also to be noted that the signal expression used in this method is an approximated expression i.e. with the assumption $TR \gg TE$.

Figure 2.3(a)-(d) shows the spin echo images of a volunteer acquired with $TR/TE = 850, 1100, 1650, 2200/20$ ms. Figure 2.3(e) is the T_1 map computed from Figure 2.3(a)-(d) images using the above method. White dots outside the brain T_1 map are due the presence of noise more than the threshold value, here it is taken as 60, in the input images. Computing T_1 map with this data using the method described above has taken 16.04 sec on a Pentium II P.C. with 350 MHz speed and 96 MB RAM.

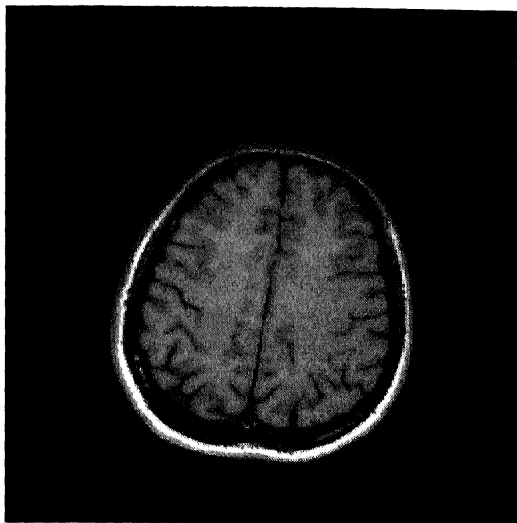
This method could be made faster by using a look up table approach. Using the look up table values as initial guesses, the accuracy in the computed values could be improved by Newton's method as

$$T_1^{n+1} = T_1^n - \left(\frac{\partial Z(T_1^n)}{\partial T_1^n} \right)^{-1} Z(T_1^n),$$

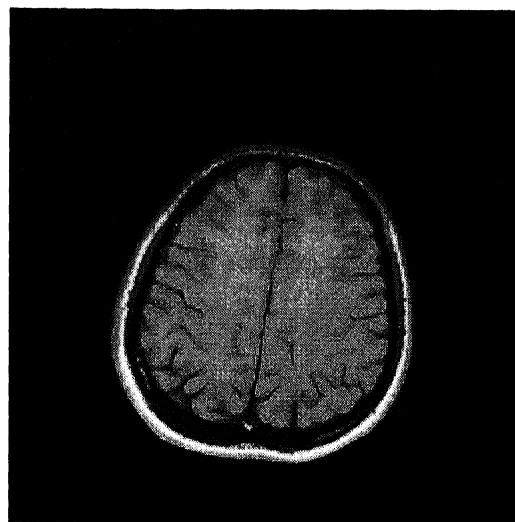
where,

$$\frac{\partial Z(T_1)}{\partial T_1} = \frac{1}{T_1^2} \sum_{i=1}^N \sum_{j=1}^N TR_j \times \{ TR_j \exp(-TR_j / T_1) (1 - \exp(-TR_i / T_1)) [S_i (1 - \exp(-TR_j / T_1)) - S_j (1 - \exp(-TR_i / T_1))] + \exp(-TR_j / T_1) (1 - \exp(-TR_i / T_1)) [S_j TR_i \exp(-TR_i / T_1) - S_i TR_j \exp(-TR_j / T_1)] \}.$$

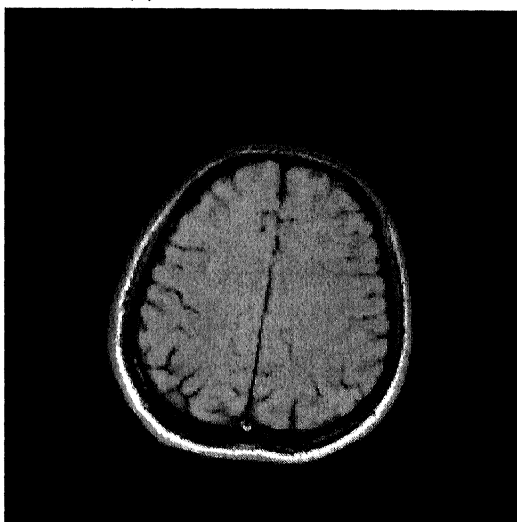
→ With this procedure, the same set of data with under same conditions, the computation of T_1 map has taken 2.31 sec only.



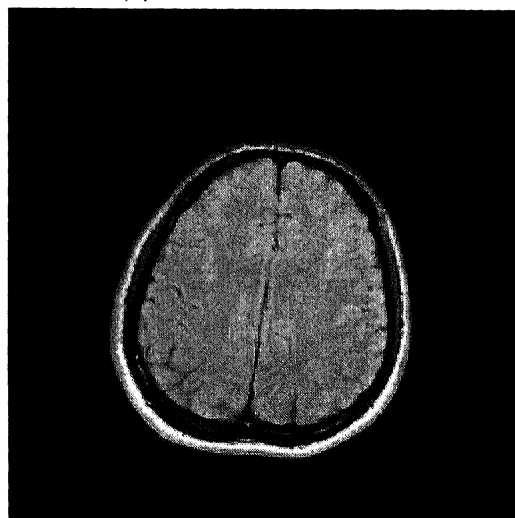
(a) TR/TE = 850/20 ms



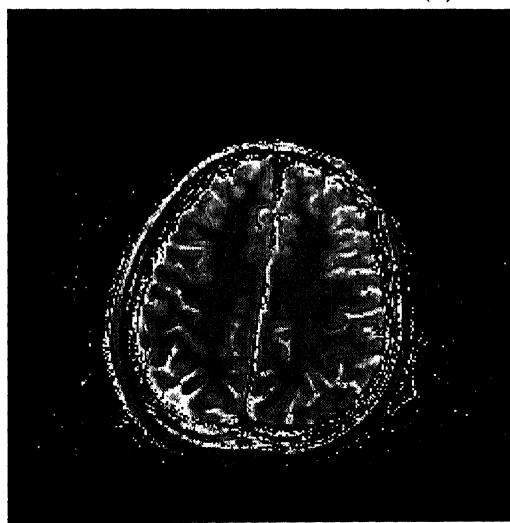
(b) TR/TE = 1100/20 ms



(c) TR/TE = 1650/20 ms



(d) TR/TE = 2200/20 ms



(e) T_1 map

Figure 2.3: First four are spin echo images with TR/TE = 850, 1100, 1650, 2200/20 ms. The last image is the computed T_1 map computed.

2.2.2. A Least Squares Method for T_2 Calculation

In this subsection, a non-linear least squares method for computation of T_2 values proposed by Xing Li and J.P. Hornak (1994) is described. The apparent T_2 is usually measured using the magnetic resonance signal from a spin-echo sequence,

$$S(TE_i) = k \exp(-TE_i / T_2) . \quad (2.2.2)$$

The proportionality constant k is dependent on such factors as the spin density, amplifier gains, spin-lattice relaxation time T_1 , and the repetition time of the imaging sequence. The apparent T_2 may be calculated from the above equation with an appropriate set of n images recorded with different TE_i values. The image represents the actual magnetic resonance signal, S_i , at time TE_i , which is composed of a contribution from the spins, $S(TE_i)$, and random additive noise N , independent of the $S(TE_i)$.

$$S_i = S(TE_i) + N_i . \quad (2.2.3)$$

Xing Li and J.P. Hornak (1994) studied two techniques for finding the best $S(TE_i)$ match with the data based on a linear and a rapid nonlinear least-squares solution to equation (2.2.2).

The linear procedure linearizes equation (2.2.2) by taking the logarithms of both sides

$$\ln(S_i) = \ln(k) - TE_i / T_2$$

such that the slope of a line obtained from plotting $\ln(S_i)$ versus TE_i is $-1/T_2$. The procedure seeks to minimize $\phi(T_2)$ by setting

$$\frac{\partial \phi}{\partial T_2} = 0 \quad \text{and} \quad \frac{\partial \phi}{\partial (\ln(S_i))} = 0$$

for the n data points, where

$$\phi(T_2) = \sum_{i=1}^n \{ \ln(S_i) - \ln[S(TE_i)] \}^2 .$$

The slope obtained from a linear least-squares solution is

$$-\frac{1}{T_2} = \frac{\left[\sum_{i=1}^n TE_i \sum_{i=1}^n \ln(S_i) - n \sum_{i=1}^n TE_i \ln(S_i) \right]}{\left(\sum_{i=1}^n TE_i \right)^2 - n \sum_{i=1}^n TE_i^2} .$$

The difficulty with this method lies in the minimization of ϕ . The deviation of $\ln(S_i)$ from $\ln[S(TE_i)]$ at each i is treated with equal significance. Taking logarithms of both sides of equation (2.2.3) yields

$$\ln(S_i) - \ln[S(TE_i)] = \ln\left[1 + \frac{N_i}{S(TE_i)}\right].$$

The above equation shows that $\ln(S_i) - \ln[S(TE_i)]$ is dependent on the S/N, which itself depends on TE_i . The presence of small signals in the data set used to calculate T_2 with a linear least squares procedure could severely affect the accuracy of the fitting.

Alternatively, T_2 could be estimated with a nonlinear regression by minimizing

$$\phi(T_2, k) = \sum_{i=1}^n \{S_i - k \exp(-TE_i / T_2)\}^2.$$

Therefore

$$\delta\phi(T_2, k) = \frac{\partial\phi}{\partial k} \delta k + \frac{\partial\phi}{\partial T_2} \delta T_2 = 0.$$

Because neither δk nor δT_2 may be zero, then

$$\frac{\partial\phi}{\partial k} = 0 \quad \text{and} \quad \frac{\partial\phi}{\partial T_2} = 0.$$

These equations give

$$\sum_{i=1}^n \{S_i - k \exp(-TE_i / T_2)\} \exp(-TE_i / T_2) = 0,$$

and
$$\sum_{i=1}^n \{S_i - k \exp(-TE_i / T_2)\} TE_i \exp(-TE_i / T_2) = 0.$$

Solving these equations for k and equating both equations yields

$$\frac{\sum_{i=1}^n S_i \exp(-TE_i / T_2)}{\sum_{i=1}^n \exp(-2TE_i / T_2)} = \frac{\sum_{i=1}^n S_i TE_i \exp(-TE_i / T_2)}{\sum_{i=1}^n TE_i \exp(-2TE_i / T_2)}.$$

Now this equation is a function of T_2 only. After reordering the summations one obtains a function $Z(T_2)$ given as

$$Z(T_2) = \sum_{i=1}^n \sum_{j=1}^n [S_i \exp(-TE_i / T_2) TE_j \exp(-2TE_j / T_2) - S_j TE_j \exp(-TE_j / T_2) \exp(-2TE_i / T_2)].$$

Xing Li and J.P. Hornak (1994) have solved this equation using a controlled iterative

calculations is less sensitive to the presence noise in the images in the data set compared to linearized least squares method. Since this method requires images acquired at different TE's with same TR values, one could use multi echo sequence images without any excess scanning time.

Figure 2.4(a)-(d) shows the multi spin echo images of a volunteer acquired with TE/TR = 20, 46, 80, 114/2200 ms. Figure 2.4(e) is the T_2 map computed from Figure 2.4(a)-(d) images using the above method. White dots outside the brain T_2 map are due the presence of noise more than the threshold value, here it is taken as 60, in the input images. Computing T_2 map with this data using the method described above has taken 37.31 sec on a Pentium II P.C. with 350 MHz speed and 96 MB RAM.

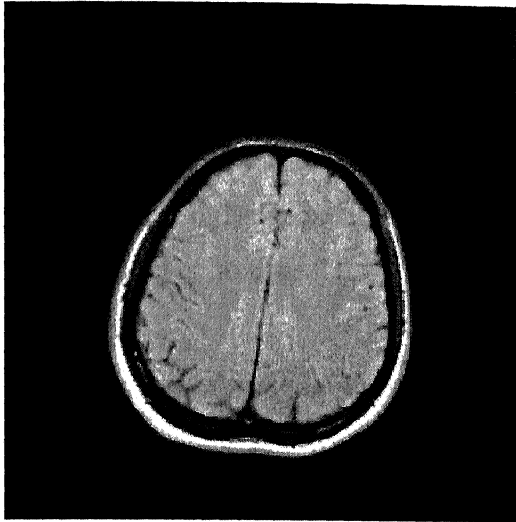
This method could be made faster by computing T_2 map using two point method with two images from the data set (preferably one image with minimum TE and other one with maximum TE to have less errors due to the presence of noise). Now using these values as initial guesses, the accuracy in the computed values could be improved by Newton's method as

$$T_2^{n+1} = T_2^n - \left(\frac{\partial Z(T_2^n)}{\partial T_2^n} \right)^{-1} Z(T_2^n),$$

where,

$$\begin{aligned} \frac{\partial Z(T_2)}{\partial T_2} = \frac{1}{T_2^2} \sum_{i=1}^N \sum_{j=1}^N TE_j \{ S_i \exp(-TE_i / T_2) \exp(-2TE_j / T_2) (TE_i + 2TE_j) \\ - S_j \exp(-TE_j / T_2) \exp(-2TE_i / T_2) (TE_j + 2TE_i) \}. \end{aligned}$$

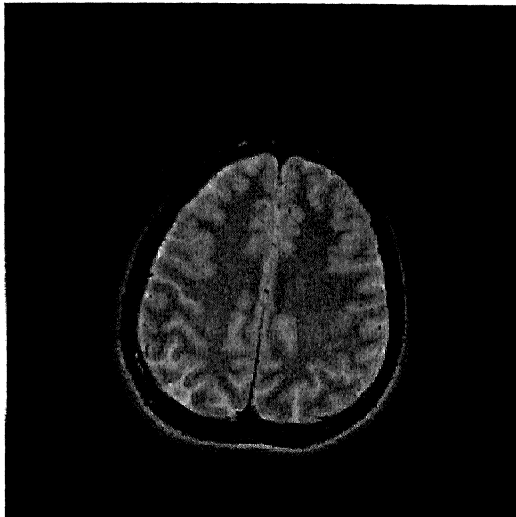
With this procedure, the same set of data under same conditions, the computation of T_2 map has taken 12.09 sec only.



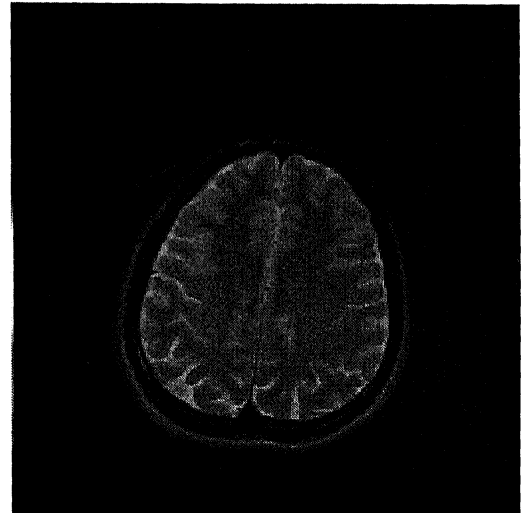
(a) TE/TR = 20/2200 ms



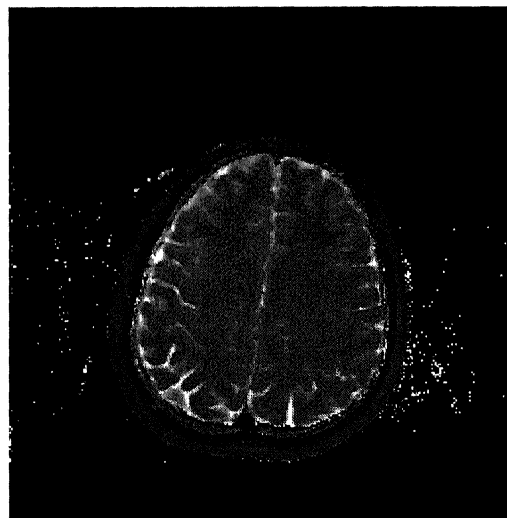
(b) TE/TR = 46/2200 ms



(c) TE/TR = 80/2200



(d) TE/TR = 114/2200



(e) T_2 map

Figure 2.4: First four are multi spin echo images with TE/TR = 20, 46, 80, 144/2200 ms. The last image is the computed T_2 map

$$\begin{aligned}
|\mathbf{A}| &= \begin{vmatrix} \frac{\partial F_1}{\partial T_1} & \frac{\partial F_1}{\partial T_2} & \frac{\partial F_1}{\partial \rho} \\ \frac{\partial F_2}{\partial T_1} & \frac{\partial F_2}{\partial T_2} & \frac{\partial F_2}{\partial \rho} \\ \frac{\partial F_3}{\partial T_1} & \frac{\partial F_3}{\partial T_2} & \frac{\partial F_3}{\partial \rho} \end{vmatrix} \\
&= \frac{\rho}{T_1^2 T_2^2} \exp(-(TE_1 + TE_2 + TE_3)/T_2) \exp(-(TR_1 + TR_2 + TR_3)/T_1) \\
&\quad \times \begin{vmatrix} TR_1 - (2TR_1 - TE_1)e^{TE_1/2T_1} & TE_1(e^{TR_1/T_1} + 1 - 2e^{TE_1/2T_1}) & (e^{TR_1/T_1} + 1 - 2e^{TE_1/2T_1}) \\ TR_2 - (2TR_2 - TE_2)e^{TE_2/2T_1} & TE_2(e^{TR_2/T_1} + 1 - 2e^{TE_2/2T_1}) & (e^{TR_2/T_1} + 1 - 2e^{TE_2/2T_1}) \\ TR_3 - (2TR_3 - TE_3)e^{TE_3/2T_1} & TE_3(e^{TR_3/T_1} + 1 - 2e^{TE_3/2T_1}) & (e^{TR_3/T_1} + 1 - 2e^{TE_3/2T_1}) \end{vmatrix}
\end{aligned}$$

$$\begin{aligned}
&= \frac{\rho}{T_1^2 T_2^2} \exp(-(TE_1 + TE_2 + TE_3)/T_2) \exp(-(TR_1 + TR_2 + TR_3)/T_1) \\
&\quad \times \{ [TR_1 - (2TR_1 - TE_1)e^{TE_1/2T_1}](TE_2 - TE_3)a_2a_3 \\
&\quad + [TR_2 - (2TR_2 - TE_2)e^{TE_2/2T_1}](TE_3 - TE_1)a_1a_3 \\
&\quad + [TR_3 - (2TR_3 - TE_3)e^{TE_3/2T_1}](TE_1 - TE_2)a_1a_2 \}
\end{aligned}$$

where $a_i = e^{TR_i/T_1} + 1 - 2e^{TE_i/2T_1}$.

Therefore

$$|\mathbf{A}| \neq 0 \Leftrightarrow k_1 TR_1 (TE_2 - TE_3) + k_2 TR_2 (TE_3 - TE_1) + k_3 TR_3 (TE_1 - TE_2) \neq 0,$$

where $k_1 = [1 - (2 - TE_1/TR_1)e^{TE_1/2T_1}]a_2a_3$,

$$k_2 = [1 - (2 - TE_2/TR_2)e^{TE_2/2T_1}]a_1a_3,$$

$$k_3 = [1 - (2 - TE_3/TR_3)e^{TE_3/2T_1}]a_1a_2.$$

Therefore, except for some physical situations where the determinant of \mathbf{A} vanishes, it is possible to compute T_1 , T_2 , and ρ simultaneously.

2.2.4. Reduction to a Single Variable Case

Most of the methods for tissue parameters T_1 , T_2 and ρ estimation in MR imaging either require very specific data (e.g., in two point fit (J.P. Jones (1988b) for T_1 -calculation, where one uses same TE but one of the TR is double of the other and in the iterative method (J. Gong and J.P. Hornak (1992)) for T_1 -calculation data at different TR's which takes more scanning time is required) or are based on solving a possibly over-determined system of nonlinear equations in three variables (H. Iwaoka, T. Hirata and H. Matsuura (1987)). In the former case it is only approximated signal expressions which are used and so some corrective procedures are still to be used. The algorithms in the latter category suffer from the well known problems arising in the case of several variables, like the close choice for the initial guess and the convergence problems in general arising due to the high degree of freedom available in dimensions larger than one. However the situation in the case of a single variable is relatively simple, where the initial guesses as well as monitoring the convergence could be affected much more conveniently. In this subsection we introduce a method based on separating the variables so that finally we end up with an equation of a single variable T_1 , whose determination subsequently leads to finding the other parameters T_2 and ρ .

The magnitude signal of spin echo can be expressed as

$$S_j = k\rho (1 - 2\exp(-(TR_j - TE_j/2)/T_1) + \exp(-TR_j/T_1))\exp(-TE/T_2)$$

If we have three independent images, considering the following ratios,

$$\frac{S_1}{S_2} = \exp(-(TE_1 - TE_2)/T_2) \times \frac{(1 + \exp(-TR_1/T_1) - 2\exp(-(TR_1 - TE_1/2)))}{(1 + \exp(-TR_2/T_1) - 2\exp(-(TR_2 - TE_2/2)))},$$

and

$$\frac{S_3}{S_2} = \exp(-(TE_3 - TE_2)/T_2) \times \frac{(1 + \exp(-TR_3/T_1) - 2\exp(-(TR_3 - TE_3/2)))}{(1 + \exp(-TR_2/T_1) - 2\exp(-(TR_2 - TE_2/2)))},$$

we can write

$$\begin{aligned} \frac{\left(\frac{S_1}{S_2}\right)^{(TE_3-TE_2)}}{\left(\frac{S_3}{S_2}\right)^{(TE_1-TE_2)}} &= \frac{(1 + \exp(-TR_1/T_1) - 2\exp(-(TR_1 - TE_1/2)))^{(TE_3-TE_2)}}{(1 + \exp(-TR_3/T_1) - 2\exp(-(TR_3 - TE_3/2)))^{(TE_1-TE_2)}} \\ &\quad \times (1 + \exp(-TR_2/T_1) - 2\exp(-(TR_2 - TE_2/2)))^{(TE_1-TE_3)}. \end{aligned}$$

Now,

$$\prod_{j=1}^3 S_j^{(TE_{j+}, -TE_{j++})} = \prod_{j=1}^3 (1 + \exp(-TR_j / T_1) - 2 \exp(-(TR_j - TE_j / 2) / T_1))^{(TE_{j+}, -TE_{j++})},$$

when

$$\begin{aligned} j &= 1, & j_+ &= 2, j_{++} &= 3; \\ j &= 2, & j_+ &= 3, j_{++} &= 1; \\ j &= 3, & j_+ &= 1, j_{++} &= 2. \end{aligned}$$

Taking logarithms on both sides yields

$$F(T_1) = \sum_{j=1}^3 (TE_{j+} - TE_{j++}) \ln \left(\frac{1 + \exp(-TR_j / T_1) - 2 \exp(-(TR_j - TE_j / 2) / T_1)}{S_j} \right) = 0,$$

and

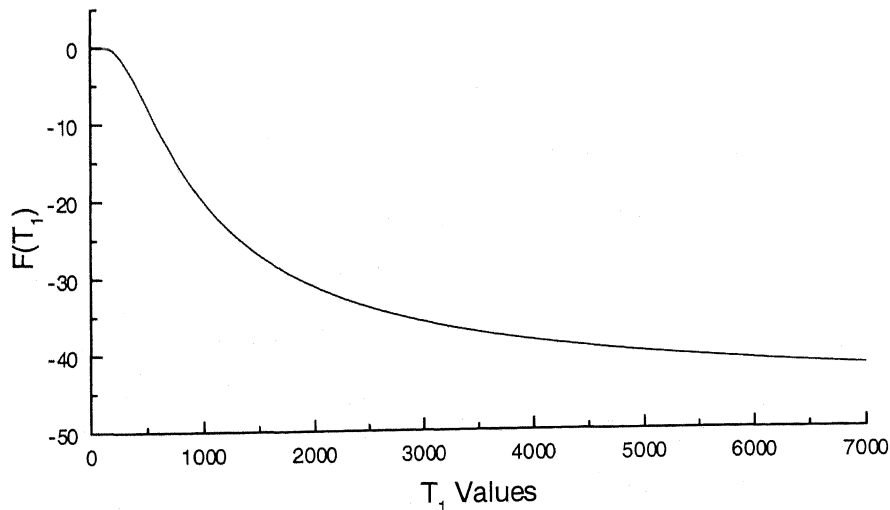
$$\begin{aligned} \frac{\partial F}{\partial T_1} &= \frac{1}{T_1^2} \sum_{j=1}^3 \frac{(TE_{j+} - TE_{j++})}{1 + \exp(-TR_j / T_1) - 2 \exp(-(TR_j - TE_j / 2) / T_1)} \\ &\quad \times (TR_j \exp(-TR_j / T_1) - 2 \exp(-(TR_j - TE_j / 2) / T_1) (TR_j - TE_j / 2)). \end{aligned}$$

Starting with the initial approximation T_1^0 , iteratively T_1 values can be computed using Newton's method as:

$$T_1^{n+1} = T_1^n - \left(\frac{\partial F}{\partial T_1^n} \right)^{-1} F(T_1^n).$$

In case of close initial guess problem, a *Look-up Table* can be used.

It is observed that at all routinely used TE, TR's and over the range of clinically interested T_1 values, the function $F(T_1)$ is, numerically, monotone and guarantees the



Graph 2.3: Plot of $F(T_1)$ vs T_1 values with $TR/TE = 2200/20, 1024/14, 2200/80$ ms

non vanishing derivative and consequently the above iterative method is meaningful. As an illustration, Graph 2.3 shows the $F(T_1)$ against the T_1 values for the spin-echo images with $TR/TE = 2200/20, 1024/14, 2200/80$ ms.

Now, T_2 and ρ can be computed as follows:

Considering two images at a time and substituting the calculated T_1 values in the signal intensity expression we can have $^p c_2$ calculated T_2 values for each pixel as

$$T_2 = \frac{(TE_{j+1} - TE_j)}{\ln\left(\frac{S_j}{S_{j+1}} \frac{f_{j+1}}{f_j}\right)}.$$

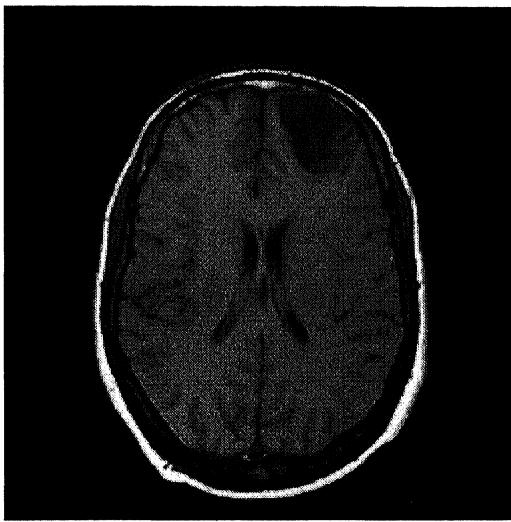
Note that this expression is different from the conventional two point fit method (J.P. Jones (1988b)) which uses the assumption that $TR \gg TE$ and leads to an approximation to actual signal expression. The average of all these values can be considered as T_2 image and it minimizes the sum of the squares of the errors (SSE). And using these T_1 , and T_2 values from intensity expression, proton density can be obtained from

$$\rho = \frac{S_j}{g_j(T_2)f_j(T_1)} \text{ and their average would give } \rho \text{ map minimizing SSE.}$$

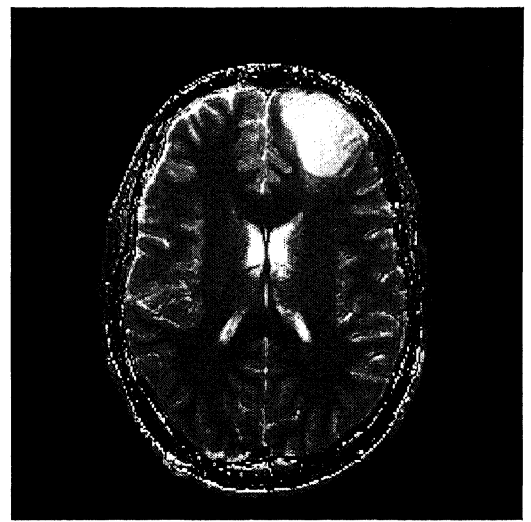
This formulation holds for any pulse sequence whose signal intensity can be written as:

$$S = \rho f(T_1) e^{-TE/T_2}.$$

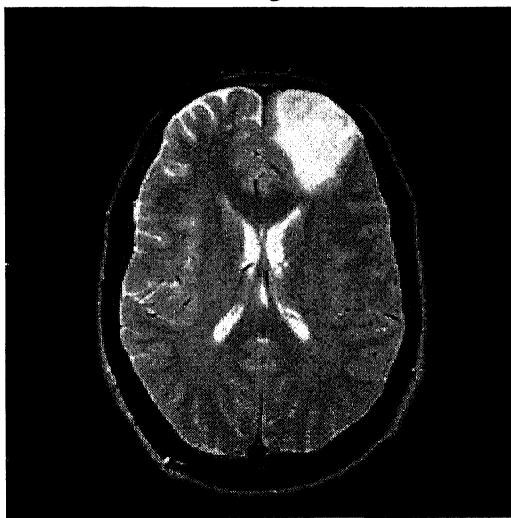
First column of Figure 2.5 shows the T_1 , T_2 , and PD weighted images. T_1 weighted image is obtained from single spin echo sequence with $TR/TE = 1014/12$ ms while PD and T_2 weighted images are the first and second echo images respectively of a double spin echo sequence with $TR/TE = 2200/20, 80$ ms. The corresponding T_1 , T_2 , and PD maps, computed using the above method, are shown in the second column of Figure 2.5. Figure 2.6 shows the divergent map where the iterative method fails to converge. Most of these divergent points are seen in the brain cranial region possibly because of mixed signals in these pixels due to the partial volume effect.



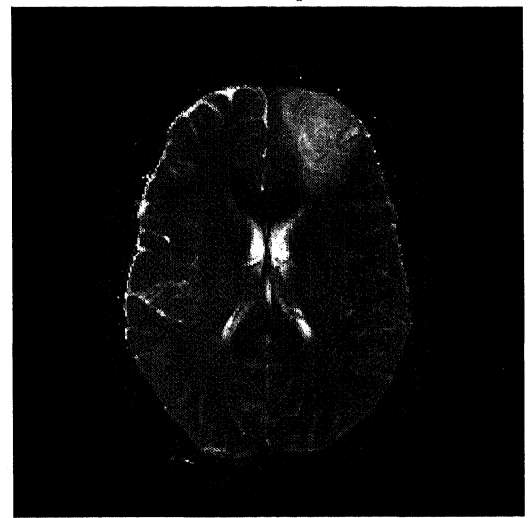
T₁ weighted



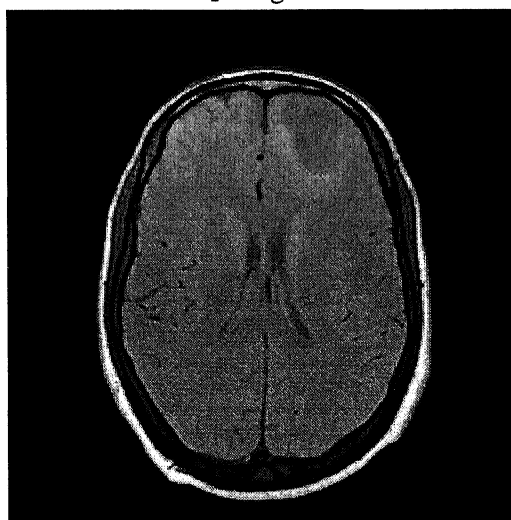
T₁ map



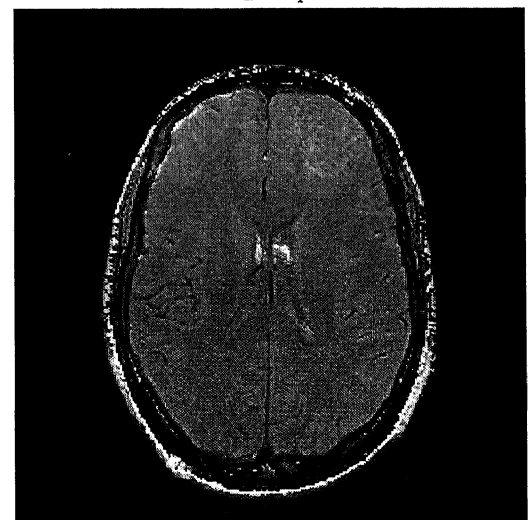
T₂ weighted



T₂ map



PD weighted



PD map

Figure 2.5: Images in the first column are T₁, T₂, and PD weighted spin echo images with TR/TE = 1012/14, 2200/80, 2200/20 ms of a patient with perilesional gliosis around the cystic cavity. Second column images are the T₁, T₂, and PD map computed using the method described in

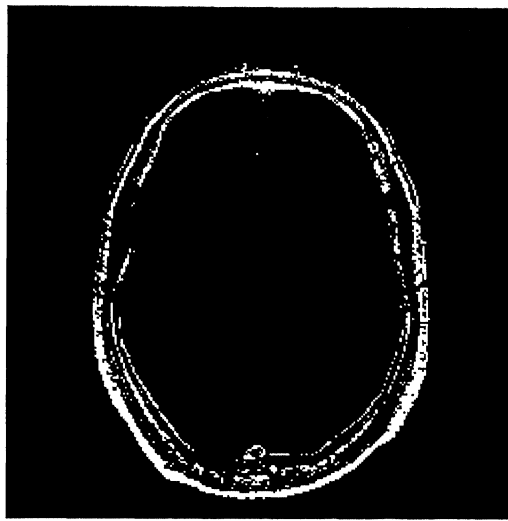


Figure 2.6: Divergent map

Parameter values computed with reducing to a single variable method and two point methods as described in section 2.1 are shown in Table 2.9. For this, spin echo signal intensity values are simulated at different T_1 , T_2 , and PD values with $TR/TE = 1100/20$, $2200/20$, and $2200/120$ ms. Parameter values computed using single variable case are close to the actual values. Computations with two point T_1 and T_2 estimations have shown significant difference in the computed values in comparison with original parameter values. These computed T_1 and T_2 values are substituted in one of the image intensity expressions to obtain PD values. These errors are due to the approximated expressions used in the two point methods.

T_1 value	T_2 value	PD value	Single variable case			Two point methods		
			T_1	T_2	PD	T_1	T_2	PD
500	70	2400	499.99	70.00	2439.99	510.35	83.84	2330.35
750	80	2760	749.99	79.99	2760.00	768.10	95.39	2661.76
1000	120	2840	999.99	119.99	2839.99	1028.01	141.78	2789.96
1500	160	3120	1499.99	159.99	3119.99	1554.54	185.82	3142.51
2000	210	3440	1999.99	209.99	3439.99	2090.22	239.02	3485.49
3000	280	4000	2999.99	279.99	3999.99	3190.07	308.47	4145.43

Table 2.9: Parameters computed with single variable and two point methods

If $n(\geq 3)$ acquired MR images with different pulse sequences or sequence parameters are available, then it is possible to make nC_3 data triples from which T_1 can be computed. By considering suitable consistence data triples, a least squares formulation can be made as:

$$\min_{T_1} \sum_{triples} \left[\sum_{i=1}^3 \omega_i (\ln(f_i(T_1)) - \ln(S_i)) \right]^2,$$

which reduces to solving

$$\sum_{triples} \left[\sum_{i=1}^3 \left(\omega_i (\ln(f_i(T_1)) - \ln(S_i)) \frac{\partial}{\partial T_1} (\omega_i \ln(f_i(T_1))) \right) \right] = 0.$$

2.2.5. Least squares method for T_1 , T_2 , and ρ

Under the ideal conditions, MRI signal expression can be written as

$$S(TE_i, TR_i) = \rho f_i(T_1) g_i(T_2).$$

Let S_i represent the signal observed at (TE_i, TR_i) .

Consider

$$\phi(T_1, T_2, \rho) = \sum_{i=1}^n [S(TE_i, TR_i) - S_i]^2,$$

where $n(\geq 3)$ is the number of input images.

Now the minimization of above equation with respect to T_1 , T_2 , and ρ gives:

$$\frac{\partial \phi}{\partial T_1} = 0 \text{ implies } \sum_{i=1}^n [S(TE_i, TR_i) - S_i] f'_i(T_1) g_i(T_2) = 0 = F_1(T_1, T_2, \rho), \text{ say.}$$

$$\frac{\partial \phi}{\partial T_2} = 0 \text{ implies } \sum_{i=1}^n [S(TE_i, TR_i) - S_i] TE_i f_i(T_1) g'_i(T_2) = 0 = F_2(T_1, T_2, \rho), \text{ say.}$$

$$\frac{\partial \phi}{\partial \rho} = 0 \text{ implies } \sum_{i=1}^n [S(TE_i, TR_i) - S_i] f_i(T_1) g_i(T_2) = 0 = F_3(T_1, T_2, \rho), \text{ say.}$$

By Taylor series expansion of $F_i(i=1,2,3)$ around some initial approximation X_0 ($X = X_0 + \Delta X$) and neglecting 2nd and higher order terms,

$$\mathbf{A} \Delta \mathbf{X} = -\mathbf{F}_{X_0},$$

$$\text{where, } \mathbf{A} = \begin{pmatrix} \left(\frac{\partial F_1}{\partial T_1}\right)_{X_0} & \left(\frac{\partial F_1}{\partial T_2}\right)_{X_0} & \left(\frac{\partial F_1}{\partial \rho}\right)_{X_0} \\ \left(\frac{\partial F_2}{\partial T_1}\right)_{X_0} & \left(\frac{\partial F_2}{\partial T_2}\right)_{X_0} & \left(\frac{\partial F_2}{\partial \rho}\right)_{X_0} \\ \left(\frac{\partial F_3}{\partial T_1}\right)_{X_0} & \left(\frac{\partial F_3}{\partial T_2}\right)_{X_0} & \left(\frac{\partial F_3}{\partial \rho}\right)_{X_0} \end{pmatrix}, \Delta \mathbf{X} = \begin{pmatrix} \Delta T_1 \\ \Delta T_2 \\ \Delta \rho \end{pmatrix}, \text{ and } \mathbf{F} = \begin{pmatrix} F_1 \\ F_2 \\ F_3 \end{pmatrix}.$$

For initial approximations, one could use the method described in subsection 2.2.4 by considering any three consistent images. This method is different from the one mentioned in the subsection 2.2.3 which linearizes the system of equations first and then solves the overdetermined system (in the case of $n > 3$) by a least squares method.

2.2.6. Computables of Tissue Parameters and Field Susceptibility Maps

Signal intensity expression for most of the pulse sequences at a pixel can be expressed as

$$k\rho f(T_1)\exp(-TE/T_2) = S,$$

here we assume that the k is slowly varying and may arise due to gradient and signal receiver coil imperfections.

Taking logarithms on both sides yields

$$\ln k + \ln \rho + \ln f(T_1) - \frac{TE}{T_2} = \ln S. \quad (2.2.5)$$

Differentiating in the x direction gives

$$\frac{1}{\rho} \rho_x + \frac{f'(T_1)}{f(T_1)} T_{1x} + \frac{TE}{T_2^2} T_{2x} = \frac{1}{S} S_x,$$

where S_x is the rate of change in the signal, and ρ_x , T_{1x} , T_{2x} are rate of changes in proton density, T_1 , and T_2 respectively in x -direction and $f'(T_1)$ denotes $\partial f(T_1)/\partial T_1$.

S_x can be calculated either by central divided differences or by direct Fourier differentiation of the image. From the well known result in Fourier analysis we have

$$[f']^{\wedge}(\xi) = \int \exp(-i\xi x) f'(x) dx = -\int (-i\xi) \exp(-i\xi x) f(x) dx = i\xi \hat{f}(\xi).$$

Using this the derivative S_x could be computed.

In the case of divided differences,

$$S_x = \frac{S(x + \frac{h}{2}) - S(x - \frac{h}{2})}{h} + O(h^2),$$

h being the pixel spacing. The values at half pixel width can be obtained by doubling the image through *zero padding*.

Suppose we have four images of a cross-section with different TE's and TR's, we can write

$$\frac{1}{\rho} \rho_x + \frac{f'_i(T_1)}{f_i(T_1)} T_{1x} + \frac{TE_i}{T_2^2} T_{2x} = \frac{1}{S_i} S_{ix}, \quad i = 1, 2, 3, 4.$$

Subtracting first equation from second and third, we have

$$\left(\frac{f'_2(T_1)}{f_2(T_1)} - \frac{f'_1(T_1)}{f_1(T_1)} \right) T_{1x} + \frac{(TE_2 - TE_1)}{T_2^2} T_{2x} = \frac{S_{2x}}{S_2} - \frac{S_{1x}}{S_1},$$

and

$$\left(\frac{f'_3(T_1)}{f_3(T_1)} - \frac{f'_1(T_1)}{f_1(T_1)} \right) T_{1x} + \frac{(TE_3 - TE_1)}{T_2^2} T_{2x} = \frac{S_{3x}}{S_3} - \frac{S_{1x}}{S_1}.$$

From the above equation,

$$\frac{T_{2x}}{T_2^2} = \frac{1}{(TE_3 - TE_1)} \left\{ \left(\frac{S_{3x}}{S_3} - \frac{S_{1x}}{S_1} \right) - \left(\frac{f'_3(T_1)}{f_3(T_1)} - \frac{f'_1(T_1)}{f_1(T_1)} \right) T_{1x} \right\}. \quad (2.2.6)$$

Substituting this in the previous equation gives

$$\begin{aligned} & \left\{ \left(\frac{f'_2(T_1)}{f_2(T_1)} - \frac{f'_1(T_1)}{f_1(T_1)} \right) - \frac{TE_2 - TE_1}{TE_3 - TE_1} \left(\frac{f'_3(T_1)}{f_3(T_1)} - \frac{f'_1(T_1)}{f_1(T_1)} \right) \right\} T_{1x} \\ &= \left(\frac{S_{2x}}{S_2} - \frac{S_{1x}}{S_1} \right) - \frac{TE_2 - TE_1}{TE_3 - TE_1} \left(\frac{S_{3x}}{S_3} - \frac{S_{1x}}{S_1} \right). \end{aligned}$$

This can be written as

$$g(T_1)T_{1x} = D,$$

where

$$g(T_1) = \left\{ \left(\frac{f'_2(T_1)}{f_2(T_1)} - \frac{f'_1(T_1)}{f_1(T_1)} \right) - \left(\frac{TE_2 - TE_1}{TE_3 - TE_1} \right) \left(\frac{f'_3(T_1)}{f_3(T_1)} - \frac{f'_1(T_1)}{f_1(T_1)} \right) \right\} T_{1x},$$

and

$$D = \left(\frac{S_{2x}}{S_2} - \frac{S_{1x}}{S_1} \right) - \left(\frac{TE_2 - TE_1}{TE_3 - TE_1} \right) \left(\frac{S_{3x}}{S_3} - \frac{S_{1x}}{S_1} \right).$$

Similarly with another combination of images we can have

$$\tilde{g}(T_1)T_{1x} = \tilde{D},$$

where

$$\tilde{g}(T_1) = \left\{ \left(\frac{f'_2(T_1)}{f_2(T_1)} - \frac{f'_4(T_1)}{f_4(T_1)} \right) - \left(\frac{TE_2 - TE_4}{TE_3 - TE_4} \right) \left(\frac{f'_3(T_1)}{f_3(T_1)} - \frac{f'_4(T_1)}{f_4(T_1)} \right) \right\} T_{1x},$$

and

$$\tilde{D} = \left(\frac{S_{2x}}{S_2} - \frac{S_{4x}}{S_4} \right) - \left(\frac{TE_2 - TE_4}{TE_3 - TE_4} \right) \left(\frac{S_{3x}}{S_3} - \frac{S_{4x}}{S_4} \right).$$

From these two equations we can have

$$\frac{g(T_1)}{\tilde{g}(T_1)} = \frac{D}{\tilde{D}},$$

which can be used for the generation of *look-up table* for T_1 values. Using these values as initial approximations, the accuracy in the computed values could be improved iteratively by Newton's method.

Once T_1 is obtained, T_{1x} can be computed from any one of these two equations as

$$T_{1x} = \frac{D}{g(T_1)}.$$

Substituting these T_1 and T_{1x} values in the equation (2.2.6), T_{2x}/T_2^2 can be computed and using these values, the relative proton density variation, ρ_x/ρ , can be obtained. In the following system of equations formulation, we show that just increasing the number of independent images would not help in computing T_2 , T_{2x} , ρ , ρ_x , and proportionality constants.

Consider three consecutive pixels at $i-1$, i , $i+1$ in four given independent images. Without loss of generality we can take $k_1=1$ and the equation (2.2.5) for four images in this case can be written as

$$\begin{aligned} \ln \rho^j - \frac{TE_1}{T_2^j} &= \ln \left(\frac{S_1^j}{f_1^j(T_1)} \right), \\ \ln k_2 + \ln \rho^j - \frac{TE_2}{T_2^j} &= \ln \left(\frac{S_2^j}{f_2^j(T_1)} \right), \\ \ln k_3 + \ln \rho^j - \frac{TE_3}{T_2^j} &= \ln \left(\frac{S_3^j}{f_3^j(T_1)} \right), \\ \ln k_4 + \ln \rho^j - \frac{TE_4}{T_2^j} &= \ln \left(\frac{S_4^j}{f_4^j(T_1)} \right). \end{aligned}$$

where ρ^j , T_2^j , $f^j(T_1)$, and S^j represent the proton density, T_2 relaxation time, function of T_1 , and acquired signal at the location j in all four images and $j = i-1, i, i+1$. These equations can be written in the matrix-vector notation as follows:

$$\begin{pmatrix} 0 & 0 & 0 & 1 & -TE_1 & 0 & 0 & 0 & 0 \\ 1 & 0 & 0 & 1 & -TE_2 & 0 & 0 & 0 & 0 \\ 0 & 1 & 0 & 1 & -TE_3 & 0 & 0 & 0 & 0 \\ 0 & 0 & 1 & 1 & -TE_4 & 0 & 0 & 0 & 0 \\ 0 & 0 & 0 & 0 & 0 & 1 & -TE_1 & 0 & 0 \\ 1 & 0 & 0 & 0 & 0 & 1 & -TE_2 & 0 & 0 \\ 0 & 1 & 0 & 0 & 0 & 1 & -TE_3 & 0 & 0 \\ 0 & 0 & 1 & 0 & 0 & 1 & -TE_4 & 0 & 0 \\ 0 & 0 & 0 & 0 & 0 & 0 & 0 & 1 & -TE_1 \\ 1 & 0 & 0 & 0 & 0 & 0 & 0 & 1 & -TE_2 \\ 0 & 1 & 0 & 0 & 0 & 0 & 0 & 1 & -TE_3 \\ 0 & 0 & 1 & 0 & 0 & 0 & 0 & 1 & -TE_4 \end{pmatrix} \begin{pmatrix} \ln k_2 \\ \ln k_3 \\ \ln k_4 \\ \ln \rho^{i-1} \\ 1/T_2^{i-1} \\ \ln \rho^i \\ 1/T_2^i \\ \ln \rho^{i+1} \\ 1/T_2^{i+1} \end{pmatrix} = \begin{pmatrix} \ln \left(S_1^{i-1} / f_1^{i-1}(T_1) \right) \\ \ln \left(S_2^{i-1} / f_2^{i-1}(T_1) \right) \\ \ln \left(S_3^{i-1} / f_3^{i-1}(T_1) \right) \\ \ln \left(S_4^{i-1} / f_4^{i-1}(T_1) \right) \\ \ln \left(S_1^i / f_1^i(T_1) \right) \\ \ln \left(S_2^i / f_2^i(T_1) \right) \\ \ln \left(S_3^i / f_3^i(T_1) \right) \\ \ln \left(S_4^i / f_4^i(T_1) \right) \\ \ln \left(S_1^{i+1} / f_1^{i+1}(T_1) \right) \\ \ln \left(S_2^{i+1} / f_2^{i+1}(T_1) \right) \\ \ln \left(S_3^{i+1} / f_3^{i+1}(T_1) \right) \\ \ln \left(S_4^{i+1} / f_4^{i+1}(T_1) \right) \end{pmatrix}$$

By the following elementary row and column operations one can see that the column rank of the above overdetermined system is less than nine which is the number of unknowns to be determined.

$$\begin{array}{ccccc}
 R_2 - R_1 & R_6 - R_5 & R_{10} - R_9 & C_5 + TE_1 C_4 & C_5 + (TE_2 - TE_1)C_1 \\
 R_3 - R_1 & R_7 - R_5 & R_{11} - R_9 & C_7 + TE_1 C_6 & C_5 + (TE_3 - TE_1)C_2 \\
 R_4 - R_1 & R_8 - R_5 & R_{12} - R_9 & C_9 + TE_1 C_8 & C_5 + (TE_4 - TE_1)C_3 \\
 \Rightarrow & C_5 + C_7 + C_9 = 0.
 \end{array}$$

Therefore,

- (i) the rank is not nine,
- (ii) if any two of TE_1, TE_2, TE_3, TE_4 are distinct, then the rank is eight, and
- (iii) if TE 's are all equal, the rank is six.

Suppose n images are given, then the coefficient matrix size will be

$$3n \times ((n-1)+6) = 3n \times (n+5).$$

Applying the following elementary row and column operations on the quotient matrix,

$$\begin{array}{ccccc}
 R_2 - R_1 & R_{n+2} - R_{n+1} & R_{2n+2} - R_{2n+1} & C_{n+1} + TE_1 C_n & C_{n+1} + (TE_2 - TE_1)C_1 \\
 R_3 - R_1 & R_{n+3} - R_{n+1} & R_{2n+3} - R_{2n+1} & C_{n+3} + TE_1 C_{n+2} & C_{n+1} + (TE_3 - TE_1)C_2 \\
 \vdots & \vdots & \vdots & C_{n+5} + TE_1 C_{n+4} & \vdots \\
 R_n - R_1 & R_{2n} - R_{n+1} & R_{3n} - R_{2n+1} & & C_{n+1} + (TE_n - TE_1)C_{n-1} \\
 \Rightarrow & C_{n+1} + C_{n+3} + C_{n+5} = 0.
 \end{array}$$

So, rank is less than $(n+5)$, which is the number of variables to be determined. Thus, just by increasing number of input images and with no conditions on TE 's, TR 's would not help in computing T_1, ρ , and the factors k_2, \dots, k_n .

However, we assume that two of these images have same proportionality constants. This assumption is meaningful because, two images from a double echo sequence which are obtained under the same experimental conditions except for different echo times may have same proportionality constants. By taking ratio of these two, T_2 can be computed as

$$T_2 = (TE_2 - TE_1) / \ln \left(\frac{S_1 f_2(T_1)}{S_2 f_1(T_1)} \right).$$

T_1 values used here are computed from above formulation which are free from the effect of proportionality constants. Substituting T_1 and T_2 in the intensity expression in which proportionality constant assumed as one, ρ can be computed. Then all other parameters

If whole image is multiplied with a single constant (say, k_3) the following least squares estimation could be used for evaluating the constant after computing T_1 , T_2 and ρ as above.

$$\min_{k_3} \sum_{i=1}^N [k_3 - \tilde{S}_{3i}]^2 = \phi \text{ (say),}$$

where $\tilde{S}_3 = S_3 / (f_3(T_1) \exp(-TE_3/T_2) \rho)$, and N is the total number of pixels in the image. $\frac{\partial \phi}{\partial k_3} = 0$ implies $\sum_{i=1}^N [k_3 - \tilde{S}_{3i}] = 0$. That is $k_3 = \frac{1}{N} \sum_{i=1}^N \tilde{S}_{3i}$, which is the average of the constants computed at each pixel.

For simulation experiments, four spin echo images are synthesized with TR/TE's as 2200/15, 1550/20, 4650/12, and 2200/120 ms. Two images are taken with same TR and different TE's. Table 2.10 shows the % relative errors in the computed T_1 , T_2 , and ρ values due to the approximations when divided differences are used for evaluating derivatives. Figure 2.7 shows the maps of T_{1x} , T_{2x}/T_2^2 , ρ_x/ρ and their histogram equalized maps.

	T₁ values	T₂ values	PD values
% L ₁ error	5.586293	0.091141	1.895488
% L ₂ error	16.126315	5.224453	9.693125
% L _∞ error	86.1	50.0	86.525781

Table 2.10 : % Errors in computed T_1 , T_2 , and PD values when derivatives are evaluated by divided differences.

One of the images is multiplied with a constant 1.1 and parameter values are computed using the method discussed in subsection 2.2.4. Figure 2.8 shows the parameter maps computed without and with constant multiplication. Errors in the computed T_1 , T_2 , and ρ values are tabulated in Table 2.11. But, computation of parameters with the present method did not show any differences in the parameters when computed with and without constant multiplication. This is clear from the formulation.

K = 1.1	T₁ values	T₂ values	PD values
% L ₁ error	29.9369	10.4630	16.8470
% L ₂ error	26.6413	33.4192	17.0726
% L _∞ error	25.3749	85.8198	34.0824

Table 2. 11: % Errors in computed T_1 , T_2 , and PD values with one of the images multiplied with

To create small variations in images, each image is multiplied with varying factors. These factors are generated from the following computational procedure with different k values.

```

do  $i = 0$  to  $N$ 
  temp1 =  $k (i - N/2)^2 / N^2$ 
  do  $j = 0$  to  $N$ 
    temp2 =  $k (j - N/2)^2 / N^2$ 
    factor =  $1 + 1/(1 + \text{temp1} + \text{temp2})$ 
  end do
end do

```

For the present study, we have taken $N = 512$. For different values of k , one can generate different factor maps.

Figure 2.9 shows the maps of proportionality constants computed as above with $k = 1, 2, 3$, and their histogram equalizations. As these factors are small, each input image is multiplied with $(1 + \text{factor})$. Tissue parameters are computed in the presence of these factors with $k_1 = k_4 = 1$, and $k_2 = 2$ & $k_3 = 3$. Errors in the computed parameters are shown in Table 2.12.

	T₁ values	T₂ values	PD values
% L ₁ error	0.084175	0.018334	0.192346
% L ₂ error	0.515941	0.050305	0.223677
% L _∞ error	26.13333	0.328222	8.951550

Table 2.12 : % Errors in computed T₁, T₂, and PD values using images multiplied with factor for different k values

Table 2.13 shows the errors in the estimation of varying multiplication factor (for k_2 & k_3). These high errors due to the approximated derivative evaluation and also, these multiplication factors are not locally constant which the present formulation assumes.

	Factor for $k=2$	Factor for $k=3$
% L ₁ error	39.985179	47.348269
% L ₂ error	58.868919	62.736832
% L _∞ error	79.385237	84.286345

Table 2.13: : % Errors in estimation of multiplication factors

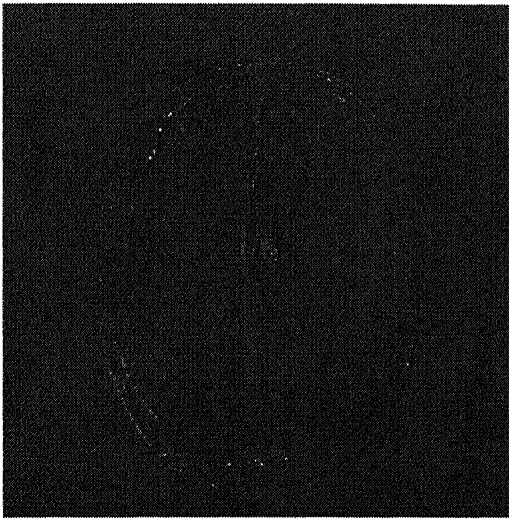
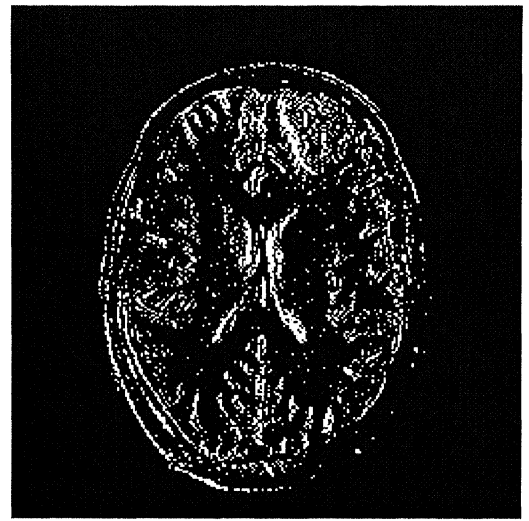
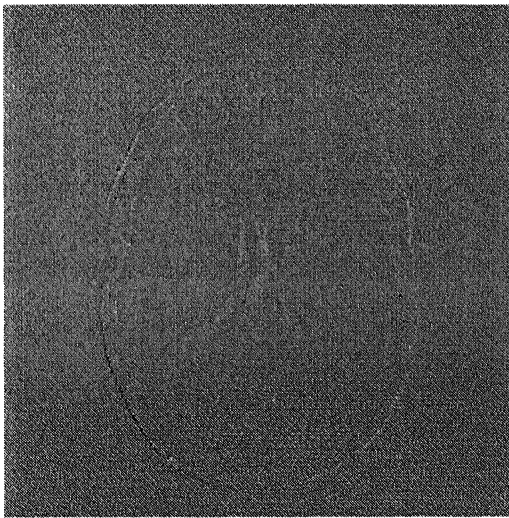
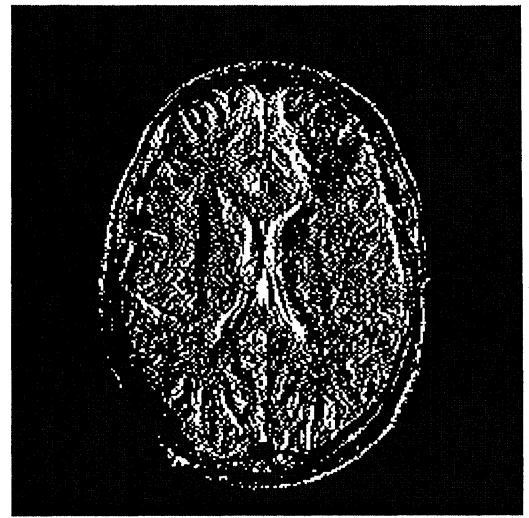
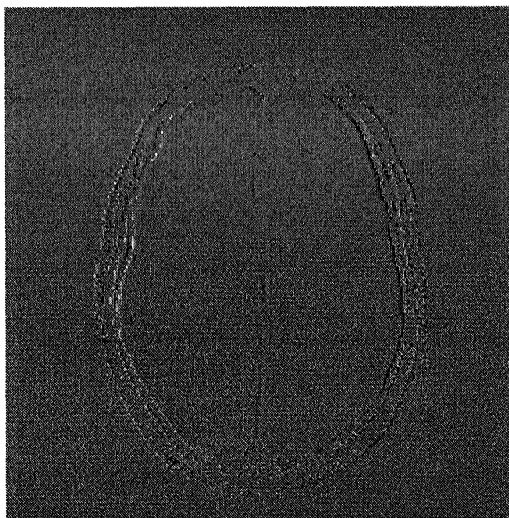
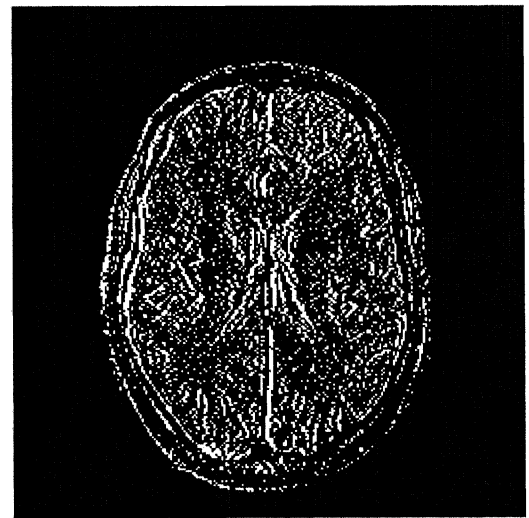
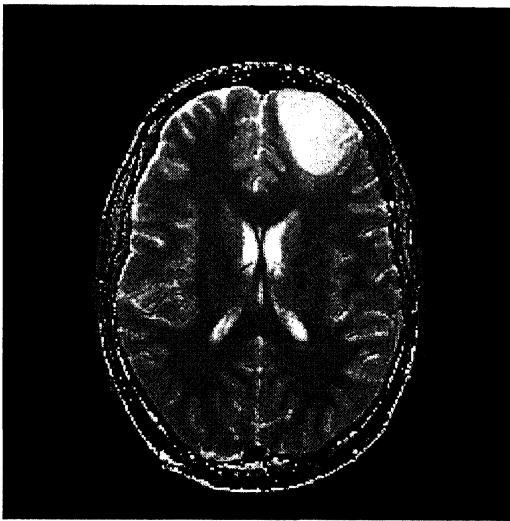
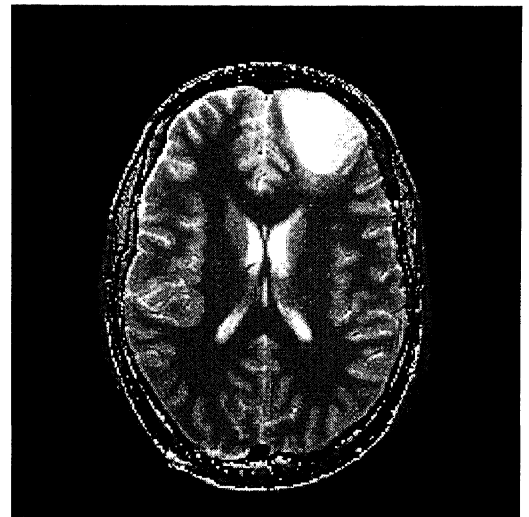
 T_{1x}  T_{1x} histogram equalization T_{2x}/T_2^2  T_{2x}/T_2^2 histogram equalization ρ_x/ρ  ρ_x/ρ histogram equalization

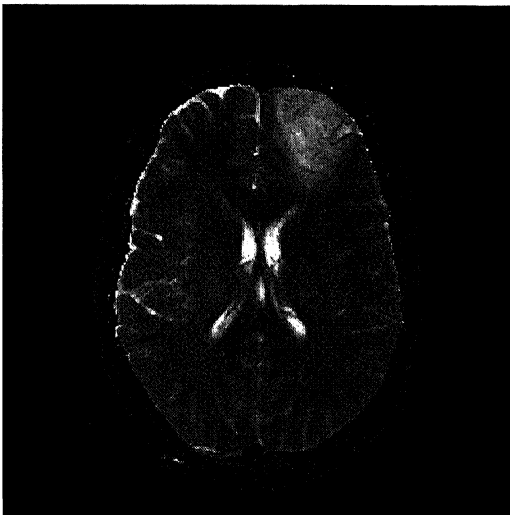
Figure 2.7: Maps of T_{1x} , T_{2x}/T_2^2 , ρ_x/ρ and their histogram equalizations



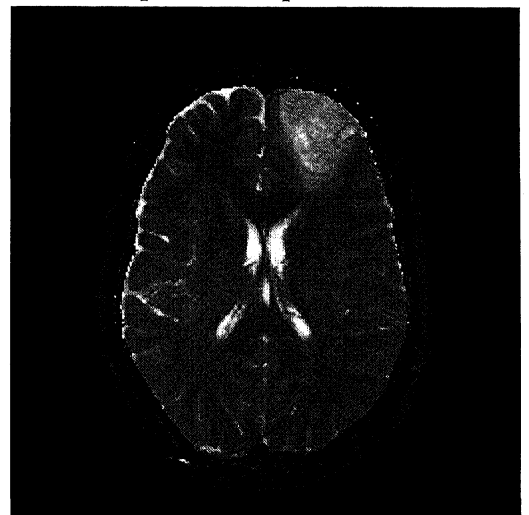
T₁ map without multiplication factor



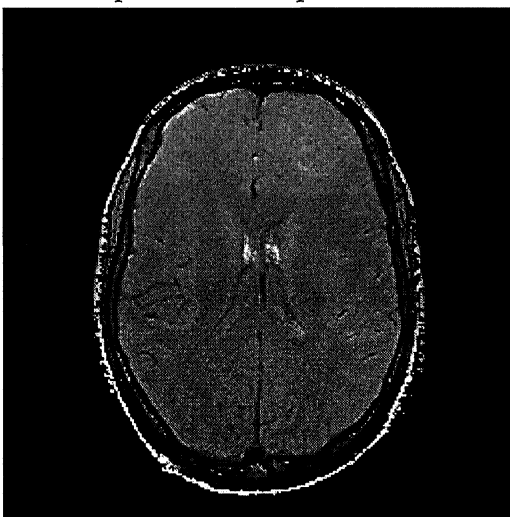
T₁ map with multiplication factor



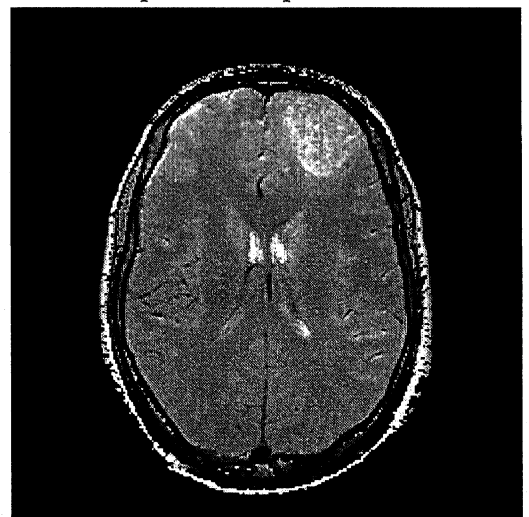
T₂ map without multiplication factor



T₂ map with multiplication factor

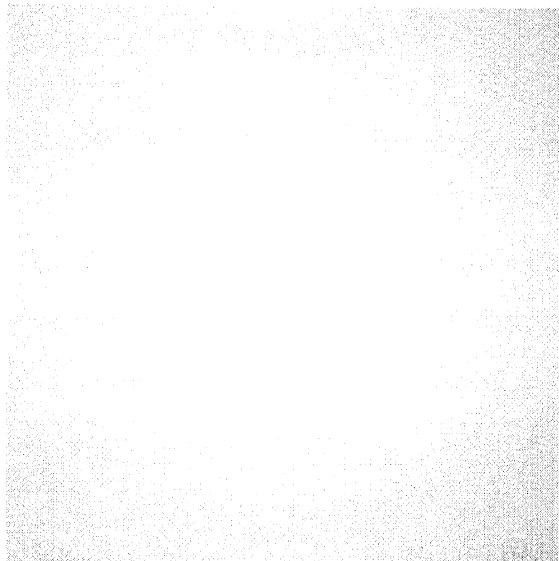


PD map without multiplication factor

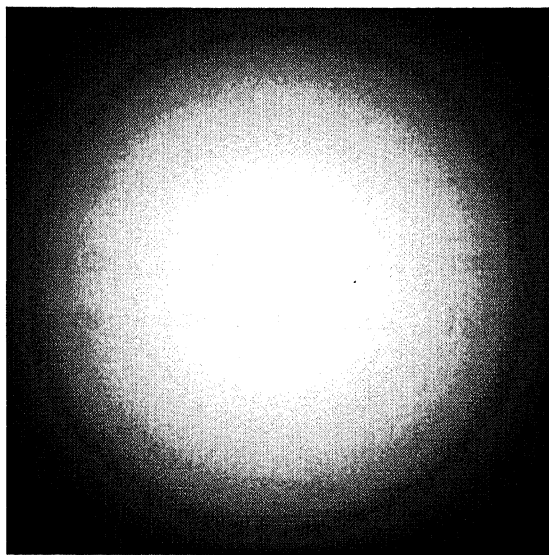


PD map with multiplication factor

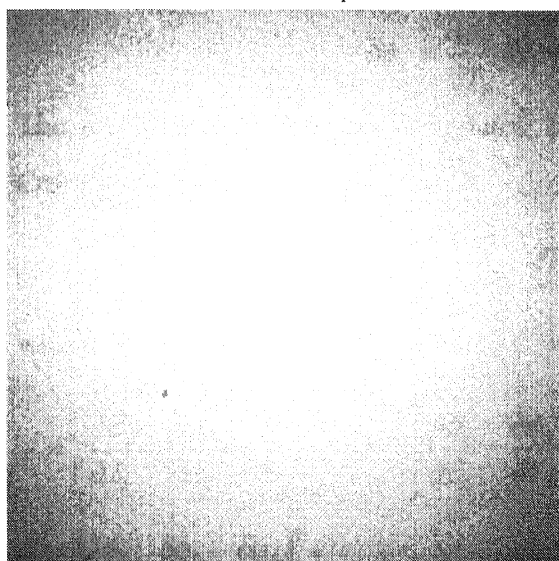
Figure 2.8: 1st column: Computed parameters from three weighted images. 2nd column: Computed parameters from the same images except for one image is multiplied with 1.1



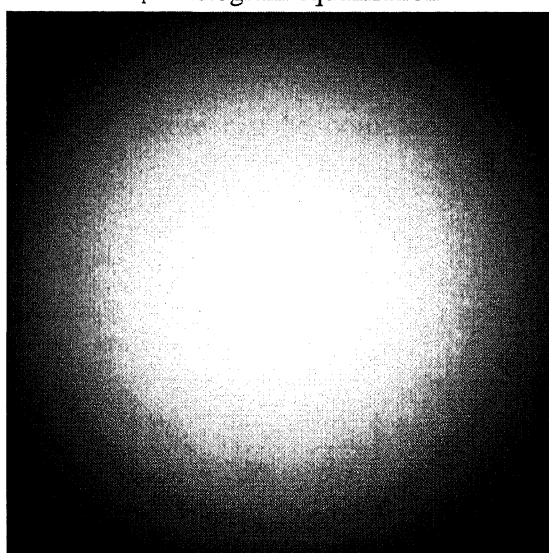
Factor for $K_1=1$



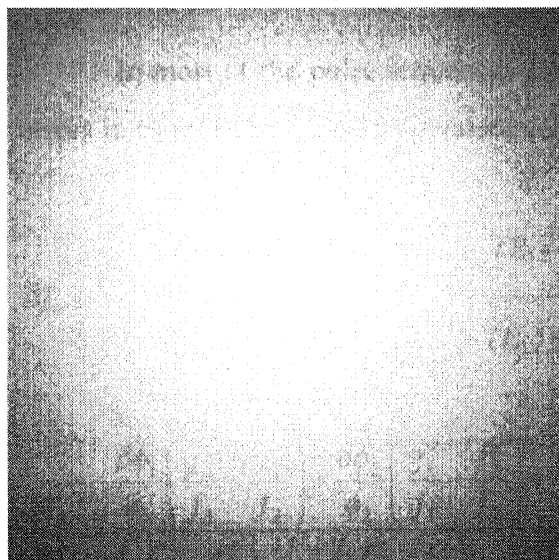
K_1 - histogram equalization



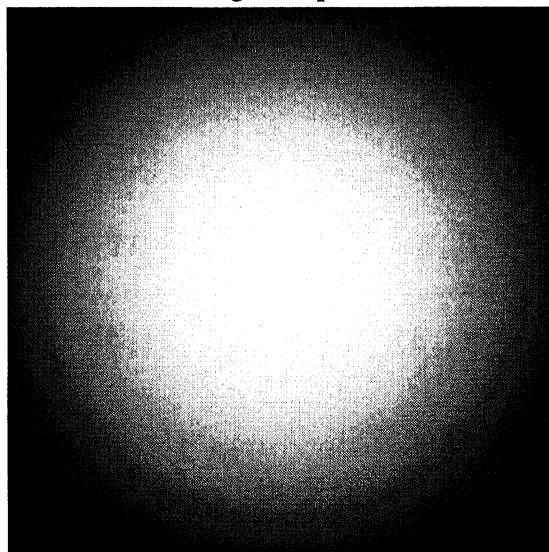
Factor for $K_2 = 2$



K_2 - histogram equalization



Factor for $K_3 = 3$



K_3 histogram equalization

Figure 2.9: Different factors and their histogram equalized maps used as simulated varying field maps

2.3. Error Propagation in Tissue Parameters Estimation

MRI signal expression can be written as

$$\phi(T_1, T_2, \rho) = \rho f(T_1) g(T_2).$$

The error propagation through these equations into the estimated T_1 , T_2 , and ρ can be found from the total differential of function ϕ of three independent variables T_1 , T_2 , and ρ and when applied to three sequences gives

$$\begin{aligned}\delta\phi_1 &= \frac{\partial\phi_1}{\partial T_1} \delta T_1 + \frac{\partial\phi_1}{\partial T_2} \delta T_2 + \frac{\partial\phi_1}{\partial \rho} \delta \rho, \\ \delta\phi_2 &= \frac{\partial\phi_2}{\partial T_1} \delta T_1 + \frac{\partial\phi_2}{\partial T_2} \delta T_2 + \frac{\partial\phi_2}{\partial \rho} \delta \rho, \\ \delta\phi_3 &= \frac{\partial\phi_3}{\partial T_1} \delta T_1 + \frac{\partial\phi_3}{\partial T_2} \delta T_2 + \frac{\partial\phi_3}{\partial \rho} \delta \rho.\end{aligned}$$

The errors in ϕ_i affects the computed T_1 , T_2 , and ρ . These can be computed using Cramer's rule as

$$\delta T_1 = \frac{A}{D}, \quad \delta T_2 = \frac{B}{D}, \quad \delta \rho = \frac{C}{D},$$

where $A = \begin{vmatrix} d & b & c \end{vmatrix}$, $B = \begin{vmatrix} a & d & c \end{vmatrix}$, $C = \begin{vmatrix} a & b & d \end{vmatrix}$, and $D = \begin{vmatrix} a & b & c \end{vmatrix}$, with

$$\begin{aligned}a &= \begin{bmatrix} \frac{\partial\phi_1}{\partial T_1} & \frac{\partial\phi_2}{\partial T_1} & \frac{\partial\phi_3}{\partial T_1} \end{bmatrix}^T, \quad b = \begin{bmatrix} \frac{\partial\phi_1}{\partial T_2} & \frac{\partial\phi_2}{\partial T_2} & \frac{\partial\phi_3}{\partial T_2} \end{bmatrix}^T, \quad c = \begin{bmatrix} \frac{\partial\phi_1}{\partial \rho} & \frac{\partial\phi_2}{\partial \rho} & \frac{\partial\phi_3}{\partial \rho} \end{bmatrix}^T, \text{ and} \\ d &= \begin{bmatrix} \delta\phi_1 & \delta\phi_2 & \delta\phi_3 \end{bmatrix}^T.\end{aligned}$$

In most of the pulse sequences $g(T_2)$ takes the form $\exp(-TE/T_2)$. Using this, the errors in estimated T_1 , T_2 , and ρ values can be expressed as

$$\delta T_1 = \frac{\frac{\delta\phi_1}{\phi_1}(TE_2 - TE_3) + \frac{\delta\phi_2}{\phi_2}(TE_3 - TE_1) + \frac{\delta\phi_3}{\phi_3}(TE_1 - TE_2)}{\frac{f'_1}{f_1}(TE_2 - TE_3) + \frac{f'_2}{f_2}(TE_3 - TE_1) + \frac{f'_3}{f_3}(TE_1 - TE_2)} = \frac{\sum_{i=1}^3 \frac{\delta\phi_i}{\phi_i}(TE_+ - TE_{++})}{\sum_{i=1}^3 \frac{f'_i}{f_i}(TE_+ - TE_{++})}$$

$$\frac{\delta T_2}{T_2^2} = \frac{\frac{\delta\phi_1}{\phi_1} \left(\frac{f'_3}{f_3} - \frac{f'_2}{f_2} \right) + \frac{\delta\phi_2}{\phi_2} \left(\frac{f'_1}{f_1} - \frac{f'_3}{f_3} \right) + \frac{\delta\phi_3}{\phi_3} \left(\frac{f'_2}{f_2} - \frac{f'_1}{f_1} \right)}{\left(\frac{f'_3}{f_3} - \frac{f'_2}{f_2} \right) TE_1 + \left(\frac{f'_1}{f_1} - \frac{f'_3}{f_3} \right) TE_2 + \left(\frac{f'_2}{f_2} - \frac{f'_1}{f_1} \right) TE_3} = \frac{\sum_{i=1}^3 \frac{\delta\phi_i}{\phi_i} \Delta_i}{\sum_{i=1}^3 \Delta_i TE_i},$$

where $\Delta_i = \frac{f'_{i++}}{f_{i++}} - \frac{f'_{i+}}{f_{i+}}$, and

$$\frac{\delta\rho}{\rho} = \frac{\frac{\delta\phi_1}{\phi_1} \left(\frac{f'_2}{f_2} TE_3 - \frac{f'_3}{f_3} TE_2 \right) + \frac{\delta\phi_2}{\phi_2} \left(\frac{f'_3}{f_3} TE_1 - \frac{f'_1}{f_1} TE_3 \right) + \frac{\delta\phi_3}{\phi_3} \left(\frac{f'_1}{f_1} TE_2 - \frac{f'_2}{f_2} TE_1 \right)}{\frac{f'_1}{f_1} (TE_2 - TE_3) + \frac{f'_2}{f_2} (TE_3 - TE_2) + \frac{f'_3}{f_3} (TE_1 - TE_2)}$$

$$= \frac{\sum_{i=1}^3 \frac{\delta\phi_i}{\phi_i} \left(\frac{f'_{i+}}{f_{i+}} TE_{i++} - \frac{f'_{i++}}{f_{i++}} TE_{i+} \right)}{\sum_{i=1}^3 \frac{f'_i}{f_i} (TE_{i+} - TE_{i++})}.$$

In all the expressions above,

when

$$\begin{aligned} i = 1, \quad i_+ = 2, i_{++} = 3; \\ i = 2, \quad i_+ = 3, i_{++} = 1; \\ i = 3, \quad i_+ = 1, i_{++} = 2. \end{aligned}$$

2.3.1. Errors due to Bit Reduction

The sensitivity of the tissue parameters computations are checked numerically by calculating tissue parameters from images with different depths. The depth (number of bits used to store image information) is reduced at each level by one bit. Images in the Figures 2.10-2.12 are obtained from T_1 , T_2 , and PD weighted spin echo images of a normal sample by reducing bits successively from them. Visually these images do not show any significant changes up to five bits reduction. In the seven bit reduction deterioration is clear. Figures 2.13-2.15 are the corresponding tissue parameter maps computed with the method described in the subsection 2.2.4 using respective images from Figures 2.10-2.12. Tables 2.14-2.16 show the errors in weighted images due to reduction of bits. The sensitivity of tissue parameters calculation on the depth of images used is shown in Tables 2.17-2.19. The computed errors are:

$$\text{Average } L_1 = \frac{1}{N} \sum_1^N |f - f_{trunc}|, \quad \text{Average } L_2 = \left(\frac{1}{N} \sum_1^N |f - f_{trunc}|^2 \right)^{1/2},$$

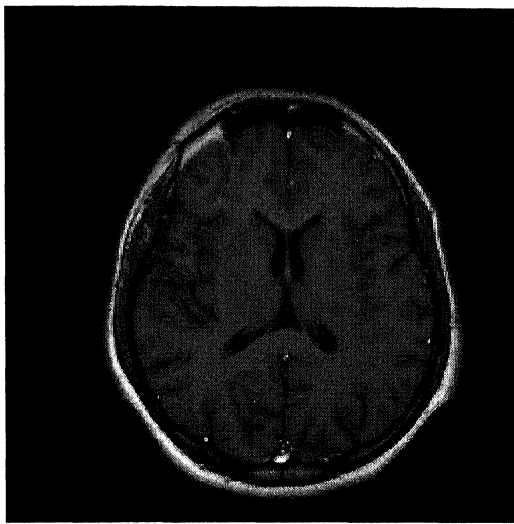
$$L_\infty = \max_N |f - f_{recon}|, \quad \text{Average Relative } L_1 = \frac{1}{N} \sum_1^N \frac{|f - f_{trunc}|}{|f|}, \text{ and}$$

$$\text{Average Relative } L_2 = \left(\frac{1}{N} \sum_1^N \frac{|f - f_{trunc}|^2}{|f|^2} \right)^{1/2}.$$

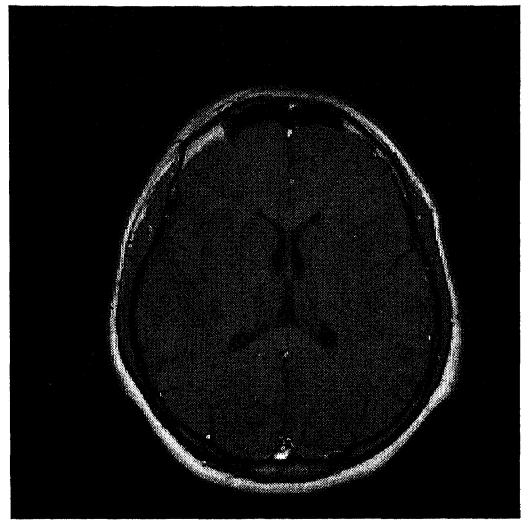
The computed average L_1 , L_2 , and L_∞ errors in T_1 , T_2 , and PD weighted images due to reduction of bits is shown in Graphs 2.4(a)-2.4(c) respectively. In all the three types of errors, these graphs reveal small amount of errors up to four bits reduction. In all three weighted images error magnitudes are almost same up to five bits reduction. Five bits onwards PD weighted image has shown more error compared to T_1 weighted image. T_2 weighted image has slightly less errors compared to PD weighted image but has more errors with respect to T_1 weighted image.

Graphs 2.5(a)-2.5(c) show the average L_1 , L_2 , and L_∞ errors respectively in T_1 , T_2 , and PD maps computed from the successively bits reduced weighted images. In all the three types of errors T_2 map has shown relatively low errors compared to errors in T_1 and PD maps.

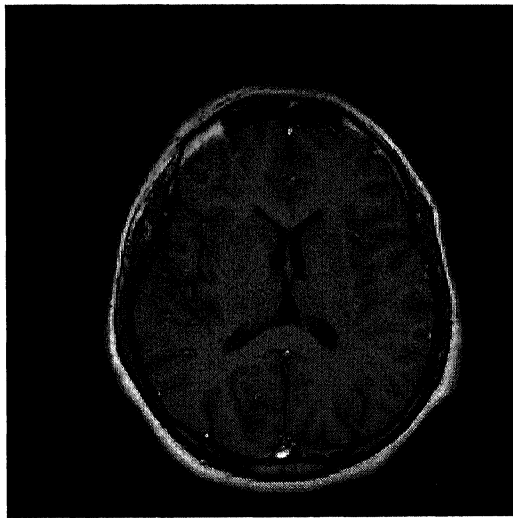
Following R.E. Hendrick (1999), the standard average T_1 values of methomoglobin, white, lower cystic fluid, gray and CSF are 460, 510, 720, 760, 2650 ms. The corresponding T_2 values are 106, 67, 43, 77, 280. From Tables 2.17 and 2.18, the removal of five bits onwards could induce average errors of magnitude around 94 in T_1 and around 3 in T_2 , which mean that there would be problems in differentiating methomoglobin and white matter as well as lower cystic fluid and gray matter. Similarly on the T_2 map the white and the gray matter regions could get mixed up. The corresponding average L_2 errors were as high as 8.5 and 269.7 for T_2 and T_1 respectively. Thus a depth of the images below 12 bit which is the current DICOM standard would severely affect the use of the parameters in relaxometry studies. Our recommendation would be to compute the gray values directly from the machine data and not to rely on the machine stored images, if the relaxometry study is to be conducted.



Original



Three bits



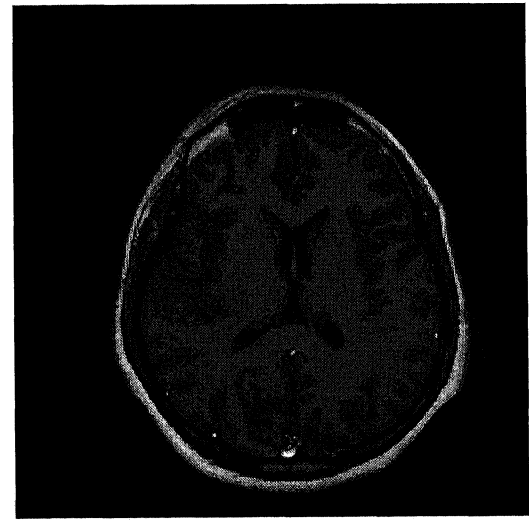
Four bits



Five bits

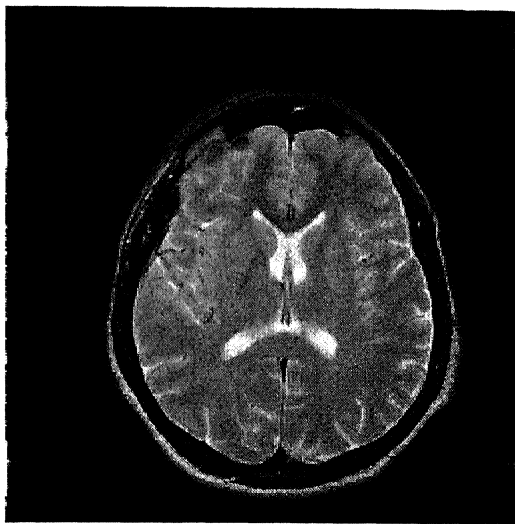


Six bits

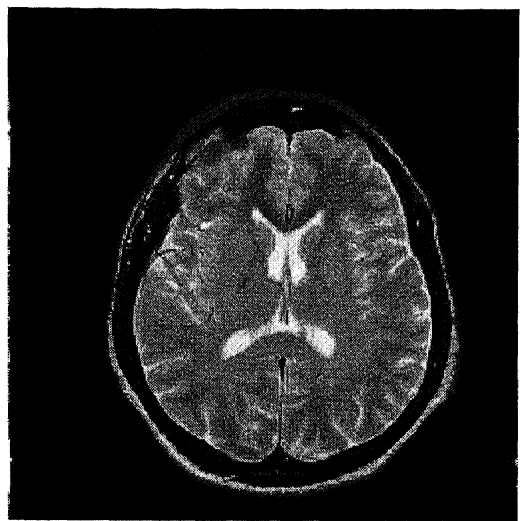


Seven bits

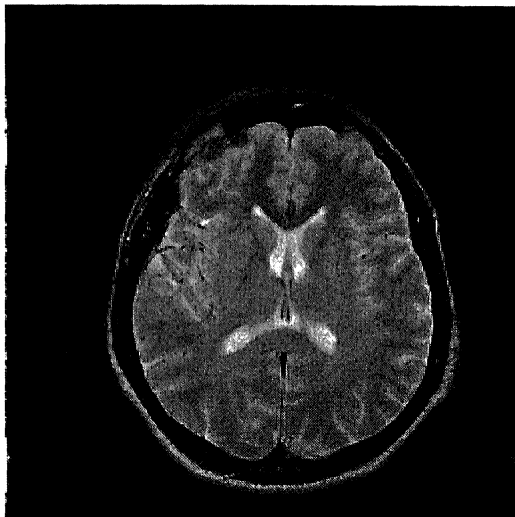
Figure 2.10: T₁ weighted image with different number of bits removed



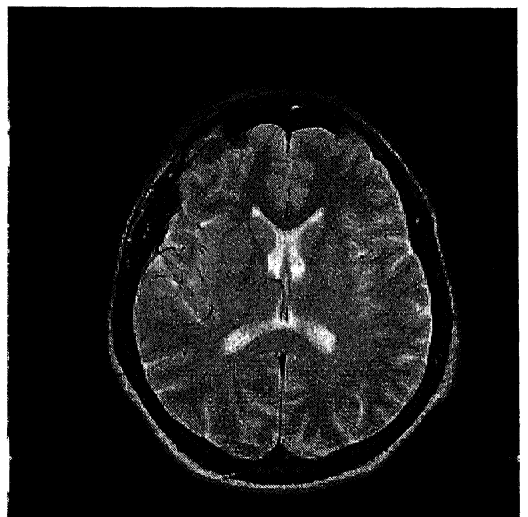
Original



Three bits



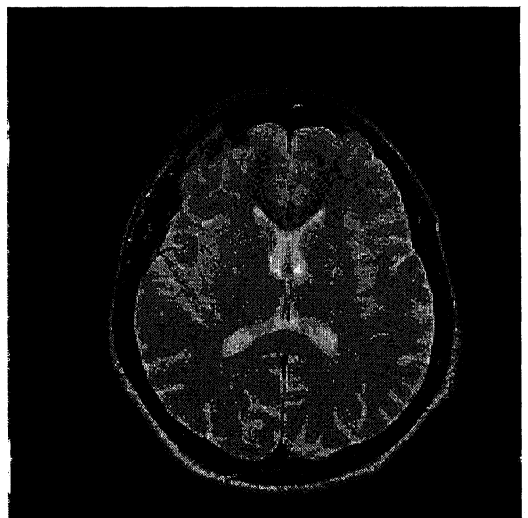
Four bits



Five bits

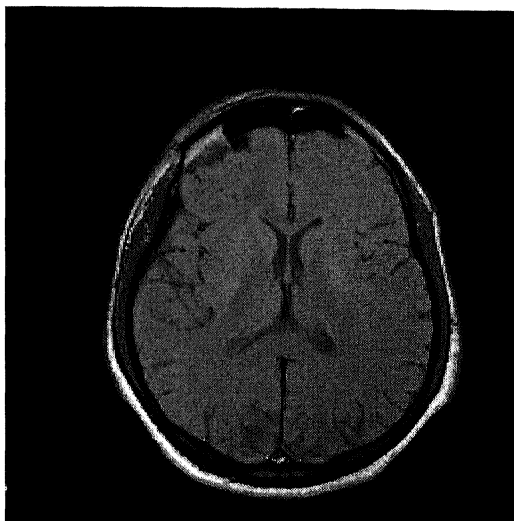


Six bits

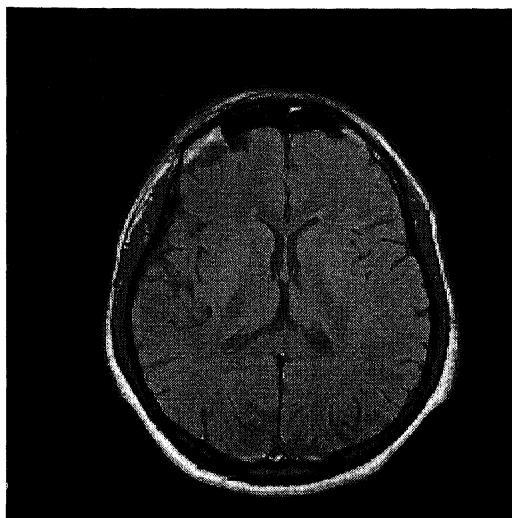


Seven bits

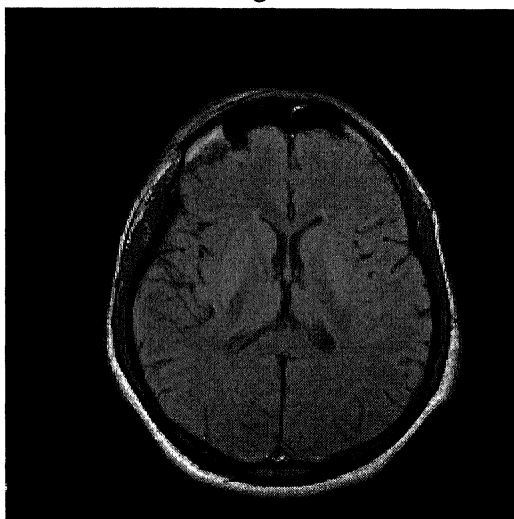
Figure 2.11: T₂ weighted image with different number of bits removed



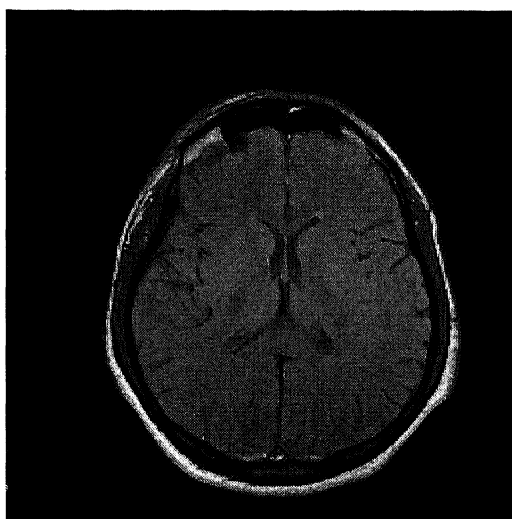
Original



Three bits removed



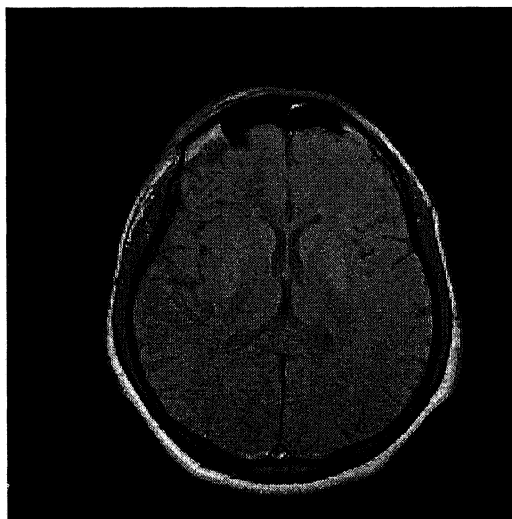
Four bits removed



Five bits removed

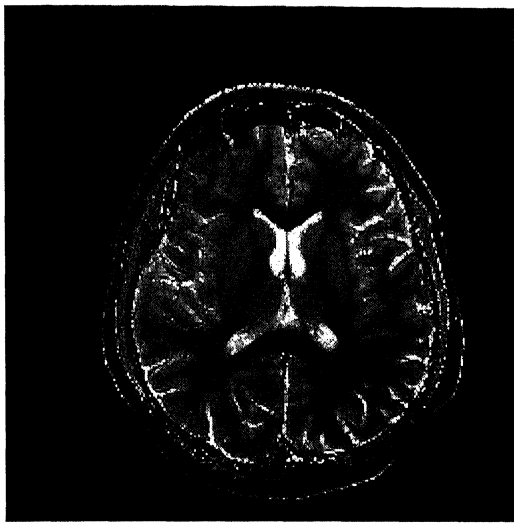


Six bits removed

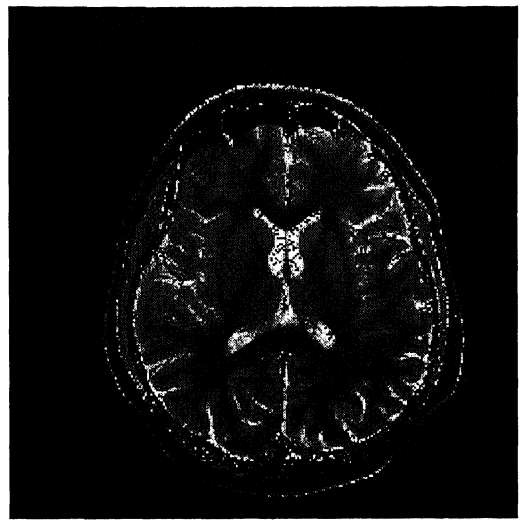


Seven bits removed

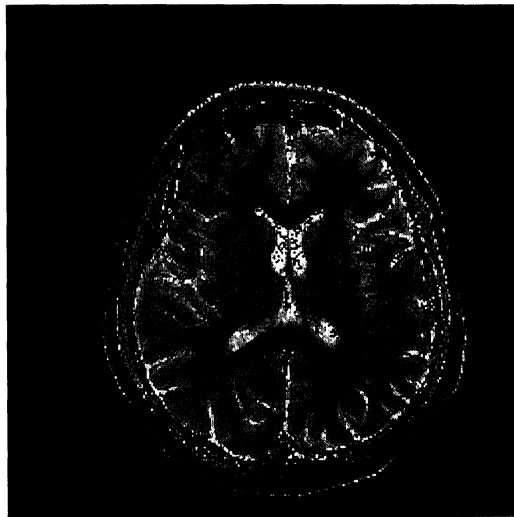
Figure 2.12: PD weighted image with different number of bits removed



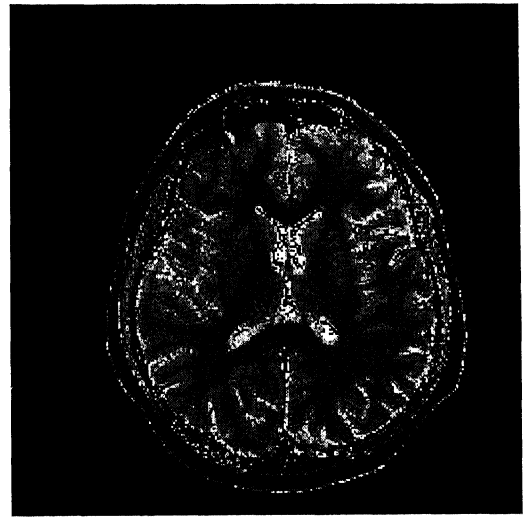
Original



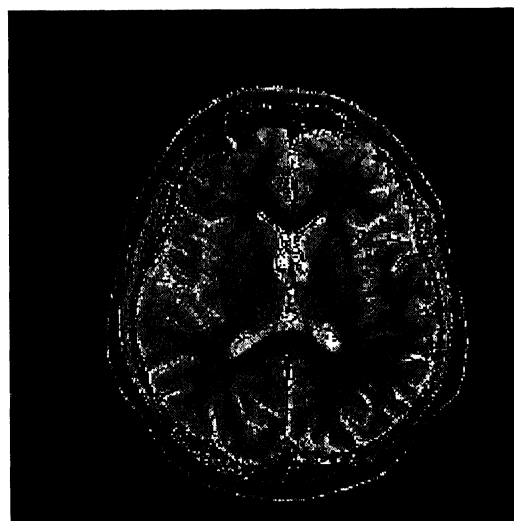
Three bits



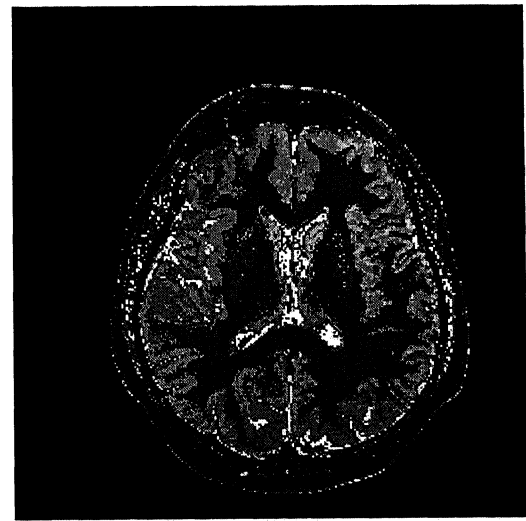
Four bits



Five bits

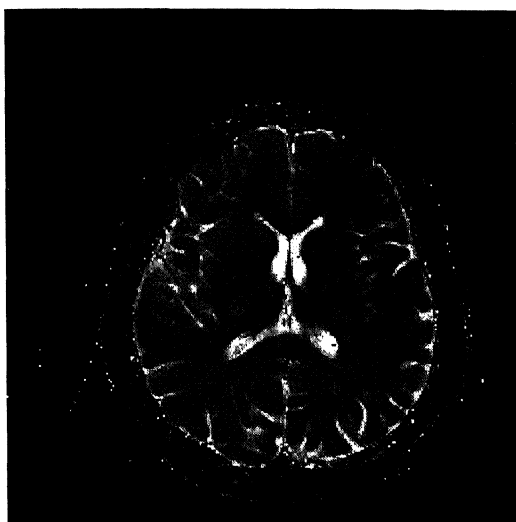


Six bits

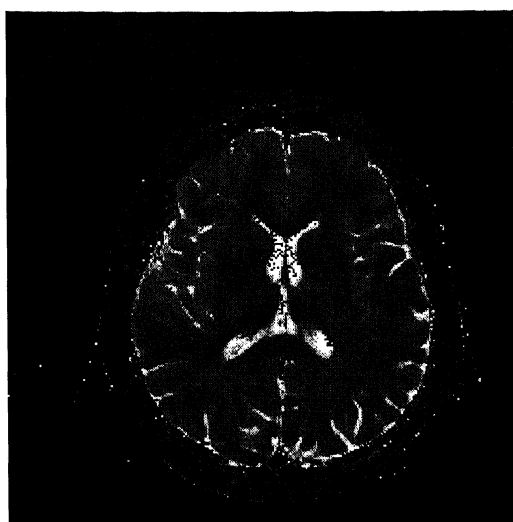


Seven bits

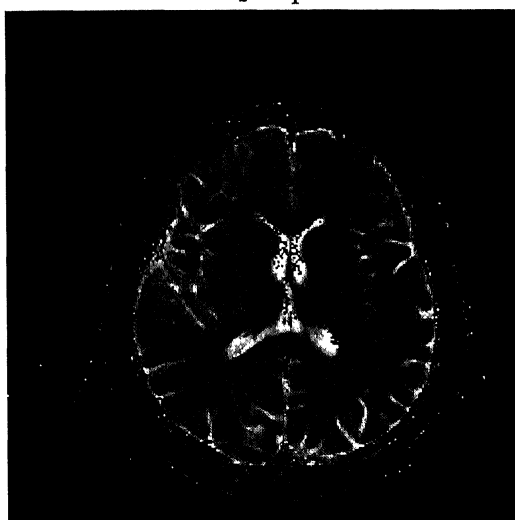
Figure 2.13: T_1 map computed from different number of bits removed weighted images



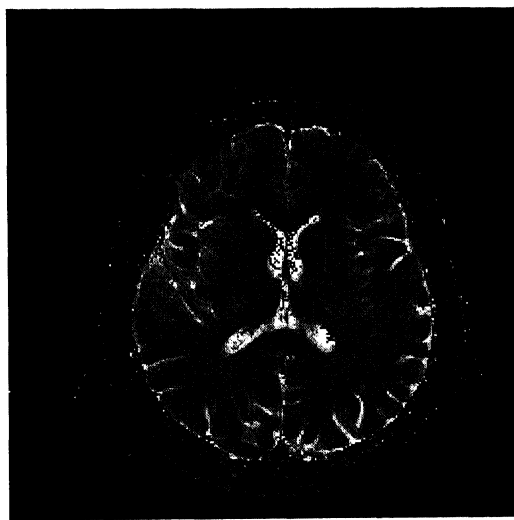
T_2 map



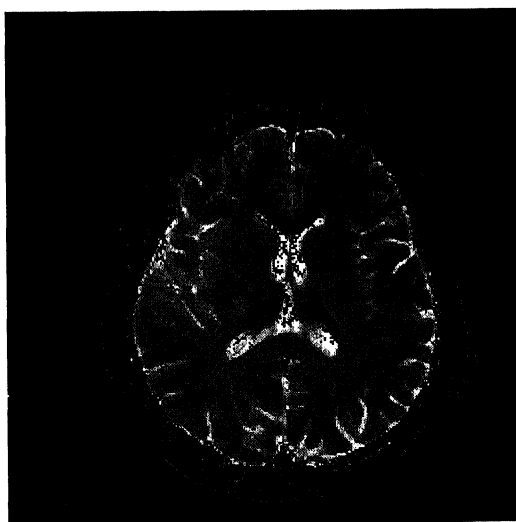
Three bits



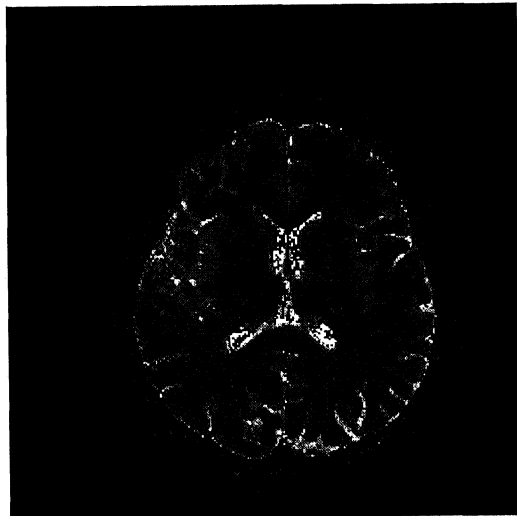
Four bits



Five bits

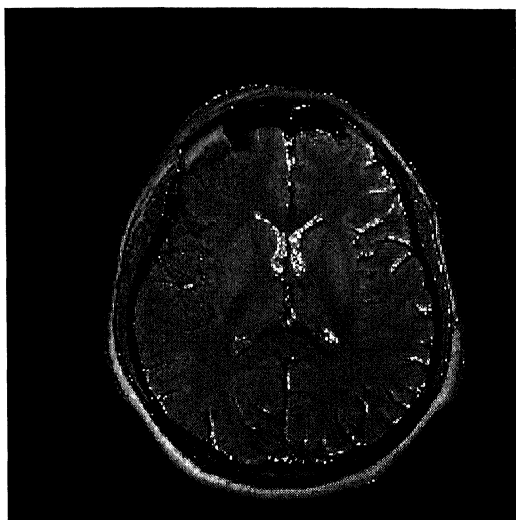


Six bits

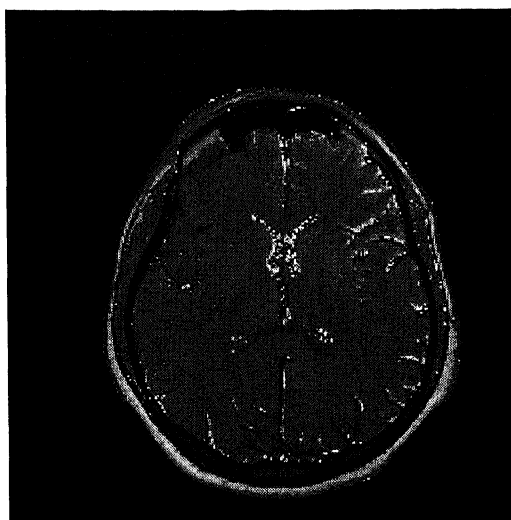


Seven bits

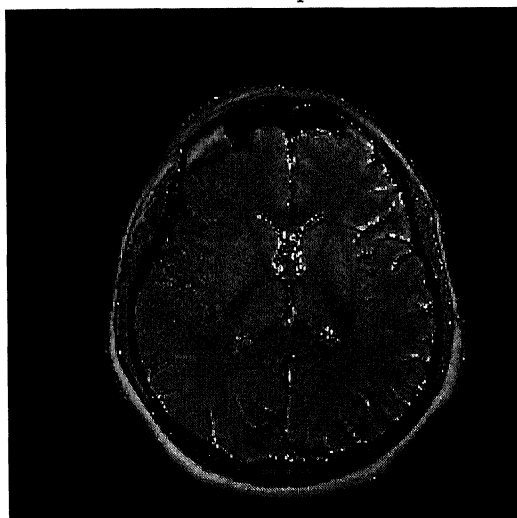
Figure 2.14: T_2 map computed from different number of bits removed weighted images



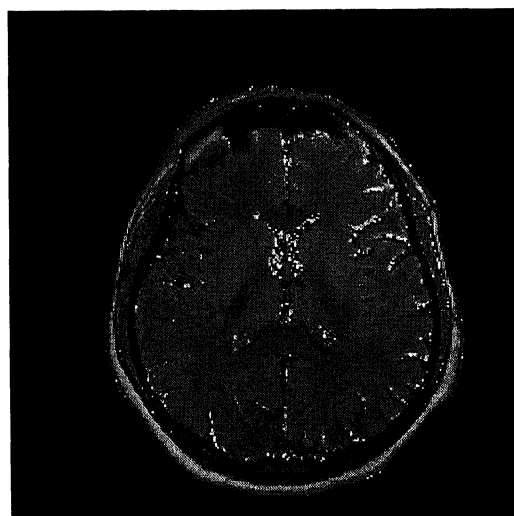
PD map



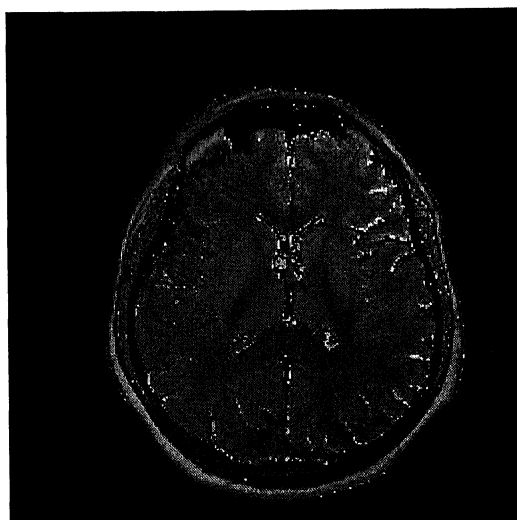
Three bits



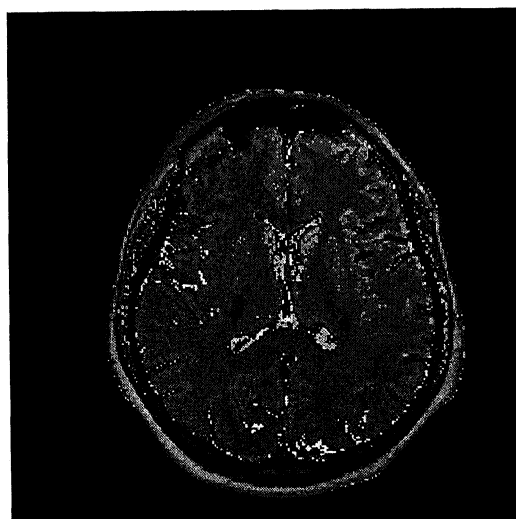
Four bits



Five bits



Six bits



Seven bits

Figure 2.15: PD map computed from different number of bits removed weighted images

No. of bits removed	Average L_1 Error	Average L_2 Error	L_∞ Error		Average Relative L_1	Average Relative L_2
One bit	0.493805	0.702713	1.000000		0.018769	0.045069
Two bits	1.499054	1.867604	3.000000		0.062837	0.147732
Three bits	3.496979	4.177157	7.000000		0.139810	0.271089
Four bits	7.488068	8.768975	15.000000		0.275875	0.452932
Five bits	15.498810	17.843015	31.000000		0.484417	0.667783
Six bits	26.406036	30.854564	63.000000		0.610945	0.757743
Seven bits	40.733185	51.932167	127.000000		0.667506	0.783768

Table 2.14: Average & average relative errors due to bit reduction in T_1 weighted image

No. of bits removed	Average L_1	Average L_2	L_∞		Average Relative L_1	Average Relative L_2
One bit	0.499908	0.707042	1.000000		0.007939	0.015571
Two bits	1.493866	1.866149	3.000000		0.023826	0.041362
Three bits	3.482758	4.166777	7.000000		0.055594	0.092985
Four bits	7.463226	8.763952	15.000000		0.119498	0.195517
Five bits	15.522552	18.055365	31.000000		0.250741	0.394480
Six bits	33.835052	38.111704	63.000000		0.525845	0.692305
Seven bits	54.470795	61.542353	127.000000		0.665562	0.786245

Table 2.15: Average & average relative errors due to bit reduction in T_2 weighted image

No. of bits removed	Average L_1	Average L_2	L_∞		Average Relative L_1	Average Relative L_2
One bit	0.499405	0.706686	1.000000		0.006696	0.013916
Two bits	1.506638	1.876468	3.000000		0.020167	0.036777
Three bits	3.497849	4.179638	7.000000		0.046810	0.082950
Four bits	7.494675	8.799033	15.000000		0.100701	0.174544
Five bits	15.468552	18.026072	31.000000		0.210812	0.355055
Six bits	33.158981	37.763136	63.000000		0.443592	0.635873
Seven bits	57.094528	64.740211	127.000000		0.591845	0.748702

Table 2.16: Average & average relative errors due to bit reduction in PD weighted image

No. of bits removed	Average L_1	Average L_2	L_∞		Average Relative L_1	Average Relative L_2
One bit	3.601414	12.980153	353.46240		0.003260	0.008054
Two bits	9.410160	32.169264	1097.1816		0.008277	0.017103
Three bits	20.585942	69.127719	1805.2458		0.017814	0.034373
Four bits	43.871006	136.76420	2770.5649		0.038467	0.073170
Five bits	94.671194	269.79157	3548.6733		0.084991	0.159106
Six bits	191.04457	455.77193	4029.3134		0.188269	0.346894
Seven bits	359.10784	734.36067	4176.5102		0.395435	0.694510

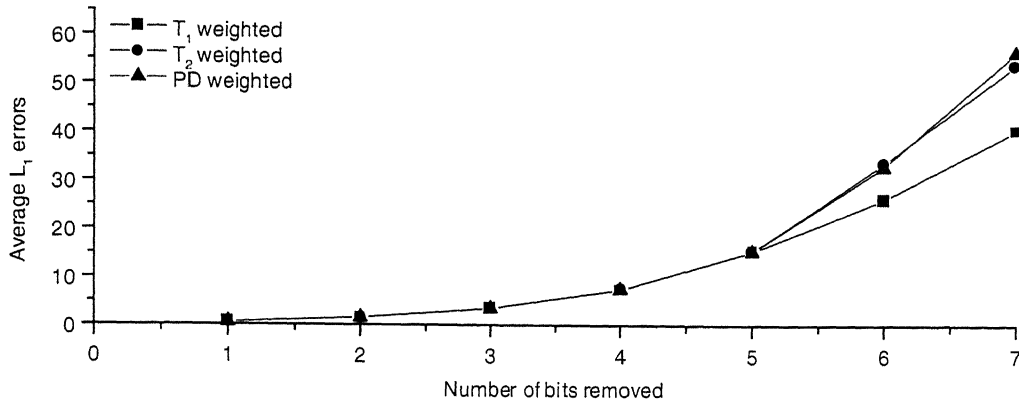
Table 2.17: Average & average relative errors due to bit reduction in T_1 map

No. of bits removed	Average L_1	Average L_2	L_∞		Average Relative L_1	Average Relative L_2
One bit	0.166511	0.584203	40.608032		0.001856	0.003125
Two bits	0.398558	1.433227	90.617401		0.004496	0.007441
Three bits	0.812391	2.629004	200.93664		0.009430	0.014707
Four bits	1.644988	4.958928	231.10553		0.019176	0.029601
Five bits	3.227306	8.553119	352.02179		0.038432	0.055804
Six bits	5.981129	11.752798	349.32559		0.073766	0.099153
Seven bits	10.592555	19.709234	399.02548		0.123114	0.158454

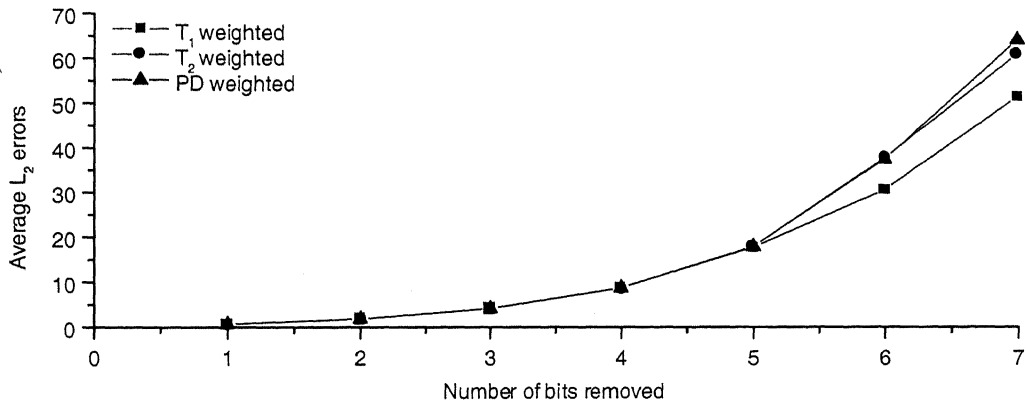
Table 2.18: Average & average relative errors due to bit reduction in T_2 map

No. of bits removed	Average L_1	Average L_2	L_∞		Average Relative L_1	Average Relative L_2
One bit	3.238593	24.301751	1877.4326		0.001781	0.006280
Two bits	8.008484	58.458150	3780.6621		0.004402	0.017449
Three bits	17.757535	117.06368	5180.9096		0.009669	0.040801
Four bits	37.699371	218.19723	5833.5683		0.021469	0.092453
Five bits	71.474286	323.30990	6612.5727		0.045625	0.181209
Six bits	134.309833	458.11723	6231.6274		0.091865	0.283429
Seven bits	231.608932	493.77429	6336.4125		0.161765	0.366470

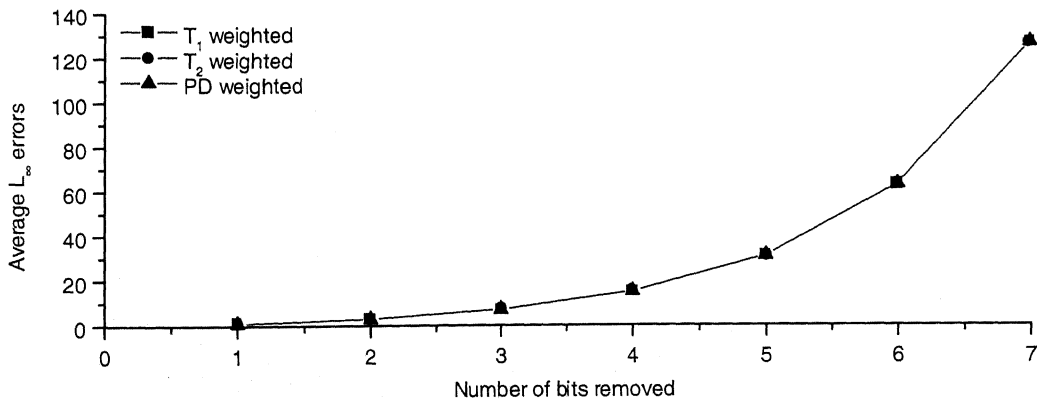
Table 2.19: Average & average relative errors due to bit reduction in PD map



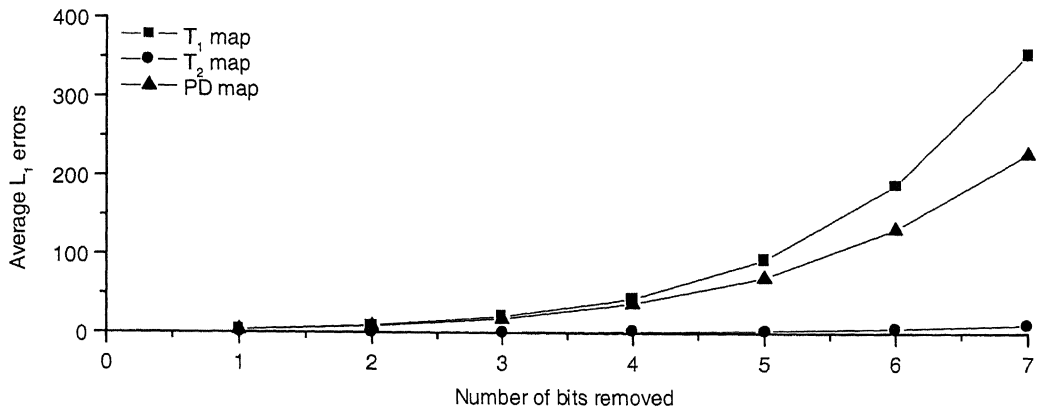
Graph 2.4(a): Average L_1 errors in T_1 , T_2 , and PD weighted images due to bit reduction



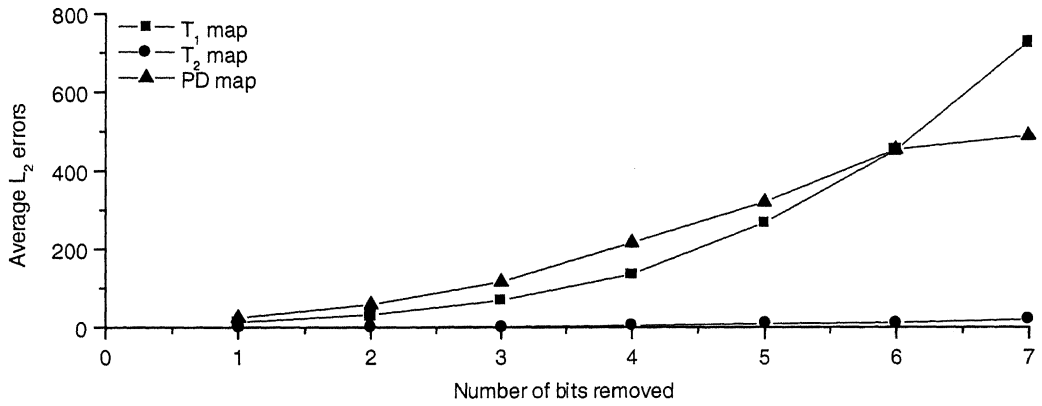
Graph 2.4(b): Average L_2 errors in T_1 , T_2 , and PD weighted images due to bit reduction



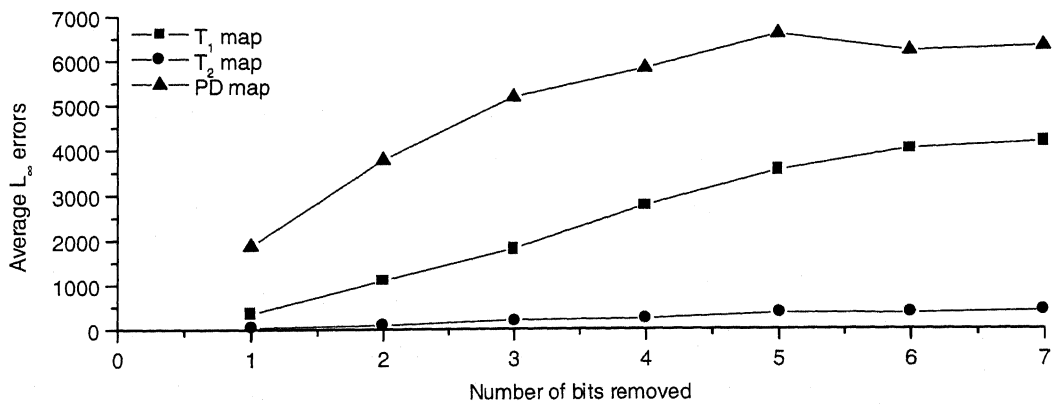
Graph 2.4(c): Average L_∞ errors in T_1 , T_2 , and PD weighted images due to bit reduction



Graph 2.5(a): Average L_1 errors in T_1 , T_2 , and PD maps computed from bit reduced images



Graph 2.5(b): Average L_2 errors in T_1 , T_2 , and PD maps computed from bit reduced images



Graph 2.5(c): Average L_∞ errors in T_1 , T_2 , and PD maps computed from bit reduced images

2.3.2. Effect of Filtering

All MR images slightly, sometimes severely, suffer with filtering (blurring) effects due to the image acquisition techniques and reconstruction methods. It is also a common practice in routine clinical diagnosis to apply some filters to minimize the noise in MR images. Due to the application of filters, signal also gets affected and if these filtered images are used for tissue parameters calculation, the parameter maps would get affected. To demonstrate this numerically, we study the effect of Poisson filter in the calculation of T_1 , T_2 and PD maps.

Poisson sums are obtained by convolving f with the Poisson kernel. For $0 \leq r \leq 1$, the Poisson kernel is given by

$$P(r, t) = 1 + 2 \sum_{j=1}^{\infty} r^j \cos jt = \frac{1 - r^2}{1 - 2r \cos t + r^2}$$
$$P_n(f) = \frac{a_0}{2} + \sum_{k=1}^n r^k (a_k \cos kx + b_k \sin kx).$$

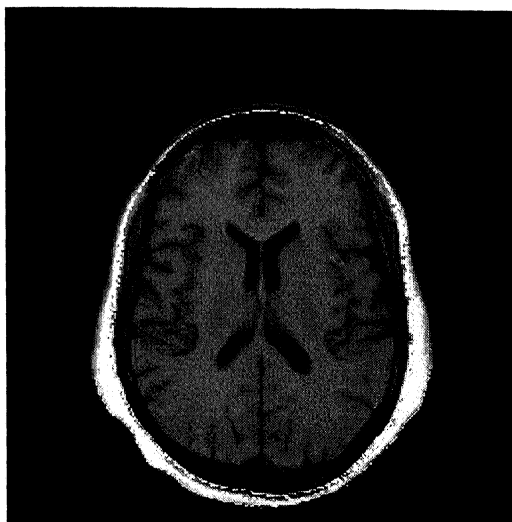
Here filter coefficients are generated by using r^k ($0 < r < 1$). In the present numerical studies we have taken $r = 0.99$.

Recently, R.K.S. Rathore, R.K. Gupta, V.S.N. Kaliprasad, S.B. Rao, and Sushmita Datta (2000) have proposed a de-blurring technique to improve image resolution by removing or minimizing the effect of filters. Images used after resolution enhancement for parameter maps calculation gave better contrast maps. For study of errors, first we have computed T_1 , T_2 , ρ values using three weighted images of a volunteer. Using these values three spin echo weighted images with $TR/TE = 1012/14$, $2200/20$, 80 ms are synthesized. These images are considered as original images and associated tissue parameter values as original T_1 , T_2 and PD values. Synthesized weighted images are blurred and iteratively de-blurred by Poisson sums. Figures 2.16-2.18 show the blurring effect and de-blurring of the three weighted images by Poisson filter. In these three Figures first image is the actual synthesized weighted image and second one is obtained by filtering the synthesized image by Poisson filter. Third, fourth, fifth, and sixth images are the de-blurred images corresponding to first, fourth, seventh, and tenth iterations of the de-blurring scheme. Visually one could observe that these images are gradually approaching to the actual synthesized image as the number of iterations increase. Figures 2.19-2.21 are the tissue parameter maps computed at different iterations of the de-blurring of weighted images. In all these Figures first image

represent the tissue parameter map computed from the actual synthesized image and the second one from the filtered images. Third, fourth, fifth and sixth images are the parameter maps computed from first, fourth, seventh and tenth iterations of the de-blurred weighted images. Even in the case of tissue parameters maps, visually, they appear to converge to the maps corresponding to the original synthesized images.

At each iteration T_1 , T_2 and PD maps are calculated and errors are computed. Errors are computed according to: $\%error = 100 \times \| \text{original-computed} \| / \| \text{original} \|$, the norm being the L_1 , L_2 , and L_∞ norm. Tables 2.20-2.22 show the errors in weighted images due to filtering and iteratively removing its effect. In all three images, in the first iteration itself the error is significantly reduced and in the later iterations it is gradually reduced. Tables 2.23-2.25 show the errors in tissue parameters computed at each iteration of the de-blurring of the weighted images. From these Tables it is clear that the errors in computed tissue parameters are less with less filtering effect. So, it is strongly recommended not to use any kind of filters while reconstructing the weighted images from acquired raw data from MRI scanners if one wishes to compute tissue parameters from them.

Graphs 2.6(a)-2.6(c) show the average L_1 , L_2 and L_∞ errors respectively in weighted images by blurring and de-blurring by Poisson filter with $r = 0.99$. From these graphs it is clear that as number of iterations increased the errors gradually decreased. Graphs 2.7(a)-2.7(c) show the average L_1 , L_2 and L_∞ errors respectively in T_1 , T_2 and PD maps computed from blurred and iteratively de-blurred T_1 , T_2 and PD weighted images by Poisson filter. Graph 2.7(a) shows decrease in L_1 errors in parameter maps computed from higher iterations of de-blurred weighted images. At all iterations, T_1 map has shown more L_1 errors compared to T_2 and PD maps. PD map has relatively low L_1 errors compared to T_1 and T_2 maps. Graph 2.7(b) shows the decrease in the L_2 errors. T_2 map has shown a significant decrease in error from iteration 5 to iteration 6. In L_2 errors T_2 map has more errors compared to T_1 and PD maps. Graph 2.7(c) shows the L_∞ errors in the computed maps.



Original



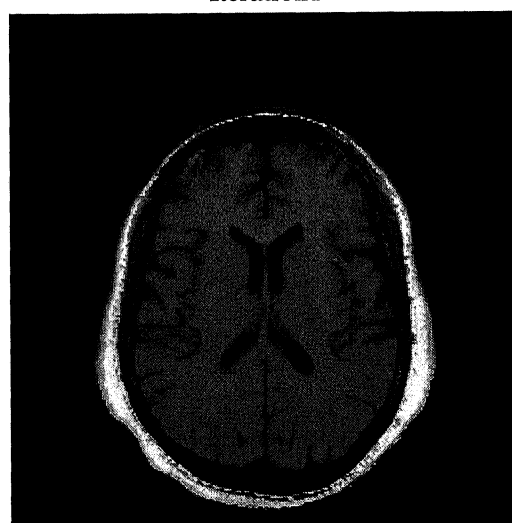
Blurred



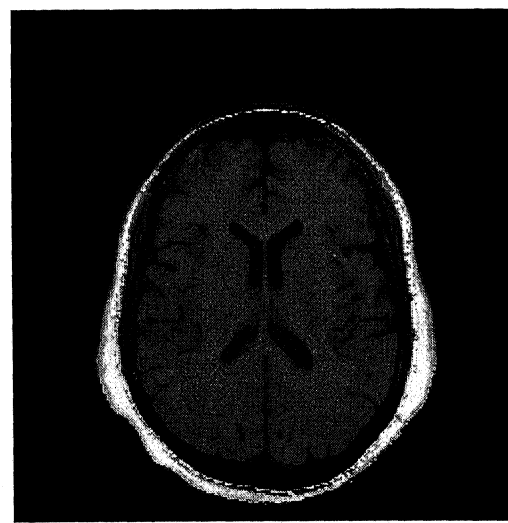
Iteration 1



Iteration 4

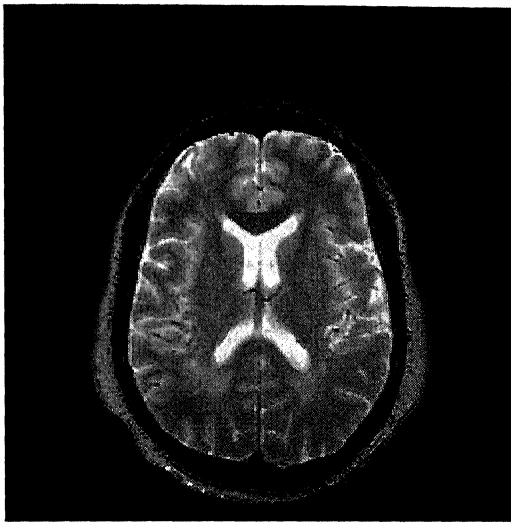


Iteration 7



Iteration 10

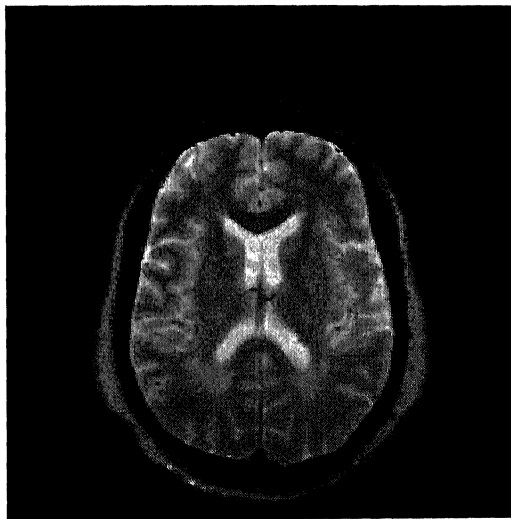
Figure 2.16: Blurred and iteratively de-blurring by Poisson filter (T_1 weighted image)



Original



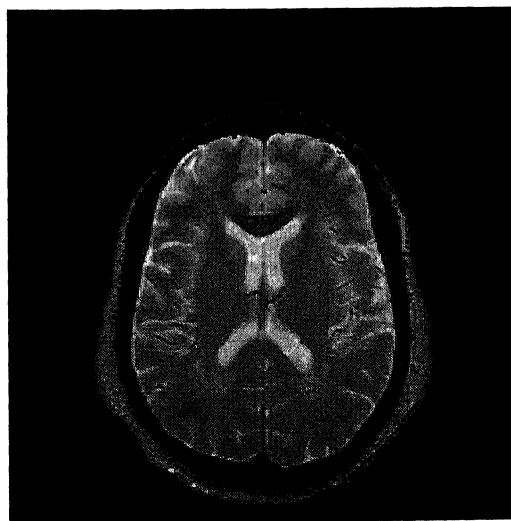
Blurred



Iteration 1



Iteration 4



Iteration 7

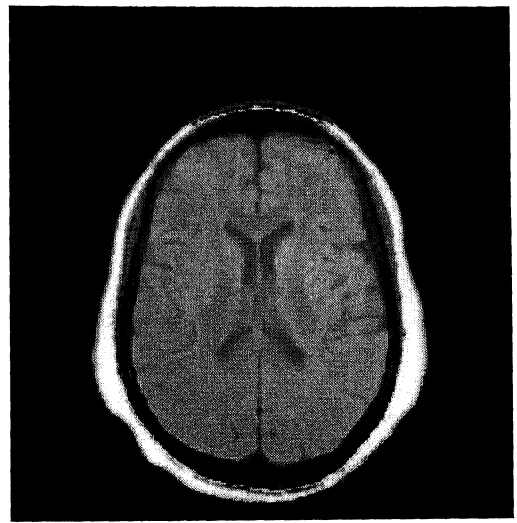


Iteration 10

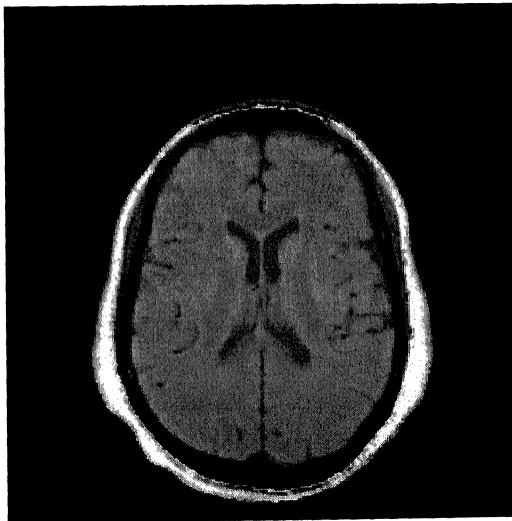
Figure 2.17: Blurred and iteratively de-blurred by Poisson filter (T_2 weighted image)



Original



Blurred



Iteration 1



Iteration 4



Iteration 7



Iteration 10

Figure 2.18: Blurring and iteratively de-blurring by Poisson filter (PD weighted image)



Original



Blurred



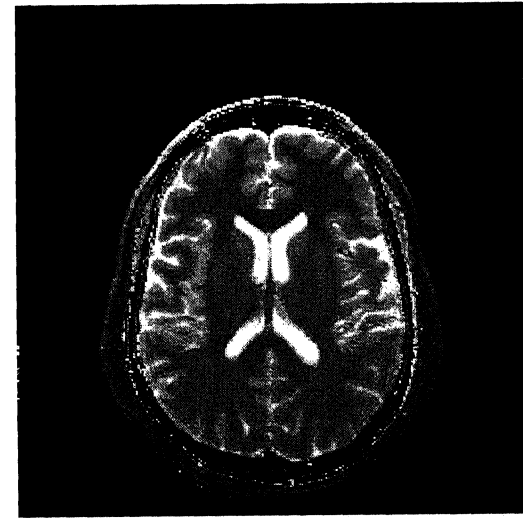
Iteration 1



Iteration 4

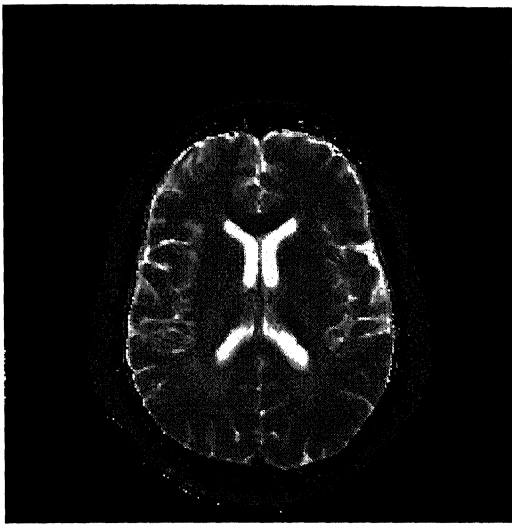


Iteration 7

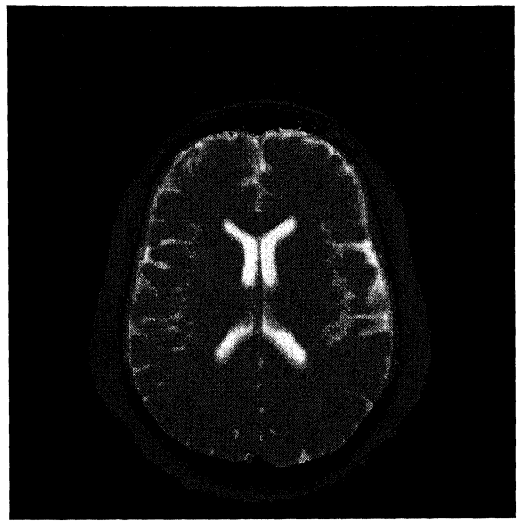


Iteration 10

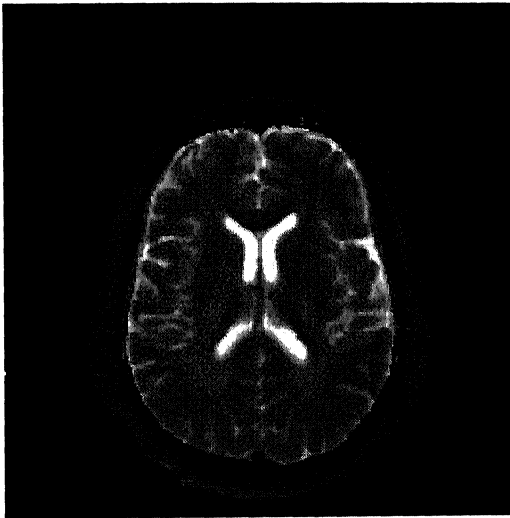
Figure 2.19: T_1 map calculated from weighted images blurred and de-blurred by Poisson filter



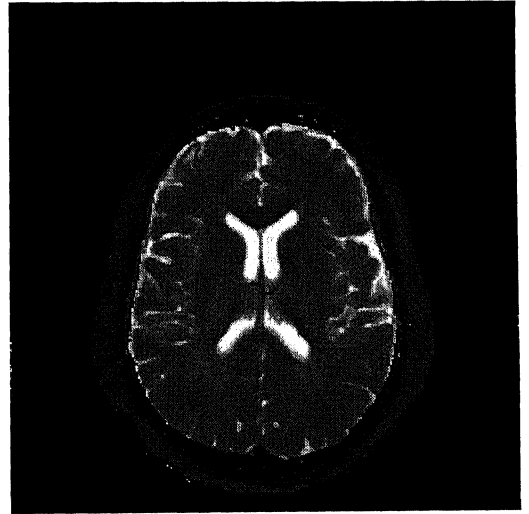
Original



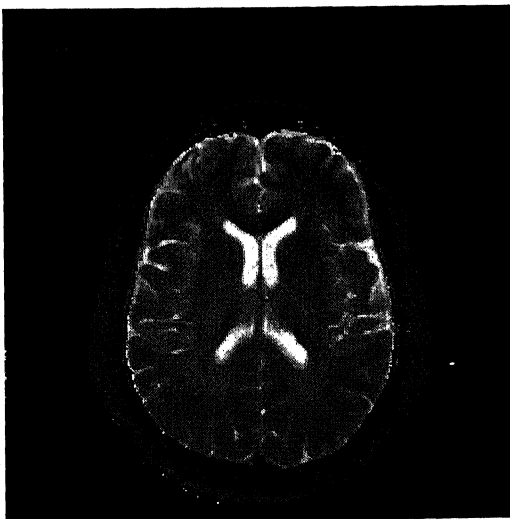
Blurred



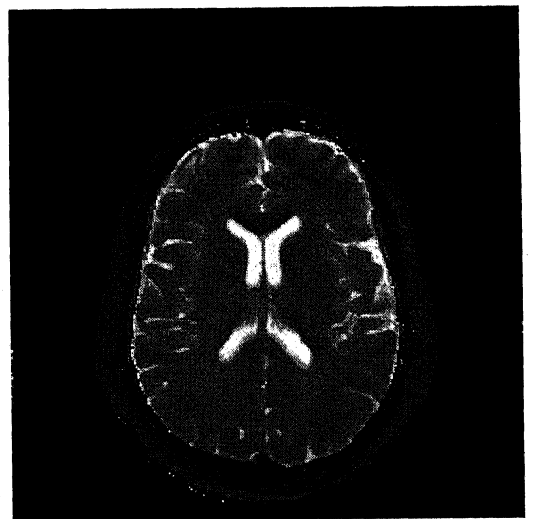
Iteration 1



Iteration 4

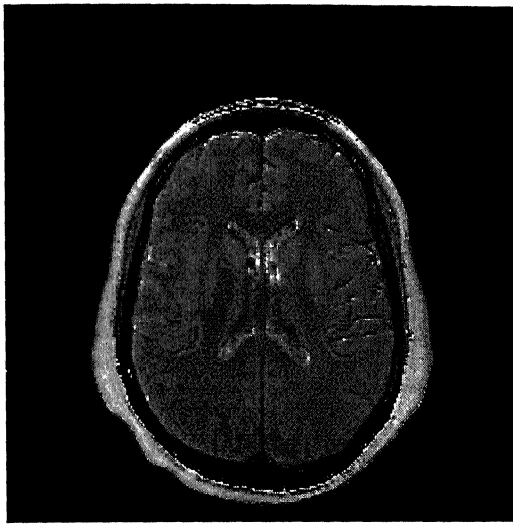


Iteration 7

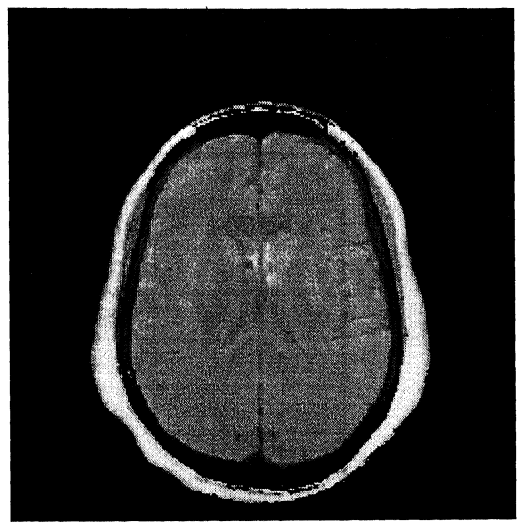


Iteration 10

Figure 2.20: T_2 map calculated from weighted images blurred and de-blurred by Poisson filter



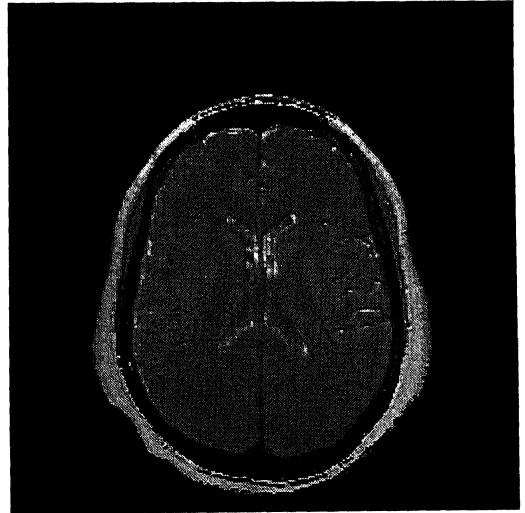
Original



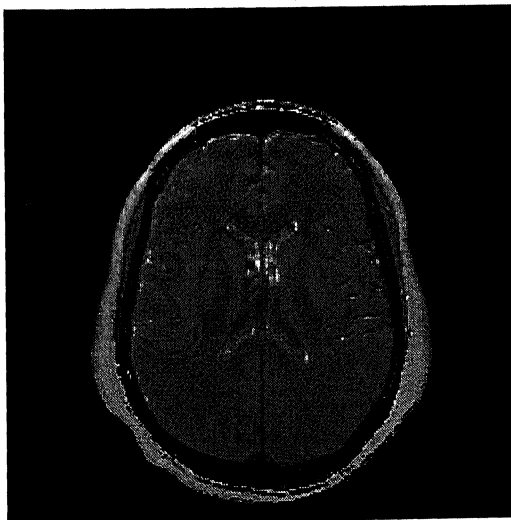
Blurred



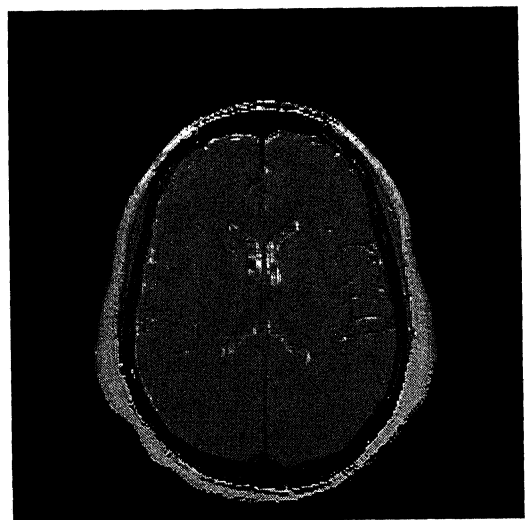
Iteration 1



Iteration 4



Iteration 7



Iteration 10

Figure 2.18: PD maps computed from weighted images blurred and de-blurred by Poisson filter

	L₁ Error	L₂ Error	L_∞ Error
Blurred	15.920006	47.029857	95.099185
Iteration 1	9.584898	38.124664	87.723128
Iteration 2	6.788624	31.447658	84.033179
Iteration 3	5.082074	26.142247	80.211153
Iteration 4	3.941934	22.289792	75.993708
Iteration 5	3.155377	19.297435	71.236598
Iteration 6	2.566577	16.853122	65.905023
Iteration 7	2.108289	14.709351	60.056701
Iteration 8	1.765043	12.837680	53.827110
Iteration 9	1.486457	11.109766	47.410174
Iteration 10	1.258534	9.594922	41.030135

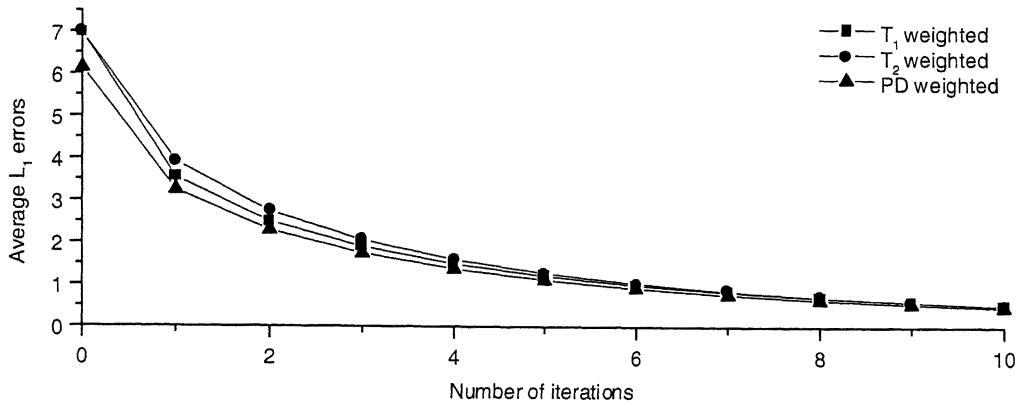
Table 2.23: % Error in deblurring by Poisson filter ($r = 0.99$) (T₁ map)

	L₁ Error	L₂ Error	L_∞ Error
Blurred	12.611589	52.643458	95.974726
Iteration 1	7.054603	45.525262	91.927930
Iteration 2	4.965641	41.441344	86.610244
Iteration 3	3.841923	37.894183	80.440234
Iteration 4	3.025411	34.243302	73.746165
Iteration 5	2.463599	31.035154	66.638912
Iteration 6	1.882758	21.886574	64.735094
Iteration 7	1.507131	18.421377	58.996586
Iteration 8	1.288753	17.660786	50.573965
Iteration 9	1.112232	17.002172	45.170086
Iteration 10	0.969051	16.410773	44.383822

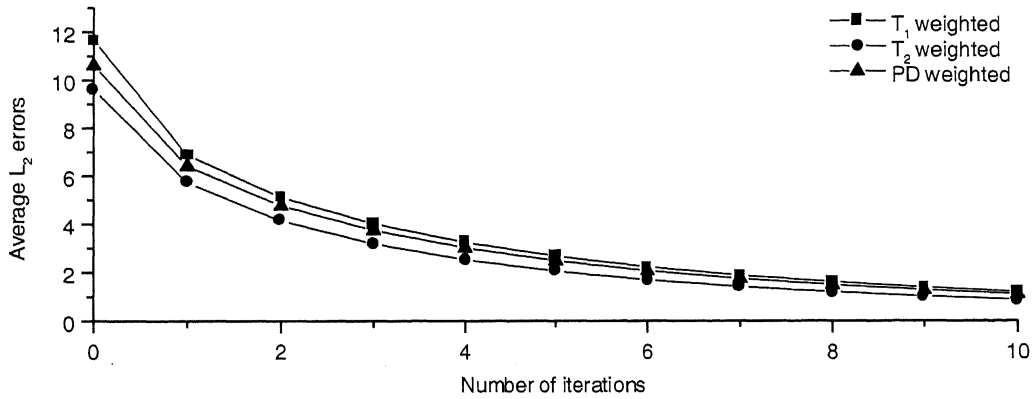
Table 2.24: % -Error in deblurring by Poisson filter ($r = 0.99$) (T₂ map)

	L₁ Error	L₂ Error	L_∞ Error
Blurred	8.434432	21.572942	84.377495
Iteration 1	4.715807	17.177758	76.940832
Iteration 2	3.367360	14.361484	70.786209
Iteration 3	2.562864	12.052858	64.917243
Iteration 4	2.032226	10.383647	59.165056
Iteration 5	1.641415	8.996978	53.534160
Iteration 6	1.345781	7.831474	48.075080
Iteration 7	1.115034	6.820065	42.849856
Iteration 8	0.935416	5.932835	37.917754
Iteration 9	0.792656	5.146250	33.327236
Iteration 10	0.674427	4.452812	29.112363

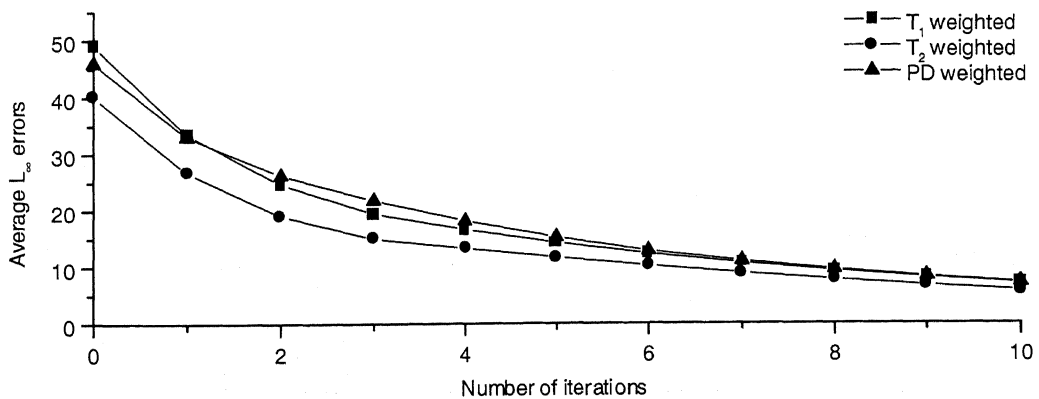
Table 2.25: % -Error in deblurring by Poisson filter ($r = 0.99$) (PD map)



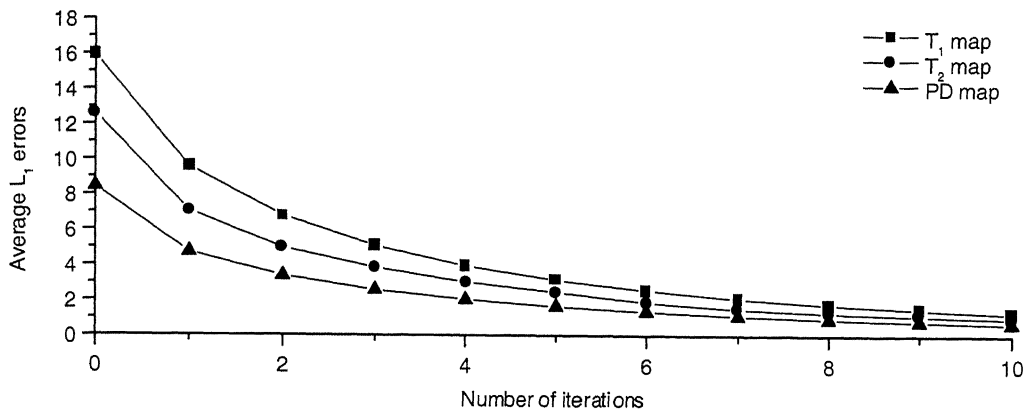
Graph 2.6(a): Average L_1 errors in T_1 , T_2 , and PD weighted images blurred and iteratively deblurred by Poisson filter ($r = 0.99$)



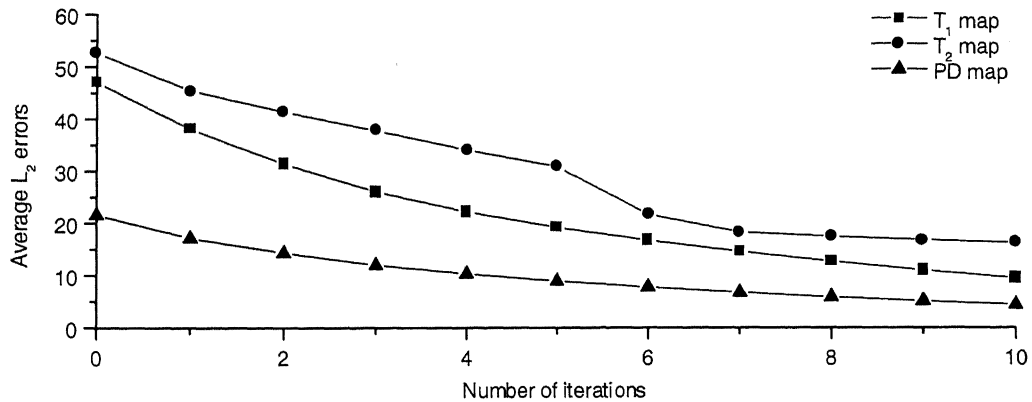
Graph 2.6(b): Average L_2 errors in T_1 , T_2 , and PD weighted images blurred and iteratively deblurred by Poisson filter ($r = 0.99$)



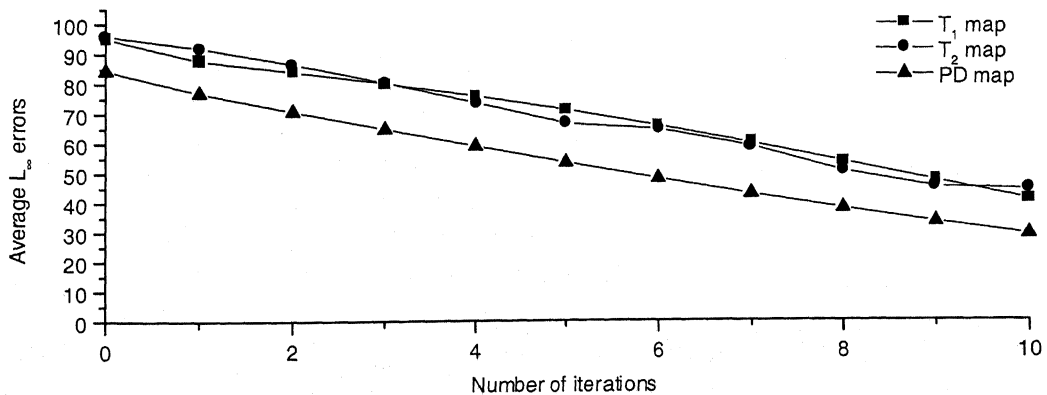
Graph 2.6(c): Average L_∞ errors in T_1 , T_2 , and PD weighted images blurred and iteratively deblurred by Poisson filter ($r = 0.99$)



Graph 2.7(a): Average L_1 errors in T_1 , T_2 , PD maps computed from blurred and iteratively deblurred images



Graph 2.7(b): Average L_2 errors in T_1 , T_2 , PD maps computed from blurred and iteratively deblurred images



Graph 2.7(c): Average L_∞ errors in T_1 , T_2 , PD maps computed from blurred and iteratively deblurred images

Chapter 3

Generation of High Contrast Images for Diagnosis

For medical diagnosis adequate contrast among normal tissues is necessary for good anatomical definition, and good contrast between normal and diseased tissues is essential for sensitivity to disease. The primary sources of inherent tissue contrast in MRI are threefold - hydrogen spin density, T_1 , and T_2 relaxation times. Although hydrogen densities within soft tissues typically vary by a few percent, the proton density contribution to the measured MR signal tends to vary by a greater amount, up to 30% among soft tissues. T_1 and T_2 relaxation times often vary even more widely, sometimes varying among soft tissues by more than 100%. For example, the T_1 and T_2 values of CSF are several times the T_1 and T_2 values, respectively, of white matter and gray matter (R.E. Hendrick (1999)).

Usually, T_1 weighted images show good anatomical details while T_2 weighted images show a good contrast between white matter, gray matter, and CSF. T_2 weighted images are generally used for pathological observations. Even though PD weighted images are relatively flat, some pathologies like, perilesional gliosis around cystic cavity are better visible on PD weighted images than on T_1 and T_2 weighted images.

This chapter mainly deals with the generation of high contrast images. In section 3.1, an entropy-like maximization procedure which computes the weights is presented. Using these weights, a weighted linear combination of the acquired images is produced. Given a set of linearly independent images, Gram-Schmidt orthogonalization process is discussed in section 3.2 to generate orthonormal images. In section 3.3, generation of contrast images through functional maps is presented. Section 3.4 deals with a least squares method to produce tissue parameter maps contrast through a weighted combination of the images. In section 3.5, generation of good contrast in perilesional gliosis region on synthesized IR images is demonstrated. Synthesis of image values at divergent points, where tissue parameter values could not be computed due to partial volume effect, is discussed in section 3.6. The utility of tissue parameter maps for segmentation is shown in section 3.7.

3.1. Entropy-Like Maximization

Given p images corresponding to a cross-section, their weighted linear combination can be written as

$$\sum_{k=1}^p c_k S_k ,$$

where c_k 's are the weights and S_k is the signal intensity in the k th image. These weights could be obtained by maximizing the function ϕ with respect to c_k 's and λ defined as

$$\phi(c_1, c_2, \dots, c_p, \lambda) = - \sum_{i=1}^N \left\{ \left(\sum_{k=1}^p c_k S_{ki} \right)^2 \ln \left(\sum_{k=1}^p c_k S_{ki} \right)^2 \right\} + \lambda \left(\sum_{i=1}^N \left(\sum_{k=1}^p c_k^2 S_{ki} \right)^2 - 1 \right),$$

where λ is a Lagrange multiplier and N is the number of pixels in one image.

This maximization process gives a system of equations given as

$$\frac{\partial \phi}{\partial c_j} = - \sum_{i=1}^N \left\{ 4 \left(\sum_{k=1}^p c_k S_{ki} \right) S_{ji} \ln \left(\sum_{k=1}^p c_k S_{ki} \right) + 2 \left(\sum_{k=1}^p c_k S_{ki} \right) S_{ji} \right\} + 2\lambda \left[\sum_{i=1}^N \left(\sum_{k=1}^p c_k S_{ki} \right) S_{ji} \right] = 0,$$

$j=1, \dots, p$, and

$$\frac{\partial \phi}{\partial \lambda} = \sum_{i=1}^N \left(\sum_{k=1}^p c_k S_{ki} \right)^2 - 1 = 0.$$

This implies

$$- \sum_{i=1}^N \left\{ \left[2 \ln \left(\sum_{k=1}^p c_k S_{ki} \right) + 1 \right] 2 \left(\sum_{k=1}^p c_k S_{ki} \right) S_{ji} \right\} + 2\lambda \left[\sum_{i=1}^N \left(\sum_{k=1}^p c_k S_{ki} \right) S_{ji} \right] = 0 = F_j, \quad j = 1, \dots, p,$$

$$\text{and } \sum_{i=1}^N \left(\sum_{k=1}^p c_k S_{ki} \right)^2 - 1 = 0 = F_{p+1}.$$

The above nonlinear system of equations can be solved iteratively by Newton's method as

$$\mathbf{C}^n = \mathbf{C}^{n-1} - \mathbf{A}^{-1} \mathbf{F}, \quad (3.1.1)$$

where

$$\mathbf{C} = \begin{pmatrix} c_1 \\ \vdots \\ c_p \\ \lambda \end{pmatrix}, \quad \mathbf{F} = \begin{pmatrix} F_1 \\ \vdots \\ F_p \\ F_{p+1} \end{pmatrix}, \quad \text{and } \mathbf{A} = \begin{pmatrix} \frac{\partial F_1}{\partial c_1} & \dots & \frac{\partial F_1}{\partial c_p} & \frac{\partial F_1}{\partial \lambda} \\ \vdots & & \vdots & \vdots \\ \frac{\partial F_p}{\partial c_1} & \dots & \frac{\partial F_p}{\partial c_p} & \frac{\partial F_p}{\partial \lambda} \\ \frac{\partial F_{p+1}}{\partial c_1} & \dots & \frac{\partial F_{p+1}}{\partial c_p} & \frac{\partial F_{p+1}}{\partial \lambda} \end{pmatrix}.$$

Here,

$$\frac{\partial F_j}{\partial c_l} = -\sum_{i=1}^N \left\{ (3 + 2 \ln(\sum_{k=1}^p c_k S_{ki})) 2 S_{ji} S_{li} \right\} + 2\lambda \left[\sum_{i=1}^N S_{li} S_{ji} \right], \quad l, j = 1, 2, \dots, p,$$

$$\frac{\partial F_{p+1}}{\partial c_l} = \sum_{i=1}^N \left\{ 2(\sum_{k=1}^p c_k S_{ki}) S_{li} \right\}, \quad l = 1, \dots, p.$$

$$\frac{\partial F_j}{\partial \lambda} = 2 \sum_{i=1}^N (\sum_{k=1}^p c_k S_{ki}) S_{ji}, \quad j=1, \dots, p, \quad \text{and} \quad \frac{\partial F_{p+1}}{\partial \lambda} = 0.$$

For initial approximation we have taken $\mathbf{C}^0 = \begin{pmatrix} 1 & \dots & 1 \\ p & & p \end{pmatrix}^T$.

Figure 3.1 (a)-(c) show the T_1 , T_2 , and ρ weighted images. Figure 3.1 (d) is the weighted linear combination of the images (a)-(c). These weights are obtained from equation (3.1.1). This image appears similar to PD weighted image, but the better appearance of perilesional gliosis (black arrow) than in any acquired weighted spin echo images could be observed.

However, we compute these weights by maximizing the following quantity over c_j 's as follows:

$$\max_{c_j} \sum_{i=1}^N \sum_{j=1}^k c_j S_{ji} \ln(c_j S_{ji}),$$

subjected to $\sum_{k=1}^p c_k = 1$. Here, N is the total number of pixels and S_{ji} is the i th pixel intensity of the j th image.

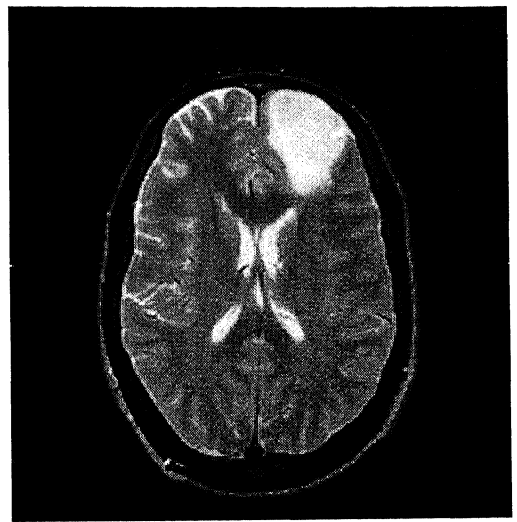
Therefore $\frac{\partial \phi}{\partial c_j} = 0$, $j=1, 2, \dots, k$ implies

$$c_j = \exp(-(1 + (\sum_{i=1}^N S_{ji} \ln(S_{ji}) / \sum_{i=1}^N S_{ji}))), \quad j=1, 2, 3, \dots, k. \quad (3.1.2)$$

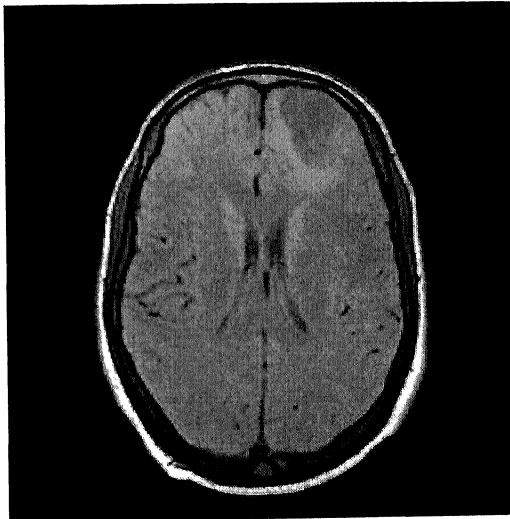
Figure 3.1 (e) is a weighted linear combination of (a)-(c), with weights being computed from equation (3.1.2). A good contrast between gliosis region and surrounding brain tissue could be seen.



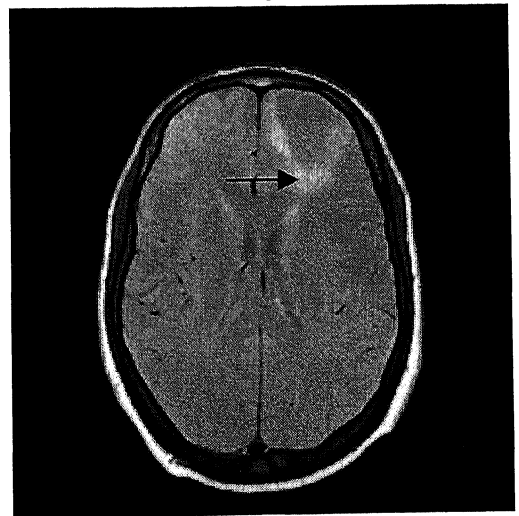
T₁ weighted



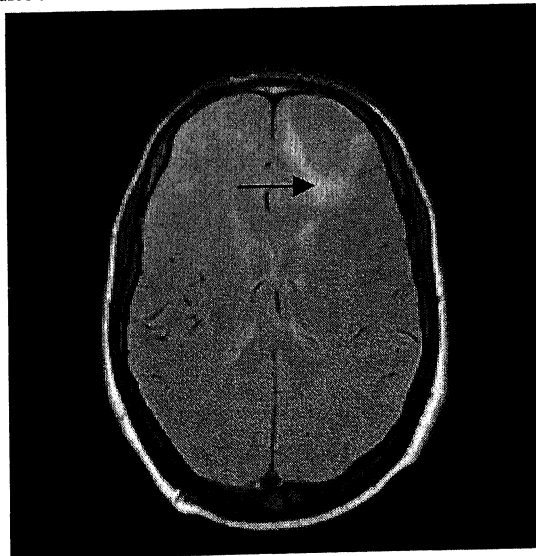
T₂ weighted



PD weighted



With weights from equation (3.1.1)



With weights from equation (3.1.2)

Figure 3.1: Generation of entropy like contrast images using weighted linear combination of acquired images

3.2. Orthonormal Images

Given a set of N linearly independent images $\{S_0, S_1, \dots, S_{N-1}\}$, we can construct an orthonormal set $\{\tilde{S}_0, \tilde{S}_1, \dots, \tilde{S}_{N-1}\}$ of images which are linear combination of the original set using Gram-Schmidt orthogonalization procedure. This sequential procedure is described as follows:

i. Set $\tilde{S}_0 = \frac{S_0}{\|S_0\|}$

ii. Define y_1 as the S_1 minus the projection of S_1 onto \tilde{S}_0 :

$$y_1 = S_1 - \langle S_1, \tilde{S}_0 \rangle \tilde{S}_0$$

The image y_1 is orthogonal to \tilde{S}_0 by construction

iii. Set $\tilde{S}_1 = \frac{y_1}{\|y_1\|}$ (i.e. normalizing the result of the preceding step)

iv. Define y_2 as the S_2 minus the projection of S_2 onto \tilde{S}_0 and \tilde{S}_1 :

$$y_2 = S_2 - \langle S_2, \tilde{S}_0 \rangle \tilde{S}_0 - \langle S_2, \tilde{S}_1 \rangle \tilde{S}_1$$

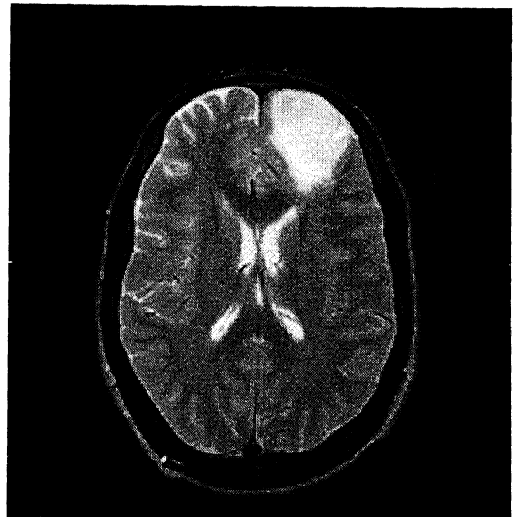
v. Normalize: $\tilde{S}_2 = \frac{y_2}{\|y_2\|}$

vi. Continue this process until \tilde{S}_{N-1} has been defined

Computed results are shown in Figure 3.2. Images in Figure 3.2 (a) and Figure 3.2 (b) are the T_1 weighted and T_2 weighted images. Figure 3.2 (c) is obtained by orthonormalization of T_1 weighted image with respect to T_2 weighted image . This shows the T_1 weighted image without gray matter and CSF. A clear white matter is conspicuous on this image. Figure 3.2 (d) is obtained by orthonormalizing T_2 weighted image with respect to T_1 weighted image. This image shows features complement to Figure 3.2 (c).



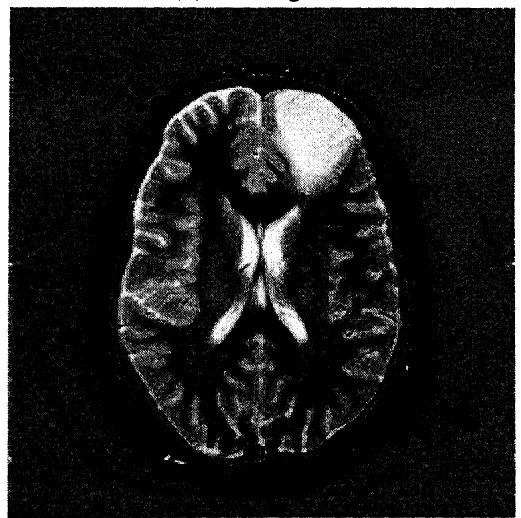
(a) T_1 weighted



(b) T_2 weighted



(c) T_1 weighted with respect to T_2 weighted



(d) T_2 weighted with respect to T_1 weighted

Figure 3.2: Generation of orthonormal images using Gram-Schmidt orthogonalization process

3.3. Functional Maps

Usually MR weighted images are acquired by selecting specific pulse sequences and sequence parameters. For example, spin echo images with short TR and short TE give T_1 weighted images whereas long TR, short TE and long TR, long TE produce PD weighted and T_2 weighted images. In these weighted images to some extent the contribution from other tissue parameters is also there.

Once T_1 , T_2 , and proton density maps of a cross-section are computed, then it is possible to generate the functional T_1 map and functional T_2 map by computing the values of the functions of T_1 and T_2 respectively. In the case of spin echo sequence these functions will be

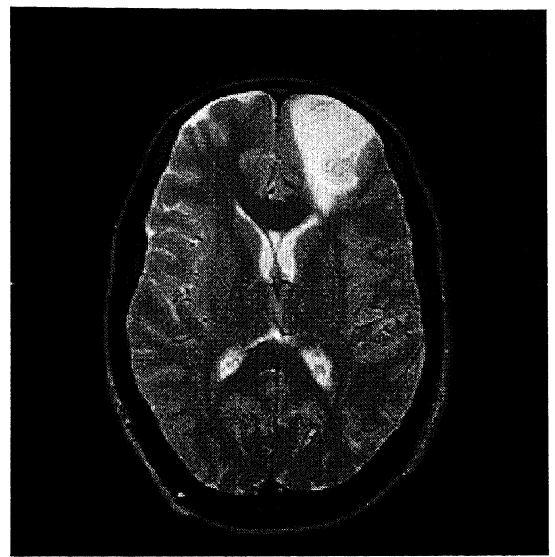
$$f(T_1) = 1 - 2\exp(-(TR - TE/2)/T_1) + \exp(-TR/T_1),$$

$$g(T_2) = \exp(-TE/T_2).$$

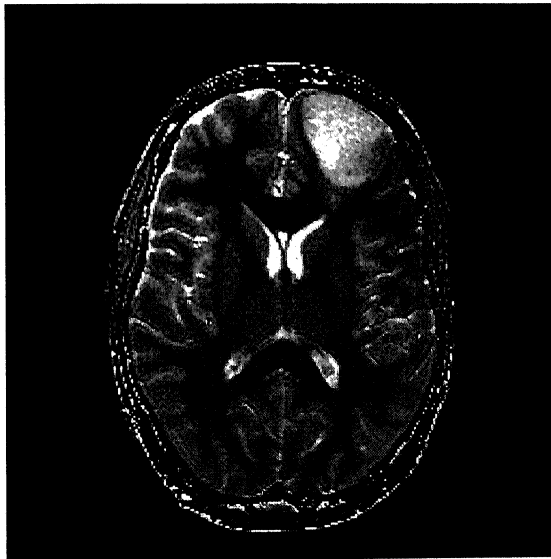
Figure 3.2 shows T_1 , T_2 weighted images, T_1 , T_2 computed maps and the corresponding T_1 , T_2 functional maps. The functional T_1 map shows excellent contrast between gray and white matter with clear anatomical details and intensities are proportional to that of T_1 weighted image. Even though T_2 functional map shows better contrast compared to T_2 map, T_2 weighted image has good contrast compared to both T_2 map and T_2 functional map.



T₁ weighted



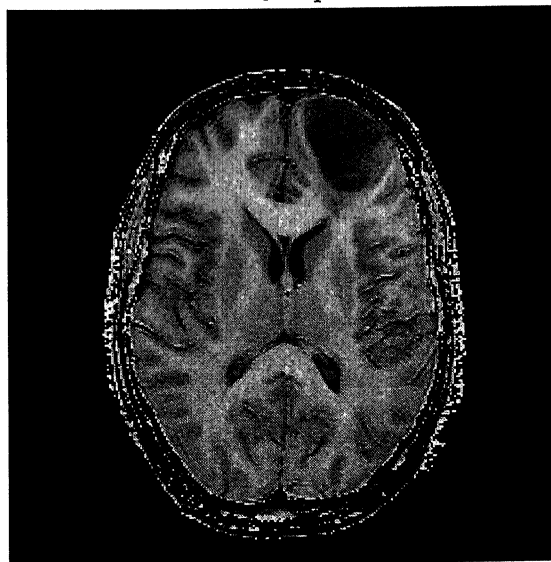
T₂ weighted



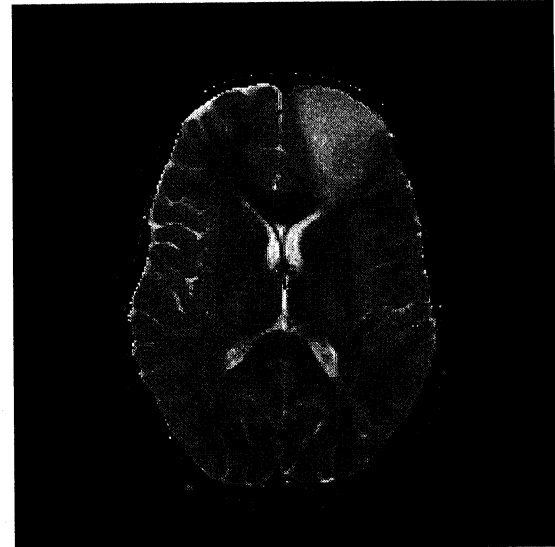
T₁ map



T₂ map



T₁ functional map



T₂ functional map

Figure 3.3: Generation of T₁ and T₂ functional maps

3.4. Generation of Parameter Map Like Contrast Images

Using a weighted combination of weighted acquired images, it is possible to obtain images with tissue parameter maps like contrast. Once tissue parameter maps are computed, these weights can be obtained by minimizing the sum of the squares of the differences between the parameter maps and weighted combination of the weighted images. The weights, c_j 's can be computed as follows.

$$\min_{c_k} \sum_{i=1}^N \left[P_i - \sum_{j=1}^k c_j S_{ji} \right]^2 = F(\text{say}),$$

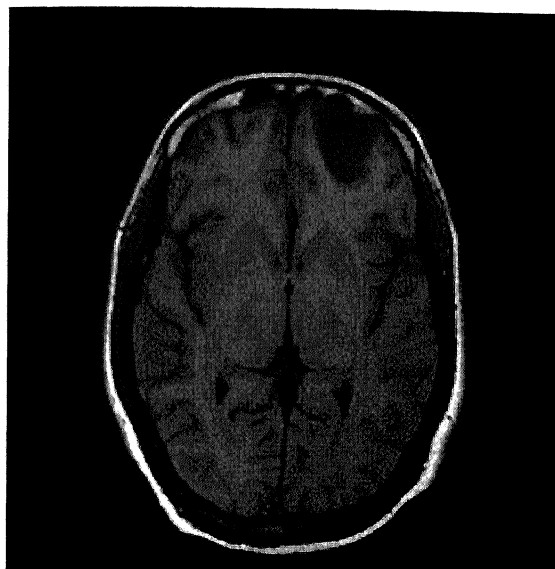
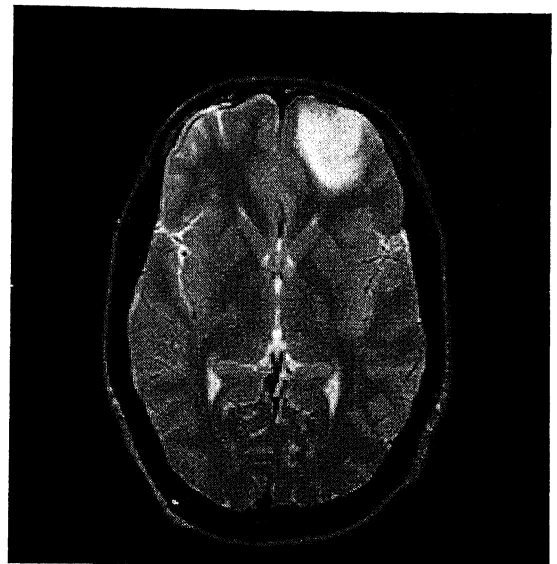
where P , S_j , N , k , and c_j are the parameter map, j^{th} acquired image, number of pixels in the image, and weight associated with j^{th} image respectively.

$$\text{Now, } \frac{\partial F}{\partial c_p} = 0, \quad p = 1, 2, \dots, k, \quad \text{gives} \quad \sum_{i=1}^N \left[P_i - \sum_{j=1}^k c_j S_{ji} \right] S_{pi} = 0, \quad p = 1, 2, \dots, k,$$

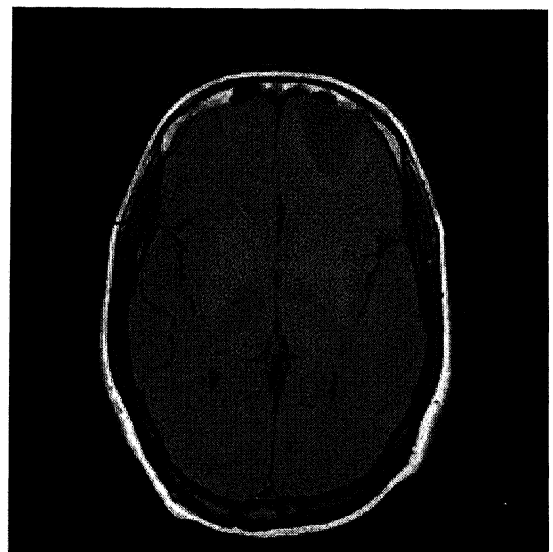
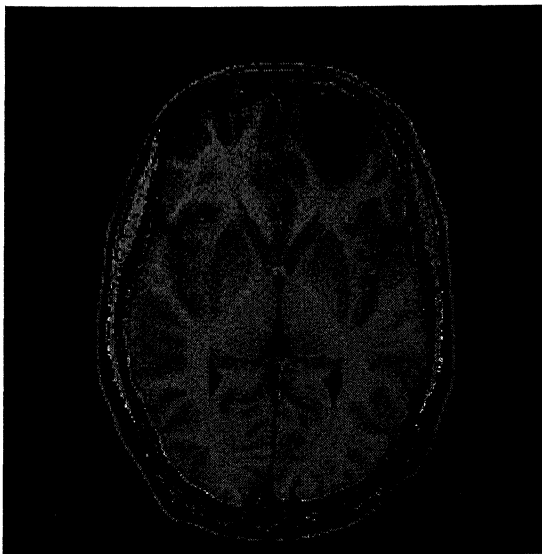
$$\text{which can be written as: } \sum_{j=1}^k \left(\sum_{i=1}^N S_{ji} S_{pi} \right) c_j = \sum_{i=1}^N P_i S_{pi}, \quad p = 1, 2, \dots, k.$$

The weights c_j 's can be computed by solving the above system of equations.

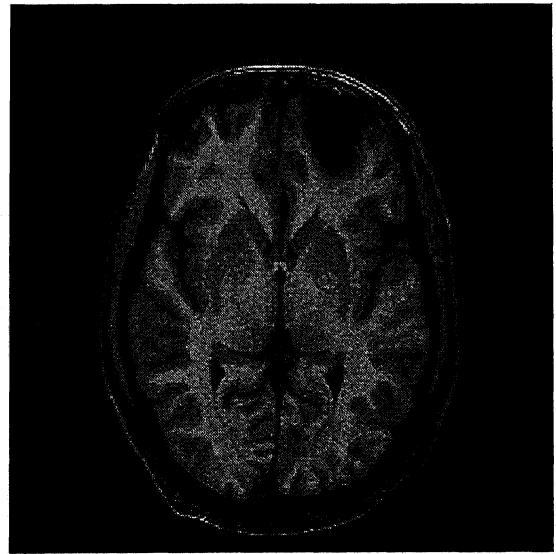
Results are shown in Figures 3.4(a) and 3.4(b). The first four images of Figure 3.4(a) show T_1 , T_2 , ρ , and MT SE T_1 weighted spin echo images respectively and the last two images are MTR map and the weighted combination with respect to MTR map. In Figure 3.4(b) first column shows the computed T_1 , T_2 , and PD maps while the second column represents corresponding weighted combinations to generate respective parameter contrast images. In all these combinations an excellent contrast similar to parameters maps is visible. These weights are computed at five consecutive slices each with slice thickness 5mm and inter-slice gap 0.1 mm in a single patient and results are tabulated in Tables 3.1-3.4. These results show that the orders of magnitudes of these weights over five slice are comparable. That means the average values of these weights could be used for all these slices without computing tissue parameters and weights at each slice level. This observation could be extended to computing the weights over the slices possessing same anatomical structures and making a data base of them which could be used to obtain tissue parameters like contrast without actually computing the tissue parameters. Generation of these images would be very fast. For a 256x256 image it takes 196608 multiplications and 131072 additions. This data base could be made for different pathological cases also.

T₁ WeightedT₂ Weighted

PD Weighted

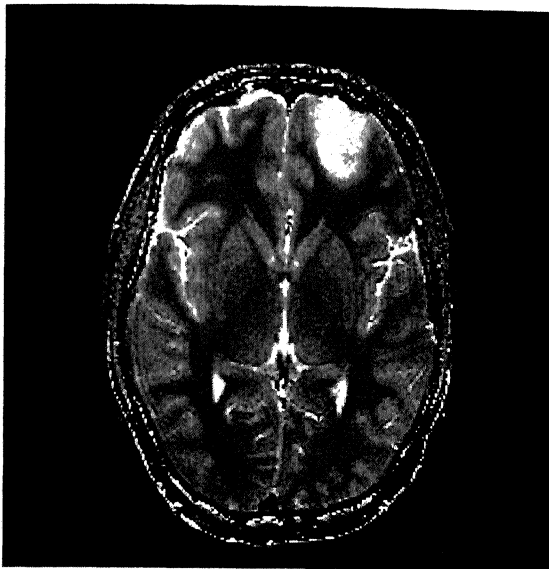
MTSE T₁ Weighted

MTR Map

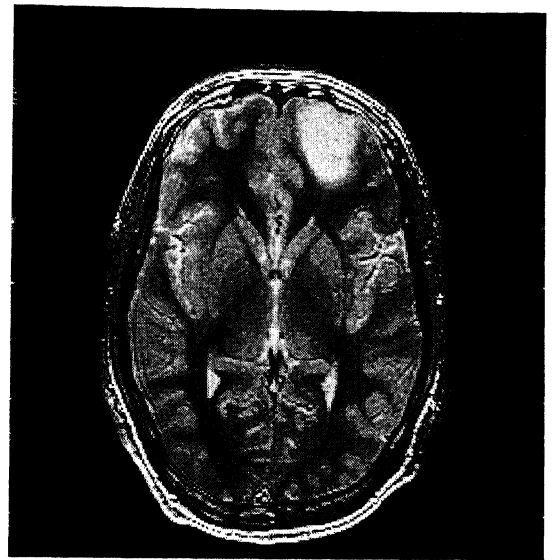


Weighted combination w.r.t MTR map

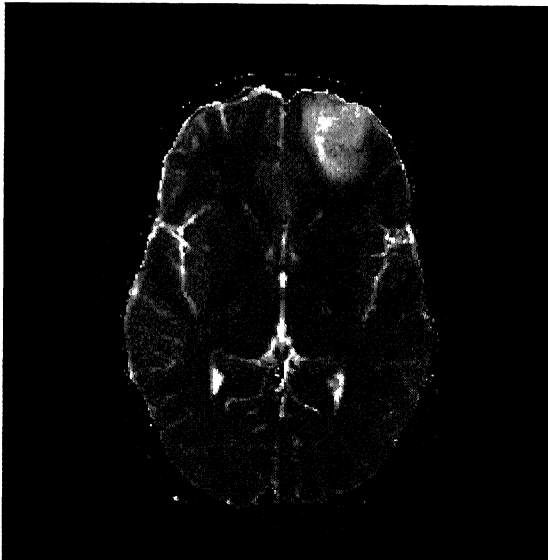
Figure 3.4(a): Generation of tissue parameter contrast Images by a linear weighted combination of images



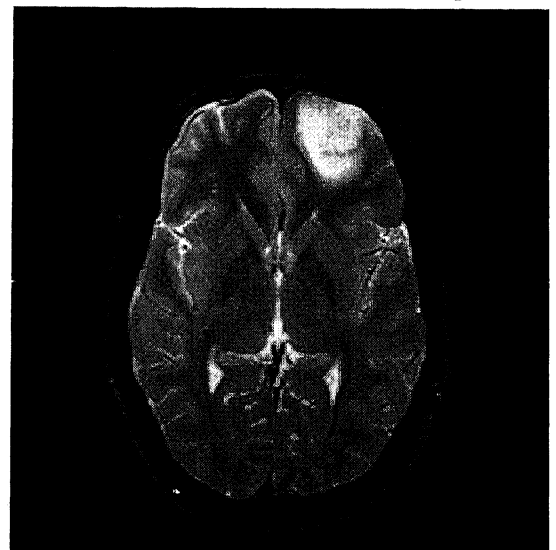
T₁ Map



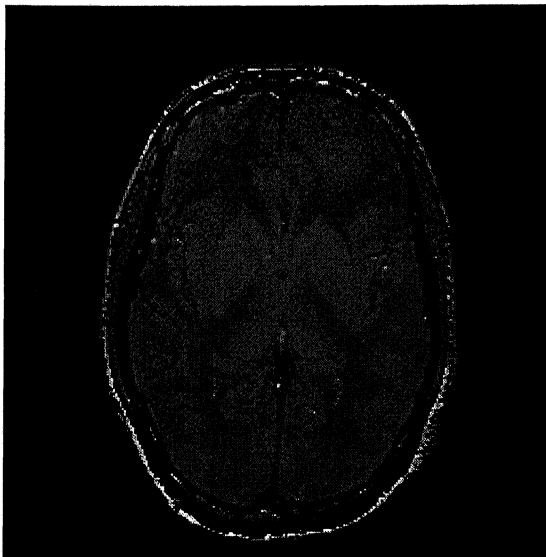
Weighted combination w.r.t T₁ map



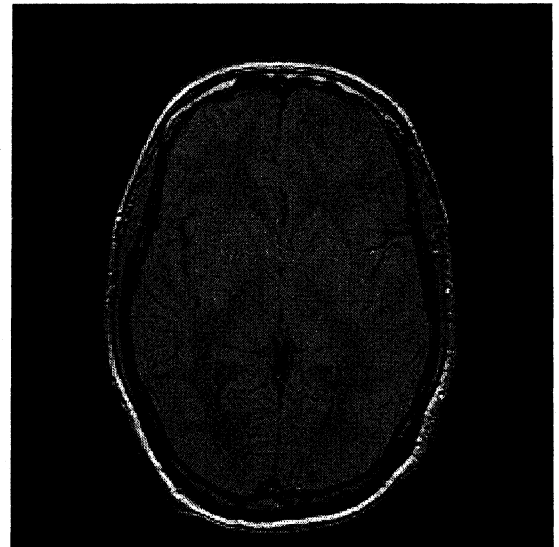
T₂ Map



Weighted combination w.r.t. T₂map



PD map



Weighted combination w.r.t. PD map

Figure 3.4.(b): Generation of tissue parameter contrast images by a linear weighted combination of images

T₁ Contrast	L₂ Ave. % Error	C₁ (PD wtd)	C₂ (T₁ wtd)	C₃ (T₂ wtd)
Slice 1	24.556313	669.596252	-681.283630	39.475903
Slice 2	25.589626	611.305359	-693.740967	60.294865
Slice 3	25.249855	656.256958	-758.47882	67.323715
Slice 4	26.137049	622.984802	-759.524658	69.148926
Slice 5	25.440390	653.556030	-748.149902	44.035568

Table 3.1: L₂ average percentage errors in weighted combinations with respect to T₁ map and corresponding weights

T₂ Contrast	L₂ Ave. % Error	C₁ (PD wtd)	C₂ (T₁ wtd)	C₃ (T₂ wtd)
Slice 1	21.594936	23.419680	-57.377502	137.748688
Slice 2	25.580469	21.918722	-70.840324	155.125931
Slice 3	28.500360	17.900223	-78.899765	196.744797
Slice 4	24.503012	16.844803	-62.885311	169.665085
Slice 5	27.511993	17.655508	-63.075607	161.335281

Table 3.2: L₂ average percentage errors in weighted combinations with respect to T₂ map and corresponding weights

PD Contrast	L₂ Ave. % Error	C₁ (PD wtd)	C₂ (T₁ wtd)	C₃ (T₂ wtd)
Slice 1	9.513255	411.917389	-228.914139	-56.176613
Slice 2	10.261456	374.833130	-227.364639	-51.715515
Slice 3	10.445120	393.376923	-249.356979	-55.402931
Slice 4	9.478690	370.599182	-230.857346	-57.778591
Slice 5	9.533550	383.339325	-243.544052	-60.875698

Table 3.3: L₂ average percentage errors in weighted combinations with respect to PD map and corresponding weights

MTR Contrast	L₂ Ave. % Error	C₁ (MTSET₁wtd)	C₂ (T₁ wtd)	C₃ (T₂ wtd)
Slice 1	16.440626	-199.524506	209.477615	6.257372
Slice 2	17.437050	-197.515884	195.639603	6.594873
Slice 3	18.460693	-213.683929	217.655014	7.248658
Slice 4	17.822056	-203.493179	211.895462	7.380937
Slice 5	18.662191	-213.680634	208.736847	6.506155

Table 3.4: L₂ average percentage errors in weighted combinations with respect to MTR map and corresponding weights

3.5. Synthetic MRI

One application of the calculation of standard MRI intrinsic parameters is the synthesis of MR images at desired pulse sequences and sequence parameters to obtain optimum contrast. MR image synthesis basically consists of three steps:

- (a) acquisition of standard MR images at different TR and TE values,
- (b) computation of T_1 , T_2 , and ρ maps, and
- (c) calculation of a synthetic MR image by substituting the computed T_1 , T_2 , and ρ values into the equation describing the pulse sequence of interest with desired sequence timing parameters.

S.A. Bobman, S.J. Riederer, J.N. Lee, S.A. Suddarth, H.Z. Wang, and J.R. MacFall (1985) have shown that synthetic results can resemble actual spin-echo images within about 5% of the measured signal level for imaging of the brain. MR image synthesis can serve two main purposes: it can be used as an educational tool and it can be used for retrospective contrast optimization in clinical diagnosis work. In the following, we demonstrate the usefulness of MR image synthesis in obtaining good contrast in ROI compared with neighboring tissues.

Figure 3.5 first row shows T_1 , T_2 , and PD weighted images of patient with gliosis around cystic cavity. On T_1 weighted image the cystic cavity appears as hypo intensity (white arrow), but the gliosis is not visible clearly (black arrow) whereas on T_2 weighted image it merges with the cystic cavity (black arrow). PD weighted image shows a better separation of gliosis from cystic cavity and surrounding brain tissue compared to T_1 and T_2 weighted images. The second row shows the computed T_1 , T_2 and PD maps respectively. A good contrast in these images can be observed. The first image in the third row, the first magnetization transfer spin echo T_1 weighted (MT SE T_1) image, shows a clearer and bigger gliosis (black arrow) compared to PD weighted image. The next two images in the same row are two inversion recovery synthesized images with sequence parameters $TR/TE/TI = 2200/80/1500, 6000/40/2500$ ms respectively. The pulse sequence parameters were chosen so that these images show an excellent contrast between gliosis and cystic cavity (black arrows). Note that the size of the gliosis on these synthesized images matches with MT SE T_1 image. Since for a new study it may not be possible before hand to figure out the pulse sequences as well as their parameters which bring out the desired feature of interest, so long as the pathology depends only on the tissue parameters, the best strategy seems to be to determine these

tissue parameters first and then pass to different syntheses. The second image in the third row is a clear demonstration of the philosophy expounded in the previous sentence.

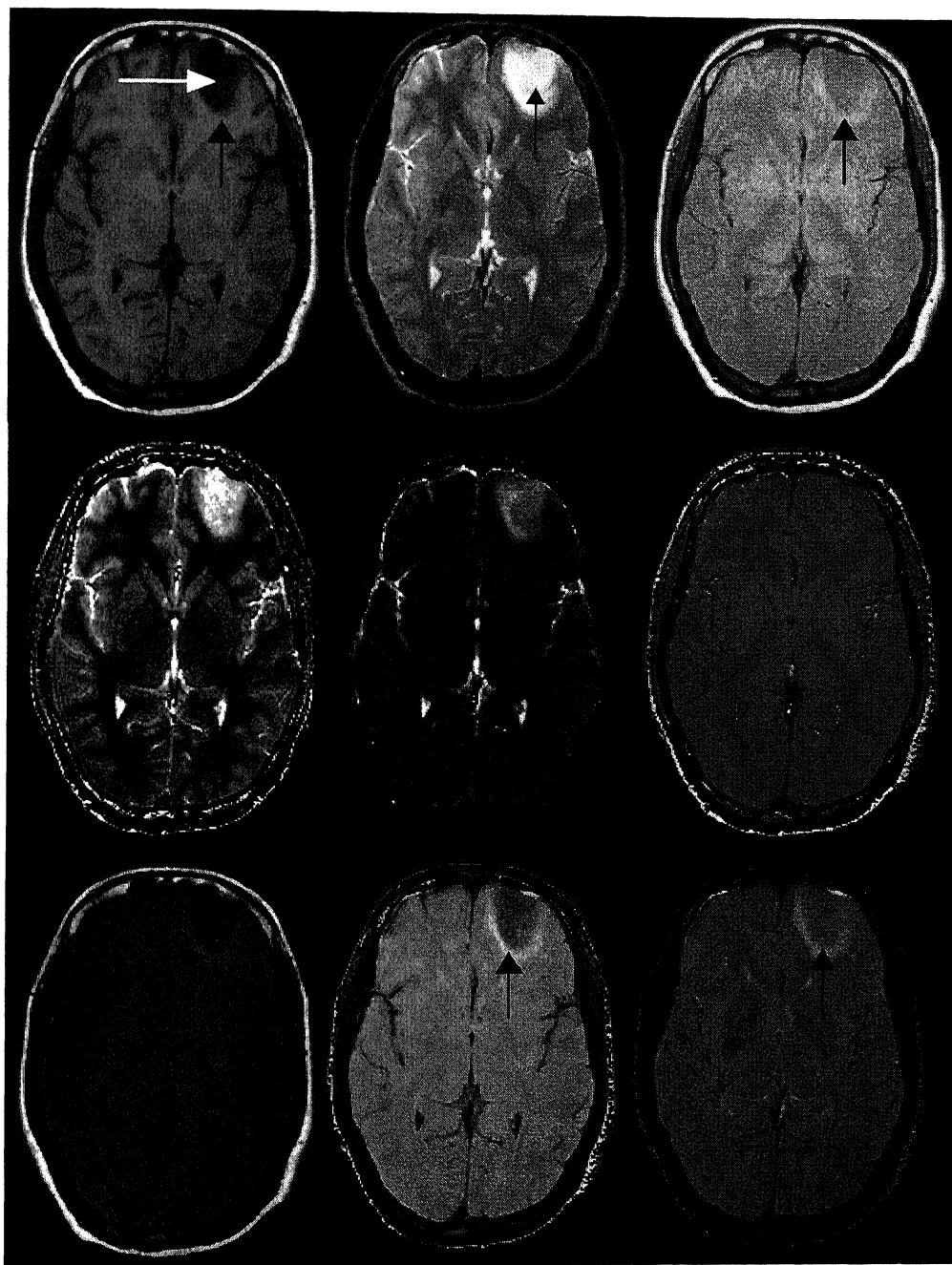


Figure 3.5: 1st row: T₁, T₂, PD weighted images
 2nd row: T₁, T₂, PD maps computed using weighted images
 3rd row: 1st image: MTSE T₁ weighted image
 2nd and 3rd images: Synthesized IRSE images at TR/TE/TI = 2200/80/1500,
 6000/40/2500 ms

3.6. Partial Volume Correction for Synthesis

In a large, homogeneous test object, regions for T_1 and T_2 estimation are available in which the entire voxel is filled with the same material. This is almost never the case in the living body. Obvious examples of this can be seen in the brain, where the gray brain tissue is a thin layer over the white matter, in intimate contact with it (and also with CSF). In such a case, a high proportion of voxels in the general gray matter regions will also contain, in variable amounts, white matter and/or CSF (M.A. Foster and A. Haase (1996)). Also, since the image reconstruction grid is small comparing with the object imaged, there would be more than one type of tissue near the boundaries that have contributed to signal in one pixel. It is observed that in these mixture signal cases, the iterative method presented in subsection 2.2.4 for tissue parameter estimation leads to divergent points (see Figure 2.6).

Suppose, in an MR image, m different neighbouring tissues are contributing to the signal of a pixel with different weights (say, ω_j ; $j = 1, \dots, m$) and we have m independent images corresponding to the same cross-section. It is assumed that sufficient independent data is available so that the tissue parameters associated with these m different tissues could be computed from it. Now the weights ω_j 's can be computed from the following system of equations

$$\sum_{j=1}^m \omega_j a_{ij} = S_i, \quad i=1,2,\dots,m,$$

subjected to $\sum_{j=1}^m \omega_j = 1$.

In the case of spin echo sequence,

$$a_{ij} = \rho_j (1 - 2 \exp(-(TR_i - TE_i/2)/T_{1j}) + \exp(-TR_i/T_{1j})) \exp(-TE_i/T_{2j}),$$

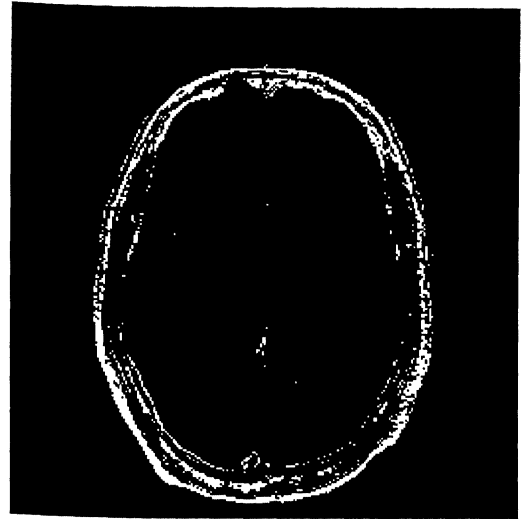
where T_{1j} , T_{2j} , and ρ_j are the T_1 , T_2 , and ρ mean values of the j th tissue and TE_i , TR_i are the echo and repetition times of the i th image. Once these weights are computed, it is possible to synthesize the pixels values corresponding to divergent points at different pulse sequences or sequence parameters.

Figure 3.6(a) shows the T_1 weighted ($TR/TE = 1012/14$ ms) image which is one of the three weighted images used for tissue parameter estimation. Figure 3.6(b) is the divergent map where the parameter values could not be computed. Figure 3.6(c) is the synthesized image with sequence parameters same as for T_1 weighted image. Image values are not computed at divergent points. Figure 3.6(d) is same as (c) except for correction at divergent points. Assuming three different types of tissue have contributed

to cause partial volume at each divergent pixel, the weights a_{ij} 's have been computed and used them in the synthesis. Resemblance of the synthesized pixels at divergent points in the cranial part (white arrows) could be observed. By using more images the synthesis could be improved.



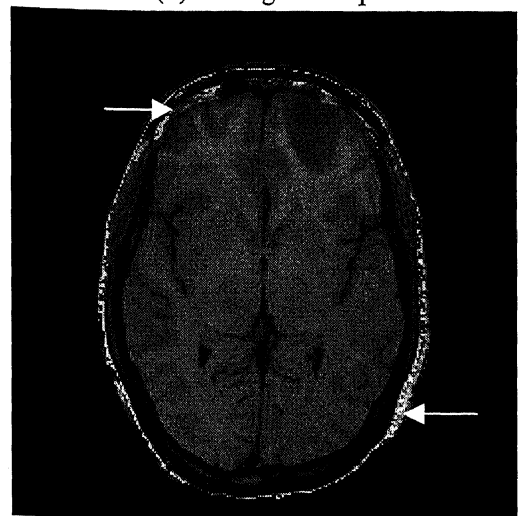
(a) T₁ weighted image



(b) Divergent Map



(c) Synthesized without partial volume correction



(d) Synthesized with partial volume correction

Figure 3.6 : Demonstration of partial volume correction for image synthesis

3.7. Tissue Parameter Maps for Segmentation

Segmentation refers to a subclass of enhancement methods by which a particular object, organ, or image characteristic is extracted from the image data for purposes of visualization and measurement. Segmentation involves associating a pixel with a particular object class based on the local intensity, spatial position, neighboring pixels, or prior information about the shape characteristics of the object class. Segmentation is a central problem of image analysis because it is a prerequisite for the majority of analysis methods including image restoration, shape analysis, motion detection, quantitative analysis of pathologies, and volume and area estimation. Even though MRI images have excellent tissue contrast compared with images produced by other medical imaging modalities, there are no clear boundaries between different organs. Therefore, the segmentation methods based on thresholding and boundary detection would not give satisfactory results. Some statistical methods use pixel intensities and its neighborhood information for segmentation. On the basis of normal distribution of pixel intensities in different regions (segments), segmentation can be done by maximizing the likelihood estimation function (R.K.S. Rathore, S. Datta, R.K. Gupta, S.B. Rao, R. Verma (2001)). All these methods depend upon pixel intensity and its neighborhood. It is observed that in different segments tissue parameters are normally distributed. In Figure 3.7, the histograms of pixel intensities of white matter in T_1 , T_2 , and PD weighted images and histograms of corresponding tissue parameter maps is shown. The normal distribution of tissue parameters within the ROI may be observed. This motivates to use tissue parameter maps for segmentation methods like MLE. Since, in most of the diseases, the parameter values are significantly different from the normal tissues, these maps may give satisfactory segmentations. However, there may be some pulse sequences which could produce good contrast in the images than in the parameter maps and consequently better segmentation. Table 3.5 shows the contrast between some brain tissues in the case of parameters as well as in weighted spin echo images. The weighted images are considered with $TR/TE = 500/15, 2200/80, 20$ ms.

Inherent Tissue Contrast

Tissue contrast derives primarily from inherent ρ , T_1 , and T_2 differences. Other sources of tissue contrast are flow, magnetic susceptibility inhomogeneities, and

chemical shift. Inherent ρ , T_1 , and T_2 contrast between two tissues (A and B) can be defined in terms of the characteristics of the two tissues as follows (R.E. Hendrick (1999)):

$$C_{\rho} = \frac{\rho_B - \rho_A}{\rho_B + \rho_A},$$

$$C_{T_1} = \frac{T_{1_B} - T_{1_A}}{T_{1_B} + T_{1_A}},$$

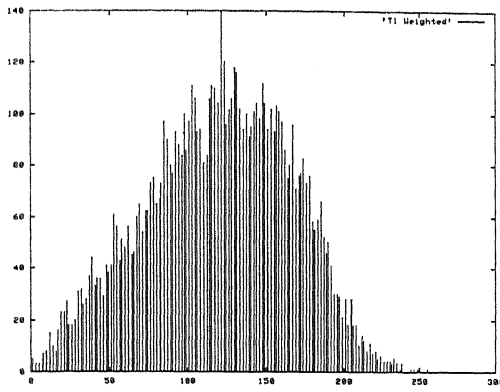
$$C_{T_2} = \frac{T_{2_B} - T_{2_A}}{T_{2_B} + T_{2_A}}.$$

Inherent tissue properties remain essentially unchanged regardless of the imaging method. Although defined only for MRI, T_1 , T_2 , and ρ will not change simply because a different pulse sequence or a different set of timing parameters is chosen.

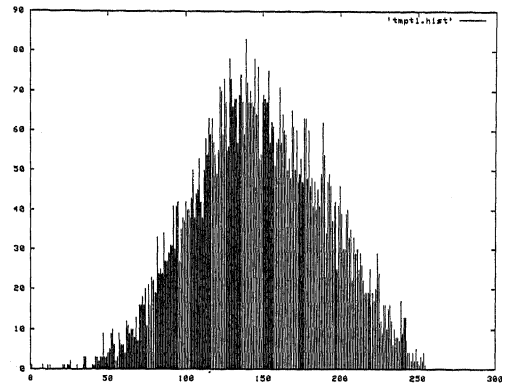
Tissue Types	Parameter Contrast			Signal Contrast (SE)		
	T_1	T_2	PD	T_1 wtd. (500/15)	T_2 wtd. (2200/80)	PD wtd. (2200/20)
Gray-White	0.196850	0.069444	0.061538	0.055296	0.114861	0.058711
-CSF	0.554252	0.568627	0.183432	0.256499	0.287247	0.019660
-Edema	0.084337	0.241379	0.109677	0.085642	0.285852	0.142429
White-CSF	0.677215	0.613833	0.242236	0.307434	0.389265	0.078281
-Edema	0.276596	0.305699	0.170068	0.030490	0.387974	0.199471
CSF-Edema	0.492958	0.379310	0.075269	0.334786	0.001521	0.123113

Table 3.5: Contrast measurements in tissue parameter maps and weighted images between different brain tissues

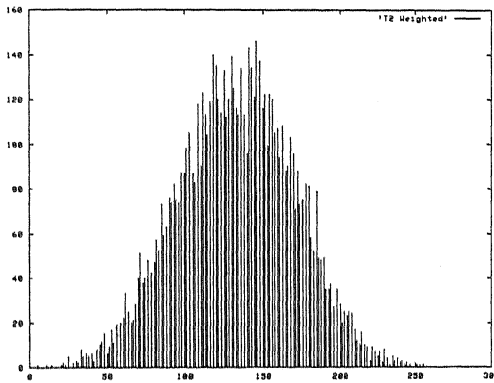
The first column of Figure 3.8(a) shows T_1 , T_2 , and proton density weighed spin echo images and second column shows the computed tissue parameter maps using these weighted images and have better contrast than the weighted images. First column of Figure 3.8(b) shows weighted combinations of weighted images with weights calculated using T_1 , T_2 , and ρ maps respectively. These have got an excellent contrast compared to weighted images similar to parameter maps. Second column of Figure 3.8(b) demonstrates the segmented images using weighted images, parameter maps, and weighted combination images respectively. Segmentation is done using a variant of maximum likelihood estimation (R.K.S. Rathore, S. Datta, R.K. Gupta, S.B. Rao and R. Verma (2001)).



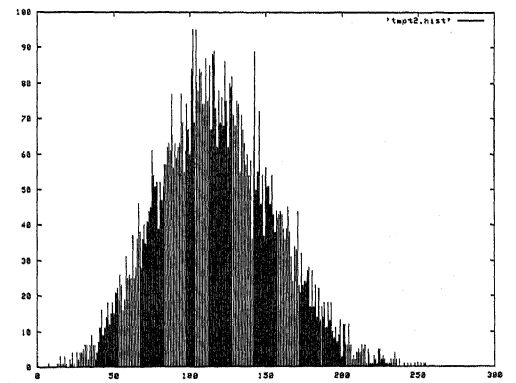
T₁ weighted



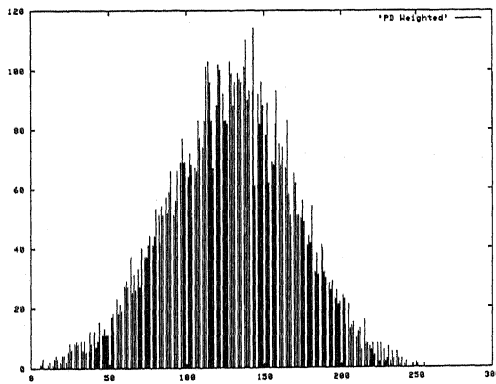
T₁ Map



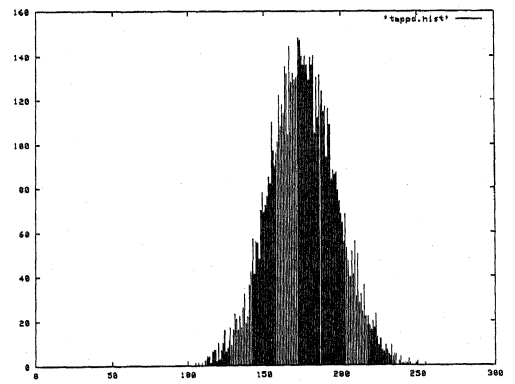
T₂ weighted



T₂ Map

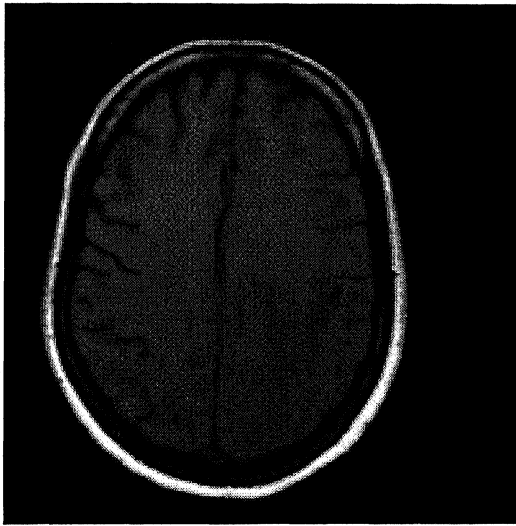


PD weighted

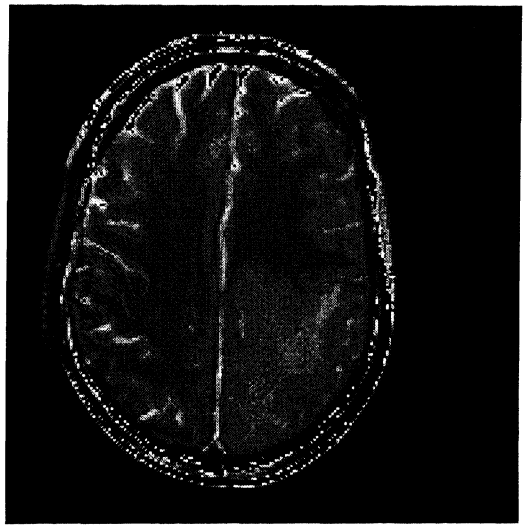


PD Map

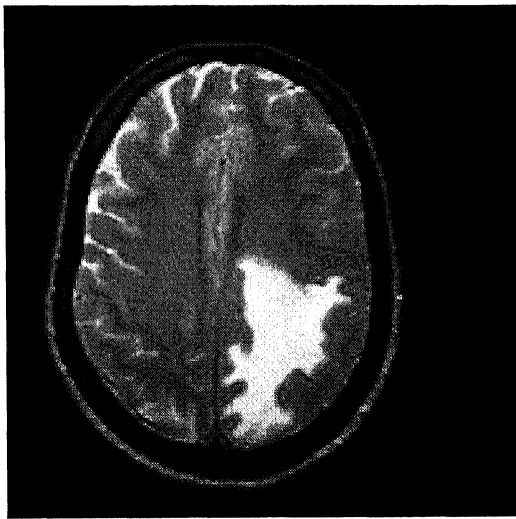
Figure 3.7: Histogram plots of white matter values in weighted images and in computed parameter maps



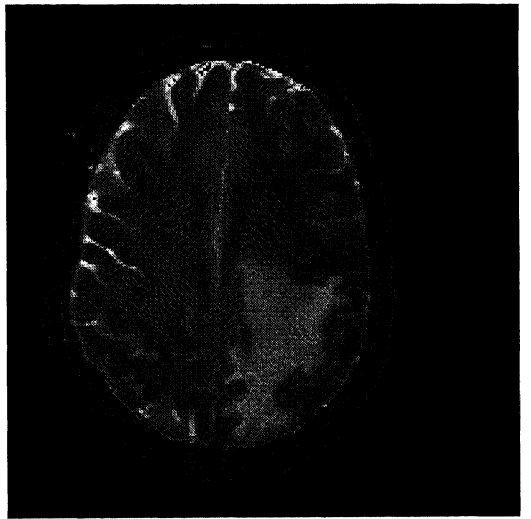
T_1 weighted



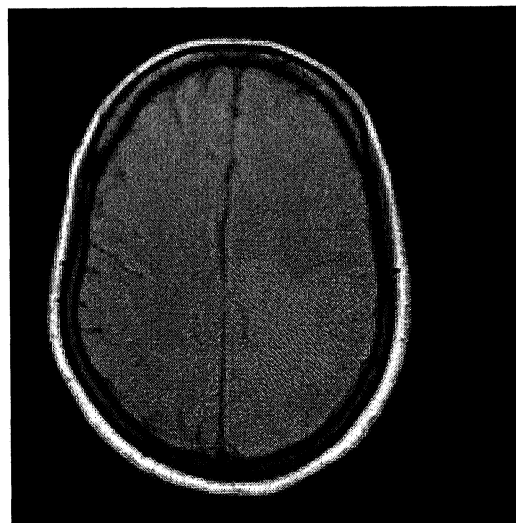
T_1 Map



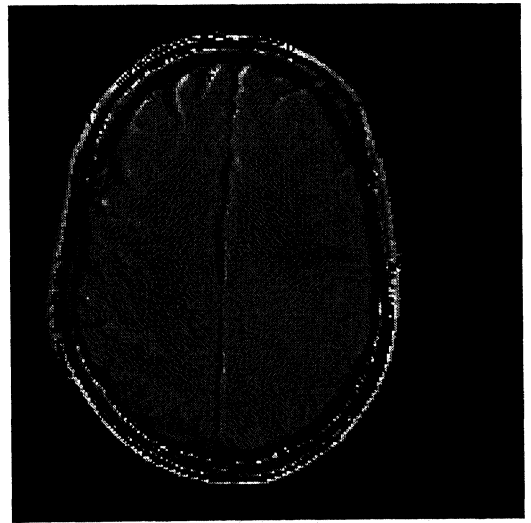
T_2 weighted



T_2 Map



PD weighted

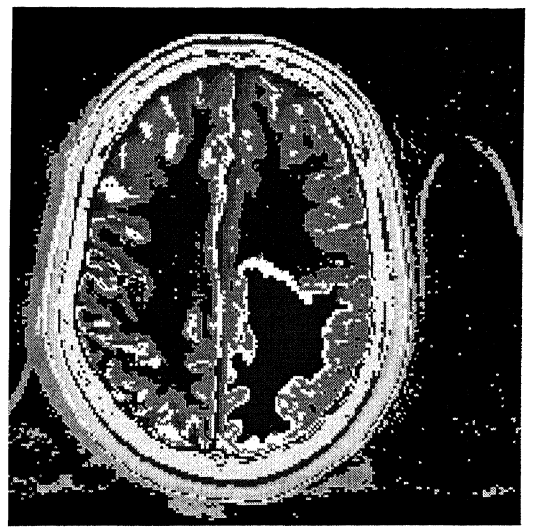


PD Map

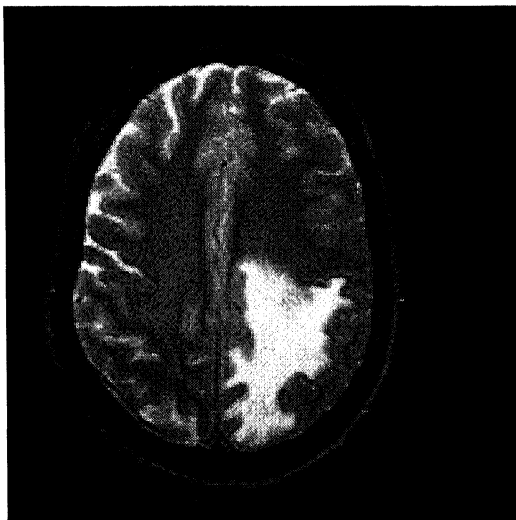
Figure 3.8(a): 1st column: weighted spin echo images 2nd column: corresponding computed parameter maps



Weighted combination with T_1



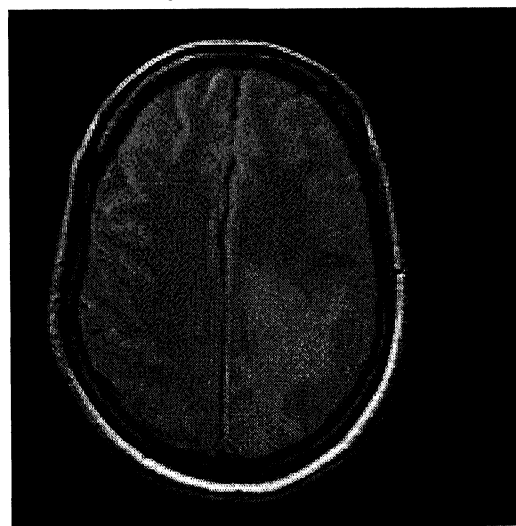
Segmented using weighted images



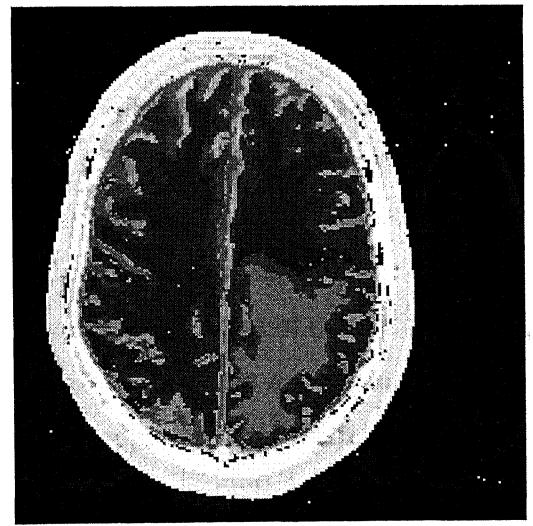
Weighted combination with T_2



Segmented using parameter maps



Weighted combination with PD



Segmented using weighted combinations

Figure 3.8(b): 1st column: weighted combination images 2nd column: segmented with different images

Chapter 4

Quantitation of Cystic Cavity, Perilesional Gliosis, and Edema

In this chapter three pathologies: cystic cavity, gliosis and edema, are quantitatively analyzed. Magnetization transfer spin-echo T_1 (MT SE T_1), T_1 , T_2 and PD weighted images along with the corresponding MTR, T_1 , T_2 and PD computed maps are used for the present quantitative study. T_1 , T_2 , and PD maps are computed using the method described in subsection 2.2.4 of chapter 2. MTR values are computed as mentioned in subsection 1.2.4 of chapter 1. All the weighted images are normalized to have values from 0 to 255 so that the computed numericals on weighted images could be compared. Parameter values are used without any normalization because of their significance and existing standards of quantitative MRI in medicine. Even though it is customary to represent PD computed values with respect to CSF, in the present study these values are presented as they are obtained. First, each pathological region is segmented using the multi-resolution MLE algorithm (R.K.S. Rathore, S. Datta, R.K. Gupta, S.B. Rao, and R. Verma (2001)) with T_1 , T_2 , and PD parameter maps to obtain the required region of interest (ROI). For comparison purpose, the contra-lateral normal region is selected by carefully placing the same size and shape of the segmented pathological region on the opposite hemisphere of the brain on each slice. This is done to have almost same number and type of tissue components in the pathological region as well as in the normal region. Otherwise, the comparison would not be justified. In some cases it may not be possible to select in this manner. For example, in the case of edema, in one of the slices, the pathological region has pushed the lateral ventricle and if one chooses the contra-lateral normal region in same location on opposite hemisphere of the brain, it would contain sufficient amount of contribution from CSF in the ventricle and consequently would contaminate the quantitative values. In such critical cases, keeping physiological structures in view, a small part of the segmented pathological region is ignored to obtain more meaningful contra-lateral normal region.

For the present study, MR imaging of the brain is performed on 1.5T superconducting system using circularly polarized head coil. Conventional spin-echo proton density, T_2 (TR/TE/1,2/n=2200/12,80/1), and T_1 (1012/14/2) weighted imaging is performed in axial plane using 256x256 matrix size, 0.1 mm inter-slice gap and 5mm slice thickness. MT SE T_1 weighted MR imaging is performed with exactly the same parameters as for T_1 weighted except for the off-resonance pulse.

In section 4.1, the statistical tools used for the quantitative analysis are discussed. Sections 4.2, 4.3, and 4.4 are devoted to the quantitative study of the pathologies: cystic cavity, perilesional gliosis, and edema with respect to the contra-lateral normal regions.

4.1. Statistical Tools

Following W.H. Press, S.A. Tenkolsky, W.T. Vellerling, and B.D. Flannery (1998), in subsections 4.1.1 and 4.1.2, F-test and Student's t test and their probability functions are briefly described. These are used to study the significance of differences in variances and means in pathological regions compared with contra-lateral normal regions. In subsection 4.1.3, formula for computing linear correlation coefficients is given.

4.1.1. F-test for Significantly Different Variances

The F-test tests the hypothesis that two samples have different variances by trying to reject the null hypothesis that their variances are actually consistent. The statistic F is the ratio of one variance to the other, so values either $\gg 1$ or $\ll 1$ will indicate very significant differences.

F-distribution Probability Function

A certain statistic F, essentially the ratio of the observed dispersion of the first sample to that of the second one, is calculated. The probability that F would be as large as it is if the first sample's underlying distribution actually has smaller variance than the second's is denoted $Q(F | \nu_1, \nu_2)$ where ν_1, ν_2 are the number of degrees of freedom in the first and second samples respectively. In other words, $Q(F | \nu_1, \nu_2)$ is the significance level at which the hypothesis "1 has smaller variance than 2" can be rejected. A small numerical value implies a very significant rejection, in turn implying high confidence in the hypothesis "1 has variance greater or equal 2."

$Q(F | \nu_1, \nu_2)$ has the limiting values

$$Q(0 | \nu_1, \nu_2) = 1 \quad \text{and} \quad Q(\infty | \nu_1, \nu_2) = 0.$$

Its relation to the incomplete beta function $I_x(a, b)$ is

$$Q(F | \nu_1, \nu_2) = I_{\frac{\nu_2}{\nu_2 + \nu_1 F}}\left(\frac{\nu_2}{2}, \frac{\nu_1}{2}\right).$$

4.1.2. Student's t-test for Significantly Different Means

Applying the concept of standard error, the conventional statistic for measuring the significance of a difference of means is termed Student's t . When the two distributions are thought to have the same variance, but possibly different means, then Student's t is computed as follows: First estimate the standard error of the difference of the means, S_D , from the "pooled variance" by the formula

$$S_D = \sqrt{\frac{\sum_{i \in A} (x_i - \bar{x}_A)^2 + \sum_{i \in B} (x_i - \bar{x}_B)^2}{N_A + N_B - 2} \left(\frac{1}{N_A} + \frac{1}{N_B} \right)},$$

where each sum is over the points in one sample, the first or second, each mean likewise refers to one sample or the other, and N_A and N_B are the numbers of points in the first and second samples, respectively.

Now the Student's t statistic can be computed from

$$t = \frac{\bar{x}_A - \bar{x}_B}{S_D},$$

and degrees of freedom can be computed from

$$df = N_A + N_B - 2.$$

If two distributions have significantly different variances, the t statistic can be computed from

$$t = \frac{\bar{x}_A - \bar{x}_B}{\left[\text{Var}(x_A)/N_A + \text{Var}(x_B)/N_B \right]^{1/2}},$$

and degrees of freedom can be computed from

$$df = \frac{\left[\frac{\text{Var}(x_A)}{N_A} + \frac{\text{Var}(x_B)}{N_B} \right]^2}{\frac{[\text{Var}(x_A)/N_A]^2}{N_A - 1} + \frac{[\text{Var}(x_B)/N_B]^2}{N_B - 1}}.$$

To find out whether the two data sets have variances that are significantly different, the F-test described in the previous section can be used.

Student's Distribution Probability Function

$A(t | \nu)$ is the probability, for ν degrees of freedom, that a certain statistic t (measuring the observed difference of means) would be smaller than the observed value if the means were in fact the same. Two means are significantly different if, e.g., $A(t | \nu) > 0.99$. In other words, $1 - A(t | \nu)$ is the significance level at which the hypothesis that the means are equal is disproved.

The mathematical definition of the function is

$$A(t | \nu) = \frac{1}{\nu^{1/2} B(\frac{1}{2}, \frac{\nu}{2})} \int_{-t}^t (1 + \frac{x^2}{\nu})^{-\frac{\nu+1}{2}} dx.$$

Limiting values are

$$A(0 | \nu) = 0, \quad A(\infty | \nu) = 1.$$

$A(t | \nu)$ is related to the incomplete beta function $I_x(a, b)$ by

$$A(t | \nu) = 1 - I_{\frac{\nu}{\nu+t^2}}(\frac{\nu}{2}, \frac{1}{2}).$$

4.1.3. Linear Correlation Coefficients

Linear correlation coefficient, r for pair of quantities (x_i, y_i) , $i = 1, \dots, N$, can be computed by the formula

$$r = \frac{\sum_i (x_i - \bar{x})(y_i - \bar{y})}{\sqrt{\sum_i (x_i - \bar{x})^2} \sqrt{\sum_i (y_i - \bar{y})^2}},$$

where \bar{x} is the mean of x_i 's and \bar{y} is the mean of y_i 's.

4.2. Quantitation of Cystic Cavity

In this section we have considered a case of young man of 35 years old with trauma in frontal lobe in 1997. For two years patient was asymptomatic but, after two years patient presented with intractable complex partial seizures with headache. MRI was done in

of encephalomalacia and cystic cavity. This is hyperintense on T_2 and hypointense on T_1 weighted images. On MT SE T_1 weighted image, there is gliosis which is hyperintense and this abnormality is beyond the T_2 abnormality. Five consecutive cross-sections of each 5mm thickness and 0.1mm inter-slice gap are considered and these are through the level of body lateral ventricles to third ventricles.

Table 4.1 shows relatively low mean values in the cystic cavity regions compared with the corresponding contra-lateral normal regions on MT SE T_1 weighted images. Variances in cystic cavity are relatively low. Significantly low mean and variances of MTR values in cystic cavity regions could be observed in Table 4.2.

MT SE T_1 wtd.	Mean \pm S.D.		t	P	F	P
	Normal	Cystic cavity				
Slice 1	75.00 \pm 5.28	72.55 \pm 3.57	10.165935	1.80e-23	2.189308	1.50e-24
Slice 2	74.15 \pm 6.72	63.81 \pm 4.49	38.567856	0.00e+00	2.233288	5.87e-33
Slice 3	69.25 \pm 6.71	61.68 \pm 3.50	25.750343	0.00e+00	3.666865	0.00e+00
Slice 4	71.83 \pm 5.35	57.39 \pm 4.86	59.287617	0.00e+00	1.213515	4.09e-03
Slice 5	69.61 \pm 6.99	64.01 \pm 5.77	17.028128	0.00e+00	1.466500	1.46e-07

Table 4.1: Mean and standard deviation of normal and cystic cavity regions and Student's t, F statistics and their probabilities on MTSE T_1 weighted images

MTR	Mean \pm S.D.		t	P	F	P
	Normal	Cystic cavity				
Slice 1	29.54 \pm 6.96	6.71 \pm 3.35	78.041046	0.00e+00	4.324141	0.00e+00
Slice 2	29.26 \pm 8.24	6.81 \pm 3.83	74.513878	0.00e+00	4.630295	0.00e+00
Slice 3	25.68 \pm 8.52	7.51 \pm 3.69	50.448616	0.00e+00	5.332147	0.00e+00
Slice 4	28.45 \pm 8.80	6.50 \pm 3.94	67.571609	0.00e+00	4.985687	0.00e+00
Slice 5	27.37 \pm 9.34	11.12 \pm 4.68	42.844620	0.00e+00	3.983310	0.00e+00

Table 4.2: Mean and standard deviation of normal and cystic cavity regions and Student's t, F statistics and their probabilities on MTR maps

Table 4.3 shows low mean pixel intensities in the cystic cavity regions with respect to the corresponding normal regions on T_1 weighted spin echo images. The variances in cystic cavity are significantly low. In contrast to the weighted images T_1 maps show significantly high T_1 relaxation times in pathological region compared with the corresponding normal regions as shown in Table 4.4.

T_1 wtd.	Mean \pm S.D.		t	P	F	P
	Normal	Cystic cavity				
Slice 1	99.29 \pm 12.56	71.77 \pm 4.18	54.964119	0.00e+00	0.00e+00	0.00e+00
Slice 2	104.25 \pm 16.25	67.02 \pm 5.14	65.873589	0.00e+00	0.00e+00	0.00e+00
Slice 3	89.91 \pm 15.28	63.28 \pm 3.86	43.552238	0.00e+00	0.00e+00	0.00e+00
Slice 4	94.87 \pm 13.62	57.10 \pm 5.40	76.549767	0.00e+00	0.00e+00	0.00e+00
Slice 5	96.64 \pm 15.50	71.60 \pm 7.68	39.895119	0.00e+00	0.00e+00	0.00e+00

Table 4.3: Mean and standard deviation of normal and cystic cavity regions and Student's t, F statistics and their probabilities on T_1 weighted images

T_1 values	Mean \pm S.D.		t	P	F	P
	Normal	Cystic cavity				
Slice 1	1091.88 \pm 488.11	1970.73 \pm 224.24	-43.25634	0.00e+00	4.73813	0.00e+00
Slice 2	1101.01 \pm 796.97	2297.30 \pm 337.48	-41.69613	0.00e+00	5.57658	0.00e+00
Slice 3	1305.80 \pm 775.07	2095.73 \pm 309.57	-24.40706	0.00e+00	6.26817	0.00e+00
Slice 4	1017.91 \pm 473.09	2694.97 \pm 424.75	-78.36119	0.00e+00	1.24057	1.38e-03
Slice 5	1182.33 \pm 627.67	2069.66 \pm 344.29	-34.15867	0.00e+00	3.32356	0.00e+00

Table 4.4: Mean and standard deviation of normal and cystic cavity regions and Student's t, F statistics and their probabilities on T_1 maps

Tables 4.5 and 4.6 show high mean values with less variances in the cystic cavity region compared with normal regions on both T_2 weighted image and T_2 map. Similar to T_1 weighted images and T_1 maps, cystic cavity has relatively low pixels intensities on PD weighted images and high mean values on PD maps compared with normal regions as shown in Tables 4.7 and 4.8 respectively.

T_2 wtd.	Mean \pm S.D.		t	P	F	P
	Normal	Cystic cavity				
Slice 1	145.21 \pm 26.65	223.87 \pm 12.93	-70.190910	0.00e+00	4.249898	0.00e+00
Slice 2	130.75 \pm 26.06	192.90 \pm 14.69	-62.642597	0.00e+00	3.145190	0.00e+00
Slice 3	124.50 \pm 25.65	177.36 \pm 9.46	-49.847652	0.00e+00	7.343417	0.00e+00
Slice 4	115.97 \pm 24.97	167.90 \pm 14.25	-53.653759	0.00e+00	3.070495	0.00e+00
Slice 5	123.69 \pm 24.96	187.48 \pm 16.69	-58.517342	0.00e+00	2.235762	7.66e-28

Table 4.5: Mean and standard deviation of normal and cystic cavity regions and Student's t, F statistics and their probabilities on T_2 weighted images

T₂ values	Mean ± S.D.		t	P	F	P
	Normal	Cystic cavity				
Slice 1	72.88±24.97	145.22±16.43	-63.972527	0.00e+00	2.307844	1.19e-27
Slice 2	69.84±30.63	127.20±17.97	-48.714535	0.00e+00	2.906606	0.00e+00
Slice 3	80.65±44.52	150.82±19.60	-37.199162	0.00e+00	5.157619	0.00e+00
Slice 4	74.76±62.09	131.23±18.16	-25.940105	0.00e+00	11.678875	0.00e+00
Slice 5	73.47±26.68	135.65±20.54	-50.875862	0.00e+00	1.686646	8.13e-13

Table 4.6: Mean and standard deviation of normal and cystic cavity regions and Student's t, F statistics and their probabilities on T₂ maps

PD wtd.	Mean ± S.D.		t	P	F	P
	Normal	Cystic cavity				
Slice 1	130.47±6.54	121.55±4.94	28.747776	0.00e+00	1.757371	1.34e-13
Slice 2	144.52±8.69	129.91±5.95	41.817730	0.00e+00	2.132167	1.56e-29
Slice 3	134.08±9.29	118.50±3.73	40.109089	0.00e+00	6.176240	0.00e+00
Slice 4	139.78±8.95	124.99±7.44	37.722557	0.00e+00	1.444870	5.05e-08
Slice 5	140.41±10.84	133.24±8.64	14.249944	2.45e-43	1.572978	5.24e-10

Table 4.7: Mean and standard deviation of normal and cystic cavity regions and Student's t, F statistics and their probabilities on PD weighted images

PD values	Mean ± S.D.		t	P	F	P
	Normal	Cystic cavity				
Slice 1	1558.15±107.13	1564.29±96.33	-1.12700	2.60e-01	1.23685	5.01e-03
Slice 2	1620.92±184.10	1665.55±118.54	-6.14876	9.57e-10	2.41172	4.94e-39
Slice 3	1509.61±107.68	1600.32±155.24	-12.38100	2.12e-33	2.07856	1.07e-20
Slice 4	1586.43±115.57	1773.32±143.89	-30.08028	0.00e+00	1.55016	8.98e-11
Slice 5	1581.26±162.41	1629.70±130.91	-6.39808	2.09e-10	1.53924	3.28e-09

Table 4.8: Mean and standard deviation of normal and cystic cavity regions and Student's t, F statistics and their probabilities on PD maps

Linear correlation coefficients between different weighted images in the cystic cavity region and contra-lateral normal region are tabulated in Tables 4.9 and 4.10 respectively. MT weighted values are strongly positively correlated with T₁ weighted and PD weighted values while negatively correlated with T₂ weighted values in the normal regions. In the cystic cavity region, MT weighted values showed same kind of

correlation with T_1 , and PD weighted values as in the case of normal regions. But, with T_2 weighted values MT SE T_1 weighted values have shown negative correlation compared with contra-lateral normal regions unlike in pathological regions. In the normal regions, T_2 weighted values are strongly negatively correlated with T_1 and PD weighted values while T_1 and PD weighted values are positively correlated. In contrast to the normal regions, T_2 weighted values are positively correlated with T_1 and PD weighted values in the cystic cavity region. But the T_1 and PD weighted values maintained same correlation as in the case of normal regions.

Tables 4.11 and 4.12 show the linear correlation coefficients between different tissue parameters in the normal and cystic cavity regions respectively. MTR map has shown negative correlations with T_1 , T_2 , and PD maps in both the regions. T_1 , T_2 , and PD maps are positively correlated among themselves in the normal regions. In the cystic cavity region, T_1 with T_2 and PD maps has shown positive correlation while T_2 has negative correlation with PD map which is not very significant.

Graphs 4.1-4.4 show the mean values in cystic cavity and contra-lateral normal regions on weighted images in consecutive five slices. On MT SE T_1 , T_1 , and PD weighted images, the mean values in cystic cavity region are less than the mean values in normal regions. But, on T_2 weighted image mean values in pathological regions are higher than in normal regions. Graphs 4.5-4.8 show the mean values in pathological regions and normal regions on computed parameter maps. On T_1 , T_2 , and PD maps, mean values in cystic cavity regions are higher compared with normal regions. But, on MTR map normal region showed high values than in cystic cavity region.

Weighted normal regions	r(MT, T ₁)		r(MT, T ₂)		r(MT, PD)		r(T ₁ , T ₂)		r(T ₁ , PD)		r(T ₂ , PD)	
	Normal	P	Normal	P	Normal	P	Normal	P	Normal	P	Normal	P
Slice 1	0.7682	0.00e+00	-0.6504	0.00e+00	0.6500	0.00e+00	-0.9151	0.00e+00	0.3704	3.40e-24	-0.1772	2.38e-06
Slice 2	0.8454	0.00e+00	-0.6652	0.00e+00	0.6955	0.00e+00	-0.8676	0.00e+00	0.5295	0.00e+00	-0.3104	8.30e-22
Slice 3	0.8692	0.00e+00	-0.6359	0.00e+00	0.7865	0.00e+00	-0.8469	0.00e+00	0.6177	0.00e+00	-0.3406	1.47e-19
Slice 4	0.7115	0.00e+00	-0.2014	1.54e-09	0.5879	0.00e+00	-0.7148	0.00e+00	0.5173	0.00e+00	-0.2330	2.32e-12
Slice 5	0.6965	0.00e+00	-0.1387	1.25e-04	0.4814	2.80e-45	-0.5882	0.00e+00	0.5914	0.00e+00	-0.0278	4.43e-01

Table 4.9: Linear correlation coefficients between different weighted images in normal regions

Weighted cystic regions	r(MT, T ₁)		r(MT, T ₂)		r(MT, PD)		r(T ₁ , T ₂)		r(T ₁ , PD)		r(T ₂ , PD)	
	Cystic cavity	P	Cystic cavity	P	Cystic cavity	P	Cystic cavity	P	Cystic cavity	P	Cystic cavity	P
Slice 1	0.7742	0.00e+00	0.1172	1.89e-03	0.5948	0.00e+00	0.0717	5.78e-02	0.6548	0.00e+00	0.4271	2.05e-32
Slice 2	0.8375	0.00e+00	0.1082	1.07e-03	0.6553	0.00e+00	0.0984	2.93e-03	0.7165	0.00e+00	0.3278	2.91e-24
Slice 3	0.7619	0.00e+00	0.4110	1.52e-28	0.3089	3.36e-16	0.4092	2.79e-28	0.3081	4.10e-16	0.1258	1.13e-03
Slice 4	0.8646	0.00e+00	0.3457	3.19e-26	0.6833	0.00e+00	0.3823	3.78e-32	0.8000	0.00e+00	0.5109	0.00e+00
Slice 5	0.8622	0.00e+00	0.3023	1.49e-17	0.6156	0.00e+00	0.3468	6.12e-23	0.7423	0.00e+00	0.5501	0.00e+00

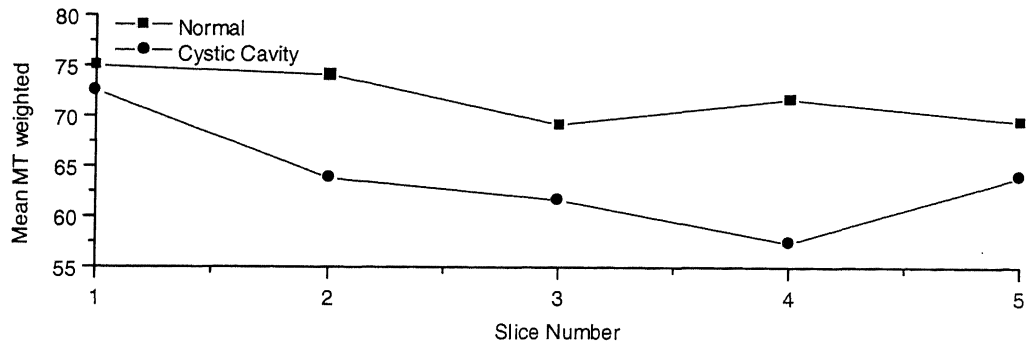
Table 4.10: Linear correlation coefficients between different weighted images in cystic cavity regions

Parametric normal region	r(MTR, T ₁)		r(MTR, T ₂)		r(MTR, PD)		r(T ₁ , T ₂)		r(T ₁ , PD)		r(T ₂ , PD)	
	Normal	P	Normal	P	Normal	P	Normal	P	Normal	P	Normal	P
Slice 1	-0.8694	0.00e+00	-0.7652	0.00e+00	-0.5607	0.00e+00	0.8734	0.00e+00	0.6395	0.00e+00	0.2617	1.97e-12
Slice 2	-0.8022	0.00e+00	-0.7447	0.00e+00	-0.5239	0.00e+00	0.7328	0.00e+00	0.8092	0.00e+00	0.2880	7.19e-19
Slice 3	-0.8626	0.00e+00	-0.7700	0.00e+00	-0.5431	0.00e+00	0.8498	0.00e+00	0.7106	0.00e+00	0.3764	7.57e-24
Slice 4	-0.8586	0.00e+00	-0.5445	0.00e+00	-0.1136	7.13e-04	0.3418	1.31e-25	0.3948	2.57e-34	0.2976	1.61e-19
Slice 5	-0.7168	0.00e+00	-0.7109	0.00e+00	-0.0998	5.88e-03	0.5034	0.00e+00	0.5940	0.00e+00	0.1207	8.59e-04

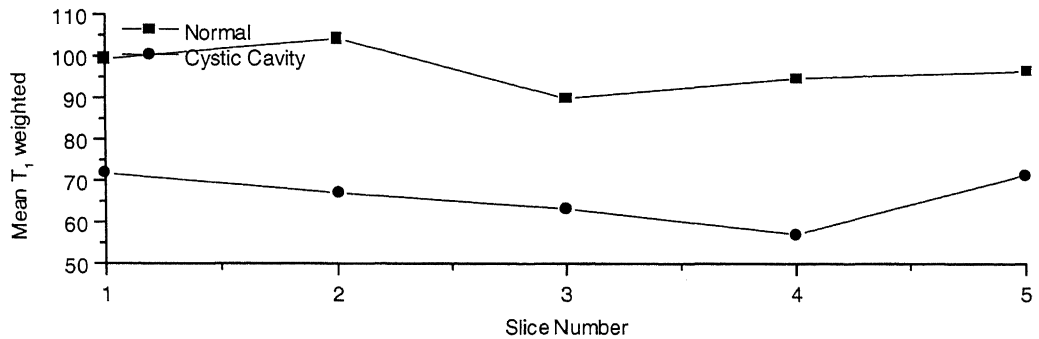
Table 4.11: Linear correlation coefficients between different parameter maps in normal regions

Parametric cystic region	r(MTR, T ₁)		r(MTR, T ₂)		r(MTR, PD)		r(T ₁ , T ₂)		r(T ₁ , PD)		r(T ₂ , PD)	
	Cystic cavity	P	Cystic cavity	P	Cystic cavity	P	Cystic cavity	P	Cystic cavity	P	Cystic cavity	P
Slice 1	-0.4903	1.27e-43	-0.2065	3.50e-08	-0.1579	2.68e-05	0.2686	4.88e-13	0.7004	0.00e+00	-0.1513	5.81e-05
Slice 2	-0.4323	8.73e-43	-0.1421	1.65e-05	-0.2268	4.22e-12	0.3274	3.27e-24	0.7178	0.00e+00	-0.0815	1.39e-02
Slice 3	-0.4326	9.34e-32	-0.0687	7.62e-02	-0.3263	5.48e-18	0.3828	1.11e-24	0.8548	0.00e+00	-0.0193	6.17e-01
Slice 4	-0.4808	0.00e+00	-0.1500	7.43e-06	-0.1483	9.44e-06	0.1612	1.45e-06	0.6787	0.00e+00	-0.1819	5.12e-08
Slice 5	-0.4804	2.80e-45	-0.1500	3.23e-05	-0.0135	7.08e-01	0.1924	8.72e-08	0.5746	0.00e+00	-0.1888	1.54e-07

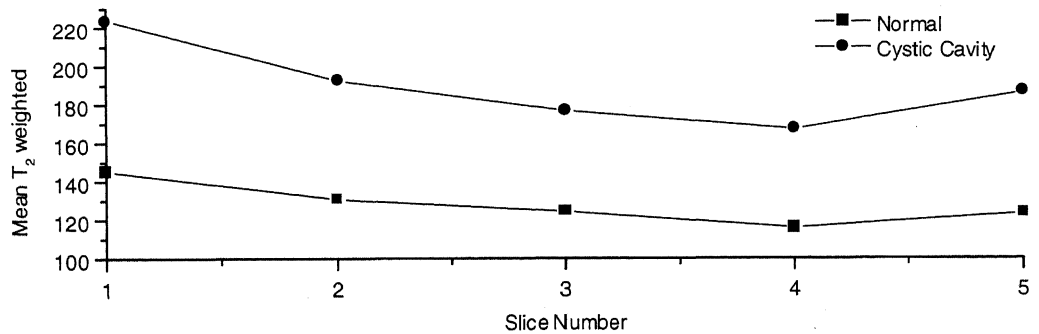
Table 4.12: Linear correlation coefficients between different parameter maps in cystic cavity regions



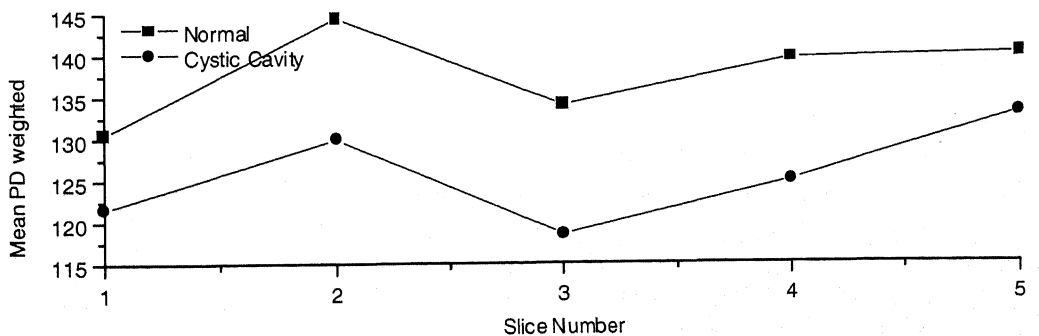
Graph 4.1: Mean values in cystic cavity and contra-lateral normal regions on MT SE T_1 weighted images



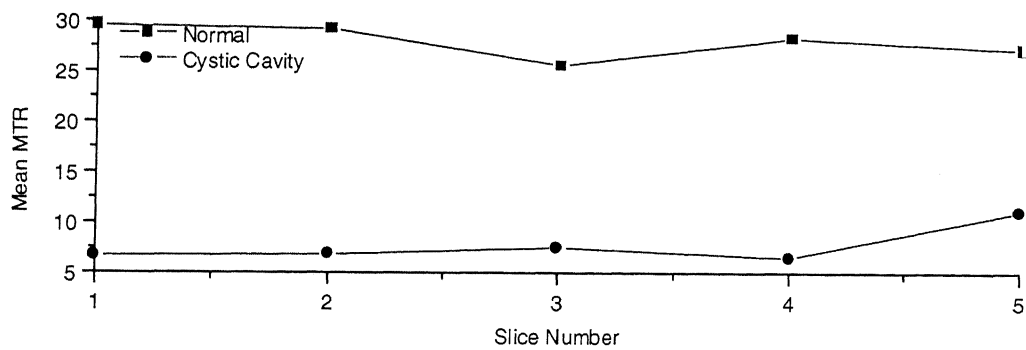
Graph 4.2: Mean values in cystic cavity and contra-lateral normal regions on T_1 weighted images



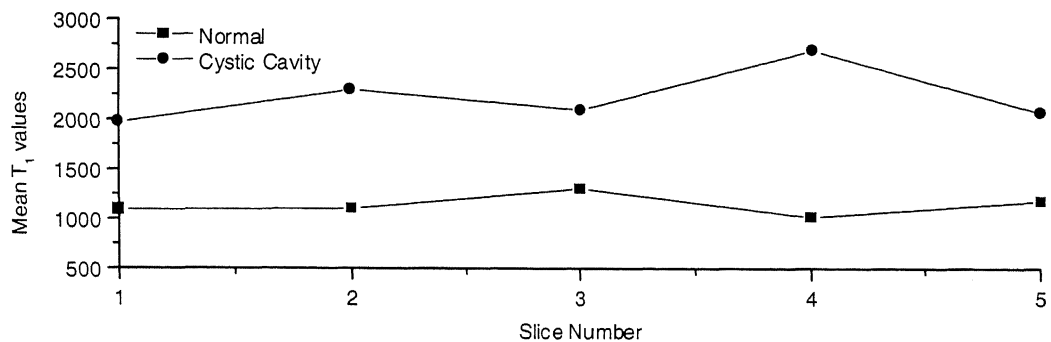
Graph 4.3: Mean values in Cystic cavity and contra-lateral normal regions on T_2 weighted images



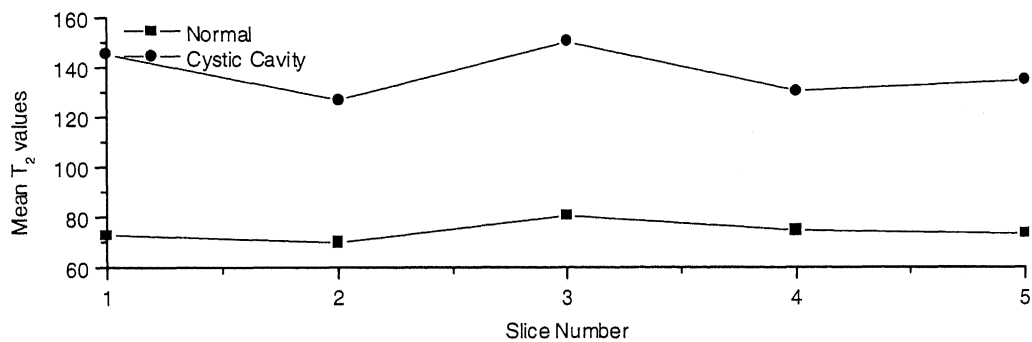
Graph 4.4: Mean values in Cystic cavity and contra-lateral normal regions on PD weighted images



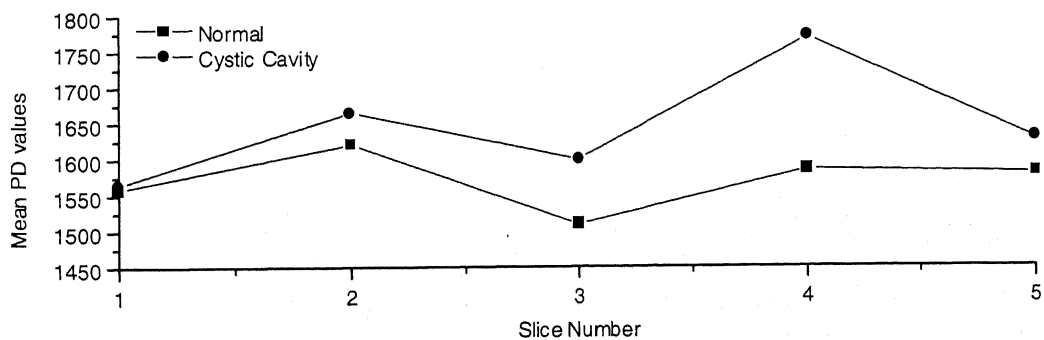
Graph 4.5: Mean values in cystic cavity and contra-lateral normal regions on MTR maps



Graph 4.6: Mean values in cystic cavity and contra-lateral normal regions on T₁ maps



Graph 4.7: Mean values in Cystic cavity and contra-lateral normal regions on T₂ maps



Graph 4.8: Mean values in Cystic cavity and contra-lateral normal regions on PD maps

4.3. Quantitation of Perilesional Gliosis

Neurocysticercosis is the most common parasitic disease of the central nervous system in the developing countries with seizures as the most common manifestation. Lesion localization is usually done with computed tomography (CT) and/or magnetic resonance imaging. Recently, hyperintense signal presumably due to gliosis has been observed on MT SE T_1 weighted image around the healed/calcified cysticercus granuloma and is shown to be related to epileptogenesis and poor long-term seizure control (R.K. Gupta, M.K. Kathuria, S. Pradhan (1999)). For the present study the same patient whose case was discussed in the previous section is considered. A perilesional gliosis around the cystic cavity is observed. The presumed perilesional gliosis is considered present when hyper intensity is seen on MT SE T_1 weighted image around the lesion; not/barely visible abnormality on T_2 weighted images. In this case also we have considered five consecutive slices each of thickness 5mm with inter-slice gap 0.1mm which are from the level of body lateral ventricles to third ventricles. Even though the gliosis is slightly visible on PD weighted images, it is difficult to observe it on T_1 weighted images. In the case of T_2 weighted images it has merged with the cystic cavity's hyper intensity.

Table 4.13 shows the mean and standard deviation values of pixels in perilesional gliosis region and corresponding contra-lateral normal regions on MT SE T_1 weighted images of five consecutive slices. Student's t and F statistics and their corresponding probabilities are also tabulated to study the significance of the changes in mean and variances of pixel values in gliosis region compared to the contra-lateral normal region. In all the slices the mean values are significantly high (very small probabilities of t -statistic) compared to normal region and justifies the appearance of gliosis on MT SE T_1 weighted images as hyper-intense. The high probabilities of F -statistic shows that the variations within the gliosis region are not significant.

MT SE T_1 wtd.	Mean \pm S.D.		t	P	F	P
	Normal	Gliosis				
Slice 1	75.57 \pm 1.98	85.05 \pm 2.44	66.625107	0.00e+00	1.521773	3.78e-06
Slice 2	74.82 \pm 2.34	82.71 \pm 2.32	48.645851	0.00e+00	1.016214	8.70e-01
Slice 3	71.22 \pm 2.92	80.83 \pm 3.01	45.799877	0.00e+00	1.077150	4.46e-01
Slice 4	73.03 \pm 2.96	79.64 \pm 2.72	24.095078	0.00e+00	1.184203	2.16e-01
Slice 5	70.80 \pm 2.50	80.74 \pm 2.63	50.604851	0.00e+00	1.112922	3.22e-01

Table 4.13: Mean, standard deviations of normal and gliosis regions and Student's t , F statistics

from Table 4.16. This increment in T_1 relaxation times is around 100 ms compared to normal region. The appearance of gliosis on T_1 maps would be bright.

T_1 values	Mean \pm S.D.		t	P	F	P
	Normal	Gliosis				
Slice 1	822.89 \pm 180.06	964.96 \pm 190.14	11.996532	4.95e-31	1.115108	2.29e-01
Slice 2	800.99 \pm 235.30	993.22 \pm 167.86	13.548338	6.33e-38	1.964858	9.64e-12
Slice 3	859.91 \pm 200.25	942.64 \pm 163.82	6.761215	2.55e-11	1.592198	1.82e-06
Slice 4	796.12 \pm 249.72	945.86 \pm 134.00	7.747007	6.83e-14	3.472716	9.09e-19
Slice 5	916.54 \pm 217.73	1041.31 \pm 204.7	7.731840	3.78e-14	1.131243	2.54e-01

Table 4.16: Mean and standard deviation of normal and gliosis regions and Student's t, F statistics and their probabilities on T_1 maps

Tables 4.17 and 4.18 show significantly high values in gliosis compared to normal region on T_2 weighted and T_2 maps respectively. On both T_2 weighted and T_2 maps gliosis would appear as bright. In both the cases the variations in gliosis region are significant.

T_2 wtd.	Mean \pm S.D.		T	P	F	P
	Normal	Gliosis				
Slice 1	126.44 \pm 13.15	178.14 \pm 32.26	32.807743	0.00e+00	6.016067	0.00e+00
Slice 2	118.82 \pm 13.65	168.52 \pm 26.63	33.821072	0.00e+00	3.804779	1.89e-39
Slice 3	108.60 \pm 16.80	148.95 \pm 27.20	25.388273	0.00e+00	2.329311	1.52e-17
Slice 4	107.94 \pm 20.49	140.44 \pm 19.41	16.879768	0.00e+00	1.113660	4.31e-01
Slice 5	113.29 \pm 15.29	160.70 \pm 24.50	30.395277	0.00e+00	2.565822	1.07e-17

Table 4.17: Mean and standard deviation of normal and gliosis regions and Student's t, F statistics and their probabilities on T_2 weighted images

T_2 values	Mean \pm S.D.		T	P	F	P
	Normal	Gliosis				
Slice 1	62.62 \pm 5.34	86.61 \pm 18.45	27.616093	0.00e+00	11.938922	0.00e+00
Slice 2	61.52 \pm 6.23	81.24 \pm 13.52	26.987143	0.00e+00	4.710935	0.00e+00
Slice 3	63.90 \pm 8.52	83.25 \pm 15.86	21.706852	0.00e+00	3.098142	1.97e-29
Slice 4	63.07 \pm 10.57	76.53 \pm 9.31	13.997484	5.99e-37	1.288386	6.39e-02
Slice 5	62.87 \pm 7.49	85.64 \pm 15.02	25.121229	0.00e+00	4.017428	2.62e-35

Table 4.18: Mean and standard deviation of normal and gliosis regions and Student's t, F

Table 4.19 shows significantly high values in gliosis region on PD weighted images confirming its hyper intensity on these weighted images. The differences in variations between gliosis and normal regions are not significant. Table 4.20 also shows significant increment in computed PD values in gliosis region with no significant difference in variances. T_2 weighted image values showed more variation compared to T_1 , PD, and MT weighted image values within the gliosis region.

PD wtd.	Mean \pm S.D.		t	P	F	P
	Normal	Gliosis				
Slice 1	126.96 \pm 3.68	134.42 \pm 4.16	29.673491	0.00e+00	1.273812	7.56e-03
Slice 2	118.82 \pm 13.65	153.95 \pm 4.16	43.012947	0.00e+00	1.179972	9.22e-02
Slice 3	108.60 \pm 16.80	144.42 \pm 5.40	28.110928	0.00e+00	1.006975	9.42e-01
Slice 4	107.94 \pm 20.49	150.75 \pm 5.46	17.827040	0.00e+00	1.369388	2.16e-02
Slice 5	113.29 \pm 15.29	153.45 \pm 4.52	29.593845	0.00e+00	1.006179	9.54e-01

Table 4.19: Mean and standard deviation of normal and gliosis regions and Student's t, F statistics and their probabilities on PD weighted images

PD values	Mean \pm S.D.		t	P	F	P
	Normal	Gliosis				
Slice 1	1472.19 \pm 71.80	1518.44 \pm 60.61	10.885725	3.96e-26	1.403464	1.86e-04
Slice 2	1516.30 \pm 82.16	1628.12 \pm 61.28	22.225010	0.00e+00	1.797602	3.07e-09
Slice 3	1508.73 \pm 81.85	1581.35 \pm 68.45	13.816566	2.63e-39	1.438682	1.86e-04
Slice 4	1557.63 \pm 99.01	1645.20 \pm 70.13	10.582300	2.05e-23	1.993117	5.68e-07
Slice 5	1562.70 \pm 83.74	1627.31 \pm 66.94	11.161126	1.07e-26	1.564804	3.69e-05

Table 4.20: Mean and standard deviation of normal and gliosis regions and Student's t, F statistics and their probabilities on PD maps

Linear correlation coefficients between different weighted images in normal and gliosis regions are shown in Tables 4.21 and 4.22 respectively. Normal regions on MT SE T_1 weighted images did not show consistent correlations with T_1 and T_2 weighted images. However, it has positive correlation with PD weighted images. T_1 weighted images in the normal regions have shown negative correlation with T_2 and PD weighted images while T_2 and PD are positively correlated. In gliosis region, MT SE T_1 weighted images are mostly positively correlated with T_2 and PD weighted images and with T_1

weighted images are negatively correlated with T_2 and PD weighted images in gliosis regions. T_2 and PD also have shown similar kind of correlation in gliosis regions compared with normal regions.

Table 4.23 shows linear correlation coefficients between MTR, T_1 , T_2 and PD maps in the normal regions. MTR is significantly negatively correlated with T_1 , T_2 and PD values. MTR is more strongly correlated with T_1 map than with T_2 and PD maps. T_1 , T_2 , and PD are all significantly positively correlated among themselves. The correlation between T_2 and PD is relatively less compared with the correlations between T_1 , T_2 and T_1 , PD.

Table 4.24 shows linear correlation coefficients between different computed parameter maps in gliosis regions. All correlations are similar to the normal regions.

Graphs 4.9-4.12 show the mean values in perilesional gliosis and contra-lateral normal regions on weighted images in consecutive five slices. On MT SE T_1 , T_2 , and PD weighted images, the mean values in gliosis regions are relatively high compared with normal regions as shown in Graphs 4.9, 4.11, and 4.12. Graph 4.10 shows no significant difference in mean values between pathological and normal regions on T_1 weighted images. Graph 4.13-4.16 show the mean values in gliosis and normal regions on computed parameter maps. Graph 4.15 and 4.16 show, respectively, the increase in mean values on T_2 and PD maps in gliosis compared with normal regions while Graph 4.13 shows decrease in mean MTR values. In contrast to T_1 weighted mean values, Graph 4.14 shows a significant increase in mean computed T_1 values in pathological regions.

This analysis indicates of the usefulness of magnetization transfer effect for the diagnosis of perilesional gliosis. The observation of significant high T_1 values in gliosis region could be used for the applicability of other pulse sequences which enhance the contrast of this region for diagnosis purposes. For example, in section 3.5, synthesized IR images at parameters $TR/TE/TI = 6000/40/2500$ ms have shown an excellent contrast between the gliosis and surrounding brain tissue.

Weighted normal regions	r(MT, T ₁)		r(MT, T ₂)		r(MT, PD)		r(T ₁ , T ₂)		r(T ₁ , PD)		r(T ₂ , PD)	
	Normal	P	Normal	P	Normal	P	Normal	P	Normal	P	Normal	P
Slice 1	0.1475	1.05e-03	-0.0614	1.74e-01	0.0410	3.65e-01	-0.8293	0.00e+00	-0.5552	5.59e-41	0.6055	0.00e+00
Slice 2	0.3218	1.75e-11	-0.0195	6.90e-01	0.3347	2.38e-12	-0.7594	0.00e+00	-0.3471	3.17e-13	0.4966	2.67e-27
Slice 3	0.0545	2.70e-01	0.4710	4.97e-24	0.6203	5.60e-45	-0.5649	6.14e-36	-0.1963	6.27e-05	0.7350	0.00e+00
Slice 4	-0.1400	3.97e-02	0.5335	2.73e-17	0.7303	2.81e-37	-0.6696	1.79e-29	-0.5328	3.04e-17	0.7872	0.00e+00
Slice 5	0.2878	5.47e-08	-0.1755	1.08e-03	0.0538	3.19e-01	-0.8099	0.00e+00	-0.4527	8.65e-19	0.6023	2.42e-35

Table 4.21: Linear correlation coefficients between different weighted images in normal regions

Weighted gliosis regions	r(MT, T ₁)		r(MT, T ₂)		r(MT, PD)		r(T ₁ , T ₂)		r(T ₁ , PD)		r(T ₂ , PD)	
	Gliosis	P	Gliosis	P	Gliosis	P	Gliosis	P	Gliosis	P	Gliosis	P
Slice 1	-0.0710	1.16e-01	0.2887	7.34e-11	0.3586	2.55e-16	-0.8757	0.00e+00	-0.5191	3.62e-35	0.6979	0.00e+00
Slice 2	-0.2859	2.86e-09	0.4653	9.51e-24	0.4481	6.14e-22	-0.8869	0.00e+00	-0.6299	0.00e+00	0.7136	0.00e+00
Slice 3	-0.2505	1.04e-07	0.5872	4.81e-42	0.6670	0.00e+00	-0.7553	0.00e+00	-0.5107	1.55e-30	0.8057	0.00e+00
Slice 4	-0.2876	1.75e-05	0.6920	3.97e-32	0.6958	1.33e-32	-0.5743	2.37e-20	-0.4628	7.23e-13	0.8927	0.00e+00
Slice 5	0.5372	4.02e-27	-0.2182	4.44e05	0.2475	3.35e-06	-0.8063	0.00e+00	-0.2452	4.17e-06	0.6339	4.63e-40

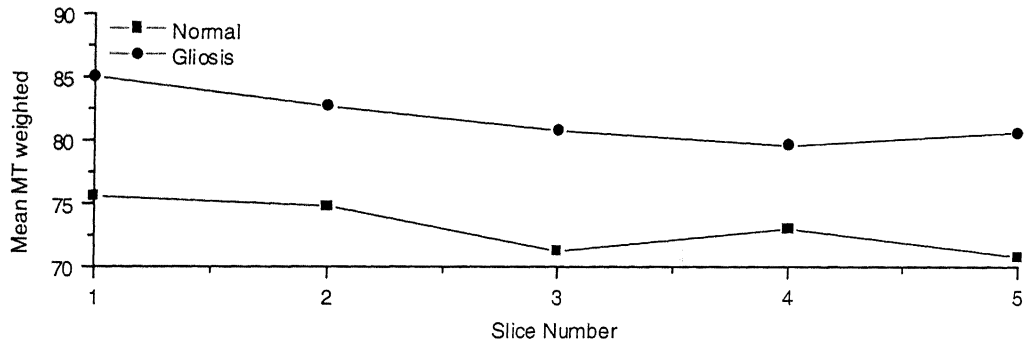
Table 4.22: Linear correlation coefficients between different weighted images in gliosis regions

Parametric normal regions	r(MTR, T ₁)		r(MTR, T ₂)		r(MTR, PD)		r(T ₁ , T ₂)		r(T ₁ , PD)		r(T ₂ , PD)	
	Normal	P	Normal	P	Normal	P	Normal	P	Normal	P	Normal	P
Slice 1	-0.8713	0.00e+00	-0.7167	0.00e+00	-0.6633	0.00e+00	0.7452	0.00e+00	0.8681	0.00e+00	0.3897	3.21e-19
Slice 2	-0.9359	0.00e+00	-0.7241	0.00e+00	-0.7188	0.00e+00	0.7094	0.00e+00	0.8230	0.00e+00	0.3086	1.24e-10
Slice 3	-0.8946	0.00e+00	-0.7320	0.00e+00	-0.6658	0.00e+00	0.7841	0.00e+00	0.8113	0.00e+00	0.5738	2.82e-37
Slice 4	-0.9583	0.00e+00	-0.7207	6.58e-36	-0.8687	0.00e+00	0.7561	2.78e-41	0.9006	0.00e+00	0.5727	3.15e-20
Slice 5	-0.8281	0.00e+00	-0.6862	0.00e+00	-0.6318	9.81e-40	0.7994	0.00e+00	0.8537	0.00e+00	0.4552	5.34e-19

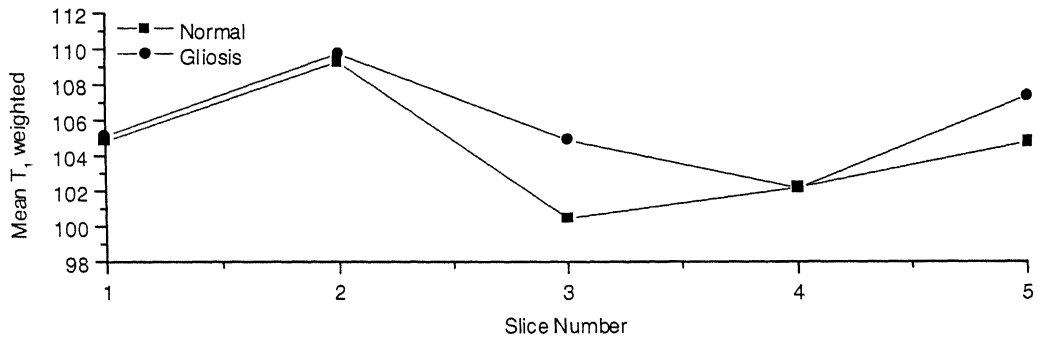
Table 4.23: Linear correlation coefficients between different parameter maps in normal regions

Parametric gliosis region	r(MTR, T ₁)		r(MTR, T ₂)		r(MTR, PD)		r(T ₁ , T ₂)		r(T ₁ , PD)		r(T ₂ , PD)	
	Gliosis	P	Gliosis	P	Gliosis	P	Gliosis	P	Gliosis	P	Gliosis	P
Slice 1	-0.8918	0.00e+00	-0.8671	0.00e+00	-0.5716	7.57e-44	0.8993	0.00e+00	0.7729	0.00e+00	0.4720	1.47e-28
Slice 2	-0.8925	0.00e+00	-0.8625	0.00e+00	-0.5950	3.32e-41	0.8650	0.00e+00	0.7966	0.00e+00	0.4364	9.02e-21
Slice 3	-0.8793	0.00e+00	-0.8139	0.00e+00	-0.6680	0.00e+00	0.8686	0.00e+00	0.8281	0.00e+00	0.5330	1.34e-33
Slice 4	-0.8602	0.00e+00	-0.7773	5.60e-45	-0.7405	8.43e-39	0.8509	0.00e+00	0.9230	0.00e+00	0.6996	4.38e-33
Slice 5	-0.8572	0.00e+00	-0.8042	0.00e+00	-0.5830	1.04e-32	0.9150	0.00e+00	0.7779	0.00e+00	0.5778	4.91e-32

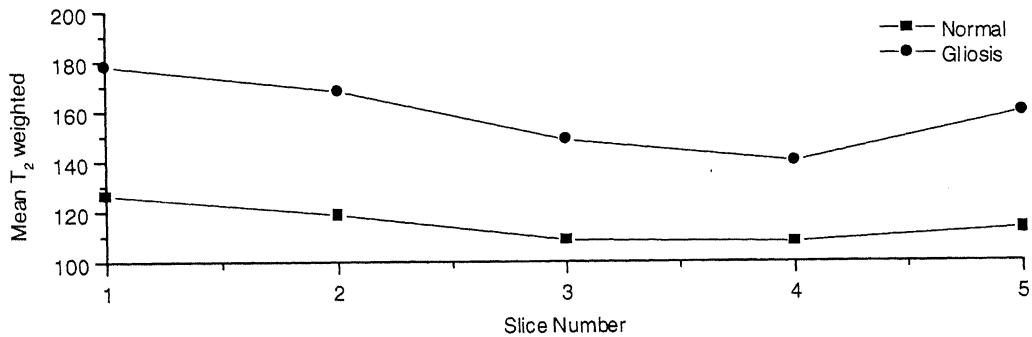
Table 4.24: Linear correlation coefficients between different parameter maps in gliosis regions



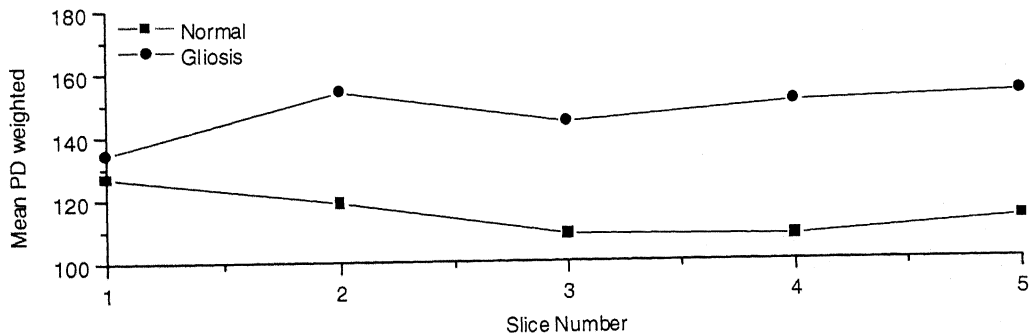
Graph 4.9: Mean values in perilesional gliosis and contra-lateral normal regions on MT SE T_1 weighted images



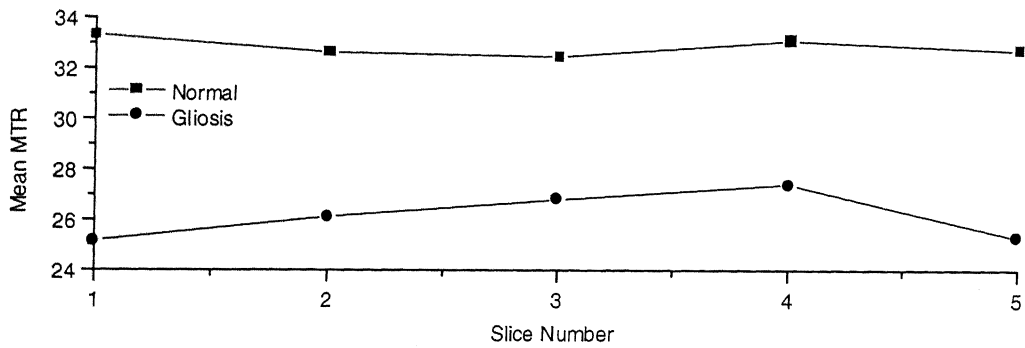
Graph 4.10: Mean values in perilesional gliosis and contra-lateral normal regions on T_1 weighted images



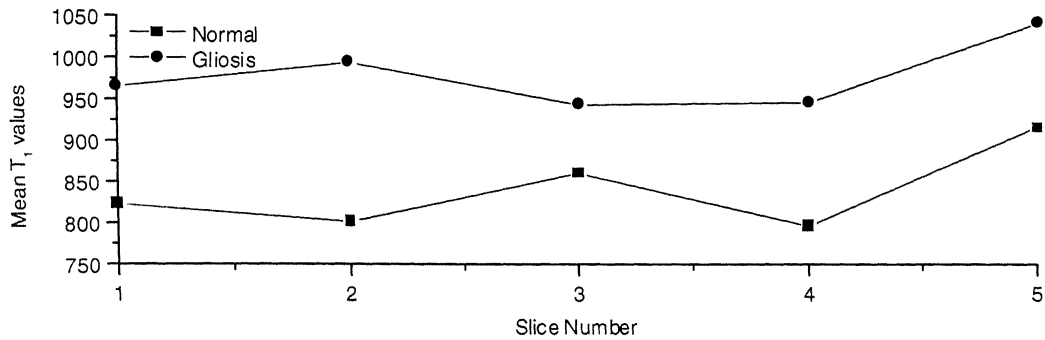
Graph 4.11: Mean values in perilesional gliosis and contra-lateral normal regions on T_2 weighted images



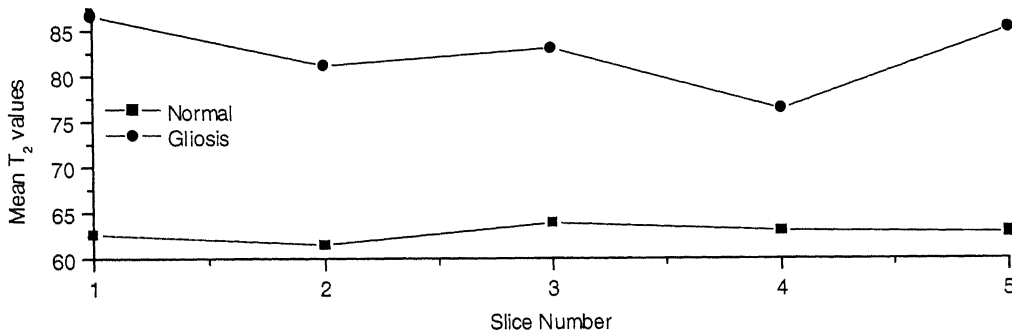
Graph 4.12: Mean values in perilesional gliosis and contra-lateral normal regions on PD weighted images



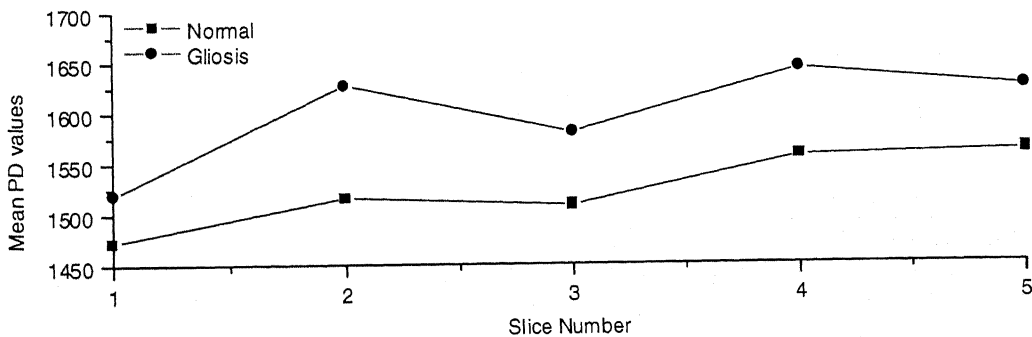
Graph 4.13: Mean values in perilesional gliosis and contra-lateral normal regions on MTR maps



Graph 4.14: Mean values in perilesional gliosis and contra-lateral normal regions on T₁ maps



Graph 4.15: Mean values in perilesional gliosis and contra-lateral normal regions on T₂ maps



Graph 4.16: Mean values in perilesional gliosis and contra-lateral normal regions on PD maps

4.4. Quantitation of Edema

In the present section a quantitative analysis of edema has been done in the case of a single patient. This patient is a 45 years old female who was in good health till April 1999 and was diagnosed with a tapeworm infection in July 1999. In July 1999, she had experienced sudden onset of seizures which manifested initially as difficulty with speech and secondary generalization, and later with left side headache and with simple partial seizures. MRI was done in July 1999 and there was healing lesion in left parietal lobe with extensive edema and anti epileptic drugs (AED) were started. For the present study, eight consecutive slices each of them with 5mm slice thickness and 0.1mm inter-slice gap are considered. These cross-sections are from high parietal lobe to the level of third ventricles. There is single lesion in left high parietal region with extensive edema which is extending from high parietal lobe to parieto-occipital lobe.

Table 4.25 shows a significant increment in MT weighted values in edema regions in comparison with contra-lateral normal regions. But there is no significant difference in variances in both the regions. In contrast to this, MTR values are significantly low in edema regions except in slice 8 as shown in Table 4.26.

MT SE T ₁ wtd.	Mean \pm S.D.		t	P	F	P
	Normal	Edema				
Slice 1	64.14 \pm 4.44	68.71 \pm 3.53	-22.338718	0.00e+00	1.580010	2.52e-10
Slice 2	66.91 \pm 4.97	72.23 \pm 3.10	-27.825333	0.00e+00	2.562336	1.40e-45
Slice 3	70.03 \pm 3.73	75.04 \pm 2.80	-40.443291	0.00e+00	1.778403	3.34e-27
Slice 4	69.89 \pm 2.97	75.87 \pm 2.09	-59.428463	0.00e+00	2.004717	1.81e-35
Slice 5	72.03 \pm 2.22	77.53 \pm 2.38	-64.569191	0.00e+00	1.147881	8.27e-03
Slice 6	71.57 \pm 2.91	74.74 \pm 1.54	-26.023315	0.00e+00	3.534718	0.00e+00
Slice 7	67.26 \pm 2.71	76.29 \pm 1.63	-71.200199	0.00e+00	2.764753	2.36e-35
Slice 8	67.37 \pm 4.79	75.18 \pm 2.29	-38.699139	0.00e+00	4.359744	0.00e+00

Table 4.25: Mean and standard deviation of normal and edema regions and Student's *t*, *F* statistics and their probabilities on MTSE T₁ weighted images

MTR	Mean \pm S.D.		t	P	F	P
	Normal	Edema				
Slice 1	28.44 \pm 7.53	21.44 \pm 4.49	22.170424	0.00e+00	2.818570	4.20e-45
Slice 2	35.82 \pm 6.25	28.06 \pm 3.26	33.725716	0.00e+00	3.675921	0.00e+00
Slice 3	27.55 \pm 6.87	18.12 \pm 4.15	44.336849	0.00e+00	2.745273	0.00e+00
Slice 4	37.59 \pm 4.88	27.97 \pm 2.60	62.823109	0.00e+00	3.515889	0.00e+00
Slice 5	29.04 \pm 5.90	16.48 \pm 3.11	72.119064	0.00e+00	3.607801	0.00e+00
Slice 6	39.20 \pm 3.04	28.42 \pm 1.62	84.767334	0.00e+00	3.505460	0.00e+00
Slice 7	29.18 \pm 4.36	17.13 \pm 3.42	54.182690	0.00e+00	1.622852	1.96e-09
Slice 8	36.29 \pm 7.33	35.88 \pm 2.93	1.353652	1.76e-01	6.267653	0.00e+00

Table 4.26: Mean and standard deviation of normal and edema regions and Student's t, F statistics and their probabilities on MTR maps

On T_1 weighted image, edema has significantly low values and T_1 map shows high values as shown in Tables 4.27 and 4.28 respectively. Both on T_2 weighted images and T_2 maps edema, on overall, has significantly high values compared with contra-lateral normal regions with significant difference in variances as demonstrated in Tables 4.29 and 4.30 respectively.

From Tables 4.31 and 4.32, on overall, PD weighted images and PD maps show significantly high values in edema region compared to the contra-lateral normal regions.

T_1 wtd.	Mean \pm S.D.		t	P	F	P
	Normal	Edema				
Slice 1	90.57 \pm 10.69	87.65 \pm 5.04	6.863605	9.69e-12	4.496512	0.00e+00
Slice 2	97.34 \pm 11.25	92.97 \pm 4.46	11.083804	1.08e-27	6.371774	0.00e+00
Slice 3	96.75 \pm 9.80	91.11 \pm 4.01	20.118578	0.00e+00	5.965241	0.00e+00
Slice 4	103.79 \pm 8.43	97.18 \pm 4.02	25.547007	0.00e+00	4.393178	0.00e+00
Slice 5	101.89 \pm 8.25	92.71 \pm 4.45	37.519688	0.00e+00	3.427851	0.00e+00
Slice 6	111.01 \pm 5.70	98.30 \pm 1.83	57.475475	0.00e+00	9.607631	0.00e+00
Slice 7	95.45 \pm 6.33	92.35 \pm 3.88	10.393809	2.54e-24	2.657025	7.22e-33
Slice 8	109.17 \pm 2.81	99.82 \pm 13.80	17.47448	0.00e+00	24.070436	0.00e+00

Table 4.27: Mean and standard deviation of normal and edema regions and Student's t, F statistics and their probabilities on T_1 weighted images

T ₁ values	Mean \pm S.D.		t	P	F	P
	Normal	Edema				
Slice 1	969.72 \pm 403.45	1202.63 \pm 158.48	-14.93623	0.00e+00	6.48048	0.00e+00
Slice 2	741.26 \pm 237.30	1053.14 \pm 109.95	-36.63475	0.00e+00	4.65783	0.00e+00
Slice 3	950.40 \pm 343.78	1336.09 \pm 132.85	-39.59203	0.00e+00	6.69596	0.00e+00
Slice 4	719.22 \pm 197.55	1065.89 \pm 89.40	-57.73639	0.00e+00	4.88250	0.00e+00
Slice 5	921.67 \pm 247.87	1395.36 \pm 141.77	-63.57553	0.00e+00	3.05685	0.00e+00
Slice 6	610.53 \pm 119.80	1082.77 \pm 69.07	-92.49870	0.00e+00	3.00832	0.00e+00
Slice 7	904.80 \pm 178.70	1248.23 \pm 102.53	-41.53815	0.00e+00	3.03800	1.42e-41
Slice 8	776.31 \pm 89.17	828.46 \pm 473.23	-2.85256	4.40e-03	28.16275	0.00e+00

Table 4.28: Mean and standard deviation of normal and edema regions and Student's t, F statistics and their probabilities on T₁ maps

T ₂ wtd.	Mean \pm S.D.		t	P	F	P
	Normal	Edema				
Slice 1	145.04 \pm 20.12	215.10 \pm 25.32	-60.174534	0.00e+00	1.583861	2.04e-10
Slice 2	121.75 \pm 13.28	198.09 \pm 13.26	-124.085564	0.00e+00	1.002524	9.69e-01
Slice 3	135.02 \pm 19.93	220.51 \pm 13.75	-133.400696	0.00e+00	2.100069	1.06e-43
Slice 4	124.87 \pm 13.53	215.25 \pm 7.73	-209.274643	0.00e+00	3.060679	0.00e+00
Slice 5	123.99 \pm 14.52	209.57 \pm 7.61	-200.056305	0.00e+00	3.637607	0.00e+00
Slice 6	120.59 \pm 10.77	211.67 \pm 7.70	-186.219406	0.00e+00	1.956700	2.17e-19
Slice 7	129.65 \pm 12.26	215.60 \pm 7.10	-151.130096	0.00e+00	2.981824	2.64e-40
Slice 8	115.33 \pm 16.58	166.08 \pm 21.05	-49.834938	0.00e+00	1.610588	4.35e-10

Table 4.29: Mean and standard deviation of normal and edema regions and Student's t, F statistics and their probabilities on T₂ weighted images

T ₂ values	Mean \pm S.D.		t	P	F	P
	Normal	Edema				
Slice 1	68.39 \pm 24.77	95.75 \pm 15.86	-25.839197	0.00e+00	2.439183	3.55e-34
Slice 2	67.83 \pm 21.64	106.47 \pm 13.15	-46.783211	0.00e+00	2.707615	0.00e+00
Slice 3	70.22 \pm 25.60	111.56 \pm 11.78	-55.477112	0.00e+00	4.723387	0.00e+00
Slice 4	65.88 \pm 11.70	116.80 \pm 8.50	-127.08400	0.00e+00	1.896296	2.28e-30
Slice 5	67.46 \pm 12.06	120.04 \pm 9.29	-132.36201	0.00e+00	1.685795	2.55e-23
Slice 6	63.99 \pm 4.68	116.49 \pm 6.04	-185.91993	0.00e+00	1.663032	7.46e-12
Slice 7	68.79 \pm 8.72	118.02 \pm 8.98	-97.939568	0.00e+00	1.059855	4.69e-01
Slice 8	67.49 \pm 20.03	90.04 \pm 13.06	-24.825291	0.00e+00	2.352493	1.35e-28

Table 4.30: Mean and standard deviation of normal and edema regions and Student's t, F

PD wtd.	Mean \pm S.D.		t	P	F	P
	Normal	Edema				
Slice 1	128.40 \pm 10.68	137.09 \pm 3.27	-21.620487	0.00e+00	10.666726	0.00e+00
Slice 2	122.44 \pm 10.74	133.96 \pm 4.06	-30.867407	0.00e+00	6.996948	0.00e+00
Slice 3	129.05 \pm 9.63	140.15 \pm 3.24	-41.299812	0.00e+00	8.802293	0.00e+00
Slice 4	127.87 \pm 5.84	138.65 \pm 3.54	-56.931942	0.00e+00	2.722035	0.00e+00
Slice 5	135.84 \pm 5.34	145.66 \pm 3.85	-57.155006	0.00e+00	1.923388	1.99e-35
Slice 6	119.30 \pm 3.43	129.60 \pm 2.77	-63.193119	0.00e+00	1.534128	7.84e-09
Slice 7	114.27 \pm 6.12	124.92 \pm 2.55	-39.985962	0.00e+00	5.766409	0.00e+00
Slice 8	134.45 \pm 7.37	147.26 \pm 3.49	-41.327747	0.00e+00	4.439348	0.00e+00

Table 4.31: Mean and standard deviation of normal and edema regions and Student's t, F statistics and their probabilities on PD weighted images

PD values	Mean \pm S.D.		t	P	F	P
	Normal	Edema				
Slice 1	1170.76 \pm 145.66	1222.27 \pm 57.09	-9.152752	1.70e-19	6.509777	0.00e+00
Slice 2	1139.66 \pm 124.56	1216.29 \pm 55.30	-17.277565	0.00e+00	5.073103	0.00e+00
Slice 3	1243.05 \pm 154.29	1337.00 \pm 51.50	-21.853928	0.00e+00	8.975176	0.00e+00
Slice 4	1214.56 \pm 84.06	1276.24 \pm 42.89	-23.603373	0.00e+00	3.841543	0.00e+00
Slice 5	1309.91 \pm 93.98	1408.28 \pm 56.37	-34.559910	0.00e+00	2.743973	0.00e+00
Slice 6	1253.86 \pm 44.29	1341.01 \pm 43.05	-38.209717	0.00e+00	1.058820	4.39e-01
Slice 7	1334.34 \pm 101.08	1435.97 \pm 40.40	-23.264595	0.00e+00	6.259330	0.00e+00
Slice 8	1293.59 \pm 106.13	1330.06 \pm 31.78	-8.668811	1.20e-17	11.153337	0.00e+00

Table 4.32: Mean and standard deviation of normal and edema regions and Student's t, F statistics and their probabilities on PD maps

Tables 4.33 and 4.34 show the linear correlation coefficients among MT SE T_1 , T_1 , T_2 , and PD weighted images in the normal regions as well as in the edema regions. In both the regions MT SE T_1 weighted values have shown positive correlation with T_1 and PD weighted values. But with T_2 weighted images no consistency in correlations is observed. Except in slice 6, T_1 weighted values have shown negative correlation with T_2 weighted values in both pathological and normal regions. However, the correlation between T_1 and T_2 weighted images in slice 6 are not significant. The correlations between T_2 and PD weighted values have not shown consistency.

A similar study done on parameter maps is tabulated in Tables 4.35 and 4.36. MTR maps have shown negative correlation with T_1 , T_2 , and PD maps in both edema and normal regions. With T_1 map the correlations are significant than with T_2 and PD maps. T_1 maps have shown positive correlation with T_2 and PD maps in both the regions while T_2 maps are negatively correlated with PD maps.

Graphs 4.17-4.20 show the mean values in edema and contra-lateral normal regions on weighted images in consecutive eight slices. On MT SE T_1 , and PD weighted images, the mean values in edema regions are relatively high compared with normal regions as shown in Graphs 4.17, 4.19, and 4.20. Graph 4.18 shows relatively low mean values in edema regions. Graphs 4.21-4.24 show the mean values in edema and normal regions on computed parameter maps. On T_1 , T_2 , and PD maps, mean values in edema regions have shown relatively high values compared with normal regions as shown in Graphs 4.22, 4.23, and 4.24. But, Graph 4.21 shows the decrease in MTR values in edema regions.

We suggest that the strong quantitative mean differences and correlations may be investigated by the biochemists/pathologists for the underlining cases so that the quantitations could be related with different stages of the pathology. As MT requires much more careful attention and MTR is susceptible to patient motion, quantitations based on routine images ought to be very useful diagnostic tools and may be investigated using a large data base.

Wtd. normal regions	$r(MT, T_1)$		$r(MT, T_2)$		$r(MT, PD)$		$r(T_1, T_2)$		$r(T_1, PD)$		$r(T_2, PD)$	
	Normal	P	Normal	P	Normal	P	Normal	P	Normal	P	Normal	P
Slice 1	0.6523	0.00e+00	-0.4122	4.93e-33	0.5308	0.00e+00	-0.5834	0.00e+00	0.4798	1.40e-45	-0.6150	0.00e+00
Slice 2	0.7478	0.00e+00	0.0191	5.63e-01	0.7733	0.00e+00	-0.1487	6.41e-06	0.6904	0.00e+00	-0.1329	5.59e-05
Slice 3	0.5806	0.00e+00	-0.3388	1.54e-39	0.5418	0.00e+00	0.5183	0.00e+00	0.3620	2.80e-45	-0.4396	0.00e+00
Slice 4	0.5284	0.00e+00	-0.3233	4.60e-33	0.5675	0.00e+00	-0.3989	0.00e+00	0.2969	6.41e-28	-0.3171	8.26e-32
Slice 5	0.4049	0.00e+00	-0.3127	1.08e-34	0.4394	0.00e+00	-0.5229	0.00e+00	0.2358	5.10e-20	-0.3462	1.28e-42
Slice 6	0.5409	0.00e+00	0.5440	0.00e+00	0.4915	0.00e+00	0.0809	2.83e-02	0.1130	2.17e-03	0.5582	0.00e+00
Slice 7	0.4989	1.80e-40	0.0187	6.41e-01	0.6896	0.00e+00	-0.2427	8.58e-10	0.3299	2.91e-17	0.0795	4.74e-02
Slice 8	0.8120	0.00e+00	-0.1913	3.88e-07	0.8217	0.00e+00	-0.4344	2.87e-33	0.6009	0.00e+00	-0.0644	9.02e-02

Table 4.33: Linear correlation coefficients between different weighted images in normal regions

Wtd. edema regions	$r(MT, T_1)$		$r(MT, T_2)$		$r(MT, PD)$		$r(T_1, T_2)$		$r(T_1, PD)$		$r(T_2, PD)$	
	Edema	P	Edema	P	Edema	P	Edema	P	Edema	P	Edema	P
Slice 1	0.4434	1.27e-38	-0.3407	1.69e-22	0.4131	2.87e-33	-0.2226	3.74e-10	0.3884	2.77e-29	-0.2348	3.66e-11
Slice 2	0.4899	0.00e+00	-0.3741	5.43e-33	0.5988	0.00e+00	-0.4034	1.41e-38	0.5057	0.00e+00	-0.3153	1.99e-23
Slice 3	0.2150	1.82e-16	0.1317	5.52e-07	0.4303	0.00e+00	-0.3363	2.91e-39	0.4039	0.00e+00	-0.0479	6.95e-02
Slice 4	0.4992	0.00e+00	0.0450	1.04e-01	0.5317	0.00e+00	-0.2260	1.34e-16	0.5739	0.00e+00	0.0573	3.82e-02
Slice 5	0.6126	0.00e+00	0.0143	5.81e-01	0.4104	0.00e+00	-0.3298	1.18e-38	0.5432	0.00e+00	0.0043	8.68e-01
Slice 6	0.3399	2.42e-21	0.3657	1.12e-24	0.4635	1.98e-40	0.0667	7.04e-02	0.1629	8.97e-06	0.5409	0.00e+00
Slice 7	0.2739	3.58e-12	-0.0370	3.56e-01	0.2211	2.49e-08	-0.4478	5.14e-32	0.6244	0.00e+00	-0.2979	3.21e-14
Slice 8	0.3049	2.00e-16	0.7088	0.00e+00	0.5977	0.00e+00	-0.6118	0.00e+00	0.3108	4.96e-17	0.7373	0.00e+00

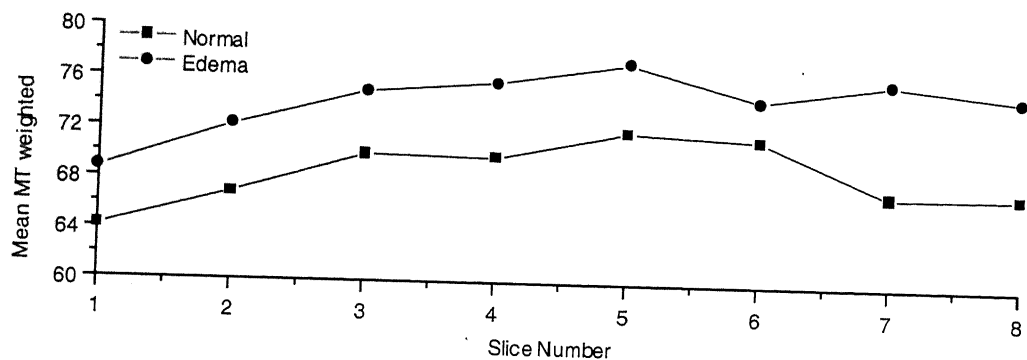
Table 4.34: Linear correlation coefficients between different weighted images in edema regions

Parametric normal regions	r(MTR, T ₁)		r(MTR, T ₂)		r(MTR, PD)		r(T ₁ , T ₂)		r(T ₁ , PD)		r(T ₂ , PD)	
	Normal	P	Normal	P	Normal	P	Normal	P	Normal	P	Normal	P
Slice 1	-0.7891	0.00e+00	-0.4698	1.19e-43	-0.1477	3.78e-43	0.3120	6.77e-19	0.4789	1.40e-45	-0.5716	0.00e+00
Slice 2	-0.8150	0.00e+00	-0.4514	0.00e+00	0.1012	2.20e-03	0.1793	4.87e-08	0.3048	4.36e-21	-0.6600	0.00e+00
Slice 3	-0.8188	0.00e+00	-0.3414	3.69e+00	-0.2900	5.67e-29	0.0730	5.85e-13	0.6660	0.00e+00	-0.5723	0.00e+00
Slice 4	-0.8882	0.00e+00	-0.2698	3.62e-23	-0.2971	5.91e-28	0.1972	6.89e-13	0.5066	0.00e+00	-0.6117	0.00e+00
Slice 5	-0.8973	0.00e+00	-0.3841	0.00e+00	-0.4087	0.00e+00	0.2340	1.01e-19	0.6561	0.00e+00	-0.4870	0.00e+00
Slice 6	-0.8169	0.00e+00	-0.3349	1.05e-20	-0.4846	1.68e-44	0.1552	2.40e-05	0.6932	0.00e+00	-0.0942	1.06e-02
Slice 7	-0.8515	0.00e+00	-0.2012	4.18e-07	-0.3397	2.83e-18	0.0563	1.60e-01	0.6417	0.00e+00	-0.5315	0.00e+00
Slice 8	-0.9021	0.00e+00	-0.5323	0.00e+00	-0.4999	4.20e-45	0.5242	0.00e+00	0.6676	0.00e+00	-0.0115	7.62e-01

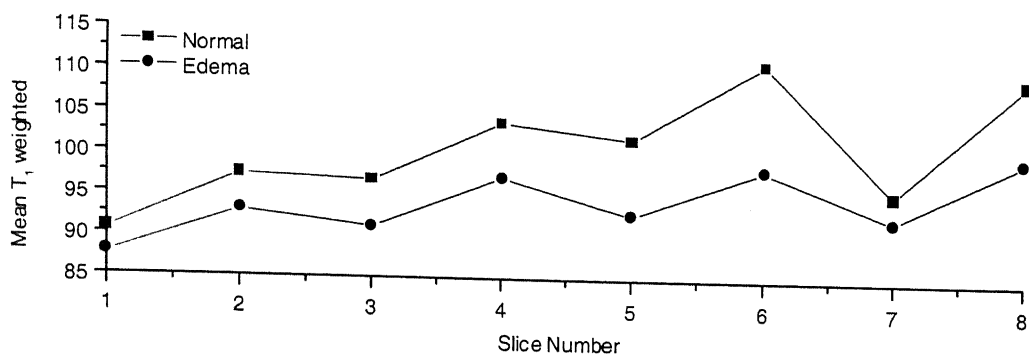
Table 4.35: Linear correlation coefficients between different parameter maps in normal regions

Parametric edema regions	r(MTR, T ₁)		r(MTR, T ₂)		r(MTR, PD)		r(T ₁ , T ₂)		r(T ₁ , PD)		r(T ₂ , PD)	
	Edema	P	Edema	P	Edema	P	Edema	P	Edema	P	Edema	P
Slice 1	-0.6342	0.00e+00	-0.0714	4.69e-02	-0.4292	4.86e-36	0.2027	1.26e-08	0.5404	0.00e+00	-0.6000	0.00e+00
Slice 2	-0.6785	0.00e+00	-0.0620	5.58e-02	-0.2904	5.75e-20	0.2077	9.62e-11	0.4262	2.61e-43	-0.6660	0.00e+00
Slice 3	-0.7332	0.00e+00	-0.3629	0.00e+00	-0.3504	1.06e-42	0.2892	4.83e-29	0.6297	0.00e+00	-0.3783	0.00e+00
Slice 4	-0.7324	0.00e+00	-0.3850	0.00e+00	-0.0650	1.88e-02	0.2730	9.12e-24	0.4302	0.00e+00	-0.5241	0.00e+00
Slice 5	-0.6608	0.00e+00	-0.5354	0.00e+00	-0.1123	1.58e-05	0.3221	7.74e-37	0.6190	0.00e+00	-0.3702	0.00e+00
Slice 6	-0.6108	0.00e+00	-0.1312	3.59e-04	-0.4067	1.19e-30	0.0139	7.07e-01	0.8551	0.00e+00	-0.2048	2.08e-08
Slice 7	-0.7824	0.00e+00	-0.5762	0.00e+00	-0.0040	9.02e-01	0.4113	8.58e-27	0.4339	5.89e-30	-0.4921	2.98e-39
Slice 8	-0.8485	0.00e+00	-0.8232	0.00e+00	-0.3403	2.64e-20	0.8110	0.00e+00	0.6372	0.00e+00	-0.2157	9.17e-09

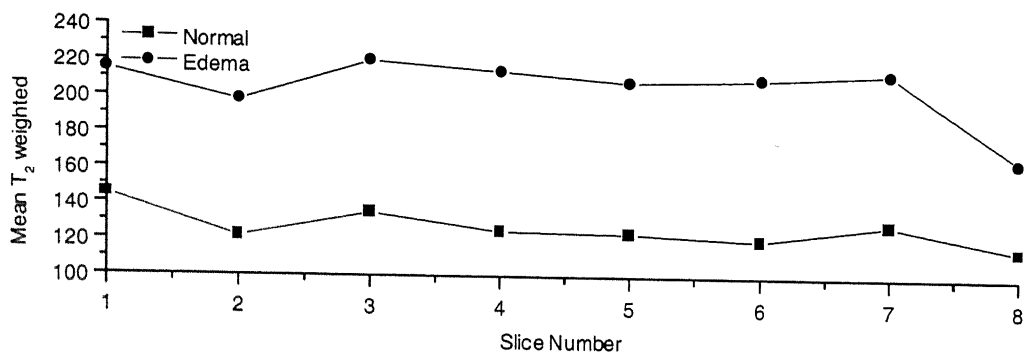
Table 4.36: Linear correlation coefficients between different parameter maps in edema regions



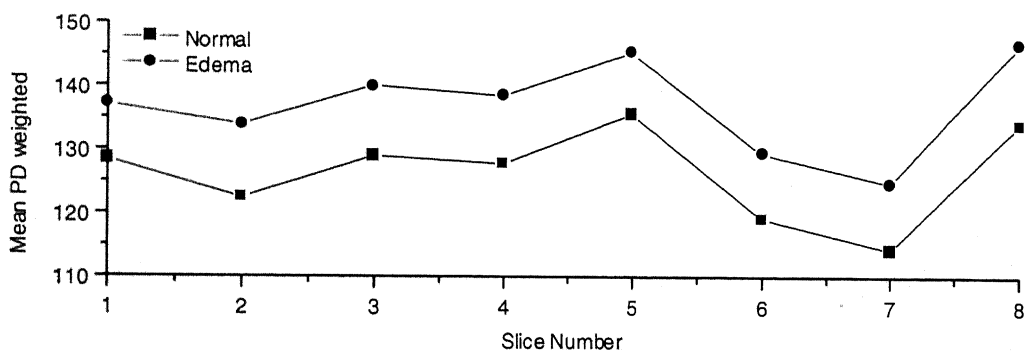
Graph 4.17: Mean values in edema and contra-lateral normal regions on MT SE T_1 weighted images



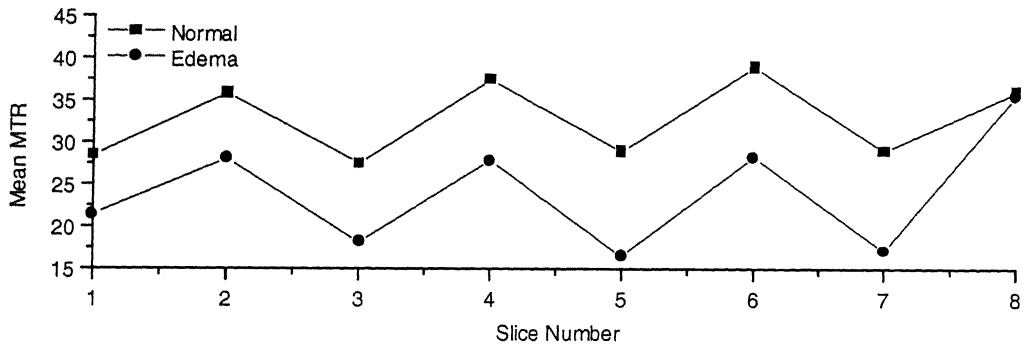
Graph 4.18: Mean values in edema and contra-lateral normal regions on T_1 weighted images



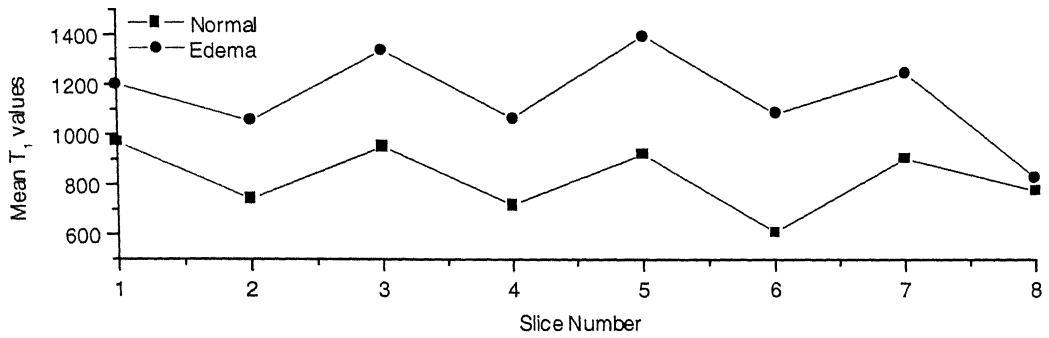
Graph 4.19: Mean values in edema and contra-lateral normal regions on T_2 weighted images



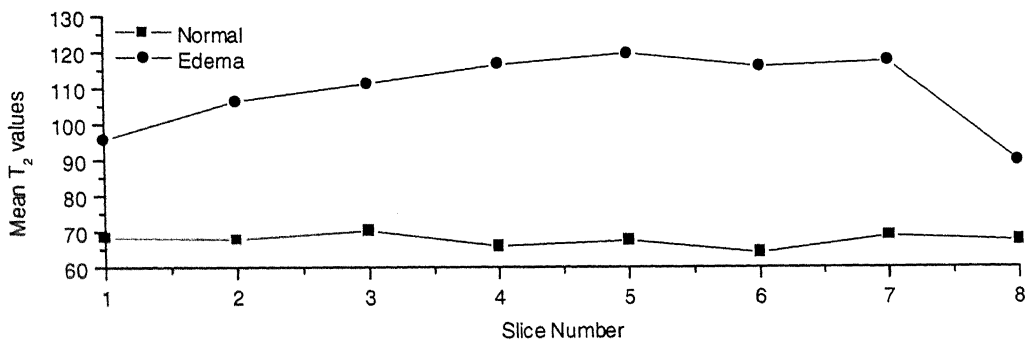
Graph 4.20: Mean values in edema and contra-lateral normal regions on PD weighted images



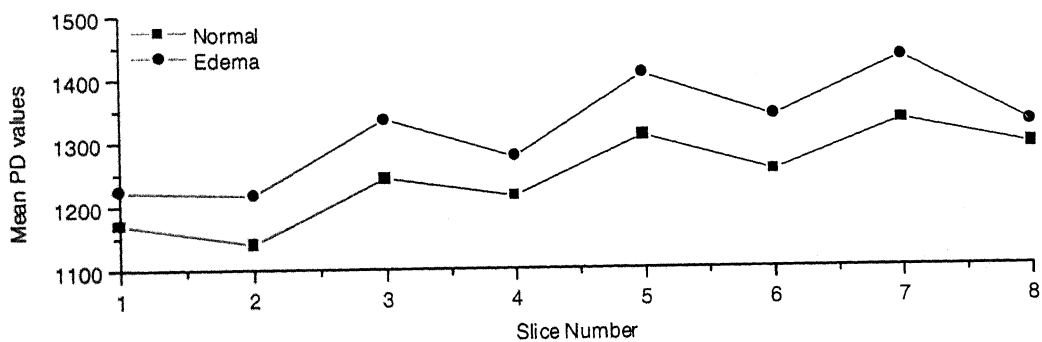
Graph 4.21: Mean values in edema and contra-lateral normal regions on MTR map



Graph 4.22: Mean values in edema and contra-lateral normal regions on T_1 map



Graph 4.23: Mean values in edema and contra-lateral normal regions on T_2 map



Graph 4.24: Mean values in edema and contra-lateral normal regions on PD map

REFERENCES

- [01] Bloch, F., (1946) Nuclear induction, *Phys. Rev.*, 70, 460-474.
- [02] Bobman, S.A., Riederer, J.N., Tasciyan, T., Farzaneh, F., and Wang, H.Z., (1986) Pulse sequence extrapolation with MR image synthesis, *Radiology*, 159(1), 253-260.
- [03] Bobman, S.A., Riederer, S.J., Lee, J.N., Suddarth, S.A., Wang, H.Z., and Mac Fall, J.R., (1985) Synthesized MR images: Comparison with Acquired Images, *Radiology*, 155, 731-738.
- [04] Bottomley, P.A., Hardy, C.J., Argersinger, R.E., and Allen-Moore, G., (1987) A review of ^1H nuclear magnetic resonance relaxation in pathology: Are T_1 and T_2 diagnostic?, *Medical Physics*, 14, 1-37.
- [05] Brown, M.A., Semelka, R.C., (1999) MR Imaging Abbreviations, Definitions, and Description: A Review, *Radiology*, 213: 647-662.
- [06] Callaghan, P.T., (1991) *Principles of Nuclear Magnetic Resonance Microscopy*, Clarendon Press, Oxford.
- [07] Damadian, R., (1971) Tumor detection by nuclear magnetic resonance, *Science*, 171, 1151-1153.
- [08] De Fontaine, D.L., Ross, D.K., and Ternai, B. (1975) A fast nonlinear least squares method for the calculation of relaxation times, *J. Magn. Reson.*, 18, 276-281.
- [09] Farrar, T., and Becker, E., (1971) *Pulse and Fourier Transform NMR*, Academic Press, New York.
- [10] Filippi, M., Campi, M.D., Dousset, V., et al. (1995) A magnetization transfer imaging study of normal-appearing white matter in multiple sclerosis, *Neurology*, 45, 478-482.
- [11] Foster, M.A., and Haase, A., (1996) Relaxation Measurements in Imaging Studies, in: Grant, D.M. and Harris, R.K., [eds.]: *Encyclopedia of Nuclear Magnetic Resonance*, John Wiley & Sons Ltd., New York, 4034-4041.
- [12] Gass, A., Barker, G.J., Kidd, D., Thrope, J.W., MacManus, D., Brennan, A., Tofts, P.S., Thompson, A.J., MacDonald, W.I., and Miller D.H., (1994) Correlation of magnetization transfer ratio with clinical disability in multiple sclerosis, *Ann. Neurol.*, 36, 62-67.
- [13] Gong, J., and Hornak, J.P., (1992) A Fast T_1 Algorithm, *Magn. Reson. Imaging*, 10, 623-626.

- [14] Gupta, R.K., Kathuria, M.K., and Pradhan, S., (1999) Magnetization transfer MR imaging demonstration of perilesional gliosis: its relationship with epilepsy in treated or healed neurocysticercosis, *Lancet*, 354, 41-42.
- [15] Hajnal, J.V., Baudouin, C.J., Oatridge, A., Young, I.R., and Bydder, G.M., (1992) Design and Implementation of Magnetization Transfer Pulse Sequences for Clinical Use, *J. Comp. Tomogr.*, 16(1), 7-18.
- [16] Harvey, I., Tofts, P.S., Morris, J.K., Wicks, D.A.G., and Ron, M.A., (1991) Sources of T_1 variance in normal human white matter, *Magn. Reson. Imaging*, 9, 53-59.
- [17] Hazlewood, C.F., Chang, D.C., Medina, D., Cleveland, G., and Nichols, B.L., (1972) Distinction between the preneoplastic and neoplastic state of murine mammary glands, *Proc. Natl. Acad. Sci., U.S.A.*, 69, 1478-1480.
- [18] Hiehle, J.F., Grossman, R.I., Ramer, K.N., Gonzalez-Scarano, F., and Cohen J.A., (1995) Magnetization transfer effects in MR-detected multiple sclerosis lesions: comparison with gadolinium-enhanced spin echo images and non-enhanced T_1 -weighted images, *AJNR*, 16, 69-77.
- [19] Hinshaw, W.S., and Lent, A.H., (1983) An introduction to NMR imaging : From the Bloch equation to the imaging equation, *Proc. IEEE*, 71, 338-350.
- [20] Hoffman, R.A. and Forsén, S., (1966) Transient and Steady-State Overhauser Experiments in the Investigation of Relaxation Processes. Analogies between Chemical Exchange and Relaxation, *J. Chem. Phys.*, 45, 2049-2060.
- [21] Hu, B.S., Conolly, S.M., Wright, G.A., Nishimura, D.G., and Macovski, A., (1992) Pulsed Saturation Transfer Contrast, *Magn. Reson. Med.*, 26, 231-240.
- [22] Iwaoka, H., Hirata, T., and Matsuura, H., (1987) Optimal Pulse Sequences for Magnetic Resonance Imaging - Computing Accurate T_1 , T_2 , and Proton Density Images, *IEEE Trans. Med. Imag.*, MI-6(4), 360-369.
- [23] Jones, J.P., (1988a) Physics of the MR Image: From the Basic Principles to Image Intensity and Contrast, in: Partain, C.L., Price, R.R., Patton J.A., Kulkarni, M.V., James, A.E., [eds.]: *Magnetic Resonance Imaging*, II, W.B. Saunders Company, Philadelphia, 1003-1027.
- [24] Jones, J.P., (1988b) T_1 and T_2 Measurement, in: Partain, C.L., Price, R.R., Patton J.A., Kulkarni, M.V., James, A.E., [eds.]: *Magnetic Resonance Imaging*, II, W.B. Saunders Company, Philadelphia, 1311-1320.
- [25] Kathuria, M.K., Gupta, R.K., Roy, R., Gaur, V., Husain, N., and Pradhan, S., (1998) Measurement of Magnetization Transfer in Different Stages of Neurocysticercosis, *J. Magn. Reson. Imaging*, 8, 473-479.
- [26] Kumar, A., Welti, D., and Ernst, R.R., (1975) NMR Fourier zeugmatography, *J. Magn. Reson.*, 18, 69-83.

- [27] Lauterbur, P.C., (1973) Image formation by induced local interactions: Examples employing NMR, *Nature*, 242, 190-191.
- [28] Loevner, L.A., Grossman, R.I., McGowna, J.C., Ramer, K.N., and Cohen, J.A., (1995) Characterization of multiple sclerosis plaques with T₁ weighted MR and quantitative magnetization transfer, *AJNR*, 1473-1479.
- [29] Mansfield, P., and Morris, P.G., (1982) *NMR Imaging in Biomedicine*, Supl. 2, Advances in Magnetic Resonance, Academic Press, New York.
- [30] Mehta, R.C., Pike, G.B., and Enzmann, D. (1996), Measure of magnetization transfer in multiple sclerosis demyelinating plaques, white matter ischemic lesions, and edema, *AJNR*, 17, 1051-1055.
- [31] Morris, P.G., (1986) *Nuclear magnetic resonance imaging in medicine and biology*, Clarendon press, Oxford.
- [32] Mugler, J.P., (1999) Overview of MR Imaging Pulse Sequences, *MRI Clinics of North America*, 7, 661-697.
- [33] Partain, C.L., Price, R.R., Patton, J.A., Kulkarni, M.V., and James Jr. A.E., (1988) *Magnetic Resonance Imaging*, II, W.B. Saunders Company, Philadelphia.
- [34] Petrella, J.R., Grossmann, R.I., McGowan, J.C., Campbell, G., and Cohen, J.A., (1996) Multiple sclerosis lesions: relation between MR enhancement pattern and magnetization transfer effect, *AJNR*, 17, 1041-1049.
- [35] Podo, F., (1990) General need for quantitative methodologies in tissue characterization by MRI, in: Higer, H.P., Bielke, G., [eds.]: *Tissue characterization in MR Imaging*, New York, Springer-Verlag.
- [36] Press, W.H., Teukolsky, S.A., Vetterling, W.T., Flannery, B.P., (1998) *Numerical Recipes in C*, Cambridge University Press.
- [37] Price, R.R., Stephens, W.H., and Partain, C.L., (1988) NMR Physical Principles, in: Partain C.L., Price R.R., Patton J.A., Kulkarni M.V., and James Jr. A.E., [eds.]: *Magnetic Resonance Imaging*, II, W.B. Saunders Company, Philadelphia.
- [38] Rathore, R.K.S., Datta, S., Gupta, R.K., Rao, S.B., and Verma, R., (2001) An MLE based segmentation method for quantitation in MR images, *9th Scientific Meeting of ISMRM*, April 21-27, Glasgow.
- [39] Rathore, R.K.S., Gupta, R.K., Kaliprasad, V.S.N., Rao, S.B., and Sushmita Datta, (2000) Iterative Sharpening of the Resolution in Magnetic Resonance Imaging, *8th Scientific Meeting of ISMRM*, April, Colorado.
- [40] Riederer, S.J., (1990) NMR Parameter Calculations, in: Higer, H.P., Bielke, G., [eds.]: *Tissue Characterization in MR Imaging*, New York, Springer-Verlag.

- [41] Riederer, S.J., Bobman, S.A., Lee, J.N., Farzaneh, F., and Wang, H.Z., (1986) Improved Precision in Calculated T1 MR Images Using Multiple Spin-Echo Acquisition, *J. Comput. Assist. Tomogr.*, 10(1), 103-110.
- [42] Rosen, B.R., Pykett, I.L., and Brady, T.J., (1984) Spin Lattice Relaxation Time Measurements in Two-Dimensional Nuclear Magnetic Resonance Imaging: Corrections for Plane Selection and Pulse Sequence, *J. Comput. Assist. Tomogr.*, 8(2), 195-199.
- [43] Schad, L.R., Brix, G., Zuna, I., Härle, Lorenz, W.J., and Semmler, W., (1989) Multiexponential Proton Spin-Spin Relaxation in MR Imaging of Human Brain Tumors, *J. Comput. Assist. Tomogr.*, 13(4), 577-587.
- [44] Sebastiani, G., and Barone, P., (1991) Mathematical principles of basic magnetic resonance imaging in medicine, *Signal Processing*, 25, 227-250.
- [45] Sinha, S., Thomas, M.A., Huda, A.S., Lufkin, R.B., (2001) Magnetic Resonance Imaging and Spectroscopy Techniques, in: Gupta, R.K., and Lufkin, R.B., [eds.]: *MR imaging and Spectroscopy of Central Nervous System Infections*, Luwer Academic/Plenum Publisher, New York.
- [46] Stark, D.D., Bradley, W.G., (1999) *Magnetic resonance imaging*, I, 3rd edition, Mosby, New York.
- [47] Tanttu, J.I., Sepponen, R.E., Lipton, M.J., and Kuusela, T., (1992) Synergistic enhancement of MRI with Gd-DtPA and magnetization transfer, *J. Comp. Assist. Tomogr.*, 16, 19-24.
- [48] Wehrli, F.W., MacFall, J.R., Shutts, D., Breger, R., and Herfkens, R.J., (1984) Mechanisms of Contrast in NMR Imaging, *J. Comput. Assist. Tomogr.*, 8(3), 369-380.
- [49] Wolf, S.D., and Balaban, R.S., (1989) Magnetization transfer contrast (MTC) and tissue water proton relaxation in vivo, *Magn. Res. Med.*, 10, 135-144.
- [50] Wood, M.L., and Wehrli, F.W., (1999) Principles of Magnetic Resonance Imaging, in: Stark, D.D., and Bradley Jr., W.G., [eds.]: *Magnetic Resonance Imaging*, I, 3rd Edition, Mosby, St. Louis.
- [51] Xing Li, and Hornak, J.P., (1994) T₂ Calculations in MRI: Linear versus nonlinear methods, *J. Imag. Sci. Tech.*, 38(2), 154-157.